Geological Applications of Synthetic Fluid Inclusions

by

S. Michael Sterner

Dissertation submitted to the faculty of the
Virginia Polytechnic Institute and State University
in partial fulfillment of the requirements for the degree of

DOCTOR OF PHILOSOPHY
in
Geological Sciences

APPROVED:

Robert J. Bodnar, Chairperson

I-Ming Chou

J. R. Craig

D. A. Hewitt

J. D. Rimstidt

October, 1989
Blacksburg, Virginia

Geological Applications of Synthetic Fluid Inclusions

by

S. Michael Sterner

Robert J. Bodnar, Chairperson

Geological Sciences

(ABSTRACT)

Vapor-saturated solubility relationships in the system NaCl-KCl-H_2O have been determined by experimentally synthesizing fluid inclusions in quartz in the presence of known brine compositions and then measuring the dissolution temperatures of halite and/or sylvite daughter crystals within the inclusions using a microscope equipped with a heating stage. These data, along with other literature values have been used in a regression routine to generate a series of equations describing vapor-saturated solubility relations within the halite, sylvite and hydrohalite stability fields. These equations, together with a recently published equation for the ice stability field (Hall et al., 1987), have been used to construct the complete vapor-saturated solubility surface in the NaCl-KCl-H_2O ternary system. The diagram may be used in the interpretation of microthermometric data to determine the compositions of fluid inclusions approximated by the NaCl-KCl-H_2O system.

P-T conditions inferred from fluid inclusions in metamorphic rocks often disagree with values predicted from mineral equilibria calculations suggesting that inclusions formed during early stages of regional metamorphism continue to re-equilibrate during burial and subsequent uplift in response to differential pressure. P-T conditions accompanying burial and uplift were experimentally simulated by forming pure-H_2O inclusions in quartz, and then re-equilibrating the inclusions such that final confining pressures ranged from 5 kbar above to 4 kbar below the original formation pressure.

Homogenization temperatures of re-equilibrated inclusions indicated densities intermediate between the initial and final P-T conditions. In short-term experiments (7 days) where the initial internal overpressure exceeded 1 kbar most H_2O inclusions re-equilibrated until their internal pressures were between ~750 and 1500 bars above the confining pressure, regardless of the initial pressure differential. In a long-term experiment (52 days) some inclusions were found to have completely re-equilibrated.

In experiments where the confining pressure during re-equilibration exceeded the original formation pressure, the densities of pure-water inclusions increased to values intermediate between the initial and final P-T conditions. Additionally, these inclusions were generally surrounded by a halo of smaller inclusions also of intermediate density and resulting in a texture similar to that previously ascribed to decrepitation resulting from internal overpressure. Pressure-volume-temperature-composition (PVTX) relations in the CO_2-H_2O system have been experimentally determined from 2 to 6 kbar and 400° to 700°C for fluid compositions between 12.5 and 87.5 mole % CO_2 using the synthetic fluid inclusion technique. The method involves trapping CO_2-H_2O fluids of known composition as inclusions in quartz at elevated pressures and temperatures (P_F and T_F) and then calculating the desired fluid properties using microthermometric data combined with available PVTX data for this system at low pressures and temperatures.

PTX properties of CO_2-H_2O mixtures were determined from the total homogenization temperatures (Th (total)) of fluid inclusions trapped in the one-fluid phase field. Internal pressures on the solvus (at Th (total)) were calculated using the equation of state of Connolly and Bodnar (1983) and the inclusion densities as determined above. The pressure and temperature of total homogenization of each inclusion defines a point on the solvus unique to that particular bulk fluid composition and density. Thus, the array of many such points determined in this manner delineates the boundary between the one-phase and two-phase fields over a portion of PTX-space.

Acknowledgments

Support for this research was provided by a grant from the National Science Foundation, EAR-8607356, to and by funds from the Virginia Mining and Mineral Resources Research Institute. I would like to thank for serving as my committee chairman and for providing scientific input and financial support. I would also like to thank the other members of my committee: J.R. Craig, I-Ming Chou, D.A. Hewitt and J.D Rimstidt for helpful discussions pertaining to several aspects of this research. I am greatly indebted to , friend, colleague and co-author of "Synthetic Fluid Inclusions IV: Solubility relations in the system NaCl-KCl-H_2O under vapor-saturated conditions," a manuscript based on Chapter 1. The assistance of in the design of hydrothermal experiments and the use of his laboratory was greatly appreciated. Finally, I thank my fellow graduate students. I hope they derived as much from our friendship and scientific interaction as I did.

Table of Contents

Chapter 1: Solubility Relations in the System NaCl-KCl-H_2O Under Vapor-Saturated Conditions 1

ABSTRACT 1

INTRODUCTION 2

EXPERIMENTAL PROCEDURE 3

RESULTS 5

NaCl-KCl-H_2O Ternary 7

NaCl-H_2O Binary 16

KCl-H_2O Binary 19

NaCl-KCl Binary 21

PHASE TRANSITIONS NEAR THE VAPOR-SATURATED SOLUBILITY SURFACE 23

ISOTHERMAL PHASE RELATIONS IN THE NaCl-KCl-H_2O TERNARY 29

NaCl-KCl Binary 29

NaCl-KCl-H_2O Ternary 36

DETERMINATION OF FLUID INCLUSION COMPOSITIONS FROM MICROTHERMOMETRIC DATA 38

Equilibrium Phase Transitions 39

Metastable Phase Transitions 47

Effect of Additional Components 54
GEOLOGIC APPLICATIONS 55
REFERENCES 58

Chapter 2: Re-equilibration of Fluid Inclusions in Quartz During Laboratory-Simulated Metamorphic Uplift 64
ABSTRACT 64
INTRODUCTION 66
EXPERIMENTAL PROCEDURE 72
RE-EQUILIBRATION OF PURE-H_2O FLUID INCLUSIONS 75
Densities and Compositions: Re-equilibration under Conditions of Internal Overpressure ($P_f > P_c$) 75
Densities and Compositions: Re-equilibration under Conditions of Internal Underpressure ($P_f < P_c$) 85
Inclusion Morphologies: Re-equilibration under Conditions of Internal Overpressure ($P_f > P_c$) 88
Inclusion Morphologies: Re-equilibration under Conditions of Internal Underpressure ($P_f < P_c$) 90
RE-EQUILIBRATION OF NaCl-H_2O FLUID INCLUSIONS 98
H_2O Diffusion 99
Re-Equilibration Across a One-Phase/Two-Phase Boundary 102
CONCLUSIONS AND GEOLOGIC IMPLICATIONS 104
REFERENCES 108

Chapter 3: The System CO_2-H_2O: Experimental Determination of Pressure-Volume-Temperature-Composition Properties from 2 to 6 kbar and 400° to 700°C 113

ABSTRACT 113

INTRODUCTION 116

EXPERIMENTAL PROCEDURE 120

Fluid Inclusion Synthesis 122

Systematics of Fluid Inclusions in the CO_2-H_2O System 125

Microthermometry 127

CALCULATION PROCEDURE (MMVs) 130

Solubility of CO_2 in the Aqueous Phase Below 31.0°C 130

Density of the Aqueous Phase Below 31.0°C 131

Solubility of H_2O in the CO_2 Phase Below 31.0°C 134

Density of CO_2 along the Liquid-Vapor Curve 134

Bulk Density of Inclusion 135

Thermal Expansion and Compressibility of Quartz 137

Error Analysis 139

RESULTS 151

Equation for the Volumetric Properties of CO_2-H_2O 151

Comparison with Previous Volumetric Determinations for CO_2-H_2O 158

Comparison with Volumetric Properties Predicted by Equations of State 158

Excess Volumes of CO_2-H_2O Mixtures 159

Partial Molar Volumes of CO_2 and H_2O 164

DETERMINATION OF THE CO_2-H_2O SOLVUS 167
SUMMARY OF RESULTS 175
REFERENCES 177
APPENDIX I. Experimental conditions, microthermometric data and calculated mean molar volumes of synthetic fluid inclusions in the CO_2-H_2O binary system 182
APPENDIX II. FORTRAN Program to calculate MMVs of CO_2-H_2O mixtures from input data from synthetic fluid inclusions 185
APPENDIX III. Volumetric properties of CO_2-H_2O mixtures calculated using Equation 3.20 188
APPENDIX IV. Experimental conditions, microthermometric data and solvus coordinates determined from synthetic fluid inclusions in the CO_2-H_2O binary system 194
APPENDIX V. FORTRAN Program to calculate uncertainties in MMVs of CO_2-H_2O mixtures using initial error estimates listed in Table 3.2 197
APPENDIX VI. Raw microthermometric data from synthetic fluid inclusions in the CO_2-H_2O binary system 208
VITA 223

List of Figures

Figure 1.1 Comparison of experimentally determined vapor-saturated solubilities (observed values) with those calculated using Eq.1.1..... 10

Figure 1.2 Comparison of experimentally determined vapor-saturated solubilities (observed values) with those calculated using Eq. 1.2..... 11

Figure 1.3 Vapor-saturated solubility surface in the NaCl-KCl-H_2O ternary system 12

Figure 1.4 Comparison of solubilities within the NaCl-KCl-H_2O ternary system from Ravich and Borovaya (1949, 1950) 15

Figure 1.5 Solubility of halite along the three-phase (solid+liquid+vapor) curve 17

Figure 1.6 Solubilities of halite and sylvite along the three-phase (solid+liquid+vapor) curves 18

Figure 1.7 Solubility of sylvite along the three-phase (solid+liquid+vapor) curve 20

Figure 1.8 One-atmosphere phase relations in the anhydrous NaCl-KCl system. 22

Figure 1.9 Schematic P-T projection of the high-salinity portion of a salt-water binary. 25

Figure 1.10 Graphical interpretation of microthermometric fluid inclusion data 31

Figure 1.11 Isothermal, polybaric projections of vapor-saturated phase relations in the NaCl-KCl-H_2O system 37

Figure 1.12 Bulk composition ranges corresponding to various possible modes of solid phase dissolution 41

Figure 1.13 Enlargement of a portion of the vapor-saturated solubility surface..... 51

Figure 2.1 Diagram illustrating segments of various P-T paths possible during regional metamorphism..... 68

Figure 2.2 Diagram showing the P-T conditions during experimental re-equilibration of pure-H_2O fluid inclusions 74

Figure 2.3 Microthermometric data from fluid inclusions in sample R4 79

Figure 2.4 P-T diagram showing the results of re-equilibration experiments R1 and R6 80

Figure 2.5 P-T diagram showing the results of re-equilibration experiment R2 81

Figure 2.6 P-T diagram showing the results of re-equilibration experiments R3 and R9 82

Figure 2.7 Results of re-equilibration experiments R4, R5, R10 and R11 83

Figure 2.8 Photomicrographs of fluid inclusions in samples re-equilibrated at 700°C under conditions of internal underpressure ($P_f < P_c$) 92

Figure 2.9 Photomicrographs of fluid inclusions from sample R9 before and after re-equilibration 94

Figure 2.10 Relationship between the percentage (wt. %) of water that must be lost from a pure-H_2O inclusion originally formed at 600°C and 3 kbar and which initially homogenizes to the liquid at 310°C in order to completely account for the indicated homogenization temperature increases by H_2O diffusion 101

Figure 3.1 Solubility of carbon dioxide in water at pressures along the liquid/vapor curve of CO_2 132

Figure 3.2 Densities of CO_2-saturated aqueous solutions at pressures along the liquid/vapor curve of CO_2 133

Figure 3.3 Volume change factor (V_Δ) relating the volume of a fluid inclusion at 20°C and 1 bar to its volume at high P and T 140

Figure 3.4 Mean molar volumes of CO_2-H_2O mixtures 154

Figure 3.5 Percent deviation of predicted values from volumetric data used to generate Equation 3.20 156

Figure 3.6 Percent deviations of individual datum at 400°C (A), 500°C (B), 600°C (C) and 700°C (D) from values predicted by Equation 3.20 157

Figure 3.7 Comparison of isochores calculated using Equation 3.20 (solid line) with those predicted from the equations of state 160

Figure 3.8 Excess molar volumes of CO_2-H_2O mixtures predicted using Equation 3.20 162

Figure 3.9 Partial molar volumes of H_2O in CO_2-H_2O mixtures derived from Equation 3.20 165

Figure 3.10 Partial molar volumes of CO_2 in CO_2-H_2O mixtures derived from Equation 3.20 166

Figure 3.11 Schematic P-T projection of the CO_2-H_2O system at $X_{CO2} = 0.5$ 169

Figure 3.12 P-T projections of the solvus in the system CO_2-H_2O 172

Figure 3.13 P-X projection of the solvus in the CO_2-H_2O system determined using synthetic fluid inclusions 174

List of Tables

Table 1.1 Microthermometric data from synthetic fluid inclusions in the system NaCl-KCl-H_2O 6

Table 1.2 Coefficients of solubility equations 1.1, 1.2, and 1.3 9

Table 1.3 Temperatures and compositions along the five cotectic boundaries in the NaCl-KCl-H_2O ternary system 14

Table 1.4 Solvus compositions determined from data in Table 1.1 33

Table 2.1 Microthermometric data from re-equilibrated synthetic fluid inclusions 76

Table 3.1 List of symbols 117

Table 3.2 Initial uncertainty estimates (2σ Errors) 142

Table 3.3 Uncertainty estimates in fluid compositins (X_{CO2}) 143

Table 3.4 Average final uncertainty estimates (2σ Errors) 145

Table 3.5 Comparison of molar volumes of H_2O determined from synthetic fluid inclusions with values determined using conventional techniques 150

Table 3.6 Coefficients $C_{(i,j)}$ of Equation 3.20c 153

Chapter 1: Solubility Relations in the System NaCl-KCl-H_2O Under Vapor-Saturated Conditions

ABSTRACT

Vapor-saturated solubility relationships in the system NaCl-KCl-H_2O have been determined by experimentally synthesizing fluid inclusions in quartz in the presence of known brine compositions and then measuring the dissolution temperatures of halite and/or sylvite daughter crystals within the inclusions using a microscope equipped with a heating stage. These data, along with other literature values have been used in a stepwise multiple regression routine to generate a series of equations describing vapor-saturated solubility relations within the halite, sylvite and hydrohalite stability fields. These equations, together with a recently published equation for the ice stability field (Hall et al., 1987), have been used to construct the complete vapor-saturated solubility surface in the NaCl-KCl-H_2O ternary system. The diagram may be used in the interpretation of microthermometric data to determine the compositions of fluid inclusions approximated by

the NaCl-KCl-H_2O system.

For the NaCl-H_2O binary system, the ternary halite field expression reduces to;

$$\text{Wt. \% NaCl} = 26.242 + 0.4928\Psi + 1.42\Psi^2 - 0.223\Psi^3 + 0.04129\Psi^4 + 0.006295\Psi^5 - 0.001967\Psi^6 + 0.0001112\Psi^7$$

$$(\Psi = T°C/100, \text{ where } 0.1° \leq T°C \leq 801°C)$$

which describes halite solubilities along the three-phase halite + liquid + vapor (H+L+V) curve. Similarly, sylvite solubilities along the three-phase sylvite + liquid + vapor (S+L+V) curve are described by the equation;

$$\text{Wt. \% KCl} = 21.886 + 20.28\Psi - 9.603\Psi^2 + 4.078\Psi^3 - 0.8724\Psi^4 + 0.09174\Psi^5 - 0.003776\Psi^6$$

$$(\Psi = T°C/100, \text{ where } -10.7° \leq T°C \leq 770°C).$$

Solubility data obtained from synthetic fluid inclusions are in good agreement with recently published data for the KCl-H_2O and NaCl-H_2O binary systems but are at variance with some earlier works.

INTRODUCTION

The presence of NaCl and KCl as major solute components in fluids from a wide variety of geologic environments has been well-documented by a number of fluid inclusion studies (e.g., Roedder, 1972). Microthermometric analyses of these fluid inclusions provide useful estimations of the chemical compositions of fluids present during periods of metamorphism, ore deposition, and hydrothermal alteration. The accuracy with which fluid chemistries may be determined from heating and freezing studies depends on the correct identification of major components, proper interpretation of

observable phase transitions, and the quality and availability of pressure-temperature-composition (PTX) data. However, solubility data presently available for the NaCl-KCl-H_2O ternary system are somewhat limited, and comparison of published values yields several inconsistencies between different data sets. In this paper we present a set of internally consistent experimental results for solubilities over all composition space in the NaCl-KCl-H_2O ternary system under vapor-saturated conditions.

EXPERIMENTAL PROCEDURE

Phase relations were determined using synthetic fluid inclusions in quartz as described by Sterner and Bodnar (1984) and Bodnar and Sterner (1987). Fluid inclusions were synthesized in the presence of NaCl-KCl-H_2O solutions of known composition by healing fractures in natural Brazilian quartz at elevated temperatures and pressures. Salt solubilities were then determined by measuring the dissolution temperatures of halite and/or sylvite daughter crystals within the inclusions using a microscope equipped with a heating stage. A detailed description of the procedure for synthesizing fluid inclusions is given by Bodnar and Sterner (1987) and will only be summarized here.

Quartz cylinders ~4.5 mm in diameter and ~8 mm in length were cut from a large, single crystal of Brazilian quartz using a diamond coring drill. The cores were heated in an oven to 350°C and fractured by quenching in distilled water at room temperature. After drying, the fractured quartz cylinders and amounts of NaCl, KCl and H_2O required to produce the desired brine composition at the experimental conditions were loaded into 18 mm long platinum capsules and sealed with an arc welder. The capsules were then loaded into cold-seal pressure vessels and placed in horizontally oriented pre-heated furnaces.

The vessels were immediately pressurized to 6 kbar and for the first two hours the pressure was cycled between 6 and 2 kbar to reopen the fractures and thus prevent the formation of any inclusions before the salt had totally dissolved to form a homogeneous one-phase fluid. The pressure vessels achieved about 96% of their final temperature within 15 minutes but the pressure cycling was prolonged to insure a uniform salinity throughout the capsules. After 5 days the pressure vessels were removed from the furnaces and allowed to air cool. The capsules were then removed from the pressure vessels and opened and the quartz cylinders were cut into 1 mm thick disks and polished on both sides.

The actual pressure and temperature conditions of each experiment were chosen to lie on the isochore which passes through the intersection of the liquidus isopleth for the bulk composition and the vapor-saturated solubility surface. In practice this is somewhat difficult because pressure-volume-temperature-composition (PVTX) properties in this system are not known; but after a few reconnaissance runs the isochores could be approximated using the method described by Bodnar and Sterner (1985). The significance of choosing this particular isochore will be discussed in detail in a later section.

Temperatures of the various phase transitions observed within the inclusions were measured using a Leitz petrographic microscope equipped with a Fluid Inc.-adapted USGS-type gas flow heating/freezing stage. The E-type thermocouple used in the stage was calibrated at -56.6°, 0.0°, and 374.1°C using synthetic fluid inclusions having compositions of (1) 1:1 mole ratio CO_2: H_2O (CO_2 melting at -56.6°C), (2) pure H_2O (ice melting at 0.0°C), and (3) pure H_2O having the critical density (liquid-vapor homogenization by fading of the meniscus at 374.1°C). An additional check on the calibration was performed by measuring the quartz α/β transition temperature (573°C)

which ranged from 571° to 577°C (see Bodnar et al., 1985). Thermal gradients within synthetic fluid inclusion samples at -56.6° and 0.0°C were less than 0.1°C across the 4.5 mm samples (Sterner, unpublished data). At 374.1°C the observed range in homogenization temperatures was less than 5°C. The accuracy of the microthermometric measurements is therefore estimated at ± 0.1°C for temperatures below 50°C, ± 2.5°C for temperatures around 375°C and ± 3°C for temperatures near 575°C. Reproducibility is in all cases within the estimated accuracy of the temperature determination.

RESULTS

Microthermometric data from over 400 individual fluid inclusions measured in this study are presented in Table 1.1. The average temperature and the total range are given for each measured phase transition within an individual sample. The range in measured salt dissolution temperatures is somewhat larger than the estimated accuracy in most cases. This is believed to result from some early-formed fluid inclusions which were trapped either before the salt had totally dissolved in the capsule or in the presence of a slight compositional gradient resulting from incomplete chemical homogenization throughout the volume of the capsule. Early-formed inclusions, trapped before the complete dissolution of salt within the capsule, would have necessarily lower dissolution temperatures, while compositional gradients caused by density stratification could result in higher or lower apparent solubilities. In order to reduce the number of fluid inclusions formed prior to complete chemical homogenization, fractures in the quartz cores were maintained open for the first two hours by cycling the pressure, as previously stated. This was found to significantly decrease the range of observed dissolution temperatures. The cycling method

Table 1.1 Microthermometric data from synthetic fluid inclusions in the system NaCl-KCl-H_2O.

Composition		Halite Dissolution Temperatures (Tm NaCl)				Sylvite Dissolution Temperatures (Tm KCl)			
Wt. %	R	Ave.	Range	Std. Dev.	No.	Ave.	Range	Std. Dev.	No.
20.0	0.0000					-9.0	9.0-9.1	0.05	6
37.7	0.0000					118.3	116-119	0.89	15
37.8	0.7905	241.2	239-243	1.15	9				
37.8	0.5883	160.1	159-161	0.63	11	59.2	58.2-59.9	0.79	4
37.8	1.0000	298.6	297-300	0.83	8				
37.8	0.1864					111.4	111-112	0.19	12
45.0	0.6912	300.9	299-302	0.89	15	59.5	59.5-59.5	0.00	1
46.9	1.0000	393.3	390-397	2.30	15				
50.1	0.3323	210.4	209-211	0.64	10	206.1	205-207	0.64	10
50.6	0.5022	288.5	284-291	2.91	10	153.3	152-155	0.67	9
51.9	0.0000					268.1	266-269	1.19	12
52.4	0.7726	390.0	386-392	1.47	15	58.7	58.0-59.3	0.66	3
53.3	0.1486					260.0	258-264	2.13	12
57.0	1.0000	481.2	478-484	1.88	13				
57.0	0.5819	372.1	369-374	1.57	11	168.1	168-168	0.07	2
57.0	0.3152	262.4	261-264	1.04	4	264.4	263-265	1.00	4
57.0	0.1282					297.7	295-300	1.97	12
57.0	0.2974	250.3	250-251	0.34	9	270.1	270-271	0.25	10
57.0	0.3329	272.0	271-273	0.73	8	258.9	258-261	1.07	8
57.0	0.2675	221.2	221-222	0.36	3	273.2	272-274	0.90	3
57.1	0.4198	311.5	310-313	0.99	4	231.2	230-232	1.30	4
61.9	0.0000					367.7	366-369	1.11	13
62.4	1.0000	518.1	514-521	2.49	10				
62.4	1.0000	518.0	487-526	5.99	25				
64.5	0.4773	390.8	389-392	0.75	12	273.3	272-274	0.67	10
67.4	0.1617	193.6	193-194	0.57	2	386.9	384-389	1.63	8
69.7	0.3574	372.7	367-377	2.92	15	356.9	352-360	2.52	15
70.1	0.0000					443.1	421-455	10.01	20
80.0	0.5470	522.3	519-526	2.21	11	380.3	379-382	1.45	4
80.0	0.4476	479.1	475-490	4.00	12	415.0	414-417	1.73	3
80.0	0.2363	357.4	351-362	3.03	8	480.7	477-482	2.04	9
80.0	0.7991	591.0	588-594	1.98	11	235.3	253-253	0.00	1
80.0	0.1106	230.8	221-240	6.87	6	517.4	513-522	3.33	17
80.0	1.0000	644.1	632-651	4.99	17				
80.0	0.3765	448.5	444-452	2.70	10	445.4	441-447	2.26	9
80.0	0.6850	566.6	564-572	1.90	14	319.8	317-326	3.04	6
80.0	0.8855	611.4	608-614	2.29	15	135.5	135-135	0.00	1
80.2	0.0000					550.5	548-553	1.47	12
89.9	0.0000					651.2	648-653	1.92	5
90.0	0.3977	492.5	490-495	3.54	2	550.8	546-556	4.76	7
90.0	1.0000	713.9	709-719	2.68	15				

Wt. % = total salinity
R = NaCl/(NaCl+KCl) weight ratio

described above was preferred over the α/β quartz fracturing procedure described by Bodnar and Sterner (1987) because the former technique produces a larger number of measurable inclusions than the latter technique. In order to minimize density stratification all experiments were conducted with the pressure vessels oriented horizontally. For the purpose of data reduction the mean temperature of each phase transition was used. This is justified because the difference between the mean dissolution temperature and the maximum dissolution temperature in most cases fell within the estimated range of accuracy. Also, solubilities in the KCl-H_2O and NaCl-H_2O binary systems determined from mean dissolution temperatures of sylvite and halite, respectively, in this study are in excellent agreement with solubilities reported by Chou (1986, 1987) determined using DTA.

NaCl-KCl-H_2O Ternary

Solubility data presented in Table 1.1 together with data from Chou (1982a) and selected data from Linke (1965) were regressed using a stepwise multiple regression routine to generate equations describing temperature - composition relations for the vapor-saturated solubility surfaces in the halite, sylvite, and hydrohalite stability fields. The corresponding equations are:

Halite Field:

$$\begin{aligned} \text{Wt. \%} = {} & a + bY + cR + d\,R\Psi + e\Psi^2 + f\,R^2\Psi + gR^3\Psi^2 \\ & + hR^3\Psi^3 + iR\Psi^3 + j\Psi^3 + kR^4\Psi^2 + lR\Psi^7 + mR^2\Psi^6 \\ & + nR^2\Psi^7 + oR^3\Psi^7 + pR^6\Psi^6 + qR^7\Psi^4 + rR^9\Psi^5 + s\Psi^6 \end{aligned} \qquad (1.1)$$

$$(-2.3 \leq T°C \leq 801°C)$$

Sylvite Field: $\mathbf{Wt.\ \%} = a + b\Psi + c\mathbf{R} + d\mathbf{R}\Psi + e\Psi^2 + f\mathbf{R}^2 + g\mathbf{R}\Psi^2$ (1.2)

$+ h\mathbf{R}^3\Psi + i\mathbf{R}\Psi^3 + j\Psi^3 + k\Psi^4 + l\mathbf{R}\Psi^6 + m\mathbf{R}^8\Psi^6$

$+ n\mathbf{R}^9\Psi^2 + o\mathbf{R}^9\Psi^9 + p\mathbf{R}^9 + q\Psi^5 + r\Psi^6$

$(-22.9 \leq T°C \leq 770°C)$

Hydrohalite Field: $\mathbf{Wt.\ \%} = a + b\Psi + c\mathbf{R}$ (1.3)

$(-22.9 \leq T°C \leq 0.1°C)$

where Ψ = T°C/100, **R** = NaCl / (NaCl+KCl) weight ratio, and **Wt. %** = total salinity. The coefficients of Eqs. 1.1, 1.2, and 1.3 are listed in Table 1.2. Each equation is valid over the entire range of stability of the appropriate phase.

The above equations predict experimental values from the present study and data tabulated in Linke (1965) and Chou (1982a) with an average deviation of ± 0.17 wt. %, and a maximum deviation of 0.67 wt. % for Eq. 1.1; with an average deviation of ± 0.14 wt. %, and a maximum deviation of 0.80 wt. % for Eq. 1.2; and with an average deviation of ± 0.1 wt. %, and a maximum deviation of 0.23 wt. % for Eq. 1.3. Differences between observed and calculated total salinities for the halite and sylvite field equations are plotted in Figs. 1.1 and 1.2, respectively.

General phase relationships on the vapor-saturated liquidus for the system NaCl-KCl-H_2O generated from the equations described above are presented in Fig. 1.3. The surface contains four distinct stability fields - halite, sylvite, hydrohalite, and ice - each in equilibrium with liquid and vapor. The intersections of adjacent stability fields define cotectic boundaries characterized by the stable coexistence of two solids. Compositions and temperatures along the five cotectic boundaries in the NaCl-KCl-H_2O

Table 1.2 Coefficients of solubility equations 1.1, 1.2, and 1.3.

Coef.	Halite Field (Eq. 1)	Sylvite Field (Eq. 2)	Hydrohalite Field (Eq. 3)
a	39.19843568	21.88644809	40.36947594
b	13.59271070	20.27990158	14.80771966
c	-12.95646989	3.25451170	-14.08238722
d	-22.39663458	-6.43202667	
e	-1.52357614	-9.60299248	
f	9.29672450	7.03770644	
g	6.55485254	5.80727278	
h	-0.66512956	6.97961319	
i	-0.39464296	-0.77994533	
j	0.83679331	4.07787875	
k	-3.61131899	-0.87240194	
l	0.00275314	0.00037040	
m	0.00822892	-0.31288876	
n	-0.00608193	-9.92786125	
o	0.00344002	0.00215197	
p	-0.00531261	17.59451286	
q	0.04128563	0.09174297	
r	0.00629464	-0.00377589	
s	-0.00488294		

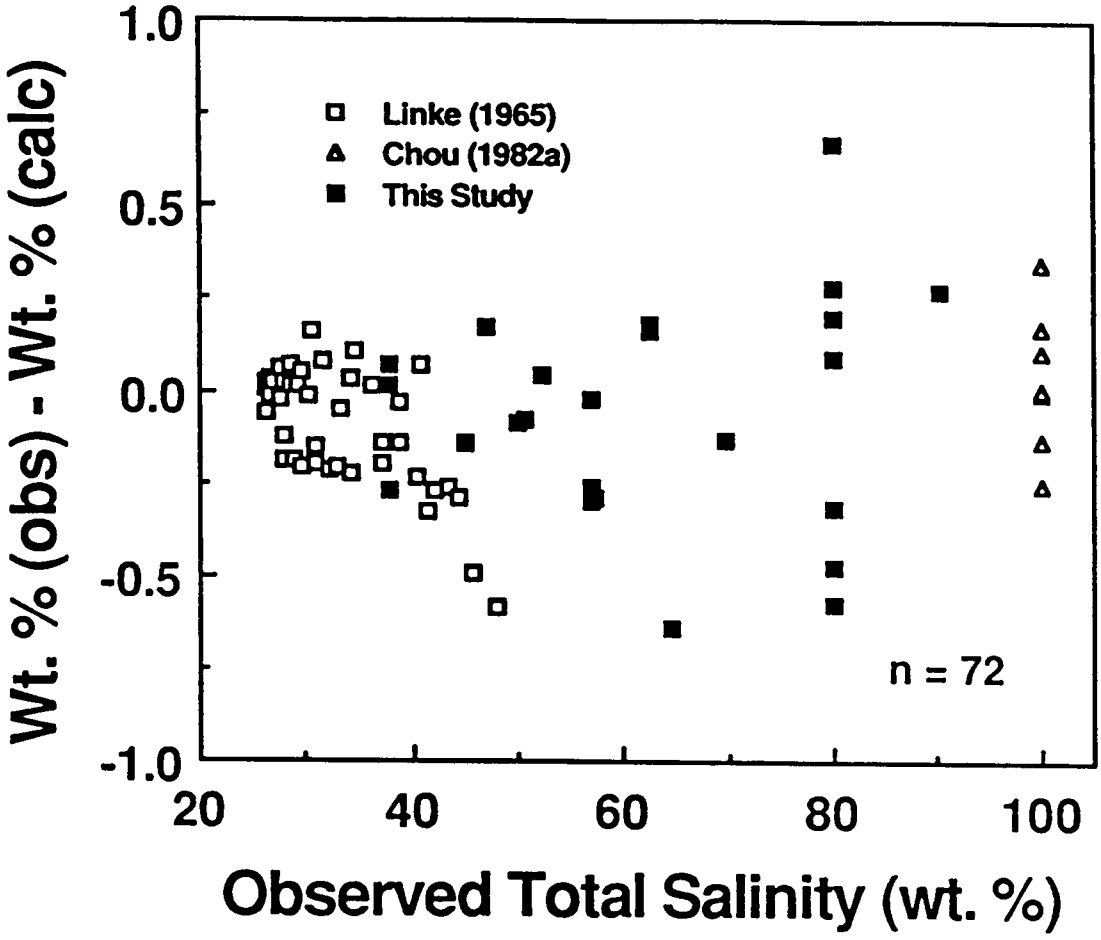

Figure 1.1 **Comparison of experimentally determined vapor-saturated solubilities (observed values) with those calculated using Eq. 1.1 for bulk compositions lying within the halite stability field in the ternary system NaCl-KCl-H_2O.**

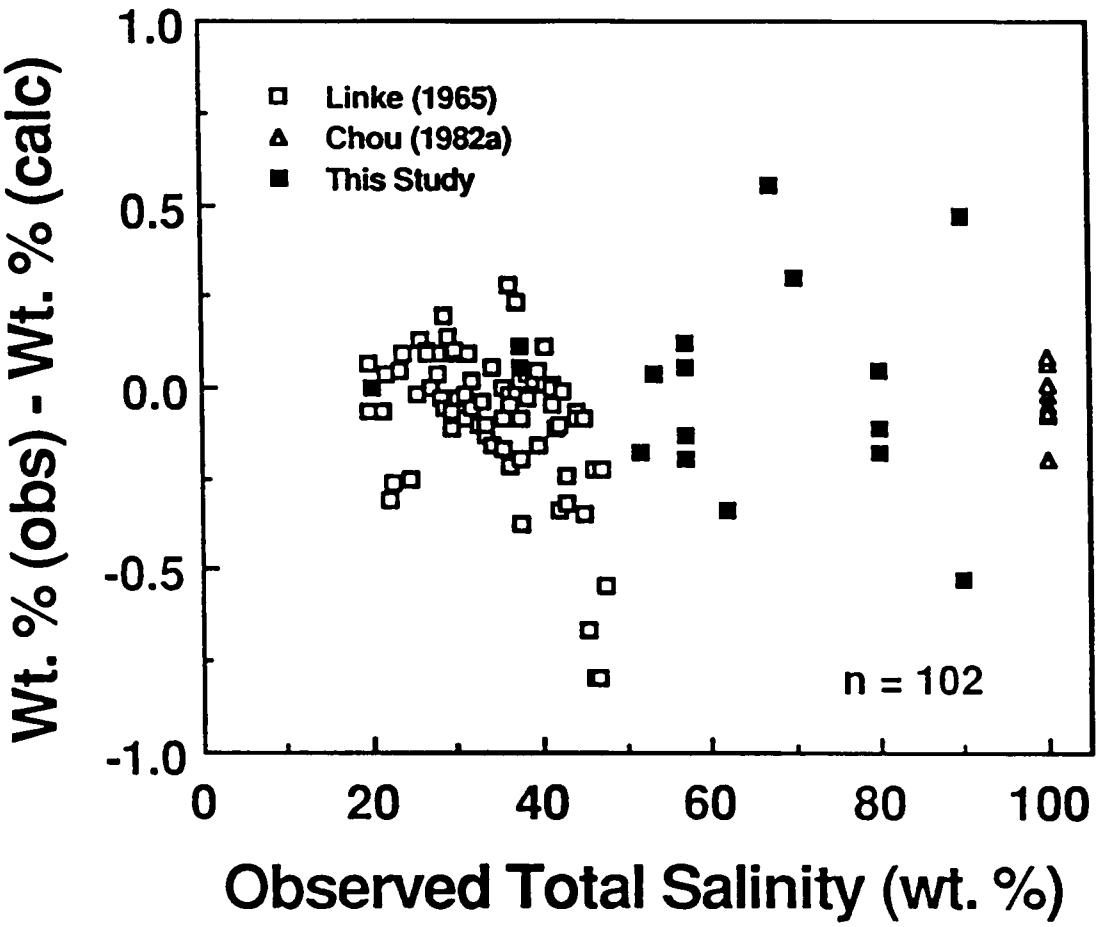

Figure 1.2 **Comparison of experimentally determined vapor-saturated solubilities (observed values) with those calculated using Eq. 1.2** for bulk compositions lying within the sylvite stability field in the ternary system NaCl-KCl-H_2O.

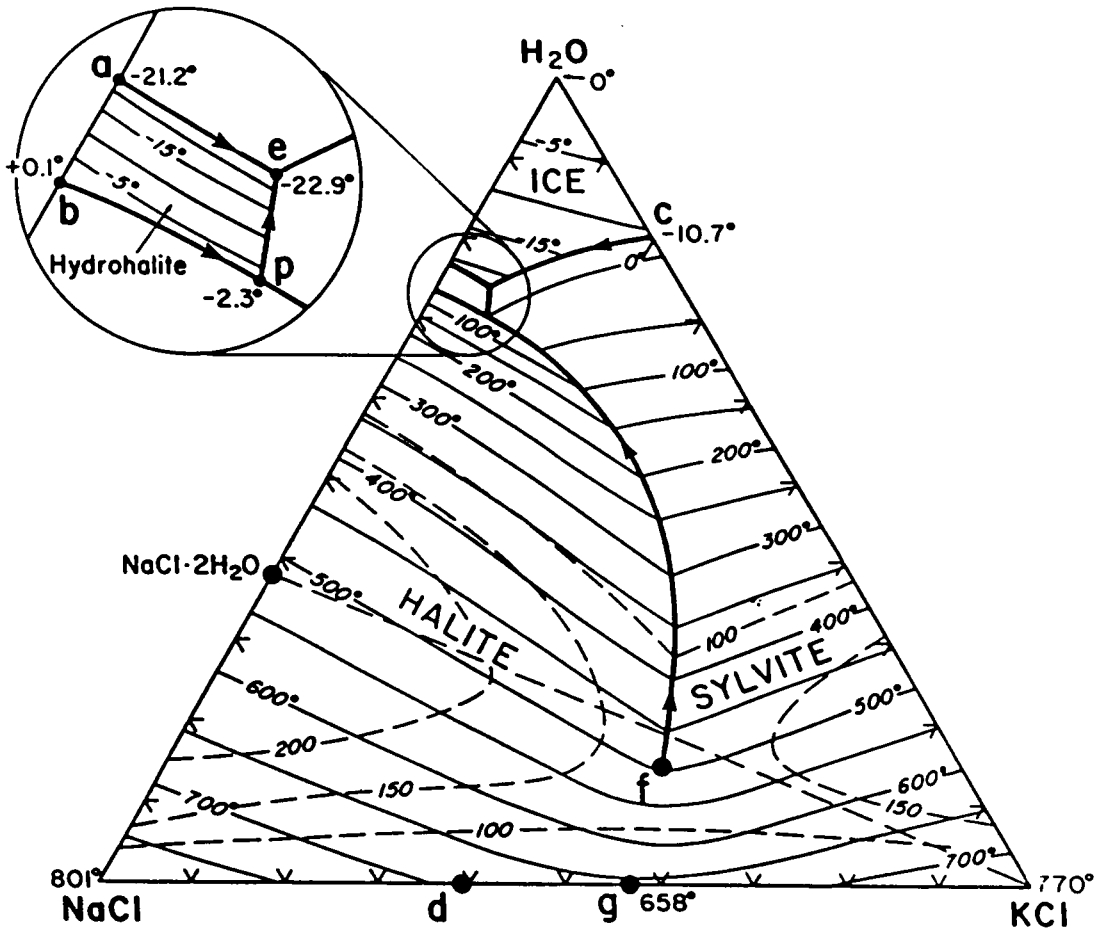

Figure 1.3 **Vapor-saturated solubility surface in the NaCl-KCl-H_2O ternary system.** Compositions are in wt. %. The surface contains four stability fields - halite, sylvite, hydrohalite ($NaCl{\cdot}2H_2O$) and ice - each in equilibrium with liquid and vapor. The heavy solid lines separating the fields are cotectics representing the simultaneous stabilities of four phases. Arrows along the cotectics point down temperature and converge at the ternary eutectic "e" at a temperature of -22.9°C. Points "a" and "c" are eutectics in the NaCl-H_2O and KCl-H_2O binary systems, respectively. Points "b" and "p" represent the peritectic compositions in the NaCl-H_2O binary, and the NaCl-KCl-H_2O ternary systems, respectively. Points "d" and "g" represent, respectively, the compositions corresponding to the solvus crest and the minimum melting point in the NaCl-KCl system. Point "f" is the high temperature end of the halite-sylvite cotectic (490°C). Isotherms (°C) within the stability fields (light solid lines) were calculated from Eqs. 1.1, 1.2 and 1.3 from the present study for solubilities in the halite, sylvite and hydrohalite fields and from Eq. 1.3 of Hall et al. (1987) for freezing point depression within the ice stable field. Compositions and temperatures along the five cotectics were determined by simultaneous solution of the solubility expressions within the adjacent fields. Pressures (bars) on the saturation surface shown by dashed lines are from Ravich and Borovaya (1949, 1950).

ternary system, determined by simultaneous solution of equations describing solubility surfaces in adjacent stability fields are listed in Table 1.3. The equation presented in Hall et al. (1987) was used in calculating the two cotectics bordering the ice field. Arrows along the cotectics point down temperature and converge at the ternary eutectic (-22.9°C; Linke, 1965). The positions of the isotherms and phase boundaries shown in Fig. 1.3 were constrained by the experimental data used to generate the above equations as described below.

Isotherms within the halite stability field above ~150°C, within the sylvite stability field above ~110°C, temperatures along the NaCl-H_2O binary above ~300°C, along the KCl-H_2O binary above ~10°C (sylvite-stable region), and compositions and temperatures along the halite-sylvite cotectic above ~110°C were determined using data from the present study. Temperatures along the NaCl-KCl binary are from Chou (1982a). Isotherms in the ice field are from Hall et al. (1987). Compositions and temperatures along the cotectics surrounding the hydrohalite field and between the sylvite and ice fields were constrained using data tabulated in Linke (1965). The lowest temperature data obtained within the halite and sylvite stability fields using synthetic fluid inclusions (Table 1.1) are in good agreement with values tabulated in Linke (1965). Thus, data below 200°C in the halite and sylvite fields compiled in Linke (1965) were included in the regression analysis to constrain the low temperature regions of Eqs. 1.1 and 1.2.

Solubility data within the ternary in the halite and sylvite stability fields have been reported up to 300°C by Linke (1965) and from 300°-650°C by Ravich and Borovaya (1949, 1950). Substantial disagreement is noted at the intersection of these two data sets. The data of Ravich and Borovaya (1949,1950) are compared with calculated values from the present study in Fig. 1.4.

Table 1.3 Temperatures and compositions along the five cotectic boundaries in the NaCl-KCl-H20 ternary system.

Ice-Sylvite Cotectic			Ice-Hydrohalite Cotectic			Hydrohalite-Sylvite Cotectic			Hydrohalite-Halite Cotectic			Halite-Sylvite Cotectic		
T(°C)	R	Wt %	T(°C)	R	Wt %	T(°C)	R	Wt %	T(°C)	R	Wt %	T(°C)	R	Wt %
-22.9	0.7797	25.96	-22.9	0.7850	25.92	-22.9	0.7806	25.99	-2.3	0.7740	29.13	-2.3	0.7558	29.36
-22.5	0.7710	25.76	-22.8	0.8000	25.73	-22.0	0.7792	26.14	-2.2	0.7850	28.99	0.0	0.7469	29.52
-22.0	0.7595	25.51	-22.7	0.8120	25.57	-21.0	0.7778	26.31	-2.1	0.7940	28.88	25.0	0.6495	31.51
-21.5	0.7474	25.26	-22.6	0.8250	25.40	-20.0	0.7764	26.47	-2.0	0.8050	28.74	50.0	0.5613	33.78
-21.0	0.7340	25.01	-22.5	0.8385	25.23	-19.0	0.7750	26.64	-1.9	0.8160	28.60	75.0	0.4908	36.17
-20.5	0.7193	24.75	-22.4	0.8510	25.07	-18.0	0.7738	26.81	-1.8	0.8260	28.47	100.0	0.4374	38.60
-20.0	0.7035	24.50	-22.3	0.8650	24.89	-17.0	0.7724	26.98	-1.7	0.8370	28.33	125.0	0.3978	41.09
-19.5	0.6863	24.24	-22.2	0.8770	24.73	-16.0	0.7710	27.14	-1.6	0.8470	28.20	150.0	0.3685	43.67
-19.0	0.6680	23.99	-22.1	0.8895	24.57	-15.0	0.7698	27.31	-1.5	0.8590	28.05	175.0	0.3475	46.35
-18.5	0.6475	23.73	-22.0	0.9030	24.40	-14.0	0.7686	27.47	-1.4	0.8700	27.91	200.0	0.3330	49.15
-18.0	0.6252	23.48	-21.9	0.9150	24.24	-13.0	0.7675	27.64	-1.3	0.8810	27.77	225.0	0.3238	52.08
-17.5	0.6015	23.22	-21.8	0.9260	24.10	-12.0	0.7663	27.80	-1.2	0.8930	27.62	250.0	0.3188	55.14
-17.0	0.5755	22.97	-21.7	0.9390	23.93	-11.0	0.7651	27.97	-1.1	0.9050	27.46	275.0	0.3175	58.31
-16.5	0.5474	22.71	-21.6	0.9510	23.78	-10.0	0.7640	28.13	-1.0	0.9170	27.31	300.0	0.3191	61.58
-16.0	0.5175	22.45	-21.5	0.9630	23.62	-9.0	0.7630	28.29	-0.9	0.9280	27.17	325.0	0.3231	64.90
-15.5	0.4850	22.19	-21.4	0.9740	23.48	-8.0	0.7619	28.46	-0.8	0.9400	27.01	350.0	0.3290	68.25
-15.0	0.4500	21.92	-21.3	0.9870	23.32	-7.0	0.7608	28.62	-0.7	0.9520	26.86	375.0	0.3364	71.57
-14.5	0.4130	21.65	-21.2	1.0000	23.15	-6.0	0.7598	28.78	-0.6	0.9640	26.71	400.0	0.3447	74.84
-14.0	0.3733	21.37				-5.0	0.7590	28.94	-0.5	0.9770	26.54	425.0	0.3539	77.99
-13.5	0.3305	21.10				-4.0	0.7580	29.10	-0.4	0.9890	26.38	450.0	0.3637	80.98
-13.0	0.2840	20.82				-3.0	0.7570	29.26	-0.3	1.0000	26.24	475.0	0.3743	83.77
-12.5	0.2335	20.54				-2.3	0.7565	29.38				490.0	0.3810	85.31
-12.0	0.1780	20.26												
-11.5	0.1170	19.99												
-11.0	0.0475	19.74												
-10.7	0.0000	19.60												

R = NaCl/(NaCl+KCl) weight ratio
Wt % = total salinity

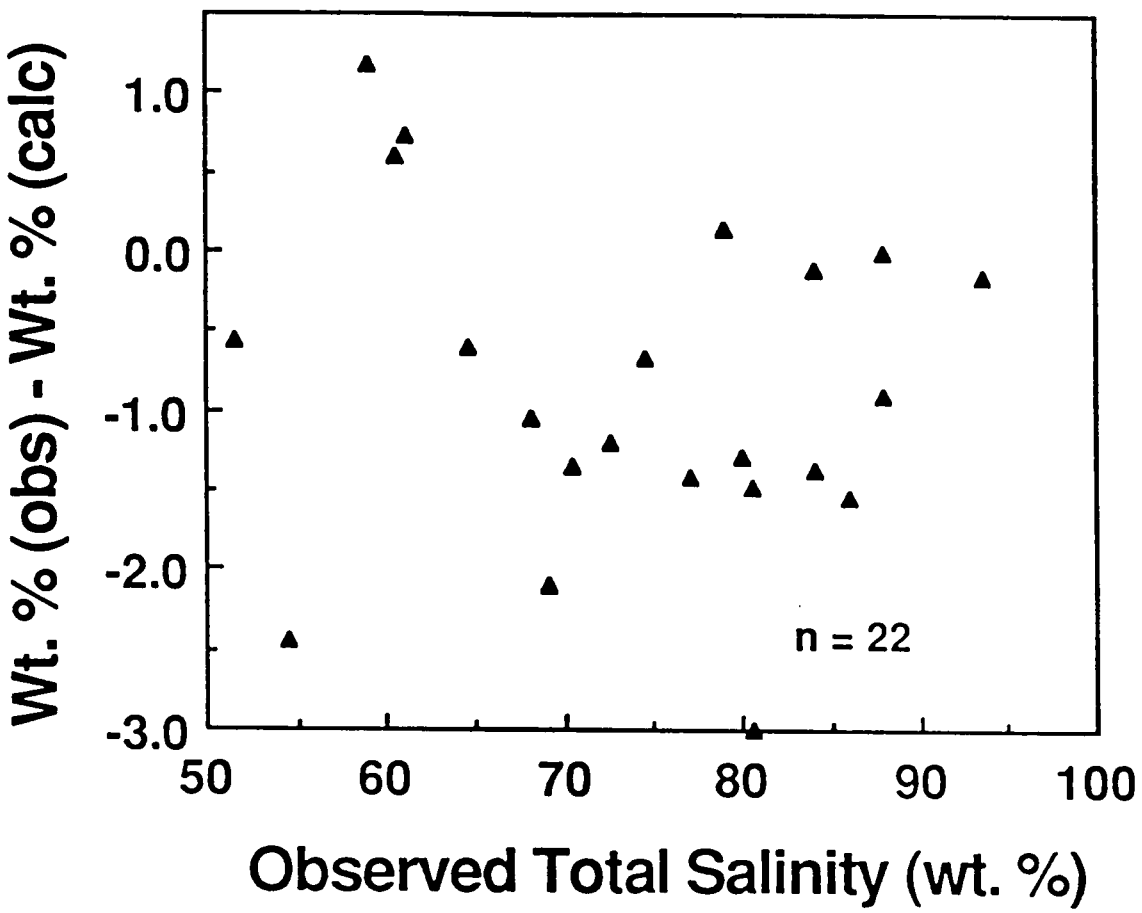

Figure 1.4 **Comparison of solubilities within the NaCl-KCl-H_2O ternary system from Ravich and Borovaya (1949, 1950)** (observed values) with those calculated by Eqs. 1.1 and 1.2 from the present study.

$NaCl$-H_2O Binary

Halite solubilities along the three-phase curve determined using synthetic fluid inclusions are shown in Fig. 1.5 (solid squares) together with previous determinations reported in the literature. Below 300°C published values are in good agreement with each other (see Fig. 4 in Potter et al. 1977). For temperatures above 300°C, considerable variation exists among the individual data sets, with a maximum deviation of 8 wt. % near 600°C. Chou (1987) has discussed possible explanations for these discrepancies and concludes that the previous studies tend to underestimate halite solubilities owing to the presence of a vapor phase at experimental conditions, or to contamination from the vessel walls. Halite solubilities determined in the present study are in close agreement with values reported by Chou (1987), with a maximum deviation between the two data sets of less than 2 wt. % near 600°C, the results of the present study being the lower.

Substituting a value of R = 1.000 into Eq. 1.1, the equation describing halite solubility within the NaCl-KCl-H_2O ternary, yields the following relationship for halite solubility in the vapor-saturated NaCl-H_2O binary system:

$$\begin{aligned} \text{Wt. \% NaCl} = \; & 26.242 + 0.4928\Psi + 1.42\Psi^2 - 0.223\Psi^3 + 0.04129\Psi^4 \\ & + 0.006295\Psi^5 - 0.001967\Psi^6 + 0.0001112\Psi^7 \\ & (0.1 \leq T°C \leq 801°C) \end{aligned} \qquad (1.4)$$

where Ψ = T°C/100. This equation is valid over the entire range of halite stability in the vapor-saturated binary from the peritectic temperature of 0.1°C (Linke, 1965), to the melting point of pure halite (801°C; Robie et al., 1979). Vapor-saturated halite solubilities predicted from Eq. 1.4 are shown in Figs. 1.5 and 1.6. Equation 1.4 predicts

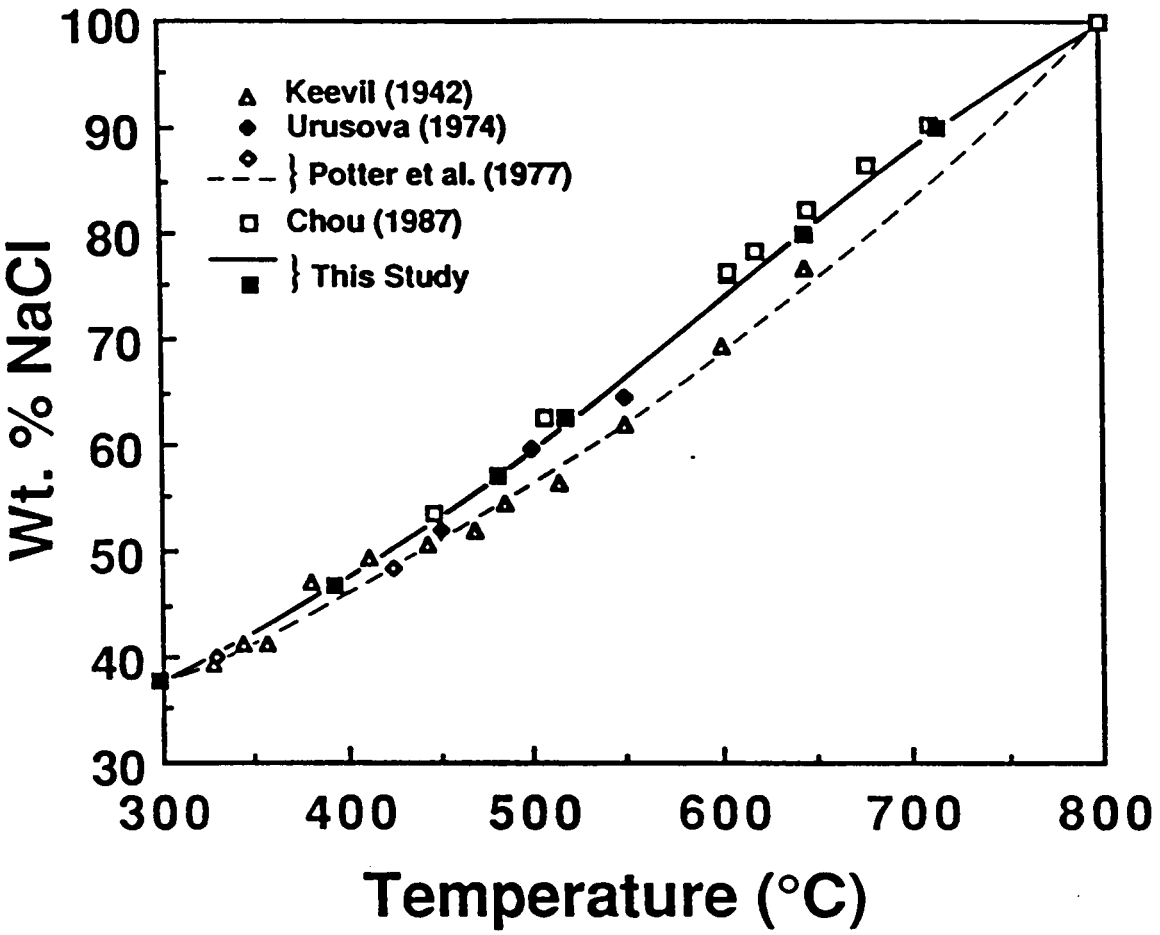

Figure 1.5 **Solubility of halite along the three-phase (solid+liquid+vapor) curve** in the system NaCl-H_2O above 300°C. Data presented by Potter et al. (1977) are shown as open diamonds, and the dashed curve represents their halite solubility equation. Solid squares represent halite solubilities determined in the present study using synthetic fluid inclusions, and the solid curve represents halite solubilities predicted by Eq. 1.4 (see text).

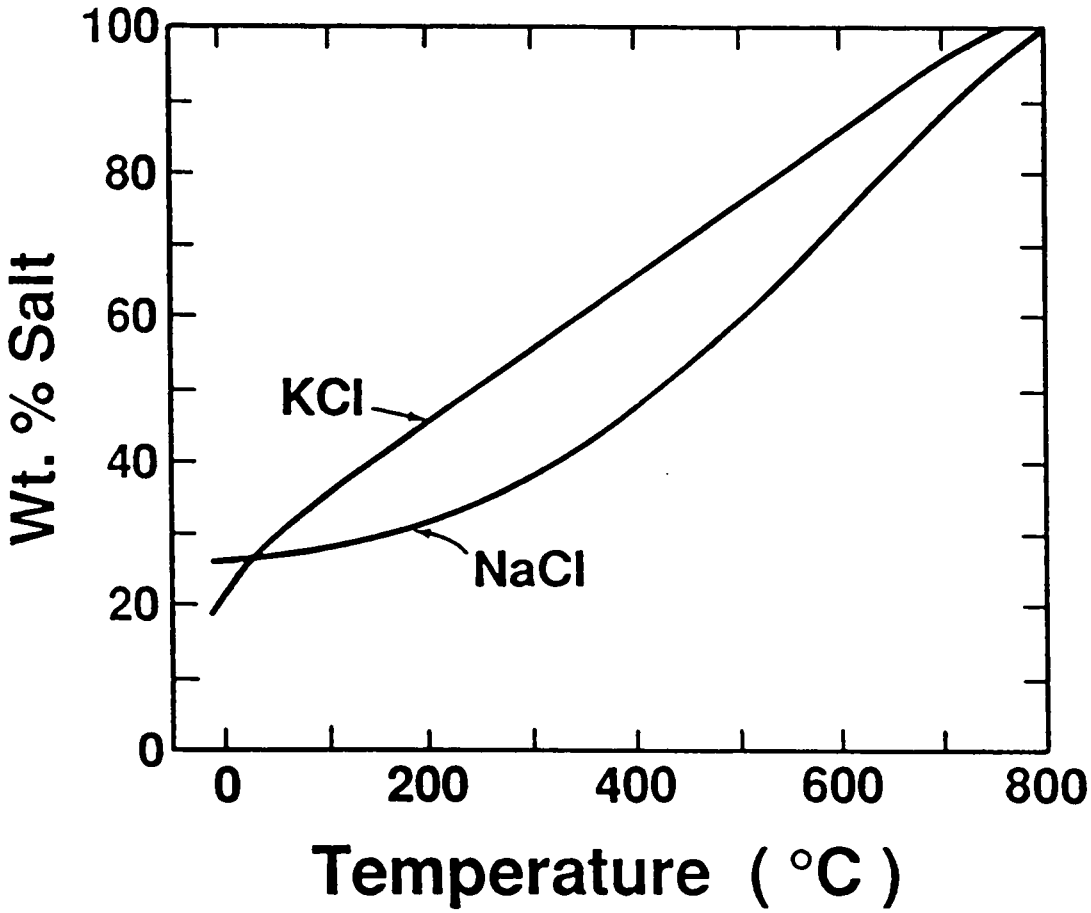

Figure 1.6 **Solubilities of halite and sylvite along the three-phase (solid+liquid+vapor) curves in the NaCl-H_2O and the KCl-H_2O binary systems predicted by Eqs. 1.4 and 1.5, respectively. The NaCl curve describes halite solubility from 0.1° to 801°C and the KCl curve describes sylvite solubility from -10.7° to 770°C.**

experimental values from the present study and data tabulated in Linke (1965) with an average deviation of ± 0.11 wt. %, and a maximum deviation of 0.31wt. %.

Also shown in Fig. 1.5 are halite solubilities predicted by the equation of Potter et al. (1977) (dashed curve). While their equation agrees closely with Eq. 1.4 (solid curve) at temperatures below 350°C, significant differences are encountered at higher temperatures resulting in a 5.5 wt. % discrepancy near 625°C.

KCl-H_2O Binary

Sylvite solubilities along the three-phase curve determined using synthetic fluid inclusions are presented in Fig. 1.7 (solid squares). The solid curve was obtained by substituting a value of R = 0.000 into Eq. 1.2, the equation describing sylvite solubility within the NaCl-KCl-H_2O ternary, yielding the following relationship for sylvite solubility in the vapor-saturated KCl-H_2O binary system:

$$\begin{aligned} \text{Wt. \% KCl} = {} & 21.886 + 20.28\Psi - 9.603\Psi^2 + 4.078\Psi^3 - 0.8724\Psi^4 \\ & + 0.09174\Psi^5 - 0.003776\Psi^6 \\ & (-10.7 \leq T°C \leq 770°C) \end{aligned} \qquad (1.5)$$

where Ψ = T°C/100. This equation is valid over the entire range of sylvite stability in the vapor-saturated binary from the eutectic temperature (-10.7°C, Hall et al., 1987) to the melting point of pure sylvite (770°C; Robie et al., 1979). Vapor-saturated sylvite solubilities predicted from Eq. 1.5 are shown in Figs. 1.6 and 1.7. Equation 1.5 predicts experimental values from the present study and data tabulated in Linke (1965) with an average deviation of ± 0.13 wt. %, and a maximum deviation of 0.47 wt. %. Sylvite

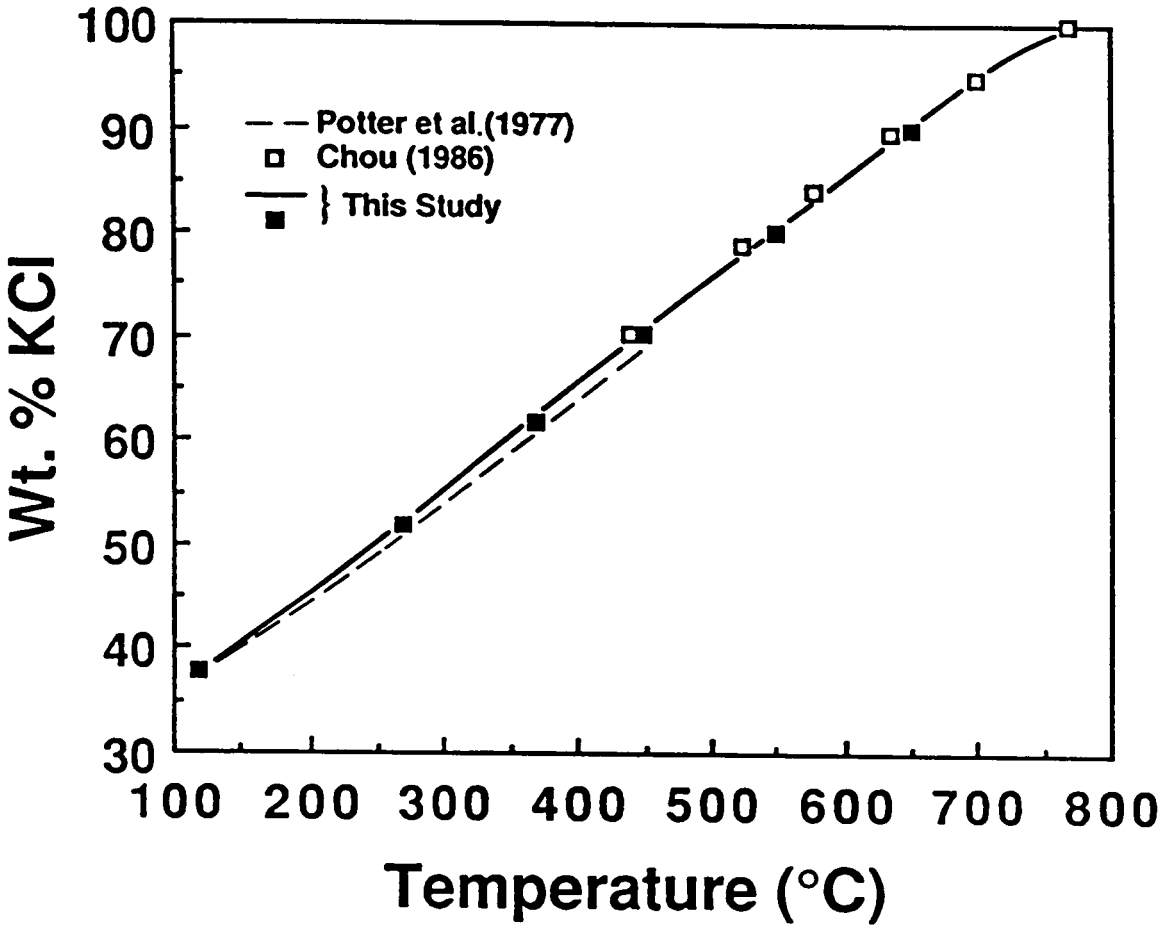

Figure 1.7 **Solubility of sylvite along the three-phase (solid+liquid+vapor) curve** in the system KCl-H_2O above 100°C. Solid squares represent sylvite solubilities determined in the present study using synthetic fluid inclusions, and the solid curve represents sylvite solubilities predicted by Eq. 1.5 (see text).

solubility data from Chou (1986), determined using DTA, are shown in Fig. 1.7. The maximum deviation between his data and solubilities predicted from Eq. 1.5 is 1.12 wt. % at 577°C, which is within the combined error estimates of the two methods.

The most likely cause of experimental error in the determination of halite and sylvite solubilities using synthetic fluid inclusions is failure of all of the salt to dissolve prior to inclusion trapping due to slow dissolution kinetics. This phenomenon would result in a wide range of salt dissolution temperatures, and calculated salt solubility at a given measured temperature would be somewhat higher than the actual value. The most probable causes of error in salinity determinations using DTA are failure to nucleate the appropriate phase during cooling scans without some degree of overstepping equilibrium saturation (supercooling), and compositional gradients due to density stratification (Chou,1986 and 1987). As pointed out by Chou (1987) these two effects tend to cancel each other. The narrow range in observed salt dissolution temperatures in the present study and the excellent agreement in the solubilities of halite and sylvite determined by these two independent methods suggests that the above equations accurately predict salt solubilities in the system NaCl-KCl-H_2O.

NaCl-KCl Binary

Temperatures along the liquidus in the anhydrous binary system NaCl-KCl at one atmosphere have been experimentally determined by Chou (1982a) and Pelton et al. (1985) who report minimum melting temperatures of 658° and 657°C, corresponding to compositions of 43.9 and 44.5 wt. % NaCl, respectively (Fig. 1.8). Although the use of synthetic fluid inclusions in the present study precluded the direct determination of phase relations along the anhydrous binary, extrapolation of our high salinity data within the

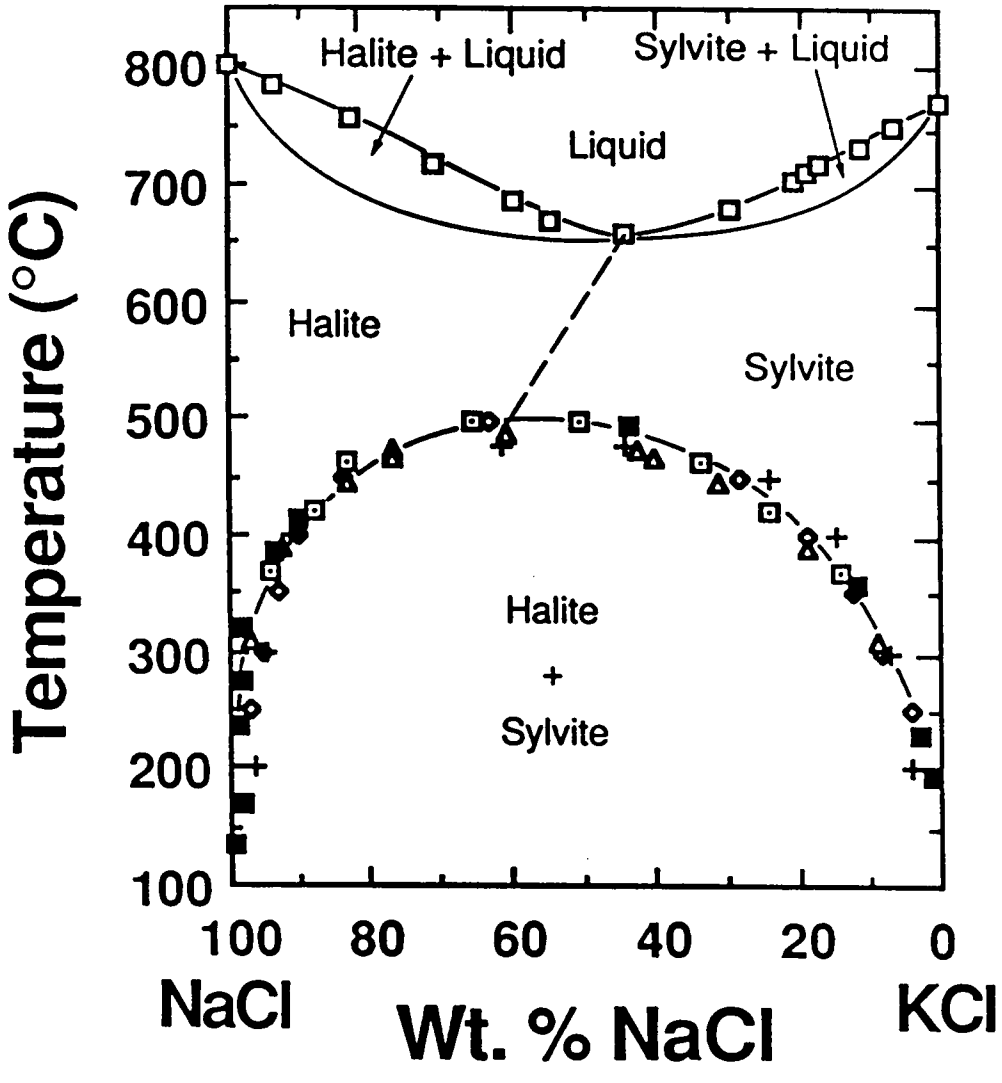

Figure 1.8 **One-atmosphere phase relations in the anhydrous NaCl-KCl system.** Solvus determinations are those of Bunk and Tichelaar (1953) (open triangles), Barrett and Wallace (1954) (dots-in-boxes), Chanh (1964) (crosses), Vesnin and Zakovryashin (1979) (open diamonds), and the present study (filled squares). Data along the liquidus are from Chou (1982a) (open boxes). Liquidus and solidus from Pelton et al. (1985) are shown by solid curves. The dashed line between the solvus crest and the minimum melting point indicates the compositional limits of the halite and sylvite phases according to the convention used in the text.

ternary agrees well with Chou's DTA determination of the halite-sylvite binary. As previously discussed, our results agree with his data for the NaCl-H_2O and KCl-H_2O binaries, so a smooth extrapolation of our data to his NaCl-KCl binary data is not surprising.

PHASE TRANSITIONS NEAR THE VAPOR-SATURATED SOLUBILITY SURFACE

The terms vapor-saturated solubility surface or vapor-saturated liquidus refer to the locus of points in PTX space representing the stable coexistence of vapor, liquid, and one to three solid phases. The projection of this surface onto the three component liquid composition space for the NaCl-KCl-H_2O system is shown in Fig. 1.3. Temperature and pressure are contoured using solid and dashed lines, respectively. Each point on the solubility surface has a unique liquid composition and liquid density associated with it.

Upon heating, an inclusion having a given bulk composition within the halite or sylvite stability field and having a bulk density corresponding to the liquid density for that composition on the vapor-saturated solubility surface will undergo complete homogenization via simultaneous disappearance of the final solid(s) and vapor phase at the temperature and pressure shown in Fig. 1.3 for that composition. An inclusion having the same bulk composition but a lower bulk density will undergo final solid dissolution at a somewhat higher temperature owing to the presence of a low-salinity vapor phase. Inclusions having this same bulk composition but a higher bulk density will undergo final homogenization via solid phase dissolution, at a temperature dependent on the P-T slope of the liquidus for that composition. The liquidus in the pure H_2O system and the

isopleths of halite and sylvite liquidii in low-salinity brines have negative slopes in P-T space. As salinity increases, the slopes of the isopleths become vertical and, eventually, positive. Data for the isopleths of halite and sylvite liquidii in the NaCl-H_2O, KCl-H_2O and NaCl-KCl-H_2O systems have been presented by Gunter et al. (1983), Chou (1982b) and Chou (1983), respectively. These data indicate that in moderate to high salinity fluids the isopleths of halite and sylvite liquidii have positive slopes. Thus, the dissolution temperature of the solid phase in high density inclusions will be lower than predicted from Fig. 1.3 for low salinity brines and higher than predicted for moderate and high salinity brines.

The above discussion is schematically illustrated using the P-T projection of the high salinity portion of a salt-water binary system shown in Fig. 1.9. The heavy lines represent the three-phase, solid + liquid + vapor curve (S+L+V), and the liquidus isopleth (L / L+S), and the bubble-point curve (L / L+V) for a fixed liquid composition. The light solid lines are isochores corresponding to three different bulk densities of fluids having the same bulk composition.

Isochore ρ° intersects the three-phase curve at the same pressure and temperature as the liquidus isopleth and the bubble-point curves and hence shall be designated the "common isochore" for this bulk composition. Isochore ρ^+ has a higher bulk density than the common isochore and isochore ρ^- has a lower bulk density.

A moderately saline fluid inclusion having a bulk density ρ° will contain 3 phases at room temperature: a salt crystal, a high salinity liquid phase and low salinity vapor phase. Upon heating, the inclusion will follow a P-T path along the three-phase curve (S+L+V) to point "a". At "a" the inclusion will homogenize via simultaneous disappearance of the salt crystal and the vapor bubble producing a one-phase fluid of composition equal to the bulk salinity of the inclusion. This salinity is therefore the vapor-saturated solubility of

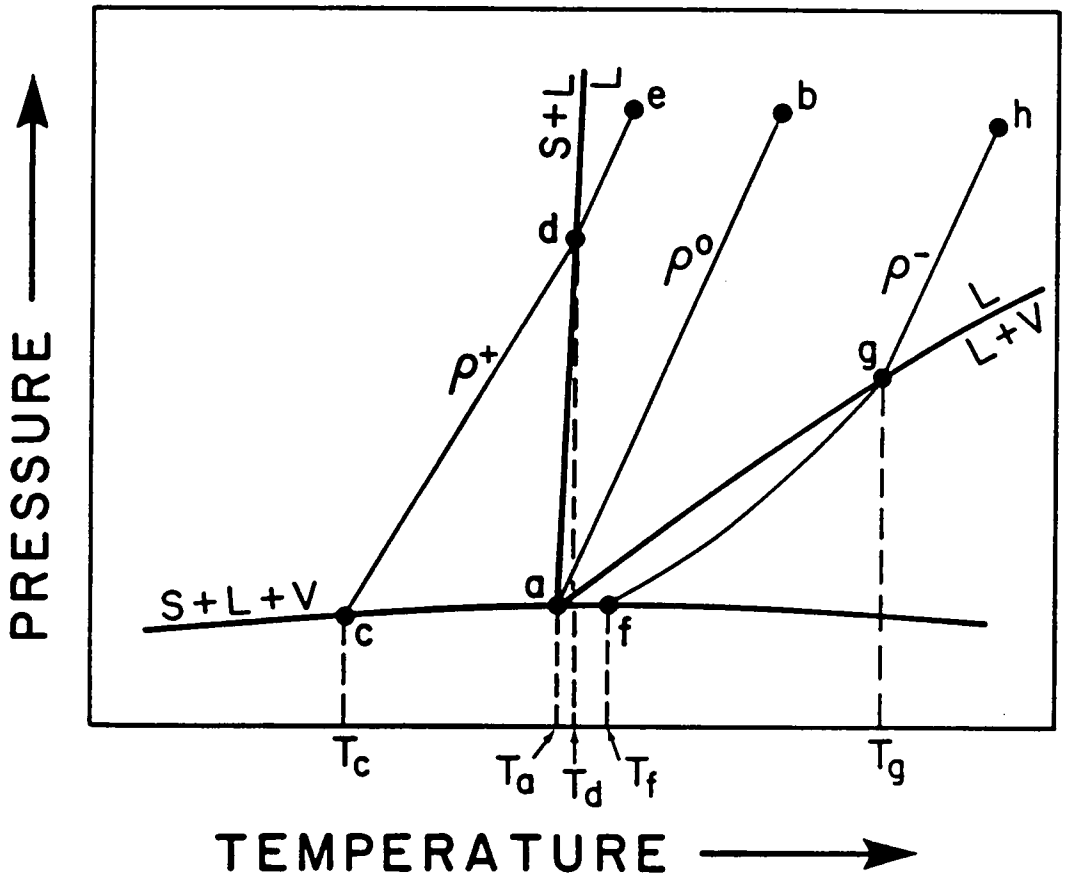

Figure 1.9 Schematic P-T projection of the high-salinity portion of a salt-water binary. The heavy lines represent the three-phase curve (S+L+V), the liquidus isopleth (S+L / L), and the bubble-point curve (L / L+V) for a fixed liquid composition. The light solid lines labled ρ°, ρ^{+}, and ρ^{-} are isochores corresponding to three different bulk densities of fluids having the same bulk composition. The break in slope of isochore ρ^{+} at point "d" is schematic and is based on Fig. 5 of Roedder and Bodnar (1980).

the salt at temperature T_a. On further heating the inclusion will follow the common isochore through the one-phase (liquid) field to its actual formation conditions (point "b").

An inclusion having a somewhat higher bulk density, ρ^+, and the same bulk composition will also contain three phases at room temperature - the vapor bubble being slightly smaller relative to the liquid and solid than in the case for ρ°. Upon heating, the inclusion will follow the three-phase curve (S+L+V) to point "c", at which point the vapor bubble will disappear. During continued heating the inclusion will follow the isochoric path ρ^+ to point "d" where the inclusion will homogenize by salt dissolution at temperature T_d. On further heating the inclusion will follow the isochore ρ^+ through the one-phase (liquid) field to its formation conditions at point "e". Because the isopleths of the liquidii of both halite and sylvite in moderate and high salinity fluids have positive slopes, the actual salt dissolution temperature will be in excess of T_a by an amount T_d-T_a degrees. The absolute magnitude of T_d-T_a cannot be calculated because data pertaining to the slopes of the isochores in the L+S field are not presently available. However, it is apparent that, owing to the steepness of the liquidus isopleth, as T_c (the vapor bubble disappearance temperature; Th L-V) approaches T_d (the salt dissolution temperature; Tm salt), (i.e., ρ^+ approaches ρ°) the quantity T_d-T_a approaches zero.

An inclusion of the same bulk composition but having a bulk density somewhat less than ρ° will homogenize by vapor bubble disappearance. The P-T path of one such inclusion having bulk density ρ^- is shown in Fig. 1.9. Upon heating the inclusion will follow the three-phase curve (S+L+V) to point "f" where the solid will completely dissolve. Further heating will result in total homogenization via vapor bubble disappearance at point "g". On continued heating the inclusion will follow isochore ρ^- through its formation conditions at point "h". The vapor-saturated salt dissolution temperature T_f of this inclusion will again be in excess of T_a. The elevated dissolution

temperature results from the strong enrichment of water in the vapor phase relative to the liquid. Hence, in the presence of this low salinity vapor phase, the actual salinity of the liquid at Tm (salt) is somewhat greater than the bulk salinity of the inclusion. By examination of Fig. 1.9 it is clear that as T_g (Th L-V) approaches T_f (Tm salt) (i.e., ρ^- approaches ρ°) the quantity T_f-T_a diminishes rapidly.

The salt-before-vapor bubble mode of homogenization (ρ^-) has been discussed by Chou (1987). He has expressed the difference between salinities estimated from observed dissolution temperatures of fluid inclusions and true vapor-saturated solubilities in the NaCl-H_2O system as a function of the liquid/vapor volume ratio at the halite homogenization temperature. According to Chou, the overestimation of inclusion salinities is most pronounced for dissolution temperatures around 550°C in the NaCl-H_2O binary system and when the vapor bubble occupies a significant volume percent of the inclusion.

In order to experimentally evaluate the magnitude of this "vapor bubble correction", we prepared synthetic fluid inclusions of two different densities from 57.0 wt. % NaCl solutions. Inclusions in the first sample had bulk densities such that halite dissolution and vapor bubble disappearance occurred nearly simultaneously (less than 5°C apart). Thus, the volume percent vapor at Tm (NaCl) was effectively zero. Inclusions in the second sample had bulk densities slightly lower than those in the first sample so that at Tm (NaCl) the vapor bubble occupied ~6 volume percent. The average salinity of inclusions in the second (lower density) sample, as determined from their halite dissolution temperatures using Eq. 1.4, was ~ 1 wt. % greater than the average salinity determined for inclusions in the first sample. This apparent difference in salinities is approximately twice that predicted by Chou (1987, his Fig. 10) at this temperature (~500°C) for a ~6 volume percent vapor bubble. However, vapor bubble disappearance temperatures for inclusions in the second

sample occur about 350°C beyond Tm (NaCl). Thus, even this large temperature difference between Tm (NaCl) and Th (L-V) yields a relatively small vapor bubble and a correspondingly small error in salinity determination. We are presently working to further quantify this correction and to correlate the magnitude of the error with observed Tm (NaCl) and Th (L-V).

The above discussions are directly applicable to fluids in the NaCl-KCl-H_2O ternary system. Under equilibrium conditions, fluid inclusions in this system having bulk salinities in excess of room temperature saturation will contain halite and/or sylvite solid phases, liquid and, generally, vapor at 25°C. Various modes of homogenization are possible depending on salinity, bulk composition and density. Completely analogous to the salt-H_2O binary, only those inclusions which homogenize via simultaneous disappearance of the final solid and vapor phase are directly correlative with vapor-saturated solubility. Differences between measured salt dissolution temperatures and those corresponding to true vapor-saturated solubilities will be small provided the inclusion has a bulk density close to that of the common isochore.

For those fluid inclusions having bulk compositions such that both halite and sylvite are present at room temperature, three pertinent phase transitions are noted (discussions presented in this paper pertain to inclusions which homogenize to liquid): (1) halite dissolution, (2) sylvite dissolution, and (3) vapor bubble disappearance. Simultaneous disappearance of all three of these phases can occur only for bulk compositions lying on the halite-sylvite cotectic and then only for bulk densities corresponding to the common isochore. In an inclusion containing any other bulk composition, the halite and sylvite phases must necessarily dissolve at different temperatures. The formation conditions of inclusions synthesized in this study were chosen so that the temperature of disappearance of the vapor phase was nearly coincident with the dissolution temperature of the last solid

phase. Thus, dissolution of the lower temperature salt crystal always occurred in the presence of a vapor bubble. The sylvite dissolution temperatures measured for inclusions having bulk compositions in the halite field and vice versa are therefore slightly higher than they would have been if the vapor bubble disappearance had been coincident with that of the lower temperature salt crystal. For this reason, only the final salt dissolution temperatures were used in determining the isotherms within the halite and sylvite stability fields.

Unfortunately, during microthermometric analysis of natural fluid inclusions the investigator is not at liberty to adjust the bulk densities of the inclusions so that the salt and vapor disappearance temperatures are the same. As a result, salinities of natural inclusions in this system estimated from measured dissolution temperatures in the presence of a vapor phase may be slightly higher than the true bulk composition. However, this effect is minor compared to errors introduced by the presence of additional components.

ISOTHERMAL PHASE RELATIONS IN THE NaCl-KCl-H_2O TERNARY

NaCl-KCl Binary

An additional complication arises in the interpretation of phase equilibria on the ternary solubility surface due to solid solution in the NaCl-KCl binary system. The solubility gap in the NaCl-KCl anhydrous system has been experimentally determined by Bunk and Tichelaar (1953), Barrett and Wallace (1954), Chanh (1964), and Vesnin and Zakovryashin (1979) (see Fig. 1.8). The solvus is asymmetric with peak temperature at

~490°C corresponding to a composition of ~61 wt% NaCl (Bunk and Tichelaar, 1953). Owing to the steepness of the halite limb of the solvus, the composition of halite in equilibrium with sylvite is essentially pure NaCl for temperatures below ~250°C. However, above 250°C the amounts of KCl in halite and NaCl in sylvite increase rapidly resulting in complete solid solution above 490°C. Upon examining Fig. 1.8 it is apparent that the terms "halite" and "sylvite" are ambiguous. For the purpose of discussion, we will use the term "halite" to refer to the compositions lying to the NaCl-rich side of the dashed line connecting the minimum melting point (~44 wt. % NaCl) with the crest of the solvus (~61 wt. % NaCl) (labeled "halite" on Fig. 1.8). Likewise, "sylvite" will be used to refer to compositions lying to the KCl-rich side of this line (labeled "sylvite" on Fig. 1.8). This results in a range of compositions between the solvus crest and the minimum melting point where the terms "halite" and "sylvite" are temperature dependent. Thus, a salt crystal of composition 50 wt. % NaCl at 500°C will be designated as sylvite, whereas, this same composition at 650°C will be designated as halite. This convention is arbitrary and the placement of the dashed line on Fig. 1.8 implies neither a chemical nor structural phase transition.

The use of synthetic fluid inclusions in the present study precluded the direct determination of the solvus in the NaCl-KCl binary system owing to the negligible solubility of quartz in anhydrous systems which makes fracture healing impossible. However, by interpreting synthetic fluid inclusion data using the ternary phase diagram (Fig. 1.3) it was possible to calculate the halite-sylvite solvus indirectly. The method used in this calculation is illustrated in Fig. 1.10. At room temperature, an inclusion having appropriate density and whose bulk chemical composition is represented by point "a" on the NaCl-KCl-H_2O ternary diagram will contain halite and sylvite of essentially pure end-member NaCl and KCl compositions, a saturated liquid phase of composition "b",

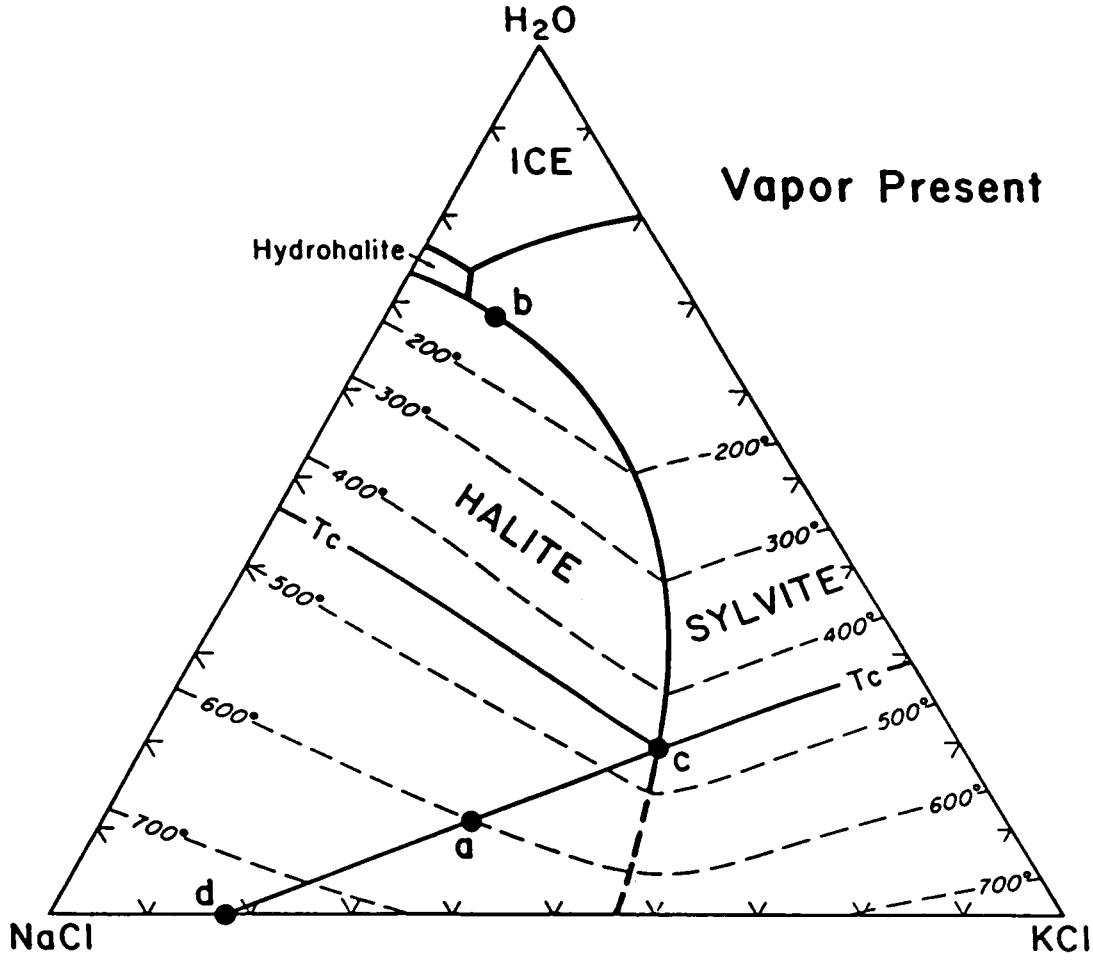

Figure 1.10 Graphical interpretation of microthermometric fluid inclusion data using the NaCl-KCl-H_2O vapor-saturated solubility diagram. Compositions are in weight %; temperatures are in degrees Celsius. Point "a" represents the bulk composition of the inclusion, "b" is the composition of the liquid in equilibrium with halite and sylvite at room temperature, points "c" and "d" represent the compositions of coexisting liquid and halite, respectively, at the temperature of sylvite dissolution (T_c).

and a vapor bubble. Upon heating, the halite and sylvite begin to dissolve (actually halite initially precipitates up to 100°C due to the orientation of the halite-sylvite cotectic) and the composition of the liquid moves along the cotectic from point "b". As temperature rises, the solid phases continually recrystallize and their compositions move toward each other in accordance with the equilibrium solid-solution compositions of coexisting halite and sylvite shown in Fig. 1.8. The process of recrystallization is immediately obvious through microscopic observation. During heating the halite and sylvite crystals grow toward each other by continuous dissolution on one side of each crystal and reprecipitation on the other side of the crystals. Justification for the assertion that the halite and sylvite maintain chemical equilibrium will be presented later in this discussion.

At the temperature of sylvite dissolution, T_C, the inclusion will contain a relatively large halite crystal, liquid and a vapor bubble. The liquid composition at this temperature is represented by point "c" if the system is in equilibrium. Provided the volume of the low density vapor phase is small, the mass of the system can be completely accounted for by considering only the liquid and the halite phases. Mass balance considerations then require that the bulk composition of the inclusion (point "a") must lie on the mixing line between the compositions of the liquid (point "c") and halite phases (point "d"). In this study, the bulk compositions of the inclusions (point "a") are known. Likewise, the liquid composition along the halite-sylvite cotectic corresponding to point "c" can be obtained from sylvite dissolution temperatures in the presence of halite. Assuming the mass of the vapor phase is negligible, and because the salt crystal is anhydrous, its composition is specified by the intersection of the line through "c" and "a" with the NaCl-KCl binary (point "d").

Halite and sylvite solid-solution compositions along the solvus determined by the above method from the data in Table 1.1 are listed in Table 1.4, and are represented by

Table 1.4 Solvus compositions determined from data in Table 1.1.

T(°C)	Halite*	Sylvite*
135.5	99.6	---
168.1	98.1	---
193.6	---	1.4
230.8	---	2.9
235.3	99.0	---
273.3	98.4	---
319.8	98.2	---
357.4	---	11.5
385.5	93.6	---
415.0	90.0	---
492.5	---	43.1

*solid solutions in Wt. % NaCl

solid squares in Fig. 1.8. Dissolution temperatures of sylvite coexisting with halite were used in calculating compositions along the halite limb and vice-versa. The sensitivity of this calculation is highly dependent on the position of the bulk inclusion composition "a" relative to points "c" and "d" of Fig. 1.10. As the bulk composition approaches the halite-sylvite cotectic, i.e., point "c", slight errors in the sylvite dissolution temperature (T_C) result in large errors in estimated halite solid-solution compositions. The same is true when calculating sylvite compositions using halite dissolution temperatures. For this reason, only those inclusions for which $ac/cd \geq 0.15$ (Fig. 1.10) were used in calculating the solvus compositions shown in Fig. 1.8.

P-T formation conditions of all inclusions in this study were chosen such that the bulk fluid densities would result in near-simultaneous disappearance of the vapor bubble and the final salt crystal. The above method for determining the NaCl-KCl solvus relies on measured dissolution temperatures of the early-dissolving salt phase which, in general, occurred in the presence of a vapor bubble. However, in most cases, at the dissolution temperature of the phase of interest, the vapor bubble was sufficiently small (i.e. occupying less than ~2-3 volume % of the inclusion) and/or of sufficiently low density that its contribution to the total mass of the system could be ignored. As evidence for this we point to the agreement between our calculated solvus compositions and the other solvus data shown in Fig. 1.8. In the example given in Fig. 1.10, if a significant mass of H_2O-rich vapor phase had been present during sylvite dissolution, the bulk composition of the remaining phases (solid + liquid) would have been more saline than the bulk inclusion composition "a". This would have resulted in sylvite dissolution at a higher temperature along the halite-sylvite cotectic than if sylvite and vapor had disappeared simultaneously. Projection of the liquid composition at this higher dissolution temperature through the known bulk inclusion composition "a" to the NaCl-KCl binary would result in

a calculated halite composition lying between "d" and the NaCl apex of Fig. 1.10, i.e., in the one phase field of Fig. 1.8.

The only remaining requirement for the above calculation procedure to be valid is that the system be in equilibrium. Had recrystallization not resulted in equilibrium solid-solution compositions, then the dissolution temperatures of the first-dissolving salt would have been necessarily higher than the observed values due to the excess of that salt caused by its omission from the other crystal. This disequilibrium condition would again result in too much NaCl and KCl in the calculated halite and sylvite solid-solution compositions, respectively. The close agreement between our calculated solvus compositions and the other data shown on Fig. 1.8 suggests that the heating rates used in measuring the salt dissolution temperatures (~0.3°C/min) were sufficiently slow to allow re-equilibration of the crystals to their equilibrium compositions, and that errors resulting from the presence of a vapor phase at the temperature of dissolution of the first salt crystal were negligible. Furthermore, the dissolution temperatures of salt crystals observed were independent of crystal size ($\leq$ 40 mm on a side) at this heating rate.

The implications of the above discussion are of great importance to the results of this study and to the study of natural fluid inclusions within the NaCl-KCl-H_2O system. During slow heating (~0.3°C/min), high-salinity inclusions may be regarded as equilibrium systems and their chemical compositions may be accurately approximated using the phase diagrams presented here. The high temperature portions of phase diagrams derived from data presented in Table 1.1 represent equilibrium phase relations and are therefore suitable for equilibrium thermodynamic calculations.

NaCl-KCl-H_2O Ternary

The effect of NaCl-KCl solid solution on phase relations in the ternary is illustrated on vapor-saturated, isothermal projections in Fig. 1.11. Pressures correspond to those along the designated isotherm on the vapor-saturated solubility surface (see Fig. 1.3). Equilibrium liquid + vapor compositions at these pressures are not known and the vapor field boundary and the liquid-solid tielines in the three-phase fields are schematic. At 25°C (Fig. 1.11a) a large four-phase (halite+sylvite+L+V) field envelops a substantial portion of the ternary composition space. For bulk fluid compositions lying anywhere within this field halite and sylvite of essentially pure end-member compositions exist in equilibrium with a vapor-saturated liquid of cotectic composition "c". For moderate to high salinity bulk compositions having high (or low) Na/K ratios halite (or sylvite) exists in equilibrium with a vapor-saturated liquid of composition along line a-c (or c-b). Low salinity bulk compositions will contain only vapor and/or liquid at 25°C.

By 400°C (Fig. 1.11b) the liquid + vapor field has expanded largely at the expense of the four-phase (halite+sylvite+L+V) field. At this temperature bulk compositions lying within the four-phase field will contain halite and sylvite solid solutions far removed from their end-member compositions in equilibrium with a vapor-saturated liquid phase of cotectic composition "c". A bulk composition lying within the three-phase field "adec" will contain a halite solid solution of composition along d-e in equilibrium with a vapor-saturated liquid of composition along a-c. Similar relations exist in the three-phase field "bcfg".

The crest of the solvus in the NaCl-KCl anhydrous binary system is at ~490°C (Bunk and Tichelaar, 1953). Above this temperature complete solid solution exists between halite and sylvite. As seen in Fig. 1.11c this results in closure of the four-phase

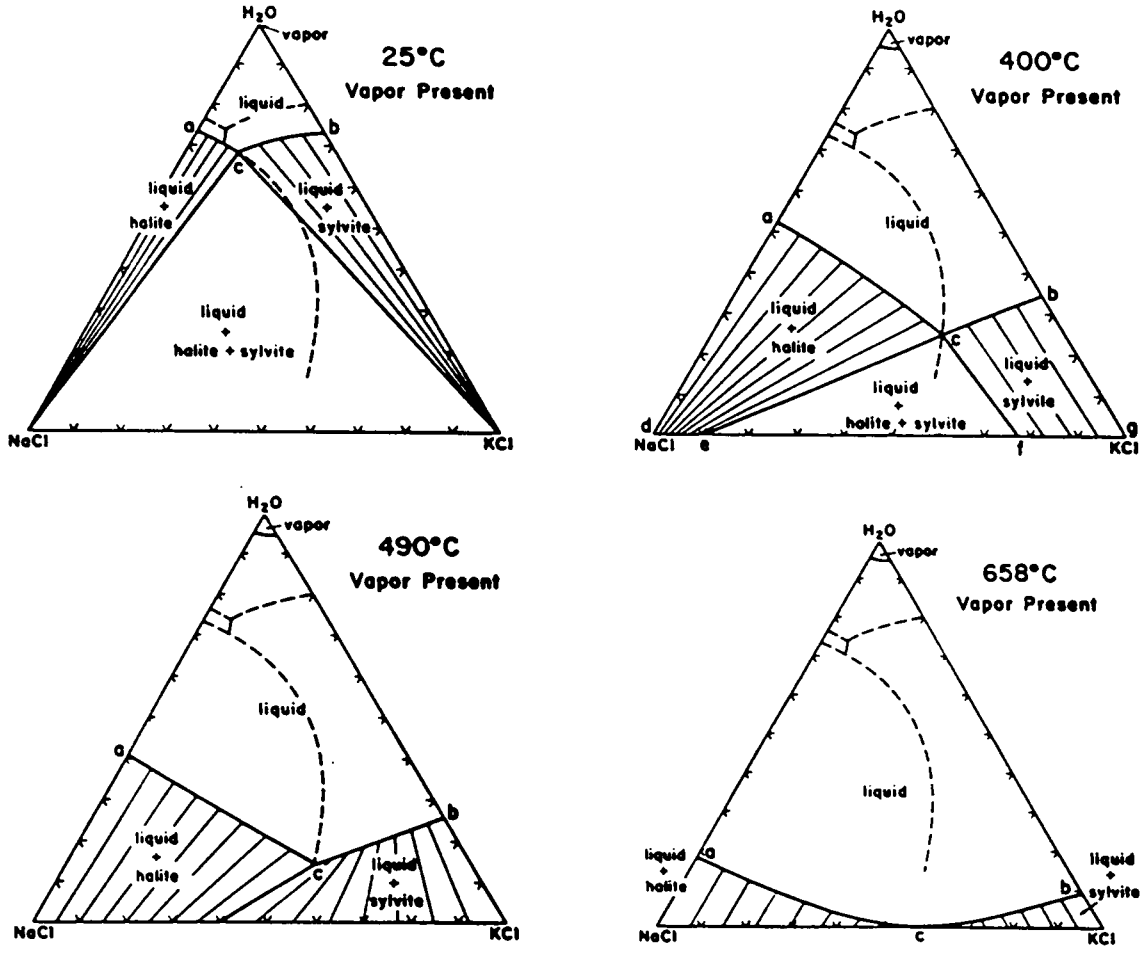

Figure 1.11 Isothermal, polybaric projections of vapor-saturated phase relations in the NaCl-KCl-H_2O system illustrating the effect of halite-sylvite solid solution. Pressures correspond to those along the designated isotherm on the vapor-saturated solubility surface (see Fig. 1.3). Compositions are in weight %. Equilibrium liquid + vapor compositions are not shown and the vapor field boundary and the liquid-solid tie lines in the three-phase fields (L+V+S) are schematic.

field and the resultant termination of the cotectic at point "c". A bulk composition lying within either of the three-phase, solid + liquid + vapor fields contains a single salt crystal having a composition somewhere along the NaCl-KCl binary in equilibrium with a vapor-saturated liquid of composition along a-c-b.

With further temperature increase, the liquid + vapor field advances until it reaches the NaCl-KCl join (Fig. 1.11d). The point at which the liquid + vapor field in the ternary first intersects the NaCl-KCl binary corresponds to the minimum melting point in the anhydrous NaCl-KCl system (point "c"; 658°C, 43.9 wt% NaCl; Chou, 1982a). Continued temperature increase results in shrinkage and eventual disappearance of the two three-phase fields (halite+L+V and sylvite+L+V) at the melting points of pure NaCl and pure KCl, 801° and 770°C, respectively.

DETERMINATION OF FLUID INCLUSION COMPOSITIONS FROM MICROTHERMOMETRIC DATA

Just as it is possible to reconstruct the T-X topology of the vapor-saturated solubility surface in NaCl-KCl-H_2O composition space using thermometric data from fluid inclusions of known composition, it is likewise possible to approximate the composition of a given inclusion by measuring appropriate phase transition temperatures and interpreting them in terms of the solubility diagram. The accuracy with which fluid inclusion compositions may be approximated using microthermometry is dependent on several variables. Because of the importance of these determinations both in evaluating natural inclusions and with regard to future PVTX studies using synthetic fluid inclusions, a detailed discussion of the observable equilibrium and metastable phase transitions in the

NaCl-KCl-H_2O ternary system, as well as some mention of the effect of additional components, is warranted.

Equilibrium Phase Transitions

Any inclusion having a composition within the H_2O-KCl-NaCl·$2H_2O$ triangle in the NaCl-KCl-H_2O ternary system (Fig. 1.12) will undergo initial melting when heated to -22.9°C, producing some amount of liquid having the ternary eutectic composition "e" shown on Fig. 1.12 (20.17 wt. % NaCl, 5.81 wt. % KCl, 74.02 wt. % H_2O; Linke, 1965). An inclusion having a composition within the NaCl-KCl-NaCl·$2H_2O$ triangle will undergo initial melting when heated to -2.3°C, producing liquid having the ternary peritectic composition "p" shown on Fig. 1.12 (22.54 wt. % NaCl, 6.96 wt. % KCl, 70.50 wt. % H_2O; Linke, 1965). There are then 16 possible equilibrium modes of solid phase dissolution that the inclusion may exhibit upon further heating. These are listed below, each in order of increasing temperature:

1) $HH+S+I \rightarrow HH+S+I+L_e \rightarrow S+I+L \rightarrow S^*+L \rightarrow L$
2) $HH+S+I \rightarrow HH+S+I+L_e \rightarrow S+I+L \rightarrow I+L \rightarrow L$
3) $HH+S+I \rightarrow HH+S+I+L_e \rightarrow HH+I+L \rightarrow I+L \rightarrow L$
4) $HH+S+I \rightarrow HH+S+I+L_e \rightarrow HH+I+L \rightarrow HH+L \rightarrow L$
5) $HH+S+I \rightarrow HH+S+I+L_e \rightarrow HH+S+L \rightarrow HH+L \rightarrow L$
6) $HH+S+I \rightarrow HH+S+I+L_e \rightarrow HH+S+L \rightarrow S+L \rightarrow L$
7) $HH+S+I \rightarrow HH+S+I+L_e \rightarrow HH+I+L \rightarrow HH+L \rightarrow HH+H+L \rightarrow H+L \rightarrow L$
8) $HH+S+I \rightarrow HH+S+I+L_e \rightarrow HH+S+L \rightarrow HH+L \rightarrow HH+H+L \rightarrow H+L \rightarrow L$

9) $HH+S+I \rightarrow HH+S+I+L_e \rightarrow HH+S+L \rightarrow HH+H+S+L_p \rightarrow$
$HH+H+L \rightarrow H^*+L \rightarrow L$

10) $HH+S+I \rightarrow HH+S+I+L_e \rightarrow HH+S+L \rightarrow S+L \rightarrow H+S+L \rightarrow H+L \rightarrow L$

11) $HH+S+I \rightarrow HH+S+I+L_e \rightarrow HH+S+L \rightarrow S+L \rightarrow S+H+L \rightarrow S^*+L \rightarrow L$

12) $HH+S+I \rightarrow HH+S+I+L_e \rightarrow HH+S+L \rightarrow HH+H+S+L_p \rightarrow$
$H^*+S^*+L \rightarrow H^*+L \rightarrow L$

13) $HH+S+I \rightarrow HH+S+I+L_e \rightarrow HH+S+L \rightarrow HH+H+S+L_p \rightarrow$
$H^*+S^*+L \rightarrow S^*+L \rightarrow L$

14) $HH+H+S \rightarrow HH+H+S+L_p \rightarrow HH+H+L \rightarrow H^*+L \rightarrow L$

15) $HH+H+S \rightarrow HH+H+S+L_p \rightarrow H^*+S^*+L \rightarrow H^*+L \rightarrow L$

16) $HH+H+S \rightarrow HH+H+S+L_p \rightarrow H^*+S^*+L \rightarrow S^{*\dagger}+L \rightarrow L$

where H = halite; S = sylvite; HH = hydrohalite; I = ice; L = liquid; L_e = liquid of ternary eutectic composition "e"; L_p = liquid of ternary peritectic composition "p"; *-indicates that the phase may contain appreciable solid solution; †-denotes that, by convention, solid-solution compositions lying between ~61 and ~44 wt. % NaCl are designated as sylvite at the temperature of halite dissolution while at some higher temperature these same compositions may be designated as halite. The numbers prefacing each mode of solid phase dissolution listed above correspond to inclusions having bulk compositions within the similarly numbered fields in Fig. 1.12. It should be noted that the halite-sylvite cotectic and the line segment joining the ternary eutectic "e" with the KCl apex of the triangle in Fig. 1.12 become very nearly tangent at approximately 100°C. In reality, the cotectic either crosses this line twice or the two do not intersect at all. If there is no intersection then a small portion of field 6 extends all the way to the KCl apex, and the observable equilibrium solid dissolution modes are as stated above. If, however, the

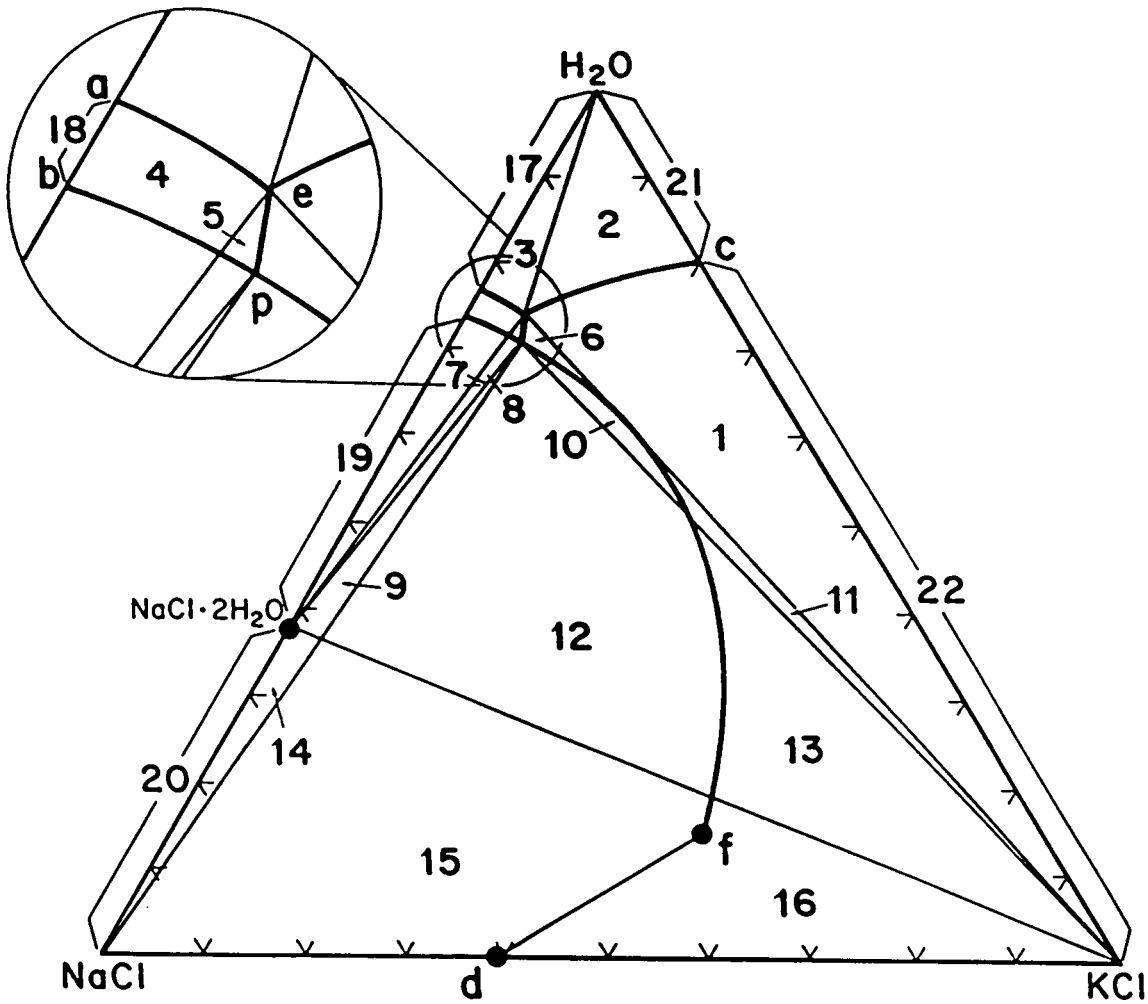

Figure 1.12 Bulk composition ranges corresponding to various possible modes of solid phase dissolution exhibited by NaCl-KCl-H_2O fluid inclusions during heating runs. Numbers correspond to similarly numbered dissolution paths described in the text. Points "a-f" and "p" are as described for Fig. 1.3.

cotectic actually crosses this line, this would introduce two more fields on Fig. 1.12 which would exhibit solid phase dissolution modes identical to those of fields 10 and 11, except that hydrohalite would disappear before ice. Within our experimental error it is impossible to tell which of these two possibilities is true; thus, for the purpose of discussion we have arbitrarily assumed that the halite-sylvite cotectic and the line segment between the ternary eutectic and the KCl apex intersect at one point. This point represents the maximum salinity of field 6 and the minimum salinity of field 11.

For bulk compositions lying within the H_2O-KCl-NaCl·$2H_2O$ triangle (fields 1-13), final dissolution of at least one of hydrohalite, sylvite or ice must occur at -22.9°C in the presence of a liquid having the ternary eutectic composition "e". Thereafter, the composition of the liquid moves away from the ternary eutectic toward the bulk inclusion composition along the path dictated by the order of solid disappearance and the phase rule. The simultaneous disappearance of the last two solid phases indicates that the inclusion has a bulk composition lying along the corresponding cotectic. The simultaneous disappearance of sylvite, hydrohalite, and ice can only occur at -22.9°C and for a bulk inclusion composition equal to the ternary eutectic composition "e".

For bulk compositions lying within the NaCl-KCl-NaCl·$2H_2O$ triangle (fields 14-16), final dissolution of sylvite and/or the decomposition of hydrohalite to form halite plus liquid must occur at -2.3°C in the presence of a liquid having the ternary peritectic composition "p". Upon further heating, the liquid composition moves along either the hydrohalite-halite cotectic until hydrohalite decomposes, or along the halite-sylvite cotectic until halite or sylvite dissolves. Simultaneous dissolution of both halite and sylvite (for bulk compositions lying within the NaCl-KCl-NaCl·$2H_2O$ triangle) can occur only for bulk compositions lying along the portion of the cotectic between fields 15 and 16.

Inclusions within the NaCl-H_2O binary system having bulk compositions less than

61.9 wt. % NaCl will exhibit initial melting at -21.2°C, producing a liquid of binary eutectic composition "a" (23.2 wt. % NaCl; Hall et al., 1987). Three modes of equilibrium solid phase dissolution are then possible:

17) $HH+I \rightarrow HH+I+L_a \rightarrow I+L \rightarrow L$

18) $HH+I \rightarrow HH+I+L_a \rightarrow HH+L \rightarrow L$

19) $HH+I \rightarrow HH+I+L_a \rightarrow HH+L \rightarrow HH+H+L_b \rightarrow H+L \rightarrow L$

where L_a = liquid of binary eutectic composition "a", and L_b = liquid of binary peritectic composition "b". Inclusions in this binary system having bulk salinities greater than 61.9 wt. % NaCl will display initial melting (actually, the decomposition of hydrohalite to form halite plus liquid) at 0.1°C, producing a liquid having the binary peritectic composition "b" (26.27 wt. % NaCl; Linke, 1965) followed by solid phase dissolution according to the sequence:

20) $HH+H \rightarrow HH+H+L_b \rightarrow H+L \rightarrow L$

Inclusions in the KCl-H_2O binary system will undergo initial melting at the binary eutectic "c" (-10.7°C, 19.6 wt. % KCl; Hall et al., 1987). Here, two modes of equilibrium solid phase dissolution are possible:

21) $S+I \rightarrow S+I+L_c \rightarrow I+L \rightarrow L$

22) $S+I \rightarrow S+I+L_c \rightarrow S+L \rightarrow L$

where L_c = liquid of binary eutectic composition "c".

Compositional determinations of fluid inclusions within the NaCl-KCl-H_2O system based on microthermometric measurements require the unequivocal identification of the last two solids that disappear during heating. Then, assuming that the vapor bubble is small near the temperature of final solid dissolution, or that the temperature, and consequently the vapor density, when the last solid dissolves is sufficiently low (see discussion attending Fig. 1.9), compositions of inclusions within the ternary and along the binaries may be estimated using Fig. 1.3 as described below.

The temperature at which the next-to-last solid phase dissolves during a heating run defines a point lying on the cotectic between the stability fields of the final two solids present. This point corresponds to the composition of the liquid present in the inclusion at that temperature. The composition of the solid remaining at that temperature must lie somewhere on the perimeter of the NaCl-KCl-H_2O triangle. Neglecting the mass of the vapor, the bulk composition of the fluid inclusion must lie along a mixing line joining these two points. Additionally, it must lie within the stability field of the phase having the higher dissolution temperature and along the isotherm corresponding to that temperature. Therefore, the bulk composition of the fluid inclusion is defined by the intersection of the isotherm corresponding to dissolution of the last solid phase with the mixing line.

For all bulk compositions in this system except for those lying in fields 12, 13, 15 and 16 of Fig. 1.12, the composition of the last solid to dissolve at the dissolution temperature of the next-to-last solid is essentially that of the pure end-member phase. Thus, halite, sylvite and ice plot at their respective apices on the triangle, and hydrohalite ($NaCl \cdot 2H_2O$) at 61.9 wt. % NaCl along the NaCl-H_2O join. However, if final dissolution occurs within fields 12, 13, 15 or 16 (Fig. 1.12) where halite and sylvite are the last two solid phases present, then at the lower dissolution temperature (<490°C) the remaining solid may contain appreciable solid solution and its composition must be

determined using Fig. 1.8.

The graphical technique described above for determining fluid inclusion compositions in the NaCl-KCl-H_2O system from microthermometric data is illustrated using Figs. 1.8 and 1.10 for an inclusion having a sylvite dissolution temperature of 450°C and a halite dissolution temperature of 600°C. The composition of the liquid phase in the inclusion at the dissolution temperature of the next-to-last solid phase (sylvite in this case at T_c) lies on the halite-sylvite cotectic at point "c". The composition of the remaining halite crystal at this temperature can be determined from the NaCl-KCl solvus of Fig. 1.8 and is represented by point "d" on Fig. 1.10. Again, neglecting the mass of the vapor phase, the bulk composition of the inclusion must lie along the mixing line d-c. The bulk composition must also lie within the halite stability field along the isotherm defined by the dissolution temperature of halite (600°C). Thus, the bulk composition of this fluid inclusion can be specified by the intersection of the 600°C isotherm and the mixing line at point "a".

An alternative method for determining fluid inclusion compositions in the NaCl-KCl-H_2O system from microthermometric data is presented by Bodnar et al. (1987). They provide a computer algorithm which uses the equations presented in this study and the equation for freezing point depression in the NaCl-KCl-H_2O system from Hall et al. (1987) to calculate inclusion compositions anywhere in the ternary composition space from the observed dissolution temperatures of the final two solid phases.

In theory, any of the modes of solid phase dissolution listed above are possible, while in practice not all of the individual transitions within a given mode will be observable. For example, consider a fluid inclusion with an NaCl/(NaCl + KCl) weight fraction of 0.5 and total salinity of 5 wt. %. This inclusion has a bulk composition lying within the ice stability field (field 2, Fig. 1.12) and contains 2.5 wt. % NaCl. Initially, all

of the NaCl is contained in the hydrohalite phase, which must melt completely at -22.9°C producing about 12.4 wt. % liquid of the eutectic composition in the inclusion. The fact that this transition occurs at constant temperature makes the eutectic reaction observable in this case. However, aside from providing a good test for impurities (a eutectic temperature of -22.9°C suggests that other electrolytes are not present in large amounts) this observation says little about the bulk composition. The next phase transition encountered is the continuous dissolution of sylvite up to -15.7°C as the liquid composition moves along the ice-sylvite cotectic. The original liquid formed at the ternary eutectic consumed about one third of the total KCl leaving 1.78 wt. % of the total inclusion contents as sylvite to dissolve over the next 7.2°C. Even after cooling and reheating in attempts to generate a single sylvite crystal, 1.78 wt. % leaves a very small crystal. The amount of ice left at the temperature of sylvite dissolution is still 77.7 wt. % of the total contents (a decrease of only about 10 wt. % along the ice-sylvite cotectic) and although ice and sylvite are distinguishable in fluid inclusions, in this example recognition of sylvite would be virtually impossible because it would be masked by the ice.

Provided the optical quality of the above inclusion is acceptable, the final melting temperature of ice (-2.7°C) may be determined. In the absence of the sylvite dissolution temperature this will allow an estimate of total salinity accurate to 1.2 wt. %, but allows any NaCl/(NaCl + KCl) weight ratio from the ternary eutectic "e" (NaCl/(NaCl + KCl) = 0.78) to the KCl-H_2O binary eutectic "c". For inclusions with NaCl/(NaCl + KCl) weight ratios greater than 0.78, hydrohalite will be the next to last phase to dissolve (field 3 of Fig. 1.12); unlike sylvite, hydrohalite can often be recognized even in tiny amounts due to its high birefringence (E. Roedder, 1987, personal communication). However, more accurate compositional determinations in field 2 of Fig. 1.12 would require some independent means of obtaining the necessary ratio. On the other hand, if the inclusion

just described had a total salinity of 20 wt. % the relative quantities of sylvite and ice would be small and nearly equal near the sylvite dissolution temperature, and careful observation would likely result in a reasonably accurate compositional determination.

The accuracy with which inclusion compositions in the NaCl-KCl-H_2O system may be estimated is also dependent on the bulk density of the inclusions. As discussed previously, very accurate compositional determinations are possible only for those inclusions whose vapor bubble disappearance temperatures are coincident with their solid phase dissolution temperatures. In practice, this is seldom the case. Often, the observed dissolution temperatures will be recorded in the presence of a large vapor bubble or well above the temperature at which the bubble has disappeared. According to Chou (1987) and the earlier discussion, in both cases salinity estimates may be in error by up to a few weight percent. More serious problems result if the bulk density is so high that the inclusion decrepitates before final dissolution of the solid phases, or if significant quantities of additional components are present in the inclusion and are not taken into account.

Metastable Phase Transitions

One need only compare the phase transitions observed during microthermometric experiments on fluid inclusions with those predicted from appropriate phase diagrams to gain an appreciation for metastable behavior. A variety of metastable phase relationships have been observed in the NaCl-KCl-H_2O fluid inclusions examined in this study, and although many are common to virtually all types of fluid inclusions, a few are unique to this system. Metastable, supercooled liquids in inclusions persist well below their equilibrium freezing points - in some cases to temperatures as low as -196°C (e.g.,

Roedder, 1984, pp. 291-304). Phase transitions observed under these conditions are often not reproducible and consequently of little value in estimating fluid compositions or densities. Failure to recognize metastable phase relationships may lead to serious interpretation errors in fluid inclusion studies.

As a first approximation, one may conclude that a fluid inclusion in this system which contains only liquid and vapor at 25°C must have a composition lying somewhere on the water-rich side of the 25°C isotherm (Fig. 1.3; Fig. 1.11a); however, this approximation may result in fluid compositional estimations which are seriously in error as discussed below.

The normal method used to determine total salinities for bulk fluid compositions within the ice field is to measure freezing point depressions. Because the nucleation of ice is generally non-reproducible and requires a substantial amount of undercooling, the determination is made by measuring the final melting temperature of ice during slow heating. However, small inclusions having bulk compositions within the low temperature portions of the ice field (see Fig. 1.3) will sometimes fail to nucleate ice even when held at liquid nitrogen temperatures for several minutes, although larger samples of these same compositions will freeze spontaneously with slight undercooling (~10°C). In the absence of freezing data, these low-salinity brine compositions in the NaCl-KCl-H_2O ternary may be estimated only within broad limits.

As with ice, the nucleation of hydrohalite, halite, sylvite and even a vapor phase requires that the system be well within the thermal stability limits for that phase. Thus, under equilibrium conditions, an inclusion formed from a 35.9 wt. % KCl brine should contain a sylvite daughter crystal at 25°C. However, synthetic inclusions having this composition were observed to contain only liquid and vapor at room temperature - even a year after their preparation in the laboratory. Only after supercooling could the sylvite be

nucleated and its dissolution temperature (100°C) be determined. Shaposhnikov and Khetchikov (1970) have reported the absence of halite or sylvite in synthetic inclusions prepared from brines containing up to 40 wt. % salt and conclude that the inclusions did not trap the expected fluid composition. From the above discussion it seems more likely that sylvite failed to nucleate in these inclusions because of metastability.

The metastable absence of halite and/or sylvite was observed in this study in synthetic inclusions having a wide range of Na/K ratios and salinities up to 38 wt. %. Sylvite daughter phases with expected dissolution temperatures as high as 140°C and halite daughters with dissolution temperatures up to 300°C often failed to nucleate while at room temperature for days to a few weeks. Thus, the range of possible fluid compositions inferred from the absence of solid phases at room temperature must be extended to at least the 38 wt. % isopleth. Note, however, that this does not necessarily apply to natural inclusions, as described below.

Similar considerations are important when only one solid is metastably absent in inclusions having bulk salinities in excess of room temperature saturation with respect to both halite and sylvite. As an example, consider the metastable absence of sylvite in an inclusion which, under equilibrium conditions should display dissolution temperatures of Tm (KCl) = 125°C and Tm (NaCl) = 350°C. Treating this inclusion as having a composition in the NaCl-H_2O binary system would result in underestimation of the total salinity by 10.4 wt. %. However, the apparent lack of potassium in this inclusion would preclude any geochemical calculations based on the Na/K ratio.

Natural fluid inclusions generally display equilibrium room temperature phase relationships because fluid systems approach equilibrium with time. However, sample preparation procedures might involve heating the sample to temperatures in excess of 100-150°C. At these temperatures, equilibrium phases originally present in the inclusions

may dissolve during sample preparation and not re-precipitate when cooled to room temperature, resulting in disequilibrium phase relations during room temperature microscopic observation. Most of the above ambiguities may be resolved by freezing the inclusion with liquid nitrogen and observing the phase transitions which occur as it begins to melt. Provided the inclusion will freeze, the problem then reduces to one of correctly identifying the phases.

Once the thermodynamically stable assemblage has been nucleated within the inclusion, the determination of a phase boundary based on the disappearance of a phase will generally reflect equilibrium conditions. Cloke and Kessler (1979) have discussed the implications of disequilibrium between coexisting halite and sylvite to interpretations of fluid inclusion data from porphyry copper deposits. They state (p. 1825) that the measured dissolution temperature would be in error ". . . if, at either the sylvite or the halite disappearance temperatures, either mineral differed significantly in composition from its equilibrium value." However, based on the evidence presented in an earlier section of the present study, it appears that during slow heating the two crystals maintain very nearly equilibrium compositions so that measured dissolution temperatures represent equilibrium phase transitions.

Metastability may cause problems, however, for compositions in the vicinity of the halite-sylvite cotectic at temperatures below approximately 185°C (Fig. 1.13). Here, features inherent to the solubility surface of the NaCl-KCl-H_2O system yield some rather peculiar phase relations. Due to the orientation of the cotectic between the halite and sylvite stability fields, inclusions having bulk compositions within fields 10-13, 15 or 16 of Fig. 1.12 should actually precipitate NaCl on heating from -2.3°C up to about 100°C, or until the sylvite dissolves. In inclusions containing bulk compositions within fields 12,13,15 or 16, some amount of halite will form at -2.3°C during the peritectic reaction

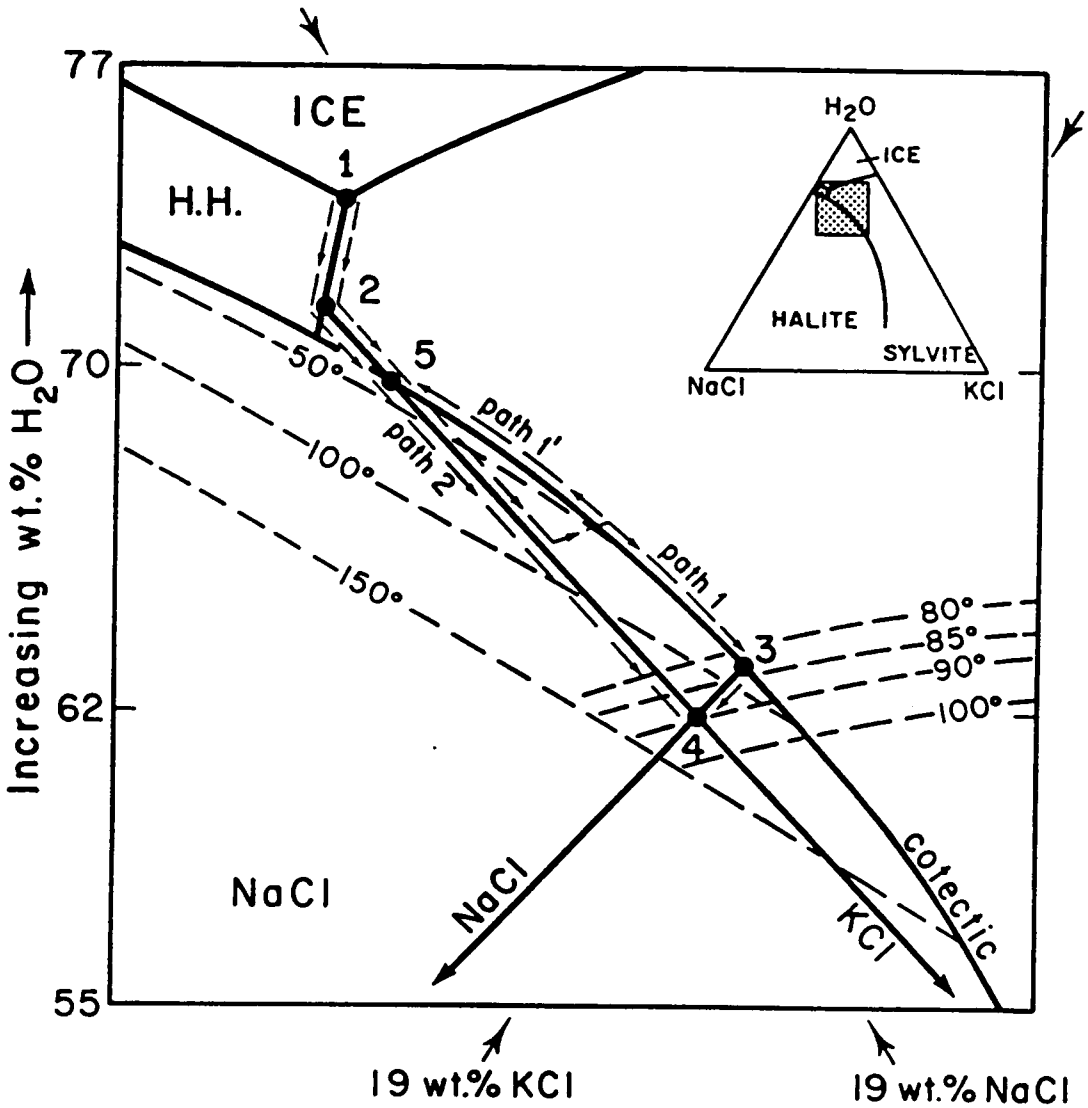

Figure 1.13 **Enlargement of a portion of the vapor-saturated solubility surface in the NaCl-KCl-H_2O system. Arrows show liquid composition changes in an inclusion having a bulk composition of 38 wt. % total salinity and NaCl/(NaCl + KCl) = 0.5 (point 4) during the two possible paths of solid phase dissolution described in the text.**

involving the dehydration of hydrohalite ($NaCl \cdot 2H_2O$). Solid phase dissolution within these fields will occur according to the previously described paths. In fields 10 and 11 hydrohalite completely dissolves before the peritectic is reached and upon further heating, when the liquid composition enters field 10, halite should precipitate. Frequently, however, the failure to nucleate halite at this point will result in the following metastable, solid phase dissolution path:

$$HH+S+I \rightarrow HH+S+I+L_e \rightarrow HH+S+L \rightarrow S+L \rightarrow L$$

To illustrate this behavior, a synthetic fluid inclusion having a bulk composition in field 10 was prepared from a fluid with an NaCl/(NaCl + KCl) weight fraction of 0.5 and total salinity of 38 wt. % (point 4 on Fig. 1.13). The phases ice, hydrohalite and sylvite were nucleated by supercooling. On heating, the ice melts isothermally at the ternary eutectic (-22.9°C) leaving hydrohalite, sylvite, vapor and a liquid of composition 1 (Fig. 1.13). With further heating the hydrohalite and sylvite continuously dissolve and the liquid composition moves along the hydrohalite-sylvite cotectic to point 2 where the hydrohalite completely dissolves at -9.0°C and the liquid composition leaves the cotectic. Continued sylvite dissolution causes the liquid composition to move directly toward the KCl apex. Once it crosses the halite-sylvite cotectic (point 5) the system becomes metastable because of the failure to nucleate halite.

Further heating results in one of two possible scenarios. Along path 1 halite nucleates before the sylvite completely dissolves and the liquid composition shifts back to the cotectic because halite, sylvite, vapor and liquid are all present. On cooling (path 1') the halite dissolves at 18.4°C in the presence of sylvite (point 5) or, on further heating (path 1), sylvite dissolves at 83.6°C in the presence of halite (point 3). Both cases are

consistent with equilibrium phase transitions predicted from the diagram. Continued heating beyond the sylvite dissolution temperature results in equilibrium halite dissolution at 124.7°C (point 4).

During some heating runs halite fails to nucleate and the liquid composition proceeds along path 2 until sylvite dissolution is observed at 89.0°C (point 4). Although this is a metastable phase transition, the dissolution temperature is highly reproducible. Furthermore, the observed temperature is exactly that predicted for this fluid composition by metastable extension of the isotherms from the sylvite stability field into the halite field. Hence, it appears that this extrapolation procedure is valid as long as the phases present and the phase transitions are correctly identified.

It should be noted that during some heating runs halite nucleates on sylvite a few degrees before sylvite dissolves. Often several degrees of cooling are then required to verify that both phases are present. Failure to note the dissolution of sylvite will allow any fluid composition along the 124.7°C halite isotherm. Likewise, in heating experiments where only sylvite is present, all fluid compositions lying along the 89.0°C sylvite isotherm will have identical sylvite dissolution temperatures. However, in each case, measurement and proper interpretation of the low temperature phase transitions (i.e. the order of disappearance of hydrohalite and ice) make the compositional determination unambiguous.

There is a possibility that two additional phase fields exist in Fig. 1.12, resulting from the halite-sylvite cotectic crossing the line segment joining the ternary eutectic and the KCl apex (discussed in the section "equilibrium phase transitions"). Even if these two fields exist, stable solid phase dissolution paths will probably not be observed due to the failure to nucleate halite. Rather, inclusions containing bulk compositions within these two fields will almost certainly display phase transitions identical to those described for

field 1.

As illustrated in the above example, even in this metastable region, the composition of NaCl-KCl-H_2O fluids can be unequivocally determined provided all observable phase transitions have been measured and interpreted correctly. Unfortunately, in natural systems, the presence of additional components will often make precise compositional determinations impossible.

Effect of Additional Components

The presence of additional components can significantly alter the phase relations from those depicted in Fig. 1.3 for the pure NaCl-KCl-H_2O system. This in turn can result in large errors when estimating fluid compositions from microthermometric data. Of the numerous additional components which could influence halite and sylvite solubilities, relatively few have been routinely encountered in appreciable quantities in geologic systems. These include the calcium, magnesium, and iron chlorides, CO_2, CH_4 and various sulfur species. A short discussion of the phase relations in multicomponent systems including references to the data available for geologically important components is presented in Roedder (1984, pp. 249-50).

Although few solubility data are available for quarternary or higher-order systems, some useful conclusions can be drawn by analogy from data on simpler systems. By examination of Fig. 1.3 it is apparent that the addition of small amounts of KCl to an NaCl saturated brine at 500°C increases the total salinity at saturation and at the same time decreases the solubility of NaCl relative to the total solution (i.e., NaCl + KCl + H_2O) at that temperature. In terms of fluid inclusion compositions, failure to account for the presence of the second salt (KCl in this case) would therefore result in underestimation of

the bulk salinity and overestimation of the relative amount of NaCl. Limited data on the system NaCl-$CaCl_2$-$MgCl_2$-H_2O (Crawford, 1981) indicate that the addition of $CaCl_2$ or $MgCl_2$ also significantly decreases the solubility of NaCl in the brine. Thus for high salinity fluid inclusions, NaCl and KCl contents estimated from microthermometric data interpreted using Fig. 1.3 will be too high if significant amounts of other chlorides are present.

The most extensive literature on the effect of dissolved gases on salt solubility at high temperatures pertains to the CO_2-H_2O-NaCl system (e.g., Gehrig, 1980). Appreciable amounts of CO_2 can be dissolved in concentrated brines only at pressures well above those along the three-phase curve in the NaCl-H_2O system. Because of the positive P-T slopes of the isopleths of the halite liquidus in this system at moderate and high salinities (Fig. 1.9) halite solubility decreases with increasing pressure. For a given pressure, the solubility of halite decreases further with the addition of small amounts of CO_2 . Thus, NaCl, and probably KCl contents of concentrated brines estimated using microthermometric data, will be too high if significant amounts of CO_2 are present in the liquid phase.

GEOLOGIC APPLICATIONS

The presence of NaCl and KCl as major solute components in fluids from a wide variety of geologic environments has been verified by numerous fluid inclusion studies (e.g., Roedder 1972). Perhaps the best known examples are from the porphyry copper deposits where exsolution of aqueous fluid from a water-saturated magma, followed by liquid-vapor phase separation can result in such high salinities that fluid inclusions from

these systems commonly contain halite and sylvite daughter crystals (e.g., Bodnar and Beane, 1980). In other systems NaCl is by far the most dominant solute species and inclusions contain only halite daughter crystals at room temperature. However, bulk analysis of these inclusions frequently reveals the presence of large, yet undersaturated concentrations of KCl. Brines from active geothermal fields generally contain Na^+ and K^+ as the major cations and Cl^- as the major anion present (Ellis, 1979), and similar results are found in their fossil equivalents, the epithermal deposits (Henley and Brown, 1985). Fluid inclusions from these environments often contain only liquid and vapor phases at room temperature. However, final melting temperatures of ice in these inclusions indicate that many have significant concentrations of dissolved salts.

Along with direct chemical characterization of the fluid phase, information obtained from inclusions in this system may be employed in the estimation of other geochemical parameters. Poty et al. (1974) have demonstrated that Na/K partitioning between feldspars and the fluid phase provides a geothermometer for adularia and high-albite bearing metamorphic rocks in the western and central Alps. In the porphyry copper environment Na/K ratios of mineralizing fluids obtained from inclusion studies, combined with observed alteration patterns, have been used to calculate the pH of ore-depositing fluids and metal solubilities in these fluids (Beane and Titley, 1981).

Aside from estimating the compositions of natural fluid inclusions, the present study provides a foundation for the interpretation of data from other PVTX studies within this system using synthetic fluid inclusions. For example, equilibrium liquid and vapor compositions of inclusions trapped within the two-phase fluid field in the ternary at high temperatures and moderate pressures may be completely determined using the solubility relations presented in this paper (Bodnar et al.,1985; Sterner and Bodnar, 1986). Likewise, the techniques described herein should be equally amenable to PVTX studies of

other electrolytes.

Finally, the excellent agreement between solubility data presented by Chou (1986, 1987) for the KCl-H_2O and NaCl-H_2O systems and those obtained from measurements of over 400 individual synthetic fluid inclusions in the present study together with similar findings reported in earlier papers in this series constitute irrefutable evidence that fluid inclusions trap representative samples of the parent solution. Inclusions from certain geologic domains may no longer contain fluids which are compositionally and volumetrically representative of the fluid phase(s) present at the time of their formation, but these differences are the result of post-entrapment changes.

REFERENCES

Barrett W. T. and Wallace W. E. (1954) Studies of NaCl-KCl solid solutions. I. Heats of formation, lattice spacings, densities, schottky defects and mutual solubilities. *J. Am. Chem. Soc.*, **76**, 366-369.

Beane R.E. and Titley S.R. (1981) Porphyry copper deposits Part II. Hydrothermal alteration and mineralization. *Econ. Geol. 75th Anniversary Vol.*, 235-269.

Bodnar R. J. and Beane R. E. (1980) Temporal and spatial variations in hydrothermal fluid characteristics during vein filling in preore cover overlying deeply buried porphyry copper-type mineralization at Red Mountain, Arizona. *Econ. Geol.* **75**, 876-893.

Bodnar R.J., Burnham C.W. and Sterner S.M. (1985) Synthetic fluid inclusions in natural quartz. III. Determination of phase equilibrium properties in the system H_2O-NaCl to 1000°C and 1500 bars. *Geochim. Cosmochim. Acta* **49**, 1861-1873.

Bodnar R.J. and Sterner S.M. (1985) Synthetic fluid inclusions in natural quartz. II. Application to PVT studies. *Geochim. Cosmochim. Acta* **49**, 1855-1859.

Bodnar R.J. and Sterner S.M. (1987) Synthetic fluid inclusions. In *Hydrothermal Experimental Techniques*. (eds. G.C. Ulmer and H.L. Barnes), Wiley and Sons, New York, 423-457.

Bodnar R.J., Sterner S. M. and Hall D. L. (1987) SALTY: A FORTRAN program to calculate compositions of fluid inclusions in the system NaCl-KCl-H_2O. *Computers & Geosciences* (in review).

Bunk A. J. H. and Tichelaar G. W. (1953) Investigations in the system NaCl-KCl. *Koninkli Nederlandse Akad. Wetensch, Proc. Sect. Sci., Ser. B, Phys. Sci.* **56**, 374-384.

Chanh N. B. (1964) Equilibres des systems binaires d'halogenures de sodium et potassium a l'etat solide. *J. Chim. Phys.* **61**, 1428-1433 (in French).

Chou I-Ming (1982a) Phase relations in the system NaCl-KCl-H_2O. Part I: Differential thermal analysis of the NaCl-KCl liquidus at 1 atmosphere and 500, 1000, 1500, and 2000 bars. *Geochim. Cosmochim. Acta* **46**, 1957-1962.

Chou I-Ming (1982b) Differential thermal analysis of the sylvite liquidus in the KCl-H_2O binary above 440°C at elevated pressures (abstr.). *Geol. Soc. Amer. Abstr.* **14**, 463.

Chou I-Ming (1983) The liquidii of the system NaCl-KCl-H_2O at elevated pressures (abstr.). *Geol. Soc. Amer. Abstr.* **15**, 543.

Chou I-Ming (1986) Solubilities of sylvite along the three-phase curve in the binary system KCl-H_2O (abstr.). *Geol. Soc. Amer. Abstr.* **18**, 564.

Chou I-Ming (1987) Phase relations in the system NaCl-KCl-H_2O. Part III: Solubilities of halite in vapor-saturated liquids above 445°C and redetermination of phase equilibrium properties in the system NaCl-H_2O to 1000°C and 1500 bars. *Geochim. Cosmochim. Acta* **51**, 1965-1975.

Cloke P. L. and Kesler S. E. (1979) The halite trend in hydrothermal solutions. *Econ. Geol.* **74**, 1823-1831.

Crawford M. L. (1981) Phase equilibria in aqueous fluid inclusions. In *Short Course in Fluid Inclusions: Applications to Petrology.* (eds. L. S. Hollister and M. L. Crawford), 75-100. Mineral. Assoc. Canada, **6**.

Ellis A. J. (1979) Explored geothermal systems. In *Geochemistry of Hydrothermal Ore Deposits*, 2nd Ed., (ed. H. L. Barnes), 632-683. New York, John Wiley and Sons.

Gehrig M. (1980) Phasengleichgewichte und PVT-Daten ternarer Mischungen aus Wasser, Kohlendioxid und Natriumchlorid bis 3 kbar und 550°C. Ph.D. dissertation, Univ. of Karlsruhe, Karlsruhe, W. Germany, 149 p.

Gunter W. D., Chou I-Ming and Girsperger S. (1983) Phase relations in the system NaCl-KCl-H_2O. Part II: Differential thermal analysis of the halite liquidus in the NaCl-H_2O binary above 450°C. *Geochim. Cosmochim. Acta* **47**, 863-873.

Hall D.L., Sterner S.M. and Bodnar R.J. (1987) Freezing point depression of NaCl-KCl-H_2O solutions *Econ. Geol.* (in press).

Henley R.W. and Brown K.L. (1985) A practical guide to the thermodynamics of geothermal fluids and hydrothermal ore deposits. In *Geology and Geochemistry of Epithermal Systems.* (eds. B.R. Berger and P.M. Bethke) 25-44, Rev. in Econ. Geol. **2.**

Keevil N. B. (1942) Vapor pressures of aqueous solutions at high temperatures. *Amer. Chem. Soc. Jour.* **64**, 841-850.

Linke W. F. (1965) Solubilities of inorganic and metal organic compounds. *Am. Chem. Soc.* **2**, Van Nostrand, 1914 p.

Pelton A.D., Gabriel A. and Sangster J. (1985) Liquidus measurements and coupled thermodynamic-phase-diagram analysis of the NaCl-KCl system. *J. Chem. Soc., Faraday Trans. I.* **81**,1167-1172.

Potter R. W., II, Babcock R. S. and Brown D. L. (1977) A new method for determining the solubility of salts in aqueous solutions at elevated temperatures. *J. Research U.S. Geol. Surv.* **5**, 389-395.

Poty B., Stalder H. A. and Weisbrod A. (1974) Fluid inclusion studies in quartz from fissures of Western and Central Alps. *Schweiz. Mineral. Petrogr. Mitt.* **54**, 717-752.

Ravich M. and Borovaya F. (1949) Phase equilibria in ternary water-salt systems at elevated temperatures. *Izvest. Sektora. Fiz.-Khim. Anal., Inst. Obshch. i Neorg. Khim., Akad. Nauk SSSR* **19**, 68-81 (in Russian; translated in Fluid Inclusion Res. -- Proc. of COFFI (ed. E. Roedder) **10**, 330-340, 1977).

Ravich M. and Borovaya F. (1950) Crystallization of melts of chlorides of K and Na in the presence of water vapor. *Izvest. Sektora. Fiz.-Khim. Anal., Inst. Obshch. i Neorg. Khim., Akad. Nauk SSSR* **20**, 165-183 (in Russian).

Robie R. A., Hemingway B. S. and Fisher J. R. (1979) Thermodynamic properties of minerals and related substances at 298.15 K and 1 Bar (10^5 Pascals) pressure and at higher temperatures. *U.S. Geol. Survey Bulletin 1452*, 456 p.

Roedder E. (1972) Compositions of fluid inclusions. *U.S. Geol. Survey Prof. Paper 440-JJ*, 164p.

Roedder E. (1984) *Fluid Inclusions.* Mineral. Soc. Amer. Reviews in Mineralogy **12**, 644 p.

Roedder E. and Bodnar R. J. (1980) Geologic pressure determinations from fluid inclusion studies. *Annual Reviews of Earth and Planetary Sciences*, 8, 263-301.

Shaposhnikov A.A. and Khetchikov L.N. (1970) Influence of solution concentration on homogenization temperature of gas-liquid inclusions in quartz. In *Geology and Experimental Studies* XII, Moscow, "Nedra", 101-103. Quoted in Beus A.A. and Khetchikov L.N. (1983) Contribution to the problem of determination of concentration and composition of mineral-forming solutions from gas-liquid inclusions in minerals. *Geol. Rudn. Mestorozhd.* **25**, 88-90 (in Russian; translated in Fluid Inclusion Res. -- Proc. of COFFI (ed. E. Roedder) **16**, 301-304, 1983).

Sterner S.M. and Bodnar R. J. (1984) Synthetic fluid inclusions in natural quartz. I. Compositional types synthesized and applications to experimental geochemistry. *Geochim. Cosmochim. Acta* **48**, 2659-2668.

Sterner S. M. and Bodnar R. J. (1986) Experimental determination of phase relations in the system NaCl-KCl-H_2O at 1 kbar and 700° and 800°C using synthetic fluid inclusions (abstr.). *Geol. Soc. Am. Abstr.* **18**, 763.

Urusova M. A. (1974) Phase equilibria and thermodynamic characteristics of solutions in the systems NaCl-H_2O and NaOH-H_2O at 350°-550°C. *Geochemistry Internat.* **1974**, 944-950.

Vesnin Y. I. and Zakovryashin S. P. (1979) About decay of solid solutions KCl-NaCl. *Solid State Commun.* **31**, 635-639 (in Russian).

Chapter 2: Re-equilibration of Fluid Inclusions in Quartz During Laboratory-Simulated Metamorphic Uplift

ABSTRACT

P-T conditions inferred from fluid inclusions in metamorphic rocks often disagree with values predicted from mineral equilibria calculations. These observations suggest that inclusions formed during early stages of regional metamorphism continue to re-equilibrate during burial and subsequent uplift in response to differential pressure. P-T conditions accompanying burial and uplift were experimentally simulated by forming pure-H_2O inclusions in quartz, and then re-equilibrating the inclusions in the presence of a 20 wt. % NaCl solution such that final confining pressures ranged from 5 kbar above to 4 kbar below the original formation pressure.

In all samples re-equilibrated at a lower confining pressure than the original formation pressure, inclusions were formed which had compositions of 20 wt. % NaCl and densities in accord with the final P-T conditions. Additionally, some inclusions were

observed to contain fluids of intermediate salinities (between 0 and 20 wt. % NaCl). Densities of these inclusions are consistent with their formation at the re-equilibration P-T conditions. Homogenization temperatures of re-equilibrated, pure-H_2O inclusions indicated densities intermediate between the initial and final P-T conditions. In short-term experiments (7 days) where the initial internal overpressure exceeded 1 kbar, no inclusions were found which contained the original density and none were found to have totally re-equilibrated. Rather, most H_2O inclusions re-equilibrated until their internal pressures were between ~750 and 1500 bars above the confining pressure, regardless of the initial pressure differential. In a long-term experiment (52 days) inclusions re-equilibrated at a lower confining pressure than the original formation pressure displayed homogenization temperatures corresponding to a range in internal pressures between 0 (i.e. total re-equilibration) and 1.2 kbar above the confining pressure.

In experiments where the confining pressure during re-equilibration exceeded the original formation pressure, the densities of pure-water inclusions increased to values intermediate between the initial and final P-T conditions. Additionally, these inclusions were generally surrounded by a halo of smaller inclusions also of intermediate density and resulting in a texture similar to that previously ascribed to decrepitation resulting from internal overpressure. In extreme cases where confining pressures were 4 to 5 kbar above the original formation pressure, the parent inclusion almost completely closed leaving only the array of small (<3 μm) inclusions the outline of which may be several times the volume of the original inclusion. A group of such inclusions closely resembles textures commonly observed in medium- to high-grade metamorphic rocks.

To evaluate the importance of H_2O diffusion as a mechanism of lowering the inclusion bulk density, inclusions containing 10 and 42 wt. % NaCl solutions trapped at 600°C and 3 kbar were re-equilibrated at 600°C and 1 kbar for five days in dry argon.

Salinities obtained from freezing point depressions and halite dissolution temperatures of re-equilibrated inclusions indicate that original compositions were preserved to within the limits of measurement (±0.15 wt. % NaCl). Density changes similar to those previously described were noted in these experiments, in inclusions showing no visible microfractures. Density variations observed in these inclusions are considered to result from an increase in the inclusion volume, without loss of contents by diffusion or leakage.

INTRODUCTION

Microthermometric analyses combined with other geologic observations and mineral stability calculations suggest that fluid inclusions formed during early stages of a regional metamorphic event continue to re-equilibrate during burial and subsequent uplift of the metamorphic terrane (Hollister et al., 1979). Thus, only in special cases will fluid inclusions found in metamorphic rocks be representative of conditions attending peak metamorphism.

The physical changes during re-equilibration relevant to the geologic interpretation of fluid inclusions may be considered in two parts. First, the bulk density of the inclusion changes in response to an imposed differential pressure. Depending on the relative rates of change of pressure and temperature accompanying metamorphism and the volumetric properties of inclusion fluids, early-formed inclusions will likely, at some later time, experience confining pressures above or below their internal pressures. Thus, if the P-T path during burial is relatively steep, inclusions formed prior to or during early stages of the metamorphic cycle may be subjected to large internal underpressures. Such inclusions will be altered, resulting in a higher fluid density. During uplift the confining pressure

decreases, often under nearly isothermal conditions (Hollister, 1979; Passchier, 1984; Santosh, 1985), resulting in an internal overpressure in the inclusion. When the magnitude of this pressure differential exceeds some threshold value determined by the inclusion size, shape and physical properties of the host mineral, the inclusion will be altered, resulting in a lower fluid density. Inferred P-T loops in some granulite-facies metamorphic environments are characterized by initial, rapid heating at relatively low pressure followed by burial and slow cooling at high pressures (Bohlen, 1987; Hensen and Warren, 1987). Under these circumstances, early formed inclusions may initially experience internal overpressures resulting in density decrease, followed by internal underpressures during burial and slow cooling under near isobaric conditions, resulting in increased fluid densities.

Segments of a variety of P-T loops possible for metamorphic terranes are shown in Fig. 2.1 together with some representative isochores (contours of constant fluid density) for pure water. A fluid inclusion formed at peak metamorphic conditions (point T_f, P_f) which later cools isochorically along path A will not be subjected to any pressure differentials and such inclusions should, therefore, be volumetrically representative of fluids present at T_f, P_f. A fluid inclusion formed at T_f, P_f which later experiences nearly isobaric cooling along path B will experience large differential underpressures causing a density increase. Likewise, if an inclusion formed at T_f, P_f is uplifted under near-isothermal conditions along path C it will encounter substantial internal overpressures resulting in a density decrease. Inclusions formed at T_f, P_f which later follow path D will first experience internal overpressure on cooling to ~600°C followed by internal underpressure with continued cooling along D below temperatures of 500-600°C (depending on how much they re-equilibrated initially). Those which follow path E will experience similar pressure differentials only in the reverse order. Although each path

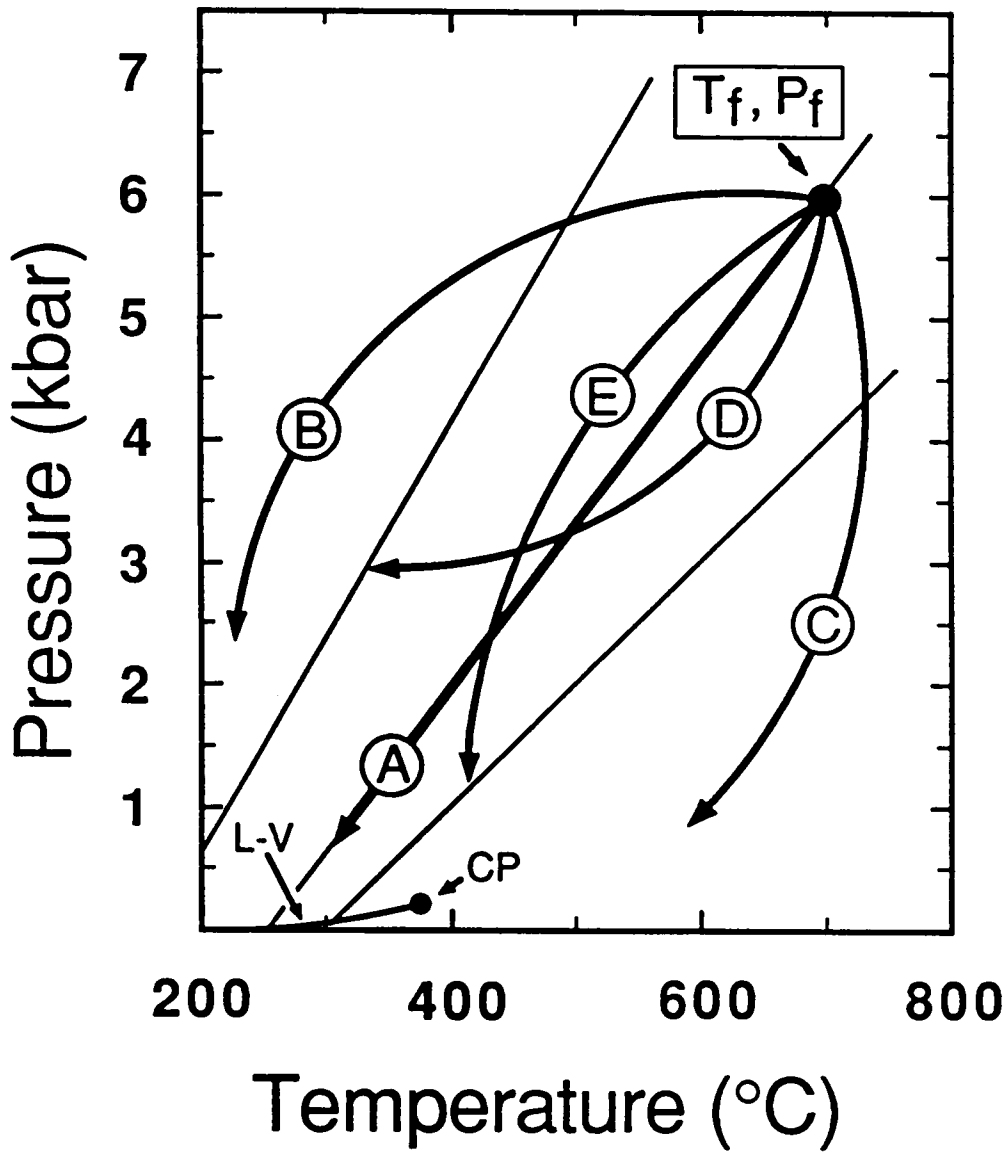

Figure 2.1 **Diagram illustrating segments of various P-T paths possible during regional metamorphism** (curves A-E). Light solid lines are representative isochores of pure water. L-V and CP represent the liquid-vapor curve and the critical point of pure H_2O, respectively. The point T_f, P_f corresponds to the initial formation conditions of inclusions discussed in the text.

described above reflects a change in P-T conditions after "peak metamorphism" it should be noted that inclusions formed prior to peak conditions will be subjected to similar pressure differentials during prograde metamorphism along the paths shown but in the direction opposing the arrows. If the host mineral is not consumed or completely recrystallized during a metamorphic cycle then such early-formed inclusions may be preserved.

The second type of re-equilibration pertinent to the interpretation of metamorphic fluid inclusions is a change in fluid composition. Changes in bulk chemistry of inclusion fluids can occur through mechanical fracturing, providing a direct conduit to pore fluids of a different composition, or through diffusional loss or gain of one or more components.

Often, the above types of re-equilibration are not independent. Rather, gross changes in bulk composition via either leakage or diffusion necessitate changes in bulk density; similarly, changes in density in response to a pressure differential might provide the driving force for changes in composition. Because the fundamental assumption in fluid inclusion studies is that inclusions represent closed, constant volume systems, geologic interpretations based on fluid inclusions in metamorphic rocks may yield erroneous results unless the mechanisms and conditions under which re-equilibration occurs are fully understood.

Several experimental investigations have reported changes in bulk densities of fluid inclusions in a variety of host minerals resulting from internal overpressures (see summary in Roedder, 1984 p. 68-77). Of these, most are concerned with stretching and decrepitation behavior under one atmosphere confining pressure. The pressure differentials were induced by heating the inclusions in standard heating stages or in one atmosphere furnaces and relative changes in bulk densities were monitored through changes in vapor bubble disappearance temperatures. The results of these studies indicate

that for a given amount of internal overpressure, the single most important factor governing re-equilibration behavior of fluid inclusions is the physical nature of the host mineral. Thus, soft minerals like barite, calcite, and fluorite tend to re-equilibrate more readily than harder materials like quartz.

For inclusions within the same host mineral and experiencing the same degree of internal overpressure, larger inclusions stretch or decrepitate more easily than do smaller ones. This relationship has been verified for inclusions in sphalerite and fluorite (Bodnar and Bethke, 1984), barite (Ulrich and Bodnar, 1987), and quartz (Binns and Bodnar, 1986). Bodnar et al. (1988) have developed an empirical equation relating inclusion size and the internal pressure required to decrepitate inclusions in quartz. Re-equilibration phenomena have been investigated at confining pressures greater than one atmosphere for inclusions in fluorite (Rowan et al., 1983) and in quartz (Pecher, 1981; Pecher and Boullier, 1984). Conclusions reported in these studies for inclusions subjected to internal overpressures are in general agreement with the one-atmosphere results. The effect of internal underpressures resulting from high confining pressures during re-equilibration has been investigated by Pecher (1981) and Pecher and Boullier (1984). Pecher (1981) reports a density decrease in re-equilibrated inclusions even where the confining pressure was several kilobars above the internal pressure, whereas Pecher and Boullier (1984) report that under similar conditions the inclusion densities increase.

Of the above investigations, only Bodnar and Binns (1986) and Bodnar et al. (1988) have studied fluid inclusions for which the exact composition of the fluid and its volumetric properties were known. This was accomplished by trapping inclusions in quartz from fluids of known composition and density and then allowing them to re-equilibrate at elevated temperatures under 1 atmosphere confining pressure. Only under these conditions can accurate densities and isochores be calculated and related to internal

pressures in the inclusions during the re-equilibration process.

In the present work we have experimentally quantified the re-equilibration behavior of inclusions in quartz under P-T conditions simulating burial and uplift of metamorphic terranes (i.e. at elevated temperatures and confining pressures). This was done using synthetic fluid inclusions grown at specific pressures and temperatures from fluids of known composition and then subjecting them to a series of different P-T conditions such that the new confining pressure (P_c) is either below or above the original formation pressure (P_f). In the first set of experiments, pure-water inclusions of known density were used. Because the volumetric properties of water are known, changes in homogenization temperatures for these inclusions could be unambiguously related to changes in bulk fluid densities. These inclusions were then re-equilibrated in a 20 wt.% NaCl solution to simulate re-equilibration in the presence of evolving fluid composition. The use of two discrete fluids in the present experiments made it possible to distinguish between original inclusions (pure H_2O) and those formed at the new P-T conditions of the re-equilibration experiments (20 wt.% NaCl).

In a second set of experiments, the role of H_2O diffusion was investigated as a possible mechanism for the change in bulk densities of fluid inclusions observed in the earlier experiments. In the final experiment, inclusions trapped initially in the presence of a high-salinity, one-phase fluid were re-equilibrated at P-T conditions in the two-fluid phase field for that brine composition.

EXPERIMENTAL PROCEDURE

Fluid inclusions used in this study were synthesized by healing fractures in quartz at elevated temperatures and pressures. The experimental procedure has been described in detail elsewhere (Bodnar and Sterner, 1987) and will, therefore, only be summarized here. Cylindrical cores, approximately 4.5 mm in diameter and ~25 mm long were cut from slabs of inclusion-free Brazilian quartz. The cores were fractured by heating them to 350°C and then immediately quenching them in cold distilled water.

For the first set of experiments, four such quartz cores were loaded, two each, into 5 mm diameter platinum capsules together with ~100 μl of distilled water and the capsules were sealed with an arc-welder. Each sample was then placed into an internally-heated pressure vessel and fluid inclusions were formed as imperfections along healed fractures during dissolution and re-precipitation of quartz at either (1) 700°C and 7 kbar or (2) 900°C and 1.6 kbar. Pure-water inclusions formed at condition "1" have a density of 0.830 g/cm^3 (Burnham et al., 1969) and homogenize to the liquid at 228°C, while those formed at condition "2" have the critical density of 0.317 g/cm^3 (Burnham et al., 1969; Keenen et al., 1978) and homogenize by critical behavior at 374.1°C (see Sterner and Bodnar, 1984, their Figures 3-5). In further discussions of this set of experiments, the inclusions formed at conditions 1 and 2 will be referred to as original, high- and low-density H_2O inclusions, respectively.

After seven days the samples were removed from the pressure vessels, the capsules opened and the quartz cores removed. A reference sample (~5 mm) was cut from each of the samples, wafered into 1 mm disks and doubly-polished for later microscopic examination on a heating/freezing stage. The remainder of the quartz was cut into ~8 mm lengths, loaded into 5 mm diameter platinum capsules together with 80 μl of a 20 wt. %

NaCl solution, and sealed with an arc-welder as before. One sample of each type was then placed sequentially back into the experimental vessel at 700°C and pressures of 6 kbar (samples R1 and R6), 5 kbar (samples R2 and R7), 4 kbar (samples R3 and R8), or 3 kbar (samples R4 and R10), for another seven day period (see Fig. 2.2). In addition, one sample of each type was re-equilibrated at 700°C and 3 kbar for 52 days (samples R5 and R11), and one sample containing pure-water inclusions originally having the critical density was re-equilibrated at 700°C and 4 kbar for 2 days (sample R9). In each run, during heating to 700°C, the reaction vessel was pressurized approximately along the isochore of pure water passing through the desired experimental conditions in order that both samples experienced their maximum differential pressure at the final P-T conditions. Thus, the original, high-density H_2O fluid inclusions would have internal overpressures at the experimental conditions of re-equilibration and the original, low-density H_2O fluid inclusions would have internal underpressures at these same conditions. At the conclusion of each run the experimental vessel was quenched (again approximately isochorically) and samples were removed and prepared for microthermometric measurements as described above.

In the second set of experiments, original inclusions were formed at 600°C and 3 kbar from 10 and 42 wt. % NaCl solutions (samples R12 and R13, respectively) and subsequently re-equilibrated at 600°C and 1 kbar for 5 days in opened capsules using dry-argon as the pressure medium. These samples were heated and quenched isobarically.

In the final experiment, original fluid inclusions were prepared as described above except that they were formed at 700°C and 2.5 kbar from a 57.0 wt. % NaCl solution (sample R14) and re-equilibrated at 850°C and 1 kbar for 35 days in opened capsules using dry-argon as the pressure medium. The sample was heated and quenched

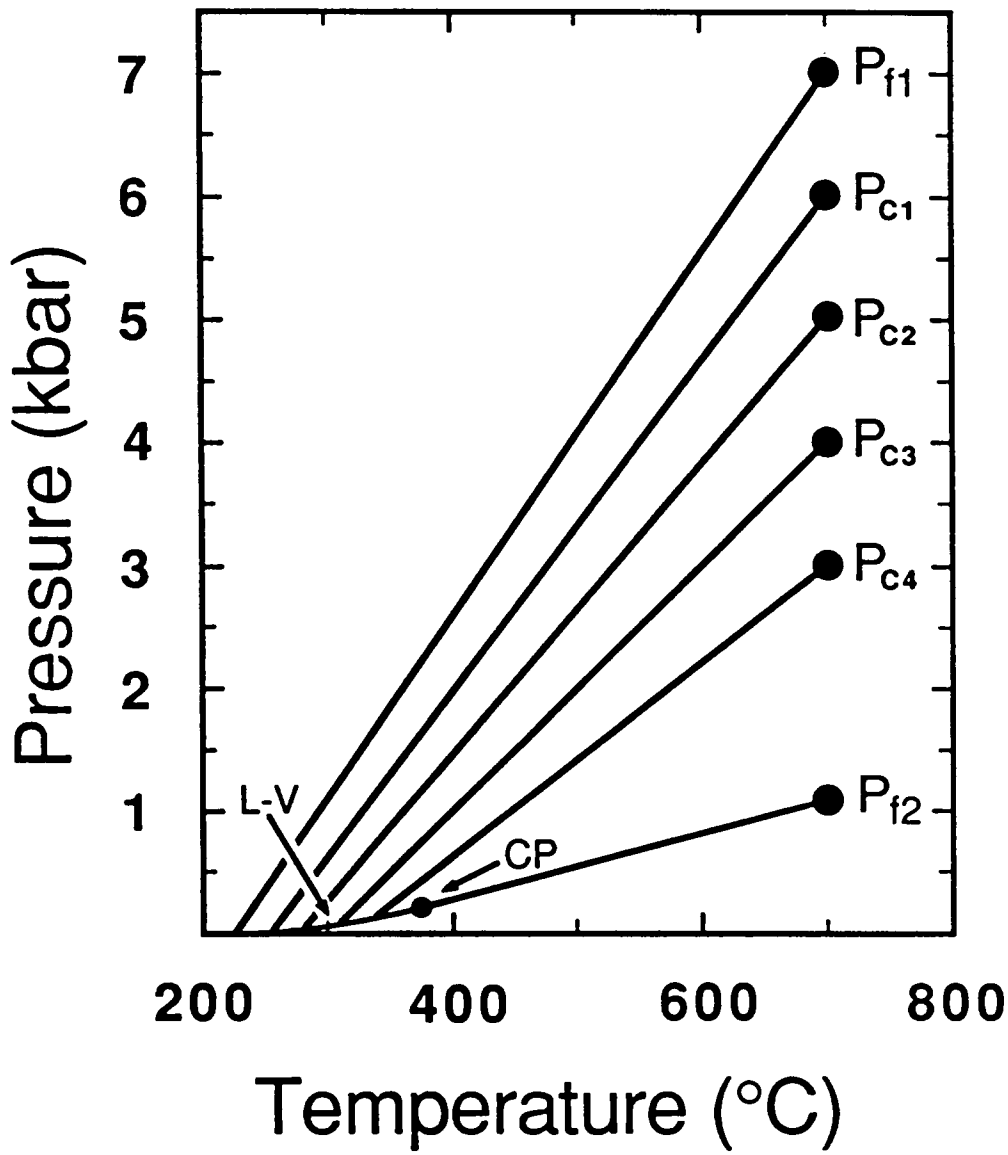

Figure 2.2 **Diagram showing the P-T conditions during experimental re-equilibration of pure-H_2O fluid inclusions** in samples R1-R11 and the isochores of pure water under these conditions. P_{c1} corresponds to the re-equilibration conditions for samples R1 and R6; P_{c2} corresponds to samples R2 and R7; P_{c3} to samples R3, R8 and R9; and P_{c4} to samples R4, R5, R10 and R11. Also shown are the internal pressures of the original high-density (point P_{f1}) and low-density (Point P_{f2}) pure-H_2O inclusions at 700°C and their corresponding isochores. L-V and CP represent the liquid-vapor curve and the critical point of pure H_2O, respectively.

isobarically.

In all experiments, approximately two hours was required to reach the final temperature and argon was used as the pressure medium. The use of argon reduced the possible ambiguities which may otherwise have resulted if a capsule leaked during the experiment or exchanged fluid with the pressure medium. To quench the samples from experimental conditions to <50°C required approximately 10-15 minutes. Details of each experiment are summarized in Table 2.1.

RE-EQUILIBRATION OF PURE-H_2O FLUID INCLUSIONS

All inclusions examined in this study contained fluids having compositions in the NaCl-H_2O system and their salinities could therefore be determined via simple freezing and heating tests. Changes in bulk density of pure water inclusions were monitored by measuring the liquid-vapor homogenization temperature of re-equilibrated inclusions and relating this temperature to density along the liquid-vapor curve using the data of Keenen et al., (1978). Densities of saline inclusions were approximated in a similar manner. Fluid compositions were obtained from freezing-point depression measurements and densities corresponding to observed homogenization temperatures were determined from the data of Khaibullin and Borisov (1966).

Densities and Compositions: Re-equilibration under Conditions of Internal Overpressure ($P_f > P_c$)

Microthermometry of original inclusions formed at 700°C and 7 kbar revealed that

Table 2.1

	Original formation conditions (P_i)					Re-equilibration conditions (P_c)						Results*				
1	T (°C)	P (kbar)	2	3	4	T (°C)	P (kbar)	5	6	7	8	9	10	11	12	13
R1	700	7.00	pure H_2O	0.830	228	700	6.00	20 wt % NaCl	0.792	255	7	228–240	25	0.830–0.814	6.5–7.0	0.5–1.0
R2	700	7.00	pure H_2O	0.830	228	700	5.00	20 wt % NaCl	0.749	281	7	241–262	26	0.812–0.781	5.7–6.5	0.7–1.5
R3	700	7.00	pure H_2O	0.830	228	700	4.00	20 wt % NaCl	0.693	309	7	277–286	19	0.756–0.740	4.8–5.3	0.8–1.3
R4	700	7.00	pure H_2O	0.830	228	700	3.00	20 wt % NaCl	0.617	338	7	290–324	38	0.732–0.657	3.5–4.7	0.5–1.7
R5	700	7.00	pure H_2O	0.830	228	700	3.00	20 wt % NaCl	0.617	338	52	306–339	32	0.700–0.617	3.0–4.2	0.0–1.2
R6	900	1.60	pure H_2O	0.317	374	700	6.00	20 wt % NaCl	0.792	255	7	277–371	12	0.756–0.439	4.8–1.7	−1.2–−4.3
R7	900	1.60	pure H_2O	0.317	374	700	5.00	20 wt % NaCl	0.749	281	7					
R8	900	1.60	pure H_2O	0.317	374	700	4.00	20 wt % NaCl	0.693	309	7					
R9	800	1.35	pure H_2O	0.317	374	700	4.00	20 wt % NaCl	0.693	309	2	361–374	25	0.523–0.317	2.2–1.1	−1.8–−2.9
R10	900	1.60	pure H_2O	0.317	374	700	3.00	20 wt % NaCl	0.617	338	7	374	21	0.317	1.1	1.9
R11	900	1.60	pure H_2O	0.317	374	700	3.00	20 wt % NaCl	0.617	338	52	371–372	24	0.439–0.422	1.7–1.6	−1.3–−1.4
R12	600	3.00	10 wt % NaCl	—	−6.6	600	1.00	Dry argon	—	—	5	Ice final melting at −6.6 °C				
R13	600	3.00	42 wt % NaCl	—	342	600	1.00	Dry argon	—	—	5	Halite dissolution at 342 °C				
R14	700	2.40	57 wt % NaCl	—	481	850	1.00	Dry argon	—	—	35	Halite dissolution > 600 °C				

* Results for samples R1–11 refer to pure H_2O fluid inclusions only.

(1) Sample number;
(2) Composition of original fluid inclusions;
(3) Density of original fluid inclusions in g/cc;
(4) L–V homogenization temperature of original pure H_2O fluid inclusions, or ice or halite dissolution temperature of original salt–water fluid inclusions;
(5) Composition of fluid in capsule during re-equilibration run;
(6) Density of pure water in g/cc at conditions of re-equilibration run;
(7) Expected L–V homogenization temperature of pure H_2O fluid inclusions if total re-equilibration to new P–T conditions occurs;
(8) Duration of re-equilibration experiment in days;
(9) Observed range in L–V homogenization temperatures of pure H_2O fluid inclusions, or observed ice or halite dissolution temperatures of salt–water inclusions;
(10) Number of inclusions studied;
(11) Range of densities of pure H_2O fluid inclusions (g/cc) calculated from observed homogenization temperatures;
(12) Range in calculated internal pressures (kbar) of pure H_2O inclusions at 700 °C obtained from isochores corresponding to measured homogenization temperatures;
(13) Effective differential pressure (internal pressure minus confining pressure) in kbar.

these inclusions contained pure water having a bulk density of 0.830 g/cm^3. The composition of these inclusions and the bulk density agree with that of pure water at 700°C and 7 kbar (Burnham et al., 1969). Microthermometric examination of samples R1-5 after the re-equilibration experiments revealed five types of inclusions.

The first type of inclusion was found only in sample R1. This type of inclusion was identical in composition and density to original inclusions, even after being subjected to an internal overpressure of 1 kbar at 700°C. Heating and freezing measurements verified that inclusions of this type had not stretched, leaked, or exchanged fluid with the surrounding 20 wt. % salt solution.

The second type of inclusion was observed in each of samples R1-5. These inclusions also contained pure water but had lower and variable bulk densities, compared to the original inclusions, as indicated by their higher homogenization temperatures.

The third type of inclusion identified was found only in sample R5. This sample was re-equilibrated at the same P-T conditions as sample R4 (700°C, 3 kbar) only for a much longer time (52 days for R5 versus 7 days for R4). These inclusions contained pure water and had bulk densities which corresponded to total re-equilibration to the new experimental conditions (700°C and 3 kbar).

The fourth type of inclusion identified in this study contained a fluid of intermediate composition between pure water and 20 wt. % NaCl. Inclusions of this type were relatively rare and formed by partial exchange of pure H_2O from the original inclusions with the surrounding solution. Densities calculated from observed homogenization temperatures of these inclusions using volumetric data from Potter and Brown (1977) and Bodnar (1985) are consistent with their formation at the final P-T conditions.

The fifth type of inclusion identified in this study was also found in each of samples R1-5. Final melting temperatures of ice in these inclusions indicate a composition of 20

wt. % NaCl, the same as the fluid surrounding the quartz during the re-equilibration stage of these experiments. Inclusions of this type had either completely exchanged fluids with the salt solution or they represent new inclusions formed during the continued fracture healing process. Homogenization temperatures of these inclusions indicate bulk densities which are consistent with trapping at the final P-T conditions.

Homogenization temperatures and calculated internal pressures of pure-H_2O fluid inclusions in samples R1-5 are presented in Table 2.1. Salinity determinations and homogenization temperatures for all inclusions in one representative sample re-equilibrated at 700°C and 3 kbar (R4) are shown in Fig. 2.3. The observed range of homogenization temperatures of pure-H_2O inclusions is shown together with their initial homogenization temperatures before re-equilibration (228°C) and the predicted homogenization temperatures (338°C) corresponding to total re-equilibration at the new P-T conditions. Observed homogenization temperatures of 20 wt. % NaCl inclusions and those of intermediate salinity are also shown. Note that no pure-H_2O inclusions were found in this sample which experienced total re-equilibration or which experienced no re-equilibration (i.e., none had homogenization temperatures of 338°C which would correspond to trapping at 700°C and 3 kbar and none had the same homogenization temperature as the original inclusions, 228°C). All observed homogenization temperatures for the 38 pure-H_2O inclusions measured fall between these limiting values.

Isochores corresponding to densities calculated from observed homogenization temperatures for pure-H_2O inclusions in samples R1-5 are shown in Figs. 2.4 through 2.7. In each figure, point P_{f1} and its associated isochore represent the original formation conditions (700°C and 7 kbar) and the corresponding density of water in the original, high-density inclusions, respectively. Point P_c and its associated isochore represent the P-T conditions of the re-equilibration experiment and the inclusion density if total

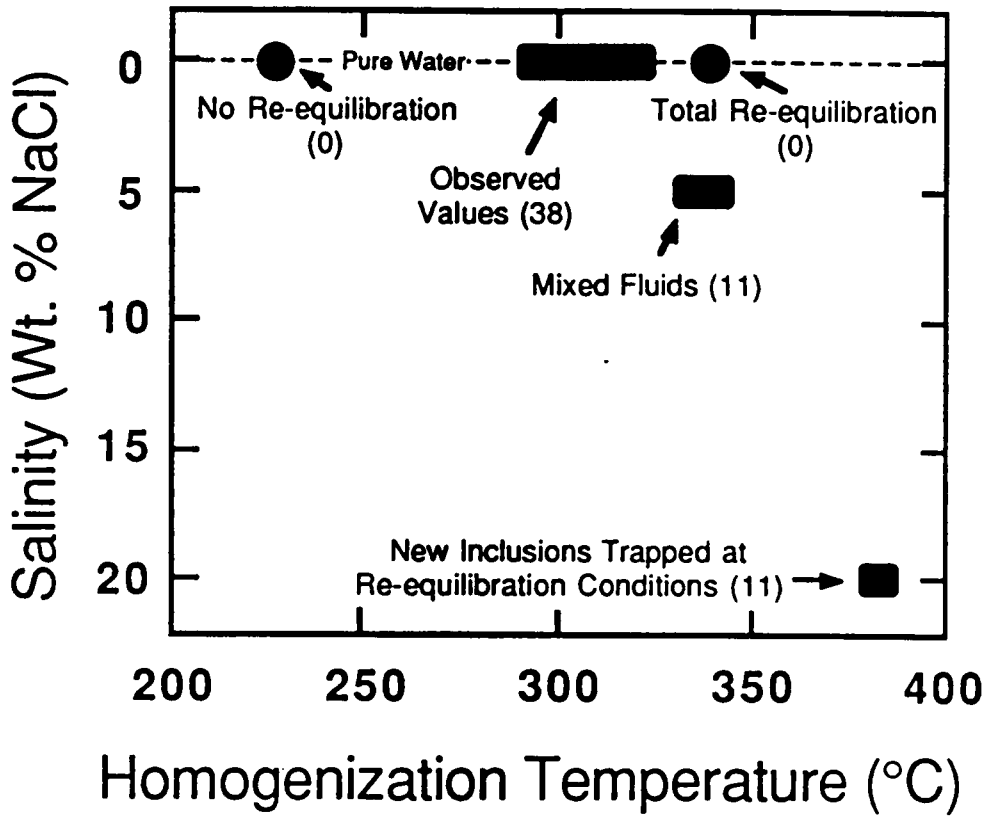

Figure 2.3 **Microthermometric data from fluid inclusions in sample R4** re-equilibrated at conditions of 700°C and 3 kbar. The numbers in parenthesis indicate the number of each type of inclusion observed.

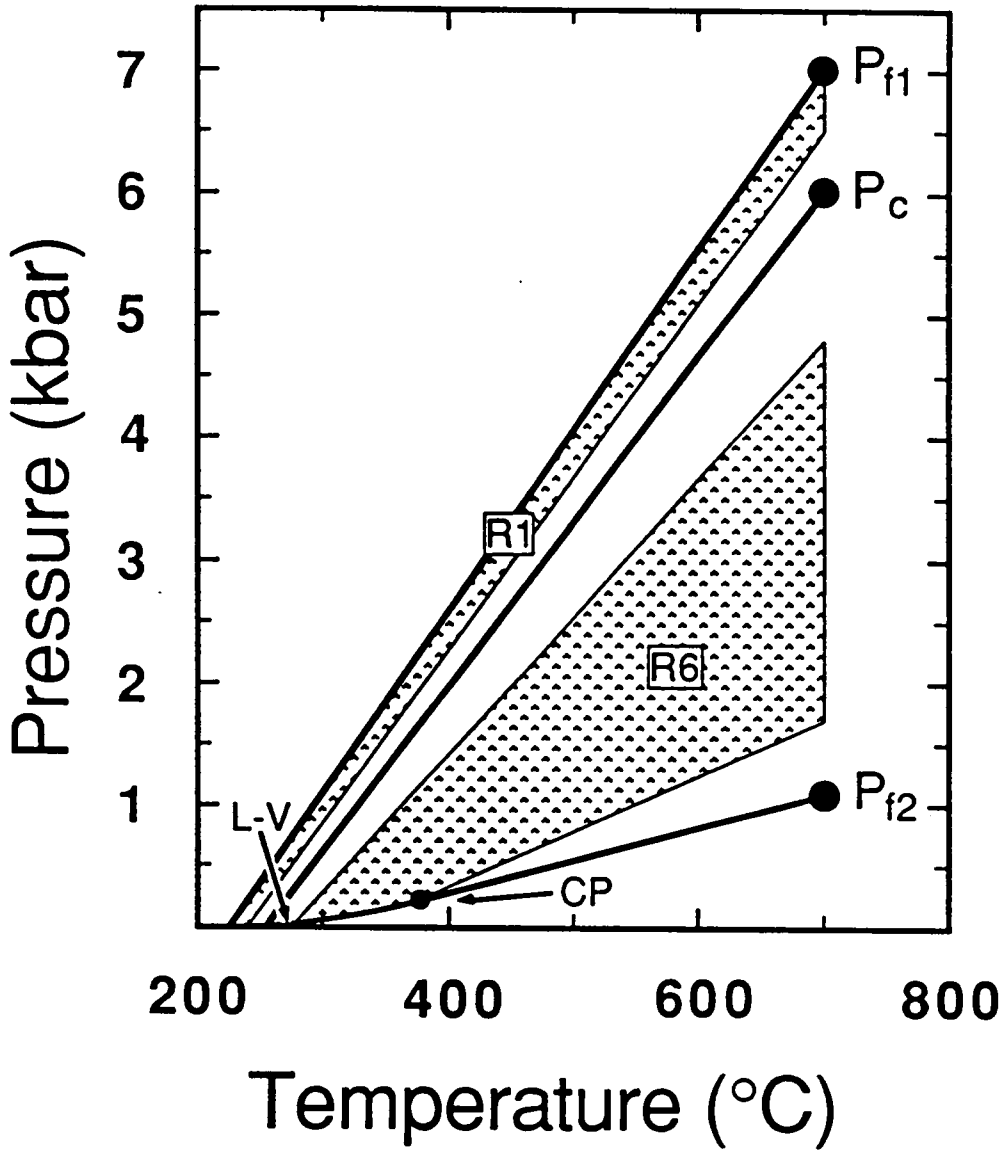

Figure 2.4 **P-T diagram showing the results of re-equilibration experiments R1 and R6.** L-V and CP are the liquid-vapor curve and the critical point of pure H_2O, respectively. P_{f1} and P_{f2} represent the internal pressures at 700°C prior to re-equilibration of original, pure-water inclusions in samples R1 and R6, respectively. P_c represents the P-T conditions of the re-equilibration experiment. The ranges of isochores calculated from liquid-vapor homogenization temperatures of pure-water inclusions after re-equilibration are shown by the shaded regions as indicated.

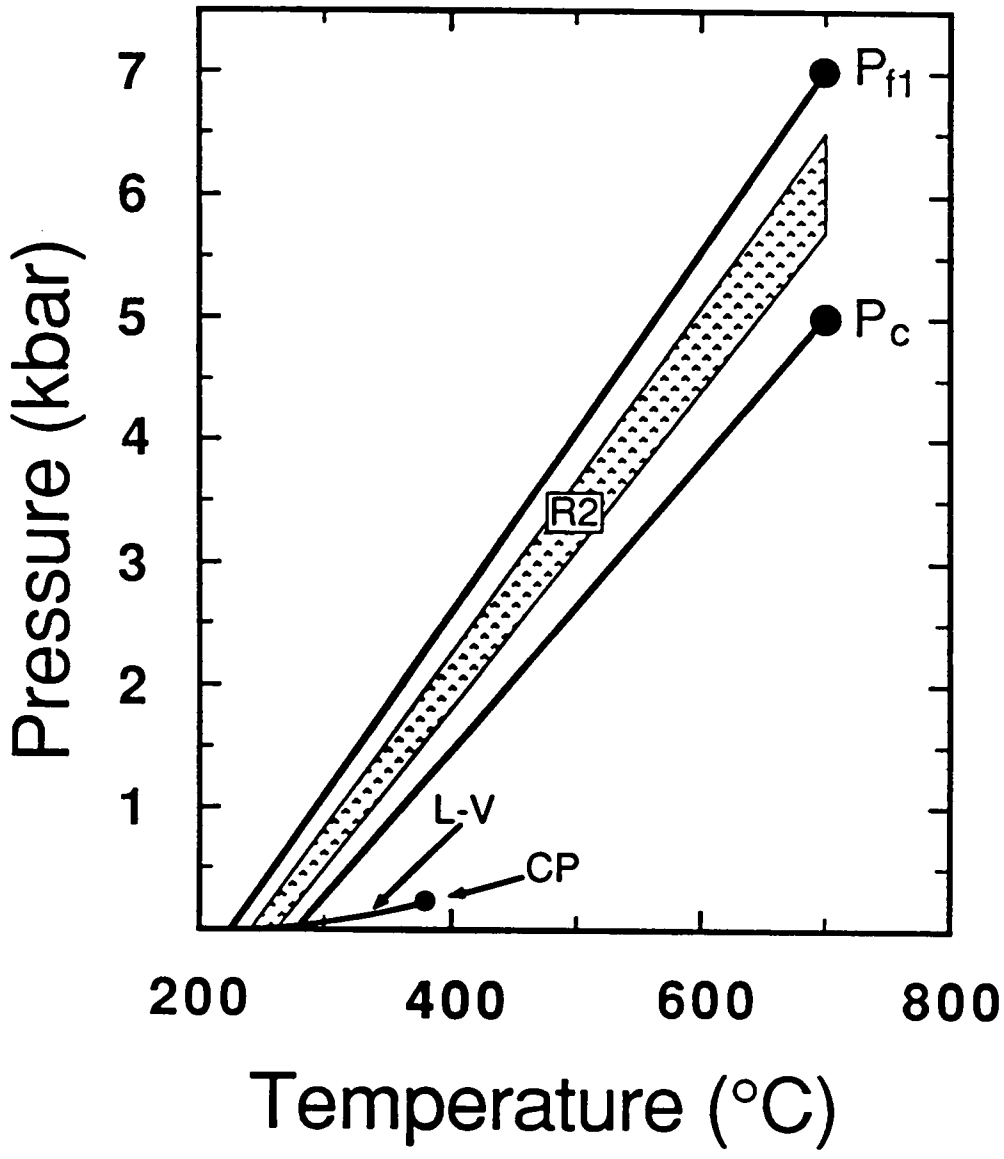

Figure 2.5 **P-T diagram showing the results of re-equilibration experiment R2.** L-V and CP are the liquid-vapor curve and the critical point of pure H_2O, respectively. P_{f1} represents the internal pressure at 700°C prior to re-equilibration of original, pure-H_2O inclusions. P_c represents the P-T conditions of the re-equilibration experiment. The range of isochores calculated from liquid-vapor homogenization temperatures of pure-water inclusions after re-equilibration is shown by the shaded region.

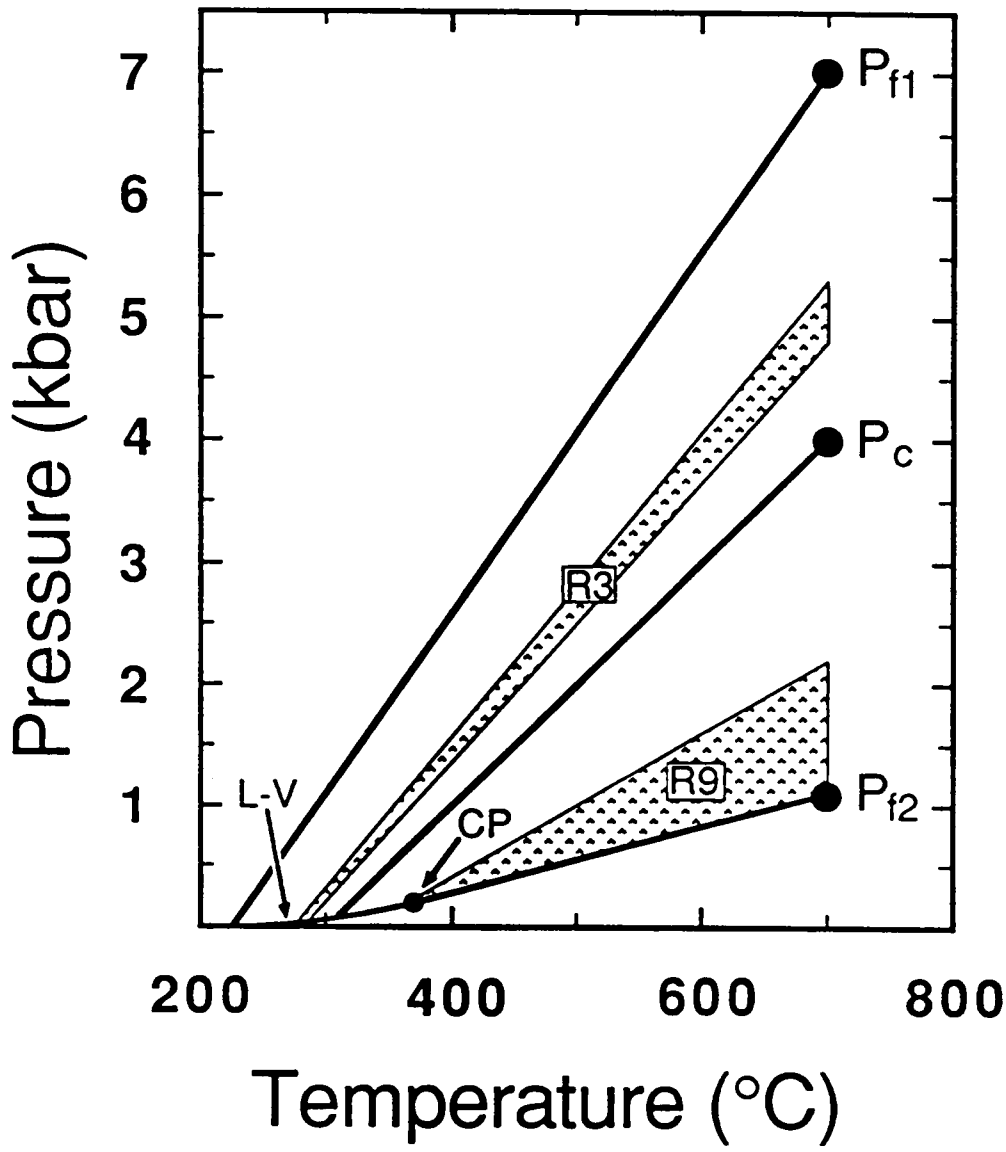

Figure 2.6 **P-T diagram showing the results of re-equilibration experiments R3 and R9.** L-V and CP are the liquid-vapor curve and the critical point of pure H_2O, respectively. P_{f1} and P_{f2} represent the internal pressures at 700°C prior to re-equilibration of original, pure-water inclusions in samples R3 and R9, respectively. P_c represents the P-T conditions of the re-equilibration experiment. The ranges of isochores calculated from liquid-vapor homogenization temperatures of pure-water inclusions after re-equilibration are shown by the shaded regions as indicated.

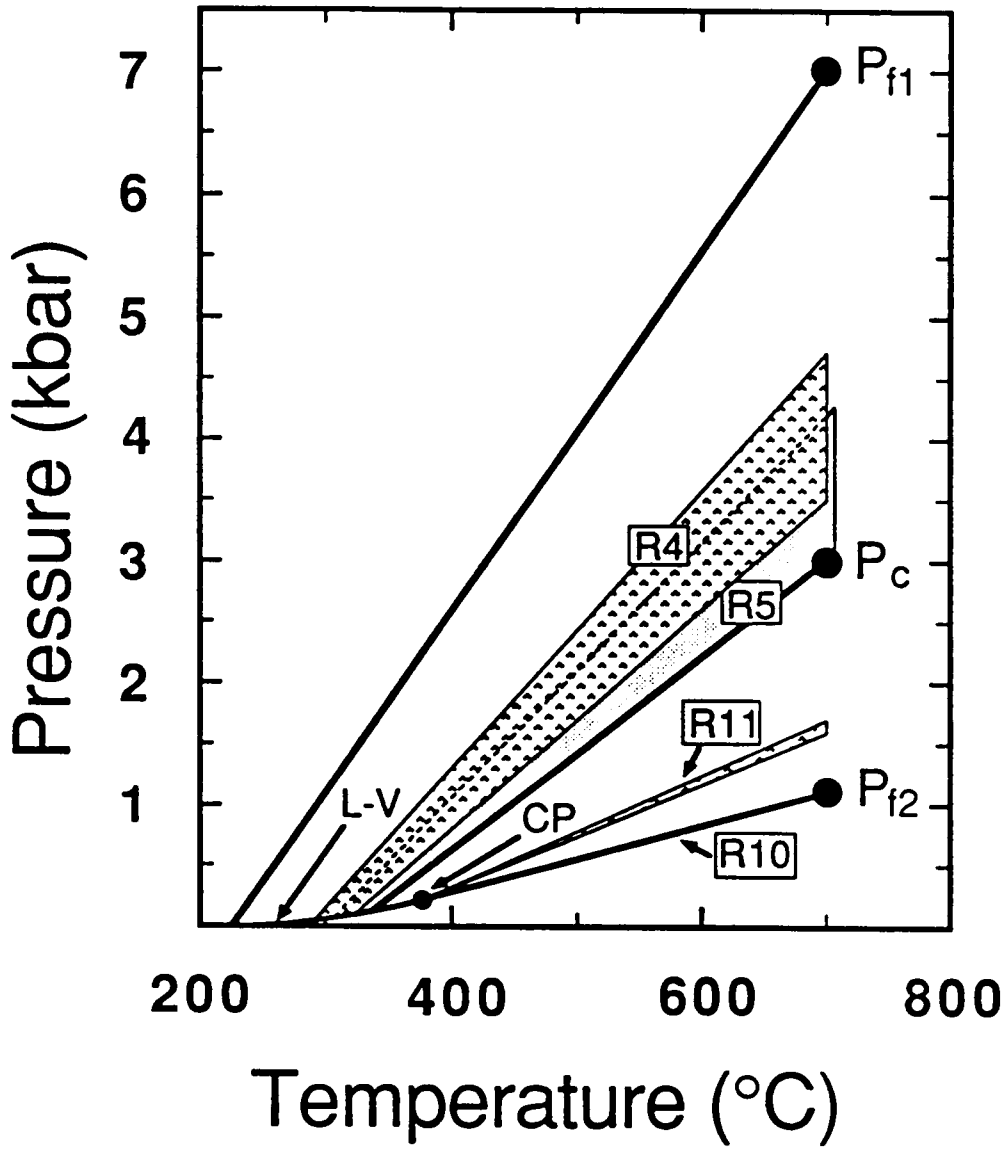

Figure 2.7 **Results of re-equilibration experiments R4, R5, R10 and R11.** L-V and CP are the liquid-vapor curve and the critical point of pure H_2O, respectively. P_{f1} represents the internal pressures at 700°C prior to re-equilibration of original, pure-water inclusions in samples R4 and R5, while P_{f2} shows the same thing for samples R10 and R11. P_c represents the P-T conditions of the re-equilibration experiment. The ranges of isochores calculated from liquid-vapor homogenization temperatures of pure-water inclusions after re-equilibration are shown by the shaded regions as indicated. The heavy shaded region above P_c represents the range of isochores calculated for inclusions in sample R4 while the light shaded region represents the data from sample R5. Densities of pure-water inclusions in sample R10 were unchanged during the seven-day experiment so that their corresponding isochores are all represented by the critical isochore between CP and P_{f2}.

re-equilibration had occurred. The shaded region between these two values represents the actual range of isochores corresponding to the densities of partially re-equilibrated, pure-H_2O fluid inclusions calculated from their homogenization temperatures. For example, Fig. 2.7 shows the data for pure-H_2O inclusions in sample R4 which was re-equilibrated at 700°C under a confining pressure of 3 kbar (point P_c). Prior to re-equilibration, this sample contained pure-H_2O fluid inclusions formed at 700°C and 7 kbar (point P_{f1}). These inclusions displayed a liquid-vapor homogenization temperature of 228°C along the pure water liquid-vapor (L-V) curve and had a bulk density of 0.830 g/cm^3 corresponding to the isochore connecting P_{f1} with the L-V curve. After re-equilibration, pure-H_2O inclusions within this sample were found to display a range of homogenization temperatures along the L-V curve from 290.3° to 323.8°C (Table 2.1) corresponding to a range in bulk densities of 0.732 - 0.657 g/cm^3. At 700°C this density range corresponds to internal pressures in fluid inclusions of 3.5 - 4.7 kbar. The corresponding isochores are represented by the shaded region in Fig. 2.7 bounded by the L-V curve between 290.3° and 323.8°C, and the calculated range in internal pressures at 700°C. The isochore between P_c and the L-V curve represents the bulk density an inclusion in this sample would have if total re-equilibration had occurred.

In sample R1 (Fig. 2.4) only one pure-H_2O inclusion was found to have a density less than its initial value whereas 24 pure-H_2O inclusions maintained their original density even after experiencing a 1 kbar differential pressure for 7 days. From Figs. 2.4-2.7 it can be seen that in 7 day experiments (samples R1-4) where the initial internal overpressure was greater than 1 kbar no inclusions were found which contained the original density and none were found to have totally re-equilibrated. Rather, most H_2O inclusions re-equilibrated until their internal pressures were between ~750 and 1500 bars above the confining pressure, regardless of the initial pressure differential. Inclusions in

the single long-term experiment (sample R5, 52 days) represent a closer approach to equilibration to the new P-T conditions. The range in final internal pressures at 700°C of inclusions in this sample was equal to that found in sample R4 which had been re-equilibrated at the same P-T conditions for only 7 days. However, several inclusions in sample R5 had final densities which corresponded to total re-equilibration to the final P-T conditions. The lack of totally re-equilibrated inclusions in samples R1-4 may therefore, be due to the relatively short duration of these re-equilibration experiments.

Densities and Compositions: Re-equilibration under Conditions of Internal Underpressure ($P_f < P_c$)

Microthermometric measurements performed on original, low-density H_2O inclusions formed at 900°C and 1.6 kbar or 800°C and 1.35 kbar revealed that these inclusions homogenize by critical behavior (fading of the meniscus at 374.1°C), indicating that they contain pure water and have bulk densities of 0.317 g/cm^3 - the critical density of water (Burnham et al., 1969; Keenen et al., 1978). Several types of inclusions were observed in samples R6-11 after the re-equilibration experiments. Similar to samples R1-5 described earlier, inclusions were found in samples R6-11 which contained 20 wt. % NaCl solutions (the same as the solution surrounding the quartz during re-equilibration). Homogenization temperatures of these inclusions were consistent with their formation at the final P-T conditions. Inclusions having salinities intermediate between pure H_2O and 20 wt. % NaCl were more common than in the first part of the study (where $P_f > P_c$) and their bulk densities were again consistent with trapping at the final P-T conditions.

Microthermometric data and calculated densities and internal pressures of

re-equilibrated, pure-H_2O inclusions in samples R6 and R9-11 are shown in Table 2.1 and on Figs. 2.4-2.7. In each figure, point P_{f2} and its associated isochore represent the internal pressure at 700°C and the bulk density of the original, low-density, pure-H_2O inclusions, respectively. Point P_c and its associated isochore represent the confining pressure and density of pure water during the re-equilibration experiment. As in the case where $P_f > P_c$, the shaded region between these two values represents the actual range of isochores corresponding to partially re-equilibrated, pure-H_2O fluid inclusions calculated from their observed homogenization temperatures. No data were obtained for samples R7 and R8 because of the poor quality of the inclusions.

Apparent homogenization via critical behavior will be observed at approximately 374.1°C in pure-H_2O inclusions having a small range in bulk densities near 0.317 g/cm^3. For this reason, observed liquid-vapor homogenization via critical behavior of re-equilibrated inclusions in these samples does not rule out the possibility that small density changes may have occurred within the original, low-density H_2O inclusions. However, the presence of pure-H_2O inclusions that homogenize to the liquid upon heating in these samples after re-equilibration provides conclusive evidence that such inclusions have undergone a definite density increase even though, in some cases, their homogenization temperatures may still be very near 374.1°C.

Density changes observed in original, low-density H_2O inclusions after re-equilibration under conditions of internal underpressure are similar to those recorded in the first part of this study (where $P_f > P_c$) in that they represent a shift toward equilibration to the new experimental conditions. Thus, where a density change was observed, in samples R1-5 ($P_f > P_c$), the final densities always represented a decrease from the original value of 0.830 g/cm^3, whereas, in samples R6 and R9-11 ($P_f < P_c$), the final densities always increased from the original value of 0.317 g/cm^3.

It can be seen in Figs. 2.4-2.7 that no pure-H_2O inclusions in samples R6 and R9-11 were found to have totally re-equilibrated to the new P-T conditions. Even in the longest run (sample R11, 52 days) all inclusions observed maintained a differential pressure of 1.3-1.4 kbar relative to the new confining pressure. This is in contrast to sample R5 ($P_f > P_c$) which, after 52 days, did yield some inclusions which had totally re-equilibrated. It is also evident from Figs. 2.4-2.7 that inclusions re-equilibrated under conditions of internal underpressure yielded a much broader range in final internal pressures at 700°C than did those where $P_f > P_c$. Thus, after re-equilibration at 700°C and 6.0 kbar for 7 days, pure-H_2O inclusions from sample R6 displayed a 3.1 kbar range in internal pressure at 700°C. The maximum range in final internal pressures at 700°C in samples R1-5 was 1.2 kbar (samples R4 and R5). Stated differently, inclusions re-equilibrated at $P_f < P_c$ might be expected to produce a wider range in homogenization temperatures than inclusions re-equilibrated at $P_f > P_c$.

Finally, in the first series of experiments (samples R1-5) where the initial differential was greater than 1 kbar, no inclusions were found which contained their original density, whereas, in samples re-equilibrated at conditions of internal underpressure, some inclusions were found to preserve their initial differential pressure of 1.8 kbar for 7 days (sample R10) or 2.8 kbar for 2 days (sample R9).

From the above discussions it is evident that even in the relatively short time frame of a laboratory experiment, substantial changes occur in the densities of fluid inclusions subjected to large differential pressures resulting from confining pressures either above or below their initial internal pressures. In the present investigation, these pressure differentials have been induced in a series of isothermal experiments but it should be obvious that similar conditions could have been created by changing the temperature during re-equilibration or by changing both temperature and confining pressure. Because

density changes of the direction and magnitude described here can be observed in these relatively short time periods, there can be no doubt that similar changes will almost certainly be experienced by fluid inclusions in natural systems over geologic time. The implications of this conclusion to the interpretation of fluid inclusion data from regionally metamorphosed terranes are clear: because significant inclusion density changes will be produced by both positive and negative differentials between internal and confining pressures, a P-T relation inferred from inclusion microthermometry alone provides neither a maximum nor a minimum estimate of the P-T conditions attending a particular stage of metamorphism.

Inclusion Morphologies: Re-equilibration under Conditions of Internal Overpressure ($P_f > P_c$)

As previously discussed, in re-equilibration experiments where $P_f > P_c$ most inclusions experienced a density decrease and a decrease in their calculated internal pressures at 700°C. This observation is consistent with the findings of other investigations as discussed in the introduction. This density decrease is accompanied by morphological changes in inclusions tending toward negative crystal shapes; those experiencing the greatest density decrease are characteristically the most regular and euhedral. An occasional fracture, obviously emanating from a re-equilibrated inclusion and along which is found a plane of "secondary inclusions" accompanies the inclusion re-equilibration although this feature is the rare exception rather than the rule. When this feature is found it is clearly related to an individual inclusion and clearly a planar feature. These observations are not in keeping with those of Pecher (1981), Gratier and Jenatton (1984) and Pecher and Boullier (1984) who describe the frequent occurrence of numerous

"secondary inclusions" along fractures surrounding a "primary inclusion" after a similar re-equilibration. These investigators provide photographs or line drawings of these features and use the terms "satellite inclusions" or "decrepitation clusters" to describe the textures found in their samples. Unfortunately, their observations regarding these secondary inclusions have not been documented by photomicrographs taken before and after re-equilibration. During numerous experimental investigations using synthetic fluid inclusions similar to those used in the above studies, we have seen the textures described by those authors many times -- in samples which have never been subjected to differential pressures. We, therefore, suggest that satellite inclusions or decrepitation clusters they describe may, in fact, be relict textures inherent in the samples prior to re-equilibration rather than a phenomenon resulting from a pressure differential. Also, we point out that when before and after photographs are presented to document changes occurring to fluid inclusions during re-equilibration (Gratier and Jenatton, 1984; Bodnar et al., 1988), the parent inclusions are not surrounded by these secondary features, rather, they appear to have become more equant and regular in shape, tending toward negative crystal morphologies like those described in the present study. In general, we see no post-re-equilibration, textural evidence to suggest that a given inclusion has experienced a density decrease as a result of re-equilibration under conditions where $P_f > P_c$. Only in the laboratory do we know the original density, which enables us to calculate the direction and magnitude of density changes. With natural samples, one can only postulate that such a re-equilibration may have occurred if densities of inclusions deduced from microthermometric measurements contrast with those inferred by independent means.

Inclusion Morphologies: Re-equilibration under Conditions of Internal Underpressure ($P_f < P_c$)

The experimental data and discussion presented thus far is not encouraging with regard to the application of fluid inclusions as geothermobarometers in regionally metamorphosed rocks. The problem is that inclusion densities change in response to differential pressure, but microthermometry alone provides no information on the direction of this change (i.e. toward increased densities or decreased densities). We will now describe a series of observations based on the limited number of experiments presented in this work which we believe may enable the investigator to determine the direction of this density change and therefore, the general trend of a P-T trajectory during metamorphism.

Morphological changes observed in inclusions re-equilibrated at $P_f < P_c$ are quite different than those observed when $P_f > P_c$. In fact, morphologic changes found in fluid inclusions re-equilibrated under conditions of internal underpressure are so striking that they alone may provide the criterion necessary to recognize re-equilibration toward higher densities. Fluid inclusions which have been re-equilibrated under conditions of $P_f < P_c$ are shown in Figs. 2.8 A-K and 2.9 B,D,F,H and I. The most immediately obvious characteristic common to almost all of these inclusions is the presence of a "halo" of "satellite inclusions" surrounding a central void. The relationship of these satellite inclusions to the central "parent" inclusion will be described shortly. Throughout this discussion it should be recalled that this texture was generated in an environment where $P_f < P_c$. Hence, the numerous secondary inclusions surrounding the central inclusion do not constitute a "decrepitation cluster", rather, they are more correctly referred to as an "implosion halo".

A representative field of view of fluid inclusions from sample R10 which have been

Figure 2.8 **Photomicrographs of fluid inclusions in samples re-equilibrated at 700°C under conditions of internal underpressure ($P_f < P_c$).** Scale bar in each picture is 25 μm. A. Inclusions from sample R10 re-equilibrated for 7 days at 3 kbar. B-C. Inclusions from sample R11 re-equilibrated for 52 days at 3 kbar. D-F. Inclusions from sample R8 re-equilibrated for 7 days at 4 kbar. G-I. Inclusions from sample R7 re-equilibrated for 7 days at 5 kbar. J-K. Inclusions from sample R6 re-equilibrated for 7 days at 6 kbar. L. Inclusions containing 20 wt. % NaCl brine and which are representative of new inclusions formed during each re-equilibration experiment, R1-R11, performed in the salt-water solution.

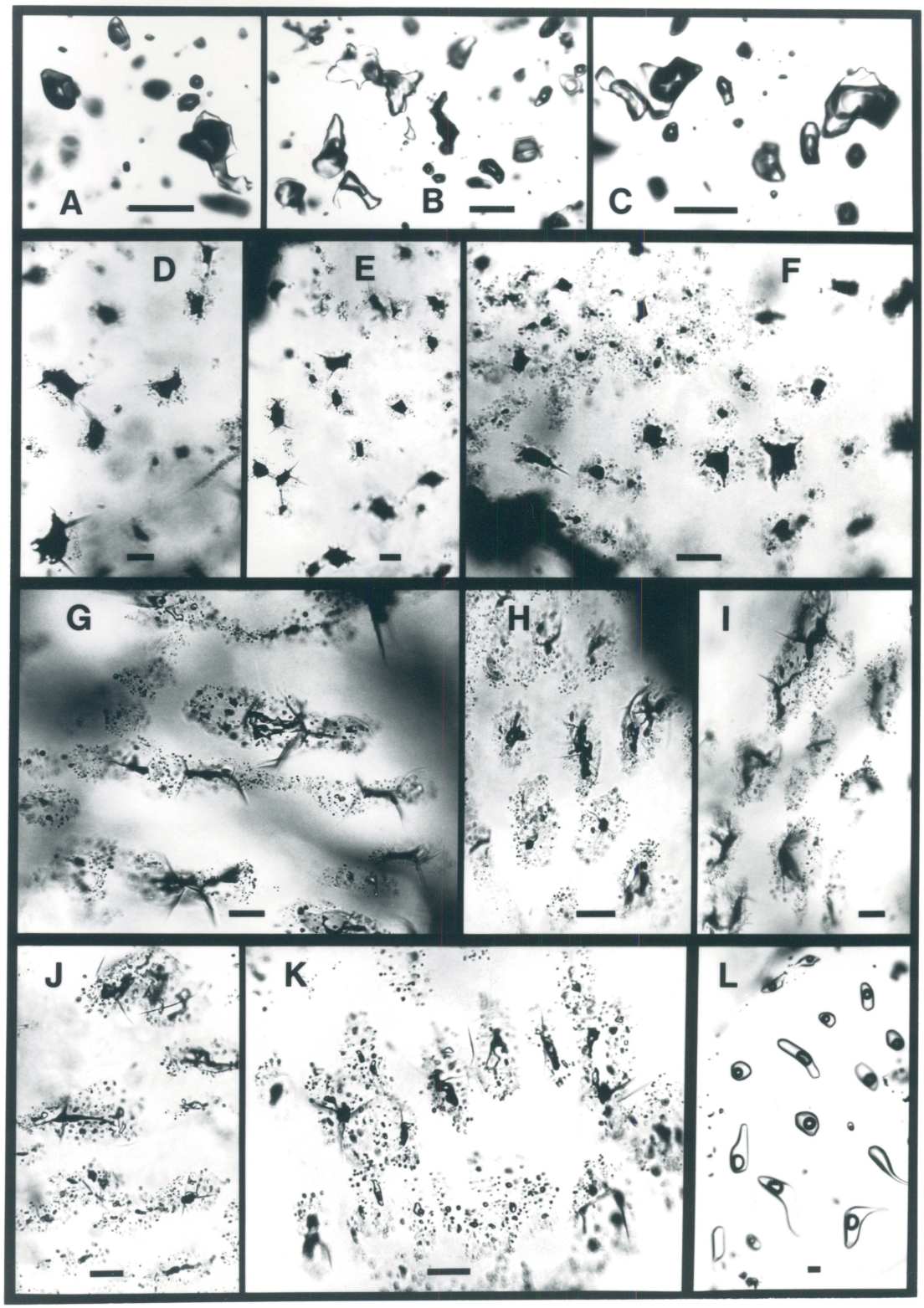
A
B
C
D
E
F
G
H
I
J
K
L

Figure 2.9 **A-I. Photomicrographs of fluid inclusions from sample R9 before and after re-equilibration at 700°C and 4 kbar for 2 days ($P_f < P_c$).** Scale bar in each picture is 25 μm. A,C,E and G. Photomicrographs of original, pure-H_2O fluid inclusions trapped at 800°C and 1.35 kbar which contain the critical density. B,D,F and H. Photomicrographs of the same inclusions shown in A,C,E and G after re-equilibration. Each photomicrograph of a given pair has been reproduced at the same magnification. In each case, after re-equilibration the original parent inclusion is surrounded by a cluster of small secondary inclusions. I. Inclusions from this sample after re-equilibration where the outer-most inclusions of the secondary clusters define a hexagonal-shaped euhedral perimeter. J-K. Natural, hydrocarbon-bearing fluid inclusions in quartz from the Tallulah Falls Dome. Note the cluster of small ≤ 3 μm inclusions surrounding each of the central voids.

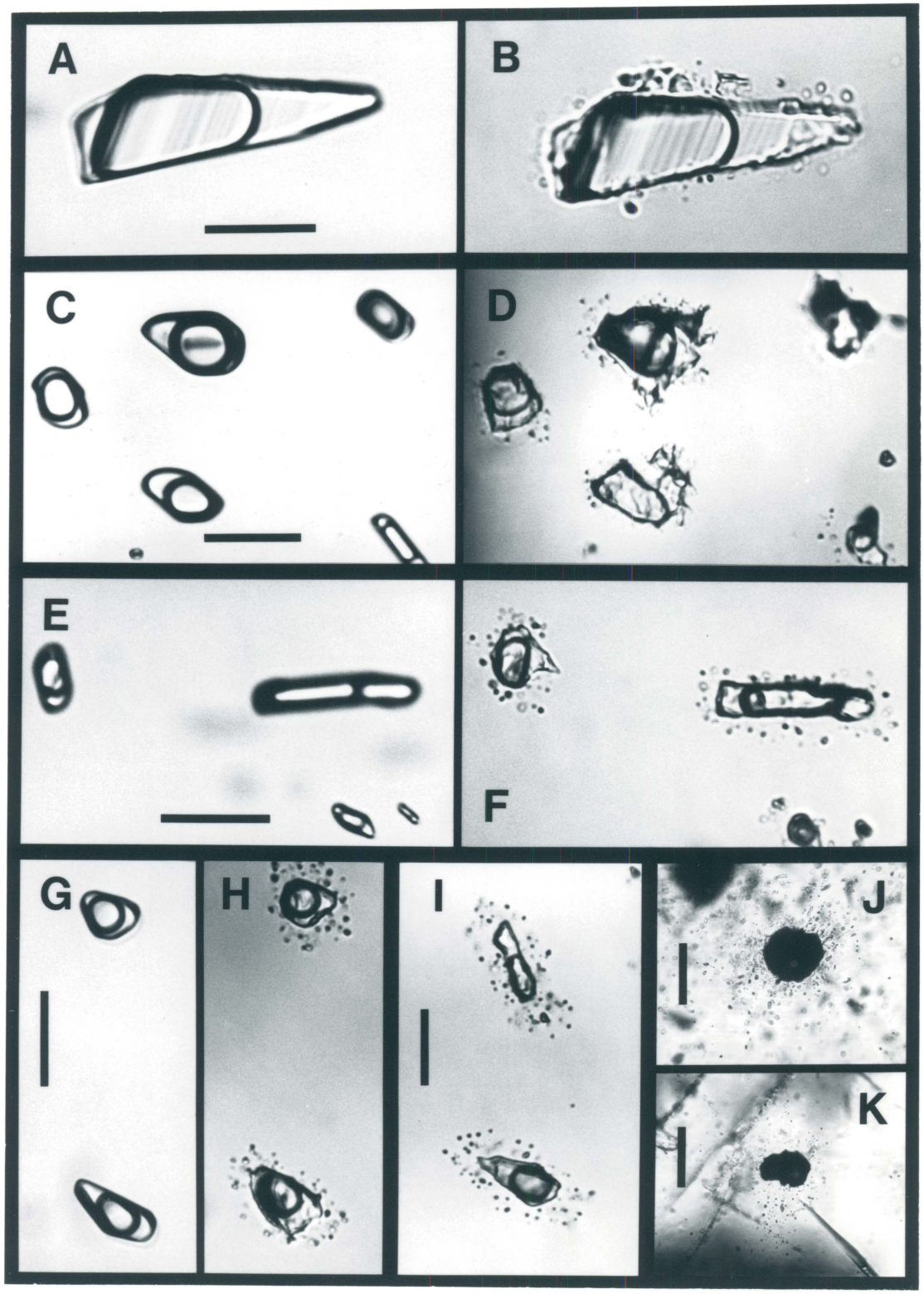
A
B
C
D
E
F
G
H
I
J
K

re-equilibrated at 700°C and 3 kbar for 7 days (Table 2.1) is shown in Fig. 2.8A. As seen in Table 2.1, pure H_2O inclusions in this sample showed no density change during the 7 day period. Figures 2.8 B and C show representative inclusions from sample R11, also re-equilibrated at 700°C and 3 kbar. The duration of this experiment was 52 days, at the end of which a slight density increase was detected in all inclusions measured but no pronounced morphologic changes were observed. Figures 2.8 D, E and F are from sample R8, re-equilibrated at 700°C and 4 kbar for 7 days. Inclusions within this sample are surrounded by a three-dimensional array of small (≤ 3 μm) secondary inclusions. The parent or original inclusions, located in the centers of these clusters show initial signs of closure: the walls of most of these parent inclusions typically contain a number of "re-entrants" and small inclusion-free micro-fractures oriented approximately 60° apart frequently emanate from the core. High-magnification microscopic observation of inclusions in this and other samples which have been cut open during sample preparation reveals that the opacity exhibited by these inclusions results from recrystallization of the inclusion walls producing a very irregular texture on the wall surface which disrupts transmitted light and so obscures the image of the fluid phases inside. For those inclusions where this effect is minimal, two phases (pure H_2O liquid and vapor) can be seen at room temperature.

Inclusions in Figs. 2.8 G,H and I are representative of those found in sample R7, re-equilibrated at 700°C and 5 kbar for 7 days. Inclusions in this sample display the same features as those in sample R8 (Figs. 2.8 D,E and F) except that, in general, the ratio of the volume of the secondary inclusion cluster to that of the parent inclusion is much larger.

Figures 2.8 J and K are from sample R6, re-equilibrated at 700°C and 6 kbar for 7 days. Pure-H_2O inclusions which could be measured in this sample showed the largest range in internal pressures at 700°C and therefore the largest range in densities of samples

R6-11 (See Fig. 2.4). Morphologically, inclusions in this sample also display the largest ratio of the volume of the secondary inclusion cluster to that of the parent inclusion. In fact, as seen in Figs. 2.8 J and K, in several of the clusters the parent inclusion has nearly or completely closed producing a simple, three-dimensional array of small ($\leq$ 3mm) secondary inclusions. An example of this is shown in the lower-central portion of Fig. 2.8 K. Here, there is no longer any trace of the original parent inclusion. All that remains is a roughly ellipsoidal, three-dimensional cluster of small inclusions which on a scale of 10's of microns bears no relationship to any two-dimensional fracture plane. The fact that these inclusions form a three-dimensional array is of paramount importance as it is this characteristic that we believe may serve to distinguish between those formed as a result of re-equilibration at $P_f < P_c$ and secondary inclusions formed along a fracture resulting from partial decrepitation of an inclusion due to excessive internal overpressure.

One can envision from Fig. 2.8 K that had the collapse of each parent inclusion proceeded to completion, what would remain would be a "sea" of small secondary inclusions which on a scale of 100's of microns would once again represent a planar feature. However, true "secondary" fluid inclusions in the normal sense of the word form by healing of fracture planes and the simultaneous trapping of fluid-filled voids. The center of these individual secondary inclusions will therefore more-or-less define a plane of symmetry coincident with the original fracture. Because of the three-dimensional nature of an individual cluster of inclusions formed by the present mechanism, no such plane of symmetry can be defined, although, on a larger scale, many clusters of these inclusions may still represent a planar feature.

The texture shown in Fig. 2.8 K, resulting from the overlap of many individual clusters, some with remnants of the original parent inclusion and some without, is very similar to inclusion arrays often found in regionally metamorphosed rocks. We suggest,

therefore, that the mechanisms and conditions described above might be responsible for the occurrence of these textures in natural systems. Furthermore, the criterion for distinguishing between dominantly isobaric cooling and dominantly isothermal uplift may rest in part on the presence or absence of these inclusion textures in a given natural system. For example, photomicrographs in Figs. 2.9 J and K show natural, hydrocarbon-bearing, fluid inclusions in quartz from the Tallulah Falls Dome (Oakes et al., 1987). The inclusion textures in these two photographs are remarkably similar to those observed in inclusions from this study re-equilibrated under conditions of internal underpressure ($P_f < P_c$; Figs. 2.8 and 2.9).

Microscopy and microthermometry on inclusions in samples R6-11 have produced a number of additional observations, the significance of which are not at present well understood. Adjacent pairs of photomicrographs in Fig. 2.9 A-H show fluid inclusions from sample R9 before (A, C, E and G) and after (B, D, F and H) re-equilibration at 700°C and 4 kbar for 2 days. Each photomicrograph of a given pair has been reproduced at the same magnification. It is immediately obvious that the total volume of the inclusion cluster exceeds the volume of the original parent inclusion. In other words, the outline of the original inclusion lies within the cluster. This is important because it shows how a group of relatively large inclusions originally spaced a few inclusion diameters apart can result in a "sea" of small inclusions -- again spaced approximately a few of their inclusion diameters apart. It is also apparent from Figs. 2.9 A-H that the original inclusions undergo rapid initial shape changes within 2 days, producing irregular shapes but rather equant overall dimensions. However, this process is not instantaneous even under the applied differential pressure here of approximately 2.8 kbar because similar inclusions re-equilibrated at 700°C and 4 kbar for 12 hours showed almost no change, and inclusions in Figs. 2.8 D-F (re-equilibration conditions: 700°C, 4 kbar, 7 days) have proceeded even

further, to a point where they are largely opaque.

Another observation regards the compositions of these inclusions. Freezing point depression measurements on inclusions within the cluster (including the parent inclusion) after re-equilibration indicated that they contained pure H_2O, even though they were re-equilibrated in the presence of a 20 wt. % NaCl solution. Although numerous inclusions were found in samples R6-11 which contained salinities up to and including 20 wt. % NaCl, saline inclusions were never surrounded by inclusion clusters nor were they obviously part of such a cluster.

Where possible, the densities of both inclusions in the cluster and the parent inclusion were determined microthermometrically. No systematic relationship was found between inclusion density and its position within the cluster. In other words, the densities of the parent inclusions appeared to be randomly distributed within the entire density range observed for a given sample.

One final observation regards the distribution of the small inclusions within the clusters. The outer-most inclusions within a given cluster frequently define a hexagonal-shaped euhedral perimeter. This is illustrated quite clearly in Fig. 2.9 I and to varying degrees in several of the other photomicrographs (Fig. 2.8 G,H and K for example). The reason for this phenomenon is not known, but it may be related to the quartz-structural control on the formation of the clusters.

RE-EQUILIBRATION OF NaCl-H_2O FLUID INCLUSIONS

While the previous experiments have shown that fluid inclusions may undergo dramatic density changes when subjected to large pressure differentials, many of these

inclusions have maintained their original, pure-H_2O fluid composition while experiencing severe deformation in the presence of a 20 wt. % NaCl solution. Thus, except for the possibility of H_2O diffusion, such inclusions have apparently remained compositionally closed systems throughout the re-equilibration process. This is an important concept because it suggests that fluid inclusions from regionally metamorphosed terranes may no longer be volumetrically representative of the fluids present at the time of their formation, but that the actual fluid compositions present at that time may still be preserved.

H_2O Diffusion

We have intentionally avoided discussing the mechanisms responsible for the density changes observed in inclusions in this study up to this point. It has been suggested by some workers that H_2O diffusion may contribute to density changes occurring during metamorphic re-equilibration of fluid inclusions in nature (Wilkins and Barkas, 1978; Roedder, 1981) and during laboratory-simulated metamorphic re-equilibration (Pecher and Boullier, 1984). To evaluate the role of H_2O diffusion in fluid inclusion re-equilibration, experiments were performed on fluid inclusions having initial compositions within the NaCl-H_2O system (Sterner and Bodnar, 1986). Fluid inclusions containing 10 and 42 wt. % NaCl solutions originally synthesized at 600°C and 3 kbar were re-equilibrated for 5 days at 600°C and 1 kbar (samples R12 and R13, respectively). The inclusions were hosted in quartz disks 4.5 mm in diameter and ~1 mm thick. Experiments were performed in opened capsules using a dry-argon pressure medium. Compositions of low-salinity inclusions in the first sample were determined from ice melting temperatures. Salinities of 14 inclusions yielded a consistent value of 10 wt. % NaCl both before and after re-equilibration. Average compositions of several

inclusions in the high-salinity sample estimated from halite dissolution temperatures before and after re-equilibration are 41.67 and 41.70 wt. % NaCl, respectively. Thus, in both cases inclusion compositions remained constant during re-equilibration within the limits of accuracy of the salinity determination (approximately ± 0.15 wt % NaCl for both samples). Although these observations do not preclude the possibility that some H_2O diffusion has occurred, they do place constraints on the the maximum amount of water lost. From the above discussion, the maximum possible salinity change which occurred in inclusions in either sample during re-equilibration is ~0.3 wt. % NaCl. This corresponds to a water loss of 0.33 wt. % H_2O in the low-salinity inclusions and 0.51 wt. % H_2O in the high-salinity inclusions. However, changes in bulk density occurring within these inclusions during the 5-day re-equilibration experiments were indicated by increases in their homogenization temperatures and were similar to those observed during the first part of this study.

To gain an appreciation for the amount of water that must diffuse out of an inclusion in order to cause density changes of the magnitudes of those observed in this study, Fig. 2.10 has been constructed using volumetric data for pure water. A pure-water fluid inclusion trapped at 600°C and 3 kbar will have a homogenization temperature of 310°C. If this inclusion is then re-equilibrated at 600°C and a lower confining pressure, its homogenization temperature will increase corresponding to a density decrease as described earlier. If the inclusion volume remains constant (i.e. the inclusion does not stretch) and density changes are only attributed to diffusional loss of water, Fig. 2.10 shows the amount of water that must be lost to account for changes in internal pressures corresponding to the indicated homogenization temperatures. Thus, a density decrease such that at 600°C the final internal pressure in the inclusion is 2 kbar requires a 15 % water loss; re-equilibration to a final internal pressure of 1 kbar would imply that nearly 30

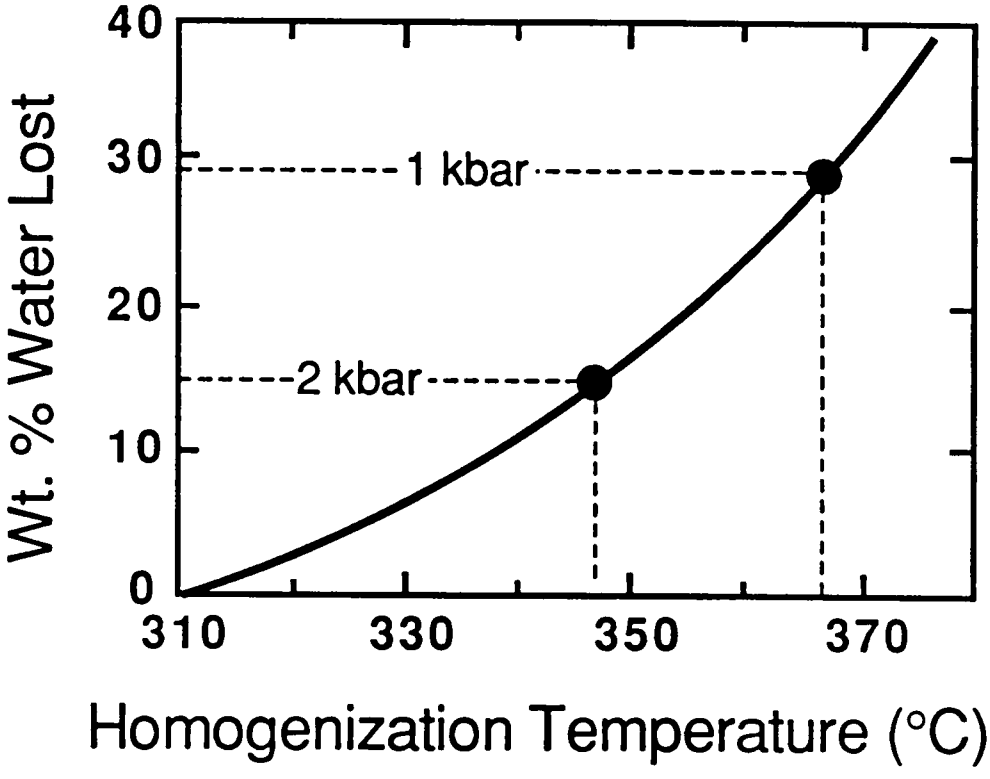

Figure 2.10 **Relationship between the percentage (wt. %) of water that must be lost from a pure-H_2O inclusion originally formed at 600°C and 3 kbar and which initially homogenizes to the liquid at 310°C in order to completely account for the indicated homogenization temperature increases by H_2O diffusion.** At 600°C, this inclusion must lose 15 % water to drop the internal pressure to 2 kbar and 29 % water for its internal pressure to drop to 1 kbar.

% of the water had diffused out.

Based on the estimated accuracy of our salinity determinations, the maximum amount of water lost through diffusion in the 10 and 42 wt. % NaCl inclusions during re-equilibration is less than ~0.5 wt. %. This quantity of water is considerably less than the amount required to produce the density changes observed in fluid inclusions in this study. We therefore conclude that density variations observed in inclusions in this study result from changes in the inclusion volumes without significant loss of contents by diffusion of H_2O. This conclusion is in complete agreement with the observations of Wilkins (1986) who reports negligible diffusion of H_2O from natural fluid inclusions in fluorite during 1 atm stretching experiments. Furthermore, this conclusion is valid for other studies of this type in which fluid inclusions have been re-equilibrated in the laboratory at similar temperatures over a time span of days or weeks. It should be noted, however, that these laboratory results do not preclude the possibility that over geologic time periods sufficient water could diffuse out of an inclusion to significantly change its density and bulk composition.

Re-Equilibration Across a One-Phase / Two-Phase Boundary

In the final re-equilibration experiment to be described in this study new inclusions were formed which contained fluids of decidedly different composition than the original inclusions - apparently without any exchange with the surrounding fluid via diffusion or leakage. Inclusions in sample R14 were originally synthesized from a 57 wt. % NaCl brine at 700°C and 2 kbar. These P-T conditions are well within the one-fluid phase field for a brine of this composition (Bodnar et al., 1985). The resulting inclusions contained three phases at room temperature; an NaCl-saturated brine, a vapor phase and a halite

daughter crystal. Measured halite dissolution temperatures in these inclusions were 481° ± 3°C (Sterner et al., 1988). The sample was then re-equilibrated at 850°C and 1 kbar for 35 days in an opened capsule using dry argon as the pressure medium. These P-T conditions are in the two-fluid phase field for a 57 wt. % NaCl brine. Subsequent microscopic observation and microthermometric measurements revealed the presence of two discrete types of fluid inclusions. Like the original inclusions, the first type of inclusion observed contained three phases at room temperature; an NaCl-saturated brine, a vapor phase and a halite daughter crystal. However, upon heating the sample to 600°C several of these inclusions still contained halite crystals indicating that their salinities were considerably greater than 57 wt. % NaCl. The second type of inclusion observed contained two phases at room temperature; liquid and a vapor bubble. Although no microthermometric measurements were performed on these inclusions, the absence of a halite crystal at room temperature indicated that their bulk salinities were considerably less than 57 wt. % NaCl. These two types of inclusions often occurred spatially isolated from each other with no obvious conduits or microfractures connecting them. Morphologically, inclusions of each type were equant and frequently nearly perfect negative crystals.

As discussed by Bodnar et al. (1985) the coexistence of these two types of inclusions in a given sample is consistent with their formation in the presence of immiscible low-salinity vapor and high-salinity liquid phases in the NaCl-H_2O system. Even though this sample was re-equilibrated in the presence of pure argon rather than a salt-water solution, fluid immiscibility remains the only reasonable explanation for the formation of the inclusions observed. Thus, at least some inclusions in this sample must have formed by initial microfracturing of an original 57 wt. % NaCl inclusion followed by phase separation during expansion into the enlarged cavity and then necking down into two or more distinct inclusions which have trapped different amounts of liquid and vapor.

The fluid inclusion re-equilibration scenario described above being complicated by the presence of a fluid phase boundary at high P and T may represent a rather exceptional case. Nevertheless, inclusions which constitute so-called "boiling pairs" frequently occur in natural systems and while their presence is easily verified by microscopic observation, their significance may not always be straightforward.

CONCLUSIONS AND GEOLOGIC IMPLICATIONS

The results of the present study suggest that fluid inclusions in metamorphic rocks will not preserve fluid densities representing the P-T conditions at the time of their formation if the trajectory of the P-T loop has deviated significantly either above or below the isochore corresponding to those conditions. In terranes where geologic evidence suggests rapid uplift resulting in near-isothermal decompression, fluid densities inferred from inclusion studies may be considerably less than those present at peak conditions. In laboratory simulated metamorphic re-equilibration experiments inclusions were found to maintain internal overpressures of 750-1500 bars for a period of one week regardless of the initial pressure differential. However, in a 52-day experiment some but not all inclusions were found to have totally re-equilibrated to the new P-T conditions. In terranes which have experienced near-isobaric cooling, inclusions formed at peak conditions may have experienced a density increase. Although no inclusions in the present study were found to have totally re-equilibrated to the final P-T conditions when $P_f < P_c$, several were found to have approached total re-equilibration to within 1 kbar. Note that this is in contrast to the results of Pecher (1981) who reports an observed density decrease in fluid inclusions re-equilibrated at confining pressures several kilobars

above their initial internal pressures. However, he states that the pressure conditions of his experiments may have been poorly constrained such that at the experimental conditions the inclusions may in fact have been under internal overpressure; based on evidence presented earlier in this paper, this appears to be the case.

The present work provides an upper limit on the maximum amount of volumetric dis-equilibrium a typical inclusion in quartz is likely to maintain through geologic time. The question of whether or not all these inclusions would experience total volumetric re-equilibration over geologic time is still unresolved. However, in this regard some insight may be gained from observations on natural systems. It is not uncommon to find inclusions in a single natural sample whose isochores do not intersect. Such inclusions are clearly out of equilibrium with respect to each other at any pressure and temperature. Similarly, the most stable morphology of a fluid inclusion is the negative crystal and while inclusions having this shape are a common occurrence in natural minerals, those with highly irregular morphologies are perhaps just as common. The intimate relationship between changes in density and shape has been demonstrated by Bodnar et al. (1988). Apparently, density changes do not occur without accompanying modifications in shape. It is therefore likely that the forces responsible for maintaining an irregular inclusion morphology through geologic time may also be responsible for preventing total volumetric re-equilibration.

Inclusions which had been re-equilibrated under conditions of internal overpressure, in general, showed no textural evidence of stretching even when a significant volume change had occurred. In experiments where inclusions were re-equilibrated toward higher densities ($P_f < P_c$), most original inclusions were surrounded by a three-dimensional halo of small (≤ 3 μm) secondary inclusions. This texture was found to be very characteristic of inclusions that had undergone shrinkage due to high confining pressure and it is

believed that this mechanism may be responsible for similar textures observed in natural systems.

During experimental re-equilibration under high confining pressures many inclusions were found to maintain their initial fluid compositions even though substantial changes had occurred in density and inclusion morphology. Thus, even under extreme differential pressures many inclusions remained compositionally closed systems during re-equilibration. This implies that although densities of inclusions may change dramatically during the metamorphic cycle, many may still contain fluids which are compositionally representative of those present at the time of trapping. This may also include inclusions formed well before peak metamorphic conditions if they have not been destroyed through reaction or recrystallization. Also, in these experiments, many new inclusions were formed which were compositionally and volumetrically representative of the fluids present during the re-equilibration part of the procedure. Finally, several inclusions were found which had compositions intermediate between the fluid in the original inclusions and the fluid present during re-equilibration. Thus, it appears to be possible to form inclusions that contain fluids of compositions that are not representative of those present during any stage in the sample's history.

In laboratory experiments H_2O diffusion was found to have a negligible effect on inclusion density and composition. During rapid re-equilibration the dominant mechanisms responsible for density change appear to be stretching or collapse. However, diffusion over geologic time may still be an important process in changing inclusion densities and compositions.

In re-equilibration experiments under one atmosphere confining pressures total decrepitation is a common phenomena. The tendency for inclusions to stretch rather than undergo total decrepitation in the present study is a result of the high confining pressure.

For a given differential pressure and relatively high confining pressure a finite volume increase in the inclusion will result in total re-equilibration. However, under a lower confining pressure the same volume increase will not result in total re-equilibration. For example, at 700°C the ΔV necessary to decrease the internal pressure of a pure H_2O fluid inclusion from 7 to 6 kbar is approximately 5% whereas that required for a decrease from 3 to 2 kbar is approximately 25%. Thus, as the confining pressure decreases, the ΔV required to produce the same 1 kbar internal pressure change increases rapidly. Any volume increase within an inclusion regardless of the mechanism must be taken up by host mineral. As ΔV increases, a greater volume of the surrounding crystal must be affected. Hence, the probability that the inclusion fluid will become opened to the surrounding fluid (total decrepitation) increases with increasing differential pressure and with decreasing confining pressure. This is consistent with the results of the present study in that the relative number of inclusions found to contain the 20 wt% NaCl solution (total decrepitation) after re-equilibration increased as the confining pressure of the experiment decreased (i.e., as ΔV increased).

REFERENCES

Binns, P.R. & Bodnar, R.J., 1986. Decrepitation behavior of fluid inclusions in quartz at one atmosphere confining pressure (abstr.). *Transactions, American Geophysical Union*, **67**, 399.

Bodnar, R.J.,1985. Pressure-Volume-Temperature-Composition (PVTX) properties of the system H_2O-NaCl at elevated temperatures and pressures. Unpub. Ph.D. Thesis, The Pennsylvania State University, University Park, PA, 183 pp.

Bodnar, R.J. & Bethke, P.M., 1984. Systematics of stretching of fluid inclusions I: Fluorite and sphalerite at 1 atmosphere confining pressure. *Economic Geology*, **79**, 141-161.

Bodnar, R.J., Binns, P.R., & Hall, D.L., 1988. Synthetic fluid inclusions. VI. Quantitative assessment of the decrepitation characteristics of fluid inclusions in quartz at one atmosphere confining pressure. *Journal of Metamorphic Geology*, **7**, 229-242.

Bodnar R.J., Burnham C.W., & Sterner S.M., 1985 Synthetic fluid inclusions in natural quartz. III. Determination of phase equilibrium properties in the system H_2O-NaCl to 1000°C and 1500 bars. *Geochim. Cosmochim. Acta* **49**, 1861-1873.

Bodnar, R.J. & Sterner S.M.,1987. Synthetic fluid inclusions. *in* Hydrothermal Experimental Techniques, H.L. Barnes and G.C. Ulmer, eds., Wiley and Sons, New York, 423-457.

Bohlen, S.R., 1987. P-T-time paths and the tectonic evolution of granulites (abstr.). *Metamorphic Studies Group Joint Meeting with IGCP Project 235, Evolution of Metamorphic Belts, Dublin, Ireland, 1987*, 2.

Burnham, C.W., Holloway, J.R., & Davis, N.F., 1969. Thermodynamic properties of water to 1000°C and 10,000 bar. *Geologic Society of America Special Paper* No. **132**, 96p.

Gratier, J.P. & Jenatton, L., 1984. Deformation by solution-deposition, and re-equilibration of fluid inclusions in crystals depending on temperature, internal pressure and stress. *Journal of Structural Geology*, **6**, 189-200.

Hensen, B.J., & Warren, R.G., 1987. The P-T evolution of the proterozoic Arunta Block, Central Australia (abstr.). *Metamorphic Studies Group Joint Meeting with IGCP Project 235, Evolution of Metamorphic Belts, Dublin, Ireland, 1987*, 10.

Hollister, L.S., 1979. Metamorphism and crustal displacements: new insights. *Episodes*, 1979, 3-7.

Hollister, L.S., Burruss, R.C., Henry, D.L., & Hendel, E.M., 1979. Physical conditions during uplift of metamorphic terranes, as recorded by fluid inclusions. *Bulletin de Mineralogie*, **102**, 555-561.

Keenen, J.H., Keyes, F.G., Hill, P.G., & Moore, J.G., 1978. Thermodynamic properties of water, including vapor, liquid, and solid phases (S.I. Units). John Wiley and Sons, New York, 156p.

Khaibullin, I.Kh. & Borisov, N.M., 1966. Experimental investigation of the thermal properties of aqueous and vapor solutions of sodium and potassium chloride at phase equilibrium. *High Temperature*, **4**, 489-494.

Oakes, C.S., Bodnar, R.J., Cole, D., & Wesolowski, D., 1987. Methane-bearing fluid inclusions from the Tallulah Falls Dome, NE Georgia: Implications for an unconventional methane resource in the southern Appalachians (abstr.). *Geologic Society of America Abstracts with Programs*, **19**, 791.

Passchier, C.W., 1984. Fluid inclusions associated with the generation of psuedotachylyte and ultramylonite in the French Pyrenees. *Bulletin de Mineralogie*, **107**, 307-315. [in French]

Pecher, A., 1981. Experimental decrepitation and re-equilibration of fluid inclusions in synthetic quartz. *Tectonophysics*, **78**, 567-583.

Pecher, A. & Boullier, A., 1984. Evolution a pression et temperature elevees d'inclusions fluides dans un quartz synthetic. *Bulletin de Mineralogie*, **107**, 139-153. [in French]

Potter, R.W., II & Brown, D.L., 1977. The volumetric properties of aqueous sodium chloride solutions from 0° to 500°C at pressures up to 2000 bars based on a regression of available data in the literature. *United States Geological Survey Bulletin*, **1421-C**, 36 p.

Roedder, E., 1981. Problems in the use of fluid inclusions to investigate fluid-rock interactions in igneous and metamorphic processes. *Forschrift de Mineralogie*, **59**, 267-302.

Roedder, E., 1984. *Fluid Inclusions*. Mineralogical Society of America, Reviews in Mineralogy **12**, 644 p.

Rowan, L.P., Bethke, P.M., & Bodnar, R.J., 1983. Stretching of fluid inclusions in fluorite at confining pressures up to one kilobar (abstr.). *Geologic Society of America Abstracts with Programs*, **15**, 674.

Santosh, M., 1985. Fluid evolution characteristics and piezothermic array of south Indian charnockites. *Geology*, 13, 361-363.

Sterner, S.M., & Bodnar, R. J., 1984 Synthetic fluid inclusions in natural quartz. I. Compositional types synthesized and applications to experimental geochemistry. *Geochim. Cosmochim. Acta* **48**, 2659-2668.

Sterner, S. M. & Bodnar, R. J.,1986. Re-equilibration of fluid inclusions in quartz at elevated temperatures and pressures: The role of H_2O diffusion [abstr.]. *Transactions, American Geophysical Union*, **67** (16), 407.

Sterner, S.M., Hall, D.L., & Bodnar, R. J., 1988 Synthetic fluid inclusions. V. Solubility relations in the system NaCl-KCl-H_2O under vapor saturated conditions. *Geochim. Cosmochim. Acta* **52**, 989-1005.

Ulrich, M.R., & Bodnar, R.J., 1987. Systematics of stretching of fluid inclusions II: Barite at 1 atm confining pressure. *Economic Geology,* **83**, 1037-1046.

Wilkins, R.W.T., 1986. The mechanisms of stretching and leaking of fluid inclusions in fluorite. *Economic Geology*, 81, 1003-1008.

Wilkins, R.W.T., & Barkas, J.P., 1978. Fluid inclusions, deformation and recrystallization in granite tectonites. *Contributions to Mineralogy and Petrology*, 65, 293-299.

Chapter 3: The System CO_2-H_2O: Experimental Determination of Pressure-Volume-Temperature-Composition Properties from 2 to 6 kbar and 400° to 700°C

ABSTRACT

Pressure-volume-temperature-composition (PVTX) relations in the CO_2-H_2O system have been experimentally determined from 2 to 6 kbar and 400° to 700°C for fluid compositions between 12.5 and 87.5 mole % CO_2 using the synthetic fluid inclusion technique. The method involves trapping CO_2-H_2O fluids of known composition as inclusions in quartz at elevated pressures and temperatures (P_F and T_F) and then calculating the desired fluid properties using microthermometric data combined with available PVTX data for this system at low pressures and temperatures.

Densities and compositions of both the CO_2- and H_2O-rich phases coexisting in the inclusions at the CO_2 liquid/vapor homogenization temperature (Th (CO_2)) were determined from available data; the bulk densities of inclusions were then calculated using

mass balance considerations involving these individual density values and the known bulk fluid composition. Densities of the fluid trapped at P_F and T_F were calculated from inclusion bulk densities determined at Th (CO_2) (i.e. at conditions $\leq$31.0°C and $\leq$74 bars) by correcting for the change in the volume of the inclusion cavity between the two sets of P-T conditions resulting from thermal expansion and compressibility of quartz. Mean molar volumes (MMVs) of CO_2-H_2O mixtures (calculated from densities of fluid inclusions) together with volumetric data for H_2O and CO_2 from the literature were used to derive an empirical volume-explicit function of pressure, temperature and fluid composition. This equation, which incorporates the equation of Haar et al. (1984) for H_2O, predicts MMVs for all CO_2-H_2O compositions to better than ±2 % over the range 2-6 kbar, 400°-700°C.

Over the 2 to 6 kbar and 400° to 700°C range, CO_2-H_2O mixtures display very limited departures from ideality with maximum positive excess volumes of mixing (V^{EX}) of 1.6 cm^3/mole (4.4 %) at 6 kbars, 700°C and X_{CO2}=0.6. At constant temperature, V^{EX} increases with increased pressure. Over all pressures and temperatures studied the maximum V^{EX} occurs between $0.4 \leq X_{CO2} \leq 0.6$; at high pressures, the maximum shifts toward more CO_2-rich values as temperature increases, while at low pressures no trend is apparent. Between 3 and 5 kbars, at constant pressure, V^E decreases with increased temperature and becomes slightly negative for low CO_2 concentrations ($\leq$ ~25 mole % CO_2) at 600° and 700°C. At 6 kbar, however, V^{EX} remains relatively constant at about 4% over the complete temperature range studied.

Isochores derived from synthetic inclusions in the present study are predicted by several published equations of state to within ±300 to 400 bars on the average. At low pressures the available equations tend to predict higher pressures than the present study for water-rich compositions, while for more CO_2-rich compositions (X_{CO2} = 0.5 - 0.75),

discrepancies of ~0.5 kbar occur at moderate to high pressures where these equations all tend to underestimate the non-ideal behavior of the mixture (predict pressures that are lower than observed). The largest differences exibited between the various equations are found for H2O-rich compositions at high pressures, and low temperatures. In this region calculated pressures span a range of nearly 800 bars with those calculated in the present study being consistently the highest values.

PTX properties of CO_2-H_2O mixtures were determined from the total homogenization temperatures (Th (total)) of fluid inclusions trapped in the one-fluid phase field. MMVs of the inclusions at Th (total) were calculated from the MMVs at P_F and T_F using equations from Hosieni et al. (1985) to correct for the change in the volume of the inclusion cavity between P_F and T_F and that at Th (total). Internal pressures of the inclusions at Th (total) were then calculated using the equation of state of Connolly and Bodnar (1983). The pressure and temperature of total homogenization of each inclusion defines a point on the solvus unique to that particular bulk fluid composition and density. Thus, the array of many such points determined in this manner delineates the boundary between the one-phase and two-phase fields over a portion of PTX-space

Phase relations in the CO_2-H_2O system between ~500 and ~3000 bars determined in this study were found to be in close agreement with the experimental determination of Todheide and Franck (1963). Somewhat higher temperatures (~15° - 20°C) were recorded for CO_2-poor (X_{CO2}=0.125) and CO_2-rich (X_{CO2}=0.75) compositions compared with their determination while considerably smaller (generally less than 5°C) discrepancies are found for intermediate compositions. Compared with the experimental data of Takenouchi and Kennedy (1964), our study indicates considerably higher solvus temperatures for CO_2-rich compositions with maximum disagreement at about 1500 bars (eg. ~75° for X_{CO2}=0.625 and ~100° for X_{CO2}=0.75). According to our data, the thermal minimum

on the CO_2-H_2O solvus occurs at approximately 2000 bars and X_{CO2}=0.37 and at a temperature of 269°C. This temperature is ~3° and 4°C higher than the above studies, respectively.

A list of symbols used throughout this chapter is given in Table 3.1.

INTRODUCTION

The CO_2-H_2O system has long been recognized as one of the most geologically important fluid systems. Fluids with compositions and therefore physical and thermodynamic properties that can be approximated by this binary system are found in a wide variety of geologic terranes including medium and high grade metamorphic environments, epithermal and lode-type gold deposits and several geothermal systems (Roedder, 1984).

In spite of the relative importance of this fluid system, presently available experimental data are inadequate to describe fluid behavior in the CO_2-H_2O binary over a wide range of crustal conditions. Available sources of pressure-volume-temperature (PVT) data on this system and its subsystems include the experimental volumetric determination of pure H_2O by Burnham et al. (1969) providing data to nearly 9 kbar and 900°C. Volumetric data for pure CO_2 at high pressures and temperatures are given by Shmonov and Shmulovich (1975; to 8 kbar and ~700°C), Juza et al. (1965; to 4 kbar and 475°C) and Kennedy (1954; to 1.4 kbar and ~1000°C) whereas densities along the two-phase liquid-vapor curve were determined by Lowry and Erickson (1927).

Volumetric properties at pressures ≤ 2 kbar and phase relationships of CO_2-H_2O binary fluids are available from Greenwood (1969), Khitarov and Malinin (1956), Malinin

TABLE 3.1 List of Symbols.

Symbol		Description
P	=	pressure (bar, kbar or MPa as indicated)
V	=	molar volume (cm^3/mole)
T	=	temperature (Celsius or Kelvin as indicated)
X, X_{CO2}	=	mole fraction CO_2
X_{H2O}	=	mole fraction H_2O
P_F	=	formation pressure of fluid inclusion
V_F	=	formation mean molar volume of fluid inclusion
T_F	=	formation temperature of fluid inclusion
P_S	=	solvus pressure of fluid inclusion
V_S	=	solvus mean molar volume of fluid inclusion
T_S	=	solvus temperature of fluid inclusion
P_C	=	critical pressure
T_C	=	critical temperature
Th (CO_2)	=	CO_2 homogenization temperature
Th (total)	=	total homogenization temperature
V^{sp}	=	specific volume of bulk CO_2-H_2O mixture at Th (CO_2) (cm^3/g)
V^{sp}_{aq}	=	specific volume of aqueous phase at Th (CO_2) (cm^3/g)
V^{sp}_{cb}	=	specific volume of carbonic phase at Th (CO_2) (cm^3/g)
F_{aq}	=	mass fraction of aqueous phase in inclusion at Th (CO_2)
F_{cb}	=	mass fraction of carbonic phase in inclusion at Th (CO_2)
F_{H2O}	=	mass fraction of H_2O in inclusion
F_{CO2aq}	=	mass fraction of the bulk fluid that is CO_2 dissolved in water
MW_{H2O}	=	molecular weight of H_2O = 18.0152 g/mole
MW_{CO2}	=	molecular weight of CO_2 = 44.0098 g/mole
M	=	mean molar mass (g/mole)
MMV	=	mean molar volume of CO_2-H_2O mixture (cm^3/mole)
V^{EX}	=	excess molar volume of CO_2-H_2O mixture (cm^3/mole)
V^{ID}	=	ideal molar volume of CO_2-H_2O mixture (cm^3/mole)
V_{H2O}	=	partial molar volume of H_2O in CO_2-H_2O mixture (cm^3/mole)

TABLE 3.1 *Cont'd.* List of Symbols.

Symbol		Description
V_{CO2}	=	partial molar volume of CO_2 in CO_2-H_2O mixture (cm^3/mole)
$V_{CO2\text{-}H2O}$	=	mean molar volume of CO_2-H_2O mixture from Eqn. 3.20
V_{H2O}	=	molar volume of H_2O
V_R	=	mean molar volume of CO_2-H_2O mixture that is in excess of V_{H2O} at the same P and T
V_Δ	=	volume change factor
V_{25}	=	mean molar volume of bulk fluid at Th (CO_2)
ΔV	=	volume change of reaction
l	=	liquid phase
v	=	vapor phase
Yld	=	calculated percent yield of CO_2 from silver oxalate
S_{CO2}	=	solubility of CO_2 in $gCO_2/100gH_2O$ in the aqueous phase
ρ_{aq}	=	density of the aqueous phase below 31°C
ρ_{CO2}	=	density of CO_2 along the liquid/vapor curve
Ψ	=	modified CO_2 homogenization temperature = 31.0-Th (CO_2)
α	=	alpha-quartz phase
β	=	beta-quartz phase
V_α, V_β	=	molar volume of alpha or beta quartz (cm^3/mole)
$T_{\alpha/\beta}$	=	temperature of the quartz lambda transition
ϕ	=	modified lambda temperature = $T_{\alpha/\beta}$ - T(°K)
σ	=	standard deviation
σV_P	=	contribution to the error in V_F from uncertainty in P_F
σV_T	=	contribution to the error in V_F from uncertainty in T_F
σV_X	=	contribution to the error in V_F from uncertainty in composition
σV_F	=	uncertainty in parameter: V_F
σ_P	=	uncertainty in parameter: P_F
σ_T	=	uncertainty in parameter: T_F
σ_{Yld}	=	uncertainty in yield of CO_2 from silver oxalate decomposition
σ_{H2O}, σ_{AgOx}	=	weighing errors for H_2O and silver oxalate

(1959, 1974), Zakirov (1984) and Franck and Todheide (1959). Densities for a limited number of binary compositions at 400° and 500°C and pressures up to 5 kbar have been determined by Shmulovich et al. (1980). The pressure-temperature-composition (PTX) topology of the CO_2-H_2O solvus has been determined by Todheide and Franck (1963) and Takenouchi and Kennedy (1964) to 3.5 and 3.0 kbar, respectively. Considerable disagreement is found between these two studies for CO_2-rich compositions.

Empirical and semi-theoretical equations available for predicting phase relations and volumetric properties in the CO_2 and H_2O unary systems include those by Keenan et al. (1978) and and Haar et al. (1984) for water and the equations of Altunin and Gadetskii (1971) and Bottinga and Richet (1981) for carbon dioxide. The equations of state of Holloway (1981), Kerrick and Jacobs (1981), Bowers and Helgeson (1983) and Connolly and Bodnar (1983) predict volumetric properties of CO_2-H_2O mixtures.

The data of Shmulovich et al. (1980) represent the only published volumetric determinations available for CO_2-H_2O at high P and T (above 2 kbar). The scarcity of data is largely due to the experimental difficulties encountered in pressure-volume-temperature-composition (PVTX) determinations of multicomponent systems at high P and T using conventional techniques. In the present study we have determined the PVTX relations in the CO_2-H_2O system from 2 to 6 kbar and 400° to 700°C for fluid compositions between 12.5 and 87.5 mole % CO_2 using the synthetic fluid inclusion technique (Sterner and Bodnar, 1984; Bodnar and Sterner, 1987). These data, together with additional data from the above sources have been used to generate an empirical volume-explicit function of pressure, temperature and fluid composition that predicts mean molar volumes (MMVs) for all CO_2-H_2O compositions over the range 2 to 6 kbar and 400° to 700°C. This algorithm incorporates the equation of Haar et al. (1984) for H_2O. A detailed comparison of the volumetric properties of CO_2-H_2O mixtures determined in the

present study with other available sources is presented.

Empirical delineation of the solvus over a portion of PTX space in the CO_2-H_2O system was accomplished using measured total homogenization temperatures (Th (total)) of synthetic fluid inclusions and the equation of state of Connolly and Bodnar (1983) to calculate their internal pressures at Th (total). The pressure and temperature of total homogenization of each inclusion defines a point on the solvus unique to that particular bulk fluid composition and density, and thus, the array of many such points determined in this manner serves to delineate the boundary between the one-phase and two-phase fields over a portion of PTX-space. PTX relations of the CO_2-H_2O solvus determined in this study are compared with other determinations from the literature.

EXPERIMENTAL PROCEDURE

Volumetric properties in the CO_2-H_2O system were determined using a modified version of the synthetic fluid inclusion technique described by Sterner and Bodnar (1984) and Bodnar and Sterner (1987). In brief, the technique involves trapping a fluid of known composition at a known (high) pressure and temperature (P_F,T_F). The density or MMV of this fluid sample is then determined at another (lower) pressure and temperature and related back to the density at P_F,T_F by correcting for the slight change in volume of the inclusion cavity between these two different sets of P-T conditions.

Fluid inclusions were synthesized in the presence of CO_2-H_2O solutions of known composition by healing fractures in natural Brazilian quartz at pre-determined temperatures and pressures within the one-fluid phase field. The CO_2 liquid-vapor homogenization temperatures (Th (CO_2)) of individual inclusions were then measured using a microscope

equipped with a heating/freezing stage. Densities and compositions of both the CO_2- and H_2O-rich phases at Th (CO_2) were determined from available PVTX data at the temperature of CO_2 homogenization and the bulk densities of inclusions were then calculated using mass balance relations. Inclusion bulk densities determined at Th (CO_2) ($\leq$31.0°C) were related to the density of the fluid at P_F and T_F by correcting for the change in the volume of the inclusion cavity due to thermal expansion and compressibility of quartz. Mean molar volumes (MMVs) (calculated from densities and compositions) were expressed as a function of pressure, temperature and fluid composition using statistical regression methods. A full account of the density calculation procedure is provided in a later section.

Whenever possible, the total homogenization temperatures (Th (total)) of several inclusions within a given sample were determined and the MMV of the inclusion fluid at Th (total) was calculated. (The measurement of (Th (total)), in general, required greater optical clarity than that necessary to measure Th (CO_2). This is because in measuring Th (CO_2), observations are restricted to the CO_2 phase (i.e. away from the inclusion walls), whereas total homogenization can occur anywhere inside the inclusion and is frequently masked by internal reflection). The internal pressure of the inclusion at Th (total) was calculated from the known bulk composition, Th (total) and the MMV at Th (total) by iteration using the Connolly and Bodnar (1983) equation. The complete array of individual P-T-X coordinates determined in this manner was used to delineate the solvus over a portion of PTX-space. Further details of the procedure for calculating solvus coordinates using synthetic fluid inclusions will be presented in a later section.

Fluid Inclusion Synthesis

A detailed description of the procedure for synthesizing fluid inclusions is given by Bodnar and Sterner (1987) and will only be summarized here along with the modifications to the technique required in this study. Quartz cylinders ~4.5 mm in diameter and ~10 mm in length were cut from a large, single crystal of Brazilian quartz using a diamond coring drill. The cores were heated in an oven to 310°C and fractured by quenching in distilled water at room temperature. After drying, the fractured quartz cylinders and amounts of silver oxalate ($Ag_2C_2O_4$) and H_2O required to produce the desired fluid composition at the experimental conditions were loaded into 18 mm long platinum capsules and sealed with an arc welder. Silver oxalate was used exclusively in this study to generate CO_2. Oxalic acid was not used because it was demonstrated (Sterner, unpub. data) that without taking special, non-routine precautions the use of this compound frequently resulted in the generation of inclusions which contained components other than the desired CO_2 and H_2O.

Distilled, deionized water was used in all experiments. The silver oxalate used to generate CO_2 was prepared by mixing saturated, room temperature solutions of reagent grade oxalic acid and silver nitrate, filtering the white precipitate, rinsing several times with distilled, deionized H_2O and drying/storing in a vacuum desiccator (pers. comm. I-Ming Chou). The yield of expandable gas (CO_2) was determined nine times by decomposing known amounts of silver oxalate in sealed capsules and measuring weight loss on puncturing. The average yield of CO_2 from the silver oxalate was 98.47% of that calculated assuming ideal stoichiometry and the standard deviation of the nine trials was 0.37%. These two values were used in computing the actual fluid compositions and associated errors in each experiment.

Two capsules were then loaded into a cold-seal pressure vessel which was in turn placed in a horizontally oriented, pre-heated furnace. Filler rods were used inside each pressure vessel to reduce thermal gradients (Boettcher and Kerrick; 1971). At the start of each experiment, the vessels were pressurized to ~500 bars. This pressure was maintained until the silver oxalate decomposed (200°-250°C) at which time the pressure was raised to ~1 kbar. If the vessels were pressurized beyond ~1 kbar prior to the decomposition of silver oxalate to produce CO_2, the capsules often developed tears and began to leak as the platinum deformed around the quartz. Thus, this pressurization procedure was adopted to minimize the strain on the capsules before sufficient CO_2 was produced to support the capsule walls. The approach was found to be far superior to pre-heating the capsules to decompose the silver oxalate before loading them into the bombs.

When the temperature reached ~300° to 350°C the pressure was increased to approximately 250 bars above the final desired pressure and maintained at that value until the temperature stabilized to ±1°C of desired value. This generally required about 20-30 minuits. After 5 to 10 days the pressure vessels were removed from the furnaces and allowed to air cool. The capsules were then removed from the pressure vessels and opened and the quartz cylinders were cut into 1 mm thick disks and polished on both sides.

The above procedure was found to result in the production of a large, homogeneous population of volumetrically and compositionally equivalent fluid inclusions within a given sample at formation temperatures ≤ 600°C. At higher temperatures, this procedure required special modifications to insure the formation of homogeneous populations of inclusions. In all 700°C experiments, the capsules were loaded, placed in bombs and brought to the desired P-T conditions as before except that the cores were not

pre-fractured and a filler rod only 7 cm long was used (the overall length of the pressure vessel, excluding the closure nut was 30 cm). During loading of the bomb care was taken to insure that the capsules and the filler rods were inserted all the way to the hot end of the bomb. Several hours after the temperature had completely stabilized (i.e. the following day) the pressure was dropped to 2 kbar and the cores were fractured in-situ by rotating the entire bomb-furnace assembly as a unit so that the capsules and filler rod would fall toward the cold end of the bomb. The assembly was then immediately rotated through 180° to allow the capsules and filler rod to return to their original positions (that the capsules and filler rod had returned to the hot end of the vessel was evident when the vessels were opened at the end of the experiment). Finally, the unit was rotated back to a horizontal position where it remained until the end of the run and the pressure was restored to the desired value. The motion of the material within the bomb was audible and entire process required less than 10 seconds. When the temperature was controlled from a furnace thermocouple (as opposed to a bomb thermocouple) the procedure created a minor (±10°C) and short-lived (~4 min.) temperature perturbation which seemed to have little or no adverse affects on the homogeneity of the population of inclusions. There are two important reasons for lowering the pressure to 2 kbar prior to fracturing the cores. First, it makes the procedure a bit safer, and second, the fracture density and therefore the number of inclusions produced using this technique decreases with increasing pressure. To compensate for the rapid expansion of fluid during this operation the pressure vessel was opened to the common line (the pressure line through which the pump, an approximately 1 liter ballast tank and all pressure vessels are interconnected). If the pressure vessel is closed off, the pressure can instantaneously rise by *several* kbar.

Temperatures were monitored 4-5 times daily at random intervals using Inconel-sheathed, ungrounded, K-type thermocouples mounted externally in 18 mm deep

wells drilled in the end of the hydrothermal bombs in conjunction with a factory-calibrated, Thermoelectric digital temperature display. At the start of the study, all thermocouples were tested for internal consistancy at 400° and 700°C by placing them together in a single furnace. The maximum variation at these two temperatures of thermocouples used in this study was in all cases less than 1.2°C. Taking into account small uncertainties in absolute temperarture arising from the use of external thermocouples and the existence of a small temperature gradient within the "hot zone" in the bombs, we estimate the accuracy of our temperature measurements at ± 0.5 % relative or ±2.0°C at 400°C and ±3.5°C at 700°C.

Pressure was monitored using factory-calibrated Heise gauges (0-5 kbar and 0-7 kbar range) with an estimated accuracy of ± 0.5 % of the total pressure.

Systematics of Fluid Inclusions in the CO_2-H_2O System

All fluid inclusions synthesized in this study contain compositions in the CO_2-H_2O system and were formed at pressures and temperatures within the one-fluid phase field. This condition has resulted in the formation of a homogeneous population of volumetrically and compositionally equivalent fluid inclusions within each sample. Before describing the interpretation of the data a brief review of the observable phase transitions pertinent to the present determination is warranted. For further discussion of phase transitions in CO_2-H_2O inclusions, including the effect of additional components see Burruss (1981).

The behavior of inclusions in this system is best illustrated by considering them as they cool from their formation temperature within the one-fluid phase field. The fluid in an inclusion that has trapped a one-phase, homogeneous mixture of H_2O and CO_2 at

elevated P and T will, upon cooling to some lower temperature, spontaneously separate into an H_2O-rich liquid and a CO_2-rich vapor phase. Initially, each phase can have substantial quantities of the minor component dissolved in it but as cooling progresses, the composition of each approaches that of the pure endmember component. Further cooling to some temperature below 31.0°C (the critical point of pure carbon dioxide; Lowry and Erickson, 1927) will result in the separation of the CO_2-rich phase into a liquid and a vapor. At such low temperatures these two phases are essentially pure CO_2. The aqueous phase may still, however, contain several wt. % CO_2 (Dodds et al.; 1956) - its composition being dependent on temperature and the total CO_2 pressure. It is at the temperature of initial CO_2 liquid-vapor phase separation (actually, the CO_2 liquid-vapor homogenization temperature Th (CO_2) measured during heating) that the bulk fluid density calculation is performed. At this temperature, the specific volume and compositions of both the CO_2 and aqueous phases may be determined.

The final important phase transition is the formation of a CO_2 clathrate ($CO_2 \cdot 5.75H_2O$) at low temperature. In the pure binary system if both liquid and vapor CO_2 are present along with an aqueous phase, clathrate is part of the stable assemblage at all temperatures below 10.0°C (Burruss, 1981). However, during slow cooling and for a broad range of bulk compositions and densities this clathrate phase will remain metastably absent down to a temperature of approximately -20°C at which point it will spontaneously and unavoidably nucleate. If CO_2 liquid-vapor phase separation occurs below this temperature during slow cooling then the CO_2 liquid-vapor homogenization temperature cannot be measured in the absence of the clathrate. Such a homogenization measurement is of little use in determining the inclusion bulk density because the clathrate formation reaction does not proceed to completion as evidenced by non-reproducible Th (CO_2)s. The presence of the clathrate phase can increase the temperature of CO_2 liquid-vapor

homogenization to the liquid by several degrees owing to the negative ΔV of the reaction $CO_2 + 5.75H_2O = CO_2 \cdot 5.75H_2O$. The important point is that on slow cooling, nucleation of the clathrate generally requires about 30°C of undercooling and thus, until that temperature is reached inclusion bulk density determinations are possible from Th (CO_2) measurements. All Th (CO_2) measurements reported in Appendix I from which MMVs were derived were collected in the absence of the clathrate phase.

Microthermometry

Temperatures of the various phase transitions observed within the inclusions were determined using a Leitz petrographic microscope equipped with a Fluid Inc.-adapted USGS-type gas flow heating/freezing stage (Werre et al., 1979). The E-type thermocouple used in the stage was calibrated at -56.6°, 0.0°, and 374.1°C using synthetic fluid inclusions having compositions of (1) 1:1 mole ratio CO_2: H_2O (CO_2 melting at -56.6°C), (2) pure H_2O (ice melting at 0.0°C), and (3) pure H_2O having the critical density (liquid-vapor homogenization by fading of the meniscus at 374.1°C). Thermal gradients within synthetic fluid inclusion samples at -56.6° and 0.0°C were less than 0.1°C across the 4.5 mm samples (Sterner, unpublished data). At 374.1°C the observed range in homogenization temperatures was less than 5°C. The accuracy of the microthermometric measurements is therefore estimated at ± 0.1°C for temperatures between -20° and +31°C corresponding to the measurement of Th (CO_2), and ± 2.5°C for temperatures between 200° and 350°C - corresponding to the observed range in Th (total). Reproducibility is in all cases within the estimated accuracy of the temperature determination.

The presence of a white, birefringent solid phase was noted in a few inclusions in some samples formed from CO_2-rich compositions at or above 600°C. The identity and

origin of this phase is unknown and no measurements were used from inclusions containing the phase. When present it appeared to represent only a small volumetric contribution to the bulk fluid in the experiment and the measured phase transition temperatures of inclusions not containing the phase from these samples yielded reasonable MMVs and solvus conditions.

Aside from the occasional presence of the unidentified white solid phase, no other impurities were detected and, in fact, their absence was frequently implied by microthermometry. The melting point of pure CO_2 is -56.6°C (Burruss, 1981), but the presence of other gases such as CH_4 and N_2 depresses the melting point from that of the pure compound. Repeated measurement of the temperature of this phase transition in several samples routinely yielded -56.6 ± 0.1°C, implying negligible quantities of other gases. While this may seem like circular logic because the stage was initially calibrated using the melting point of CO_2 in synthetic inclusions, it should be added that this calibration technique has been corroborated by checks at -21.2°C using the eutectic melting temperature of NaCl-H_2O solutions in synthetic inclusions.

An additional check on the purity of the CO_2-H_2O fluids was provided by measuring the final melting point of the $CO_2 \cdot 5.75H_2O$ clathrate phase which occurs at +10.0°C in the presence of aqueous liquid, and liquid and vapor CO_2. The presence of small amounts of dissolved salts depresses this temperature measurably while the presence of gases other than CO_2 will generally elevate the final melting point. Repeated measurements of this phase transition yielded 10.0 ±0.1°C again attesting to the purity of the binary fluids.

Implicit in the synthetic fluid inclusion approach to PVTX studies of fluids at elevated pressures and temperatures is that the effect of dissolved silica on the fluid properties being measured is negligible. This assumption has been addressed by Bodnar

et al. (1985) as it applies to salt-water systems. In the present application (CO_2-H_2O fluids) we also assert that dissolved silica can be ignored. This assumption is supported by determinations of the molar volume of H_2O at high P and T described in a later section.

The majority of inclusions studied displayed CO_2 homogenization to the liquid while relatively few were found to homogenize to the vapor phase (see Appendix I). Measurements of phase transitions where partial homogenization occurs to the vapor phase give erroneously low temperatures and large ranges believed to result from the observer's inability to see the last bit of liquid evaporate (see discussion in Bodnar et al.; 1985). Thus, in the measurement of Th (CO_2), even after liquid CO_2 becomes invisible to the observer, a thin rim remains between the CO_2 vapor-water interface which apparently can persist a few degrees before true CO_2 liquid-vapor homogenization actually occurs. The inclusion geometry becomes important in determining when the CO_2 liquid disappears from sight although this obviously can have no bearing on the true value of Th (CO_2). This phenomena has been discussed many times in the literature (e.g., Roedder, 1984 p.256; Bodnar, 1985) and it has been tacitly assumed that those inclusions for which the liquid disappears into a narrow corner yield the most accurate measurements of homogenization to the vapor. While this is often the case, even under the best circumstances observed Th (CO_2)'s for homogenization to the vapor are frequently a few degrees too low. These assertions regarding errors in the measurement of Th (CO_2) to the vapor are confirmed by calculation of MMVs using these values and then comparing them with our best estimates of the appropriate MMVs. In each case the calculated MMVs are too large. A similar phenomenon occurs in the measurement of Th (total) generally resulting in the underestimate of this measurement for those inclusions displaying total homogenization to the vapor (CO_2-rich) phase. The consequences of this will be discussed in a later section.

CALCULATION PROCEDURE (MMVs)

Mean molar volumes (MMVs) of CO_2-H_2O fluids at high pressures and temperatures were calculated from microthermometric data obtained from synthetic fluid inclusions. Assumptions and approximations involved in the calculations are described below and an estimate of the magnitude of maximum possible error introduced in the final MMV calculation is provided in a later section. The initial determination of bulk inclusion density is performed at the CO_2 liquid-vapor homogenization temperature (Th (CO_2)). At this temperature the bulk density is determined from the composition and density of each of the two remaining phases - the CO_2-rich "carbonic" phase and the H_2O-rich "aqueous" phase, respectively. As discussed below, at Th (CO_2), the pressure in the inclusion (equal to the pressure along the CO_2 liquid/vapor curve at this temperature), the relative amount of CO_2 dissolved in the H_2O-rich phase and vice versa, and the density of each phase can be determined from data reported in the literature. Because the composition of the inclusion is known, the specific volume (cm^3/g) of the fluid can be calculated as the sum of the reciprocal density of each phase times its the mass fraction. Specific details of the calculation procedure are given in the following sections.

Solubility of CO_2 in the Aqueous Phase Below 31.0°C

Data on the solubility of CO_2 in H_2O at pressures along the CO_2 liquid-vapor curve from 31.0 to 0.0°C was taken from Dodds et al. (1956). CO_2 solubilities along the curve between 0.0 and -20.0°C were extrapolated linearly from their figure 1. These data are expressed as a function of temperature between 31.0 and -20.0°C using the following relationship:

$$S_{CO2} = 7.2754 - 5.6634x10^{-2}T + 7.8770x10^{-4}T^2 - 2.0370x10^{-5}T^3 \qquad (3.1)$$

where S_{CO2} is the solubility of CO_2 in grams of CO_2 per 100 grams of H_2O and T is in °C. At pressures along the CO_2 liquid-vapor curve carbon-dioxide solubility increases with decreasing temperature reaching a value of about 8 wt. % (~9 grams CO_2/100 grams H_2O) by -20°C (Fig. 3.1).

Density of the Aqueous Phase Below 31.0°C

Densities of CO_2-saturated aqueous solutions along the CO_2 liquid-vapor curve from 31.0 to 4.95°C have been determined by Parkinson and De Nevers (1969). Their data have been extrapolated to -20.0°C using density data for supercooled H_2O from Zheleznyi (1969). These data are expressed as a function of temperature between 31.0 and -20.0°C using the following relationship:

$$\rho_{aq} = 1.0014 + 5.2777x10^{-5}T - 1.0113x10^{-5}T^2 + 9.3537x10^{-8}T^3 \qquad (3.2)$$

where ρ_{aq} is the density of the aqueous phase in g/cm^3 and T is in °C. The aqueous phase reaches a maximum density of 1.0014 g/cm^3 at about 4°C. The density decreases at both high and low temperatures, but the total range in density from -20 to +31°C is only 0.006 g/cm^3 (Fig. 3.2).

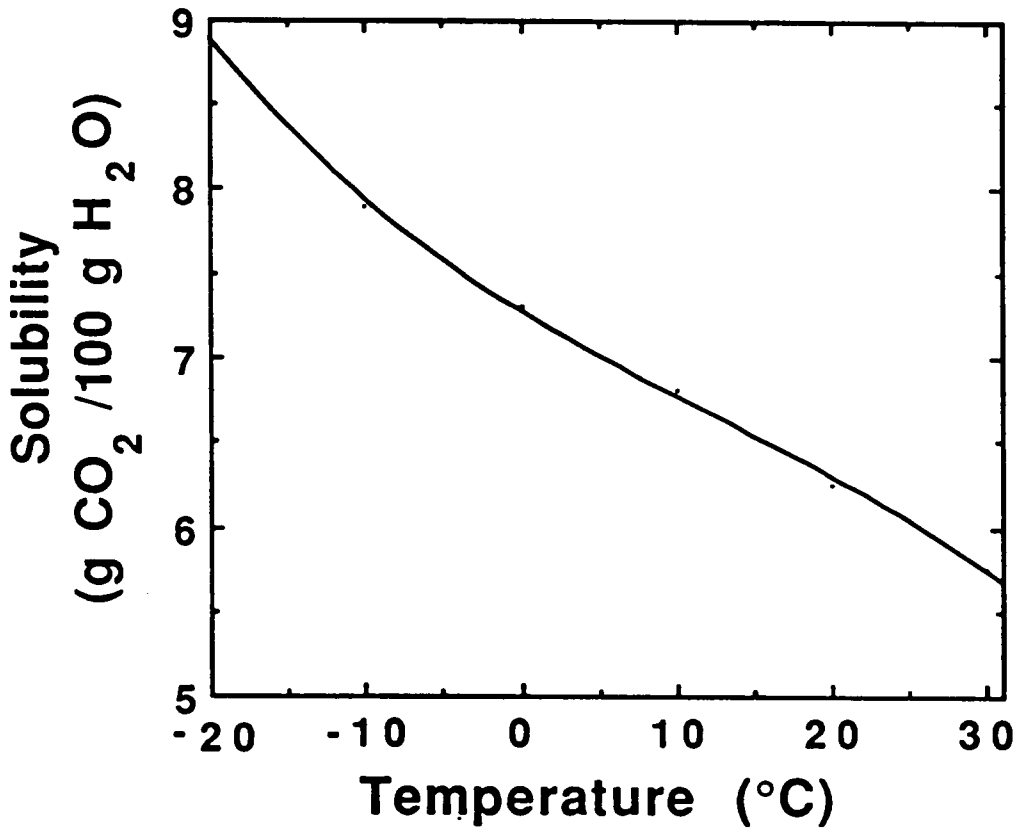

Figure 3.1 Solubility of carbon dioxide in water at pressures along the liquid/vapor curve of CO_2.

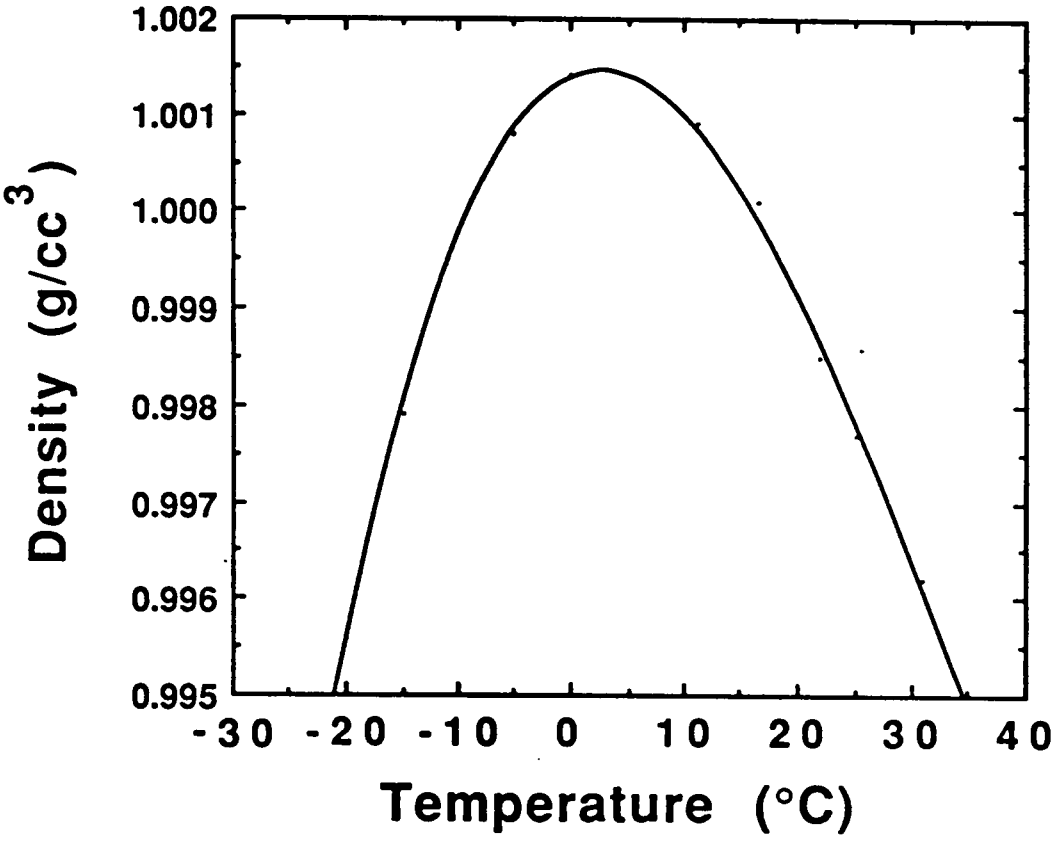

Figure 3.2 Densities of CO_2-saturated aqueous solutions at pressures along the liquid/vapor curve of CO_2.

Solubility of H_2O in the CO_2 Phase Below 31.0°C

The solubility of H_2O in both liquid and vapor CO_2 at P-T conditions along the CO_2 liquid/vapor curve is extremely small, reaching a maximum value of 0.22 mole percent near the critical endpoint (Song and Kobayashi; 1987). Thus, in the present calculations H_2O dissolved in the CO_2 phase has been neglected in determining the total H_2O budget at Th (CO_2).

Density of CO_2 along the Liquid-Vapor Curve

Densities of CO_2 liquid and vapor along the liquid-vapor curve were calculated from the equations of Lowry and Erickson (1927):

$$\rho_{CO2}(l) = 0.4683 + 0.001442\psi + 0.1318\psi^{1/3} \quad (3.3a)$$

and $$\rho_{CO2}(v) = 0.4683 + 0.001442\psi - 0.1318\psi^{1/3} \quad (3.3b)$$

where ρ_{CO2} is the density in g/cm^3 of liquid or vapor CO_2 and ψ = 31.0 - Th (CO_2) in °C. These equations are based on regression of experimental data from -5.6° to 22.9°C, and have an estimated accuracy of ±0.1 % (author's estimate) over that range. Based on the discussions presented by Lowry and Erickson, we conclude that extrapolation of these equations to the critical point of CO_2 (31.0°C) and down to the lowest Th (CO_2) encountered in this study (-20°C) should introduce errors no greater than ±0.25 % in ρ_{CO2}.

Bulk Density of Inclusion

The bulk density of the inclusion is derived from mass balance constraints combined with the known bulk fluid composition. At the homogenization temperature of the CO_2 phases (Th (CO_2)) the two remaining phases in the inclusion are an H_2O-rich aqueous phase (designated by the subscript "aq") and a CO_2-rich carbonic phase (designated by the subscript "cb"). The specific volume of the bulk inclusion fluid is equal to the sum of the specific volumes of each phase times the mass fraction of that phase:

$$V^{sp} = V^{sp}_{aq} \times F_{aq} + V^{sp}_{cb} \times F_{cb} \tag{3.4}$$

where V^{sp}_{aq} and V^{sp}_{cb} are the specific volumes of the aqueous and carbonic phases and F_{aq} and F_{cb} refer to the mass fractions of each of these phases, respectively. The individual specific volumes are given by:

$$V^{sp}_{aq} = 1/\rho_{aq} \tag{3.5}$$

$$V^{sp}_{cb} = 1/\rho_{CO2} \tag{3.6}$$

where ρ_{aq} is the density of the aqueous phase from Eq. 3.2 and ρ_{CO2} is the density of the carbonic phase (essentially pure CO_2) from Eq. 3.3. The mass fraction of the aqueous phase (F_{aq}) is equal to the sum of the mass fraction of the bulk fluid that is water (F_{H2O}) plus the mass fraction of the bulk fluid that is CO_2 dissolved in water (F_{CO2aq}):

$$F_{aq} = F_{H2O} + F_{CO2aq} \tag{3.7}$$

whereas the mass fraction of the carbonic phase (F_{cb}) refers only to the CO_2 that is not dissolved in the aqueous phase. Thus,

$$F_{cb} = 1 - F_{aq} \tag{3.8}$$

The mass fraction of H_2O in the inclusion (F_{H2O}) is calculated from the known bulk composition (X_{CO2}) and the molecular weights of CO_2 and H_2O using the relations:

$$X_{H2O} = 1 - X_{CO2} \tag{3.9}$$

$$F_{H2O} = \{(X_{H2O} \times MW_{H2O})/(X_{CO2} \times MW_{CO2} + X_{H2O} \times MW_{H2O})\} \tag{3.10}$$

where MW_{CO2} = 44.0098 g/mole, MW_{H2O} = 18.0152 g/mole. The mass fraction of the total inclusion fluid that is CO_2 dissolved in the aqueous phase ($F_{CO2}aq$) is given by:

$$F_{CO2}aq = (F_{H2O} \times (S_{CO2}/100)) \tag{3.11}$$

where S_{CO2} is the solubility of CO_2 in the aqueous phase from Eq. 3.1. Finally, the mean molar volume of the inclusion fluid at Th (CO_2) (V_{25}) is calculated from the specific volume (V^{SP}) by multiplying by the mean molar mass (M):

$$M = (X_{CO2} \times MW_{CO2}) + (X_{H2O} \times MW_{H2O}) \tag{3.12}$$

$$V_{25} = V^{SP} \times M \tag{3.13}$$

Where V_{25} is the mean molar volume of the CO_2-H_2O fluid at Th (CO_2) in cm^3/mole.

The above calculation was performed on the data in Appendix I using the FORTRAN program in Appendix II. The program is included to allow recalculation of the MMVs as better low-temperature density and solubility data become available.

Thermal Expansion and Compressibility of Quartz

In order to calculate the mean molar volumes of fluids at elevated P and T from the MMVs determined at Th (CO_2) (Eq. 3.13), an adjustment must be made to account for the change in the volume of the inclusion cavity due to thermal expansion and compressibility of quartz (Bodnar and Sterner, 1985). In other words, a correction must be applied to account for the slight non-isochoric character of fluid inclusions. This was accomplished in the present study using equations for the volumes of α- and β-quartz from Hosieni et al. (1985). These authors present equations that predict the volumes of α- and β-quartz over the range 0° to 1500°C and from 1 bar to 40 kbar. In their formulation, P-T space is divided into three regions: the α-quartz field at low temperatures and the β-quartz field at high temperatures separated by a 60°C-wide strip bounded on the high-temperature side by the lambda transition. The P-T dependence of the quartz lambda transition is given by:

$$T_{\alpha/\beta} = 846 + 0.265P - 0.11303229\times10^{-4}P^2 - 2.4632558\times10^{-9}P^3 \qquad (3.14)$$

The molar volume of quartz outside the center region is given by:

$$V_{\alpha or \beta} = C_{(1,1)} \times \{1 + \Sigma_i\Sigma_{j,i=j\neq1}C_{(i,j)}(T-1000)^{j-1}P^{i-1}\} \qquad (3.15)$$

Where T is in K, P is in MPa and $C_{(i,j)}$ refer to the coefficients of the 35- and 25- term polynomials for α- or β-quartz, respectively, given in Table 7 of Hosieni et al. (1985). It should be emphasized that the summation in Eq. 3.15 does not include the $C_{(1,1)}$ term (Howald, 1989; pers. comm.). Also, two of the coefficients for the β-quartz polynomial should be negative ($C_{(2,5)}$=-0.714101E-16; $C_{(3,2)}$=-0.806657E-11) to generate the values listed in their Table 5.

The third region is that portion of the α-quartz field in P-T space ocurring between the quartz α/β transition (Eq. 3.14) and a temperature 60°C below it. To predict the volume of α-quartz in this region Hosieni et al. (1985) recommend the equations:

$$f(\phi) = (0.00351508 \times \phi - 0.158514 \times 10^{-4}\phi^2 + 0.733660 \times 10^{-7}\phi^3 - 0.116609 \times 10^{-9}\phi^4)^{1/2} \quad (3.16)$$

$$V_\alpha = V_\beta - (r/r_0) \times f(\phi) \quad (3.17)$$

where $\phi = T_{\alpha/\beta} - T$ in K, P is in MPa, r equals the pressure derivative ($d T_{\alpha/\beta}/dP$) of Eq. 3.14 and r_0=0.265.

The change in the volume of an inclusion cavity in quartz between 20°C and 1 bar and any other pressure and temperature may be calculated using a volume change factor expressed as:

$$V_\Delta = V_{\alpha or \beta} / V_{20°C,\ 1\ bar} \quad (3.18)$$

where $V_{20°C,1\ bar}$ = 22.656 cm^3/mole and $V_{\alpha or \beta}$ is the volume of quartz at the P and T of

interest calculated from Eq. 3.15 or 3.17. The final calculation of MMV at P and T is then:

$$V_F = V_{25} \times V_\Delta \tag{3.19}$$

where V_{25} is the mean molar volume of the bulk fluid at Th (CO_2) and V_F is the mean molar volume of the CO_2-H_2O fluid in cm^3/mole at P and T - the actual formation conditions of the fluid inclusion. The magnitude of V_Δ is shown graphically in Fig. 3.3 where it can be seen that over the P-T range of the present study (2-6 kbar; 400°-700°C) the volume of quartz varies approximately 4.5 %. Thus, neglecting this effect could result in errors of up to 4.5 % in the MMVs determined in this study.

The above calculations are embodied in the FORTRAN program in Appendix II in the subroutine "QTZ" which calculates the quantity V_Δ from input pressures and temperatures. This subroutine is amenable to use with natural samples as well, although, it should be recalled that these specific equations are applicable only to inclusions in quartz.

Error Analysis

Because the synthetic fluid inclusion technique for determining PVT properties of fluids is relatively new (Bodnar and Sterner, 1985; 1987), and one that has potential application to several other fluid systems besides CO_2-H_2O, particular attention has been given to the sources and magnitudes of errors inherent in the method and their cumulative effect on the final calculated volumetric properties. In previous sections we have presented a detailed description of the procedure used to calculate MMVs of CO_2-H_2O

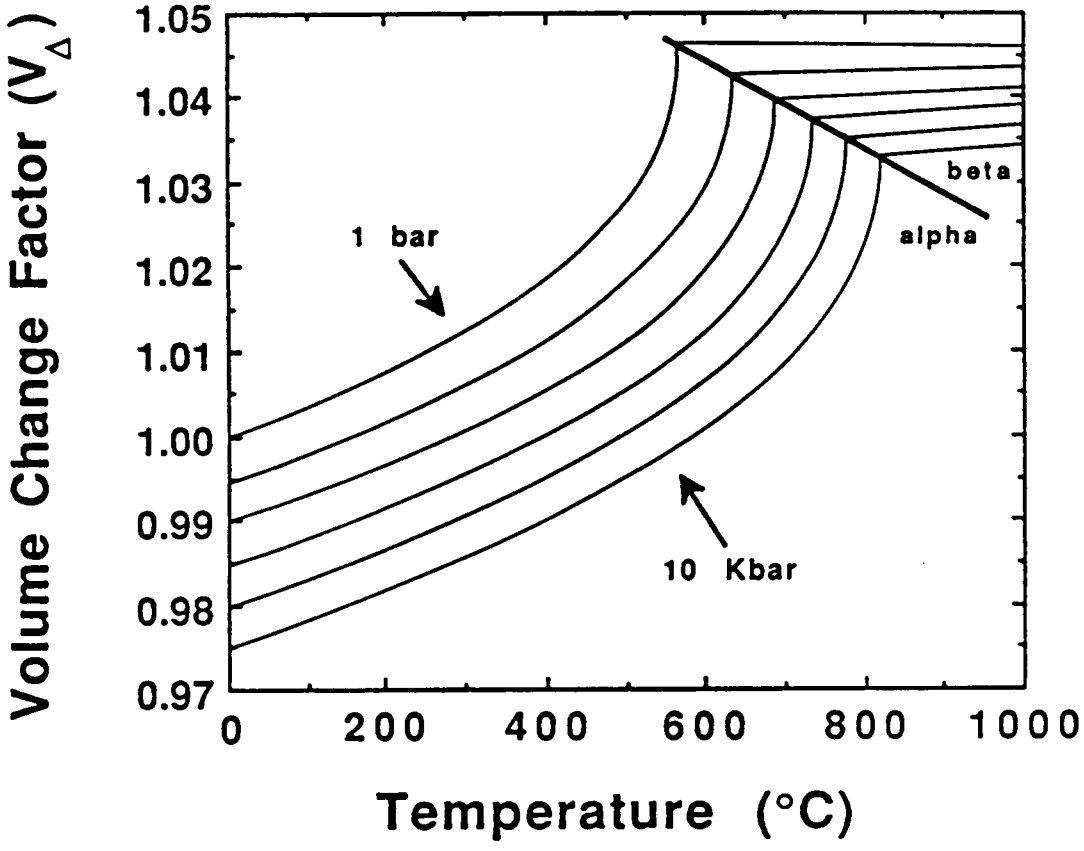

Figure 3.3 **Volume change factor (V_Δ) relating the volume of a fluid inclusion at 20°C and 1 bar to its volume at high P and T.** The light solid lines correspond to the 1 bar, and 2, 4, 6, 8 and 10 kbar isobars of V_Δ. The heavy solid line separates the alpha and beta quartz regions as indicated. The diagram was constructed using equations from Hosieni et al. (1985).

mixtures. We now present our best estimates of the accuracy of the final calculated MMVs stemming from both random and systematic errors associated with the synthetic fluid inclusion data.

In order to provide a meaningful estimation of the accuracy of the final MMVs given in Appendix I, it was first necessary to establish a reasonable error estimate for each of the starting parameters. These initial uncertainties are summarized in Table 3.2 and represent our best estimate of the total error in each variable at the 2σ level (i.e. that encompasses ~95 % of the measurements). In the case of the variable Th (CO_2), an initial value was derived from the average of several measurements, and the estimated error (σ_{Th}) was taken as two calculated standard deviations of the measurements or 0.1°C - whichever was greater (0.1°C reflecting the estimated microthermometric accuracy). The initial uncertainty estimates were then used to estimate the final errors in fluid compositions and MMVs of the binary mixtures using standard formulas given in Taylor (1982) for the propagation of random, independent errors. An additional benefit of this approach is that the relative contribution of each individual error can be readily established, thus, making it apparent which parameters would most profit from "fine tuning" in future work.

Results of the error propagation exercise on individual samples are given in Appendix I. Absolute uncertainties associated with each calculated MMV are tabulated in the under σV_F and the relative uncertainties are given in the column headed "% Error". Uncertainties in fluid compositions resulting from weighing errors and the uncertainty in the yield of CO_2 from silver oxalate decomposition are listed separately in Table 3.3. It can be seen from the last column (% Error) in Appendix I that the largest uncertainties correspond to those samples for which CO_2 homogenization occurred in the vapor phase (signified by a "v" under "Mode"). This results from the relatively large errors in the measurement of Th (CO_2) for inclusions that display CO_2 homogenization to the vapor as

TABLE 3.2 Initial uncertainty estimates (2σ Errors).

	Parameter	Uncertainty
σ_P	Uncertainty in experimental pressure	±0.5 %
σ_T	Uncertainty in experimental temperature	±0.5 %
σ_{H2O}	Uncertainty in mass of H_2O	±0.00006 grm
σ_{AgOx}	Uncertainty in mass of silver oxalate	±0.00006 grm
σ_{Yld}	Uncertainty in yield of silver oxalate	±0.73 %
σ_{Th}	Minimum uncertainty in Th (CO_2)	±0.1°C

TABLE 3.3 Uncertainty estimates in fluid compositions (X_{CO2}).

X_{CO2}	Uncertainty
0.1234	±0.0009
0.2473	±0.0019
0.3716	±0.0030
0.4964	±0.0043
0.6216	±0.0056
0.7473	±0.0073
0.8736	±0.0091

discussed previously. MMVs calculated from these samples are incorrect, and have only been included for the purpose of discussion.

The final error in MMV can be initially subdivided into three parts: errors in volume resulting from uncertainties in pressure (σV_P), in temperature (σV_T), and in fluid composition* (σV_X). The contributions of initial uncertainties in pressure and temperature to σV_F were calculated using values for σ_P and σ_T from Table 3.2 and the partial derivatives $\delta V/\delta P$ and $\delta V/\delta T$ of the Kerrick and Jacobs (1981) equation of state for CO_2-H_2O. The calculations yielded average values for σV_P and σV_T of only 0.06 and 0.07 cm^3/mole, respectively. It is apparent that errors resulting from these two parameters represent on the average only a small portion of the total error in MMV. It should be pointed out, however, that these two error sources reflect only our ability to accurately measure the pressure and temperature during the hydrothermal experiment and do not include errors resulting from fluctuations in these two parameters during the experiments.

By systematically omitting each of the initial error estimates (Table 3.2) and then repeating the error calculation we have ranked the remainder of the initial uncertainties according to their relative importance in the estimate of σV_F. The results of this analysis are given in Table 3.4 where the first entry corresponds to the average percent error in the MMVs calculated from all inclusions that display CO_2 homogenization to the liquid. Subsequent rows show the same calculation differing only in that the contribution to the total error from the source indicated has been eliminated.

The leading cause of uncertainty in the final MMV calculation can be traced back to

****

* The partial error "σV_X" actually incorporates some P- and T- dependent uncertainties to be discussed shortly; this notation is used mostly for convenience.

TABLE 3.4 Average final uncertainty estimates (2σ Errors).

Parameter*	% Uncertainty
Total Average Uncertainty in V_F (σV_F)	1.16 %
Average Error Estimate Without σ_T and σ_P	1.13 %
Average Error Estimate Without σ_{Yld}	0.77 %
Average Error Estimate Without σ_{Th}	0.89 %
Average Error Estimate Without σ_{H2O} and σ_{AgOx}	1.12 %

* See *List Of Symbols*

uncertainties in X_{CO2} originating from the decomposition of silver oxalate. Volumetric determinations using the synthetic fluid inclusion technique, as with any other technique, are very sensitive to the bulk fluid composition and no doubt fluid homogeniety. Because the puncturing technique was not employed in the determination of fluid compositions in the actual experiments, the use of this somewhat insensitive technique to determine the error associated with the yield of CO_2 from the silver oxalate may result in a larger estimated uncertainty in this variable than is really warranted. In any case, we have chosen a value of ±0.73% of the average yield as a reasonable upper limit on the error of this variable.

The second most important error is that associated with Th (CO_2) - not so much in our ability to measure this quantity, but rather, from the true range in this parameter that has resulted from fluctuations in pressure and temperature during the experiments. This experimental error is unique to the synthetic inclusion approach. Most other volumetric methods involve the simultaneous and comparatively instantaneous determination of P, T, X and V, whereas in our approach, the quantity V (V_F) is the average of several determinations over a period of about a week (i.e. corresponding to the actual times of trapping of given inclusions and the prevailing P-T conditions). However, during the course of an experiment, there is generally a positive correlation between fluctuations in pressure and temperature (for example, as the temperature rises slightly in a sealed bomb, it causes a slight increase in the pressure). Because this is a more less isochoric effect it tends to minimize the effective variation in MMV.

The contribution of weighing errors for silver oxalate (σ_{AgOx}) and H_2O (σ_{H2O}) during capsule loading are dwarfed by σ_{Yld} and $\sigma_{Th\ (CO2)}$ and require no further mention.

Other potential sources of error, aside from those listed in Table 3.2, arise from the use of Eqs. 3.1-3 taken from the literature or derived from published figures. We have

already given a brief description of any assumptions or approximations associated with these equations. We now discuss the potential uncertainties arising from their use. Because these errors are largely systematic and of small magnitude we have elected to consider the effect of each one individually on the final calculated MMV and in so doing, demonstrate that they have a negligible contribution to the calculation as a whole.

Errors in the final MMV calculation resulting from the extrapolation of CO_2 solubility data to -20.0°C (Eq. 3.1) are insignificant because only the most CO_2-rich inclusions in this study homogenize at these low temperatures and within them the relative mass of the aqueous phase and thus the CO_2 dissolved in it is small. For example, a ±10 % error in the amount of dissolved CO_2 in a 75 mole % CO_2 inclusion for which Th (CO_2) = -15.6°C results in only a ±0.0025 % error in the calculated MMV. Water-rich inclusions have commensurately larger aqueous phases at low temperature although their higher Th (CO_2)'s result in lower concentrations of dissolved CO_2. Thus, in a 12.5 mole % CO_2 inclusion for which Th (CO_2) = 24.5°C these competing affects still result in only a ±0.18 % error in the calculated MMV corresponding to an initial ±10 % error in the amount of dissolved CO_2.

Errors resulting from the extrapolation of ρ_{aq} to -20.0°C (Eq. 3.2) are small by the same logic as outlined above. Even an error as large as ±0.004 gram/cm^3 (a range larger than the total variation of this parameter) in the density of the aqueous phase present in a 75 mole % CO_2 inclusion for which Th (CO_2) = -15.6°C results in only a ±0.054 % error in the calculated MMV. While for a 12.5 mole % CO_2 inclusion with Th (CO_2) = 24.5°C a ±0.004 gram/cm^3 error in the density of the aqueous phase still results in only a ±0.29 % error in the final MMV.

Neglecting to account for the H_2O dissolved in the CO_2 phase would create a maximum error in calculating the volume occupied by the aqueous phase of ~1.5 % for

very CO_2-rich bulk fluid compositions (i.e. 87.5 mole % CO_2) and then only for those inclusions which have Th (CO_2) near 31.0°C. However, because the relative volume of the aqueous phase in inclusions having this bulk composition is so small, maximum errors introduced under these circumstances in the calculation of MMV would be about 0.004 volume percent.

Finally, errors in the final calculated MMV resulting from systematic uncertainties in ρ_{CO2} (Eqs. 3.3a&b from Lowry and Erickson (1927)) will be no larger than the initial uncertainty. Thus, if a ±0.25 % error exists in the density of the CO_2 phase in an extremely CO_2-rich inclusion, then this same relative error will exist in the final calculated MMV. As the inclusion becomes more H_2O-rich, the effect of this initial error diminishes.

No correction was made to ρ_{CO2} to account for the small amount of dissolved H_2O at Th (CO_2). Lowry and Erickson (1927) performed ρ_{CO2} determinations in both the presence and absence of H_2O and conclude that the small quantity of H_2O dissolved in either the liquid or vapor CO_2 phases has a negligible effect on ρ_{CO2} to within ±0.1 %.

From discussions presented above it is apparent that if reasonable (or, in some cases, even if rather large) relative systematic uncertainties exist in the calculated quantities S_{CO2}, ρ_{aq}, the solubility of H_2O in the CO_2 phase, or in ρ_{CO2}, the resultant effect of each of these errors on the final MMV determination is still small. This convenient conclusion, unfortunately, does not always apply to errors in the determination of ρ_{CO2} arising from uncertainties in Th (CO_2) and the eventual effect on the error in the calculated MMV. Because ρ_{CO2} changes very rapidly with temperature near the critical point of pure CO_2, rather large uncertainties result in the final MMV calculation for inclusions with Th (CO_2) near 31°C. This is readily apparent in Appendix I by comparing Th (CO_2) with the final volume percent error estimate (σV_F). Fortunately, the variation in Th (CO_2) of

inclusions in this study decreases as Th (CO_2) increases and is generally quite small for CO_2 homogenation near the critical point. This can be seen from the fact that as Th (CO_2) approaches 31.0°C (Appendix I), σ_{Th} rarely exceeds the estimated accuracy of the heating/freezing stage (±0.1°C). Still, for a theoretical 50 mole % CO_2 inclusion with Th (CO_2) = 31.0°C, a ±0.1° uncertainty results in an uncertainty of ±11.0 % in the final calculated MMV. This effect diminishes very rapidly so that for Th (CO_2) = 30.5 ±0.1°C the final error drops to ±1.0 % and if Th (CO_2) = 30.0 ±0.1°C the final estimated uncertainty in the calculated MMV is only ±0.6 %.

A final source of error in the MMV calculations comes from potential effects of dissolved silica. For reasons described below we believe that SiO_2 has a negligible effect on the volumetric properties of CO_2-H_2O fluids over the P-T range of our experiments.

The results of three separate synthetic fluid inclusion determinations of the molar volume of H_2O at high pressures and temperatures are given in Table 3.5. Inclusions were synthesized from pure H_2O at the conditions indicated using the method of in-situ fracturing described above. Molar volumes of H_2O at P and T were calculated from measured total homogenization temperatures as outlined by Bodnar and Sterner (1985) using the equation of Haar et al. (1984) for densities along the H_2O liquid-vapor curve and equations from Hosieni et al. (1985) to account for differences in the volume of the inclusion cavity between the P-T conditions at homogenization and those of formation. Molar volumes of pure H_2O determined in this way are compared with those reported by Burnham et al. (1969) and Haar et al. (1984). It can be seen that molar volumes of H_2O determined using synthetic inclusions are in good agreement with both studies. More to the point, the close agreement between the molar volume of water at elevated P and T determined in the present study using synthetic inclusions with values from Burnham et al. (1969) and Haar et al. (1984) is taken to signify that dissolved silica has a negligible

TABLE 3.5 Comparison of molar volumes of H_2O determined from synthetic fluid inclusions with values determined using conventional techniques.

	Conditions		Results				
	P (bar)	T (°C)	(1)	(2)	(3)	(4)	(5)
1)	5000	700	24.084	24.077	-0.03	23.834	-1.04
2)	5000	700	24.013	24.077	0.27	23.834	-0.75
3)	6000	700	22.532	22.737	0.91	22.393	-0.62

(1) Molar volume of H_2O determined from Synthetic Fluid Inclusions

(2) Molar volume of H_2O determined from Burnham et al. (1969)

(3) % Deviation $(V_{Burnham}-V_{SynFlinc}/V_{SynFlinc}) \times 100$

(4) Molar volume of H_2O determined from Haar et al. (1983)

(5) % Deviation $(V_{Haar}-V_{SynFlinc}/V_{SynFlinc}) \times 100$

effect on the volumetric determination. Furthermore, because the addition of CO_2 decreases the solubility of silica this effect will likely be even less in CO_2-H_2O fluids at similar pressures and temperatures.

RESULTS

Equation for the Volumetric Properties of CO_2-H_2O

Experimental details and microthermometric data from 712 synthetic fluid inclusions in 107 samples are presented in Appendix I along with MMVs (V_F) calculated as described in the preceding sections and estimated uncertainties at the 95 % confidence level. Ninety-two of the MMVs given in Appendix I were calculated from fluid inclusions that displayed CO_2 homogenization to the vapor (signified by an "l" in the column labled "Mode") and were formed over a range of experimental conditions from 2 to 6 kbar and 400° to 700°C from fluids of composition $0.125 \leq X_{CO2} \leq 0.875$. These ninety-two MMVs of CO_2-H_2O mixtures together with twenty values for pure CO_2 over the same P-T range taken from Table 3.2 of Shmonov and Shmulovich (1974) were regressed using a Quasi-Newton minimizer coded by M.B. Boisen and L.W. Johnson in the Dept. of Mathematics at the Virginia Polytechnic Institute & State University to generate a volume-explicit function of pressure, temperature and mole fraction CO_2 that predicts the MMVs of CO_2-H_2O mixtures from 2 to 6 kbar and 400° to 700°C from fluids of composition $0.0 \leq X_{CO2} \leq 1.0$. The equation incorporates molar volumes of pure H_2O (V_{H2O}) predicted by the Haar et al. (1984) equation so that the complete expression for the MMV of CO_2-H_2O mixtures is:

$$V_{CO2\text{-}H2O} = V_{H2O} + V_R \qquad (3.20a)$$

where V_{H2O} is the molar volume of H_2O predicted by Haar et al. and V_R is the mean molar volume of the CO_2-H_2O mixture that is in excess of the molar volume of pure H_2O at the same pressure and temperature. This residual volume "V_R" is given by

$$V_R = \Sigma_{ij} X^j \times \{\Phi_{(i,j)}\} \qquad (3.20b)$$

$$\begin{aligned}\Phi_{(i,j)} = \{&C_{(1,j)} + (C_{(2,j)}/P) \\ &+(C_{(3,j)} + C_{(4,j)} \times T + C_{(5,j)} \times T^2) \times EXP(C_{(6,j)} \times (P - C_{(7,j)})) \\ &+(C_{(8,j)} + C_{(9,j)} \times T) * EXP(-C_{(10,j)}/P)\}\end{aligned} \qquad (3.20c)$$

where **T** is in °C, **P** is in kbar, **X**= mole fraction CO_2 and the coefficients $C_{(i,j)}$ of Eq. 3.20c are given in Table 3.6. To insure that when X_{CO2}=0, the complete expression ($V_{CO2\text{-}H2O}$) would reduce to the molar volumes of pure H_2O (V_{H2O}) predicted by Haar et al. (1984), the appropriate V_{H2O} was subtracted from each of the 112 data points prior to regression. The regression was then performed without an intercept term which forces the expression for V_R (Eq. 3.20b) through zero for pure H_2O.

Mean molar volumes of CO_2-H_2O mixtures predicted by Eq. 3.20 are shown in Figs. 3.4a-d. In each case the intercepts for X_{CO2}=0 are molar volumes of pure H_2O predicted by the Haar et al. (1984) equation, whereas the intercepts for pure CO_2 (X_{CO2}=1) are predictions based in part on Eq. 3.20c. The 2 kbar isobars at 600° and 700°C (Figs. 3.4c and d, respectively), and the 6 kbar isobar at 400°C are actually outside the range of data used to generate Eq. 3.20 and while they appear to represent reasonable volumes they should be regarded as extrapolations. Mean molar volumes calculated from

TABLE 3.6 Coefficients $C_{(i,j)}$ of Equation 20c.

i	j=1	j=2	j=3	j=4
1	0.6732537E+ 01	0.3609206E+ 02	-0.3702393E+ 02	0.7640406E+ 01
2	0.4338309E+ 02	-0.2890292E+ 02	0.1688120E+ 01	0.1973572E+ 02
3	-0.2866506E+ 03	0.1933196E+ 03	-0.2211378E+ 03	0.1067997E+ 03
4	0.9678724E+ 00	-0.3210269E+ 00	0.1848737E+ 03	-0.3825645E+ 01
5	-0.5299542E- 03	-0.3550759E- 02	0.1021388E+ 01	-0.6900536E- 01
6	-0.2694655E+ 01	-0.4303117E+ 01	-0.1004729E+ 02	-0.7132958E+ 01
7	0.1024664E+ 01	0.9318259E+ 00	0.9783982E+ 00	0.8888806E+ 00
8	0.7699372E+ 02	-0.3591408E+ 03	0.3196773E+ 03	-0.2483753E+ 02
9	-0.9576748E- 01	0.5150177E+ 00	-0.5210969E+ 00	0.5757237E- 01
10	0.7515128E+ 01	0.8889788E+ 01	0.9161576E+ 01	0.4316113E+ 01

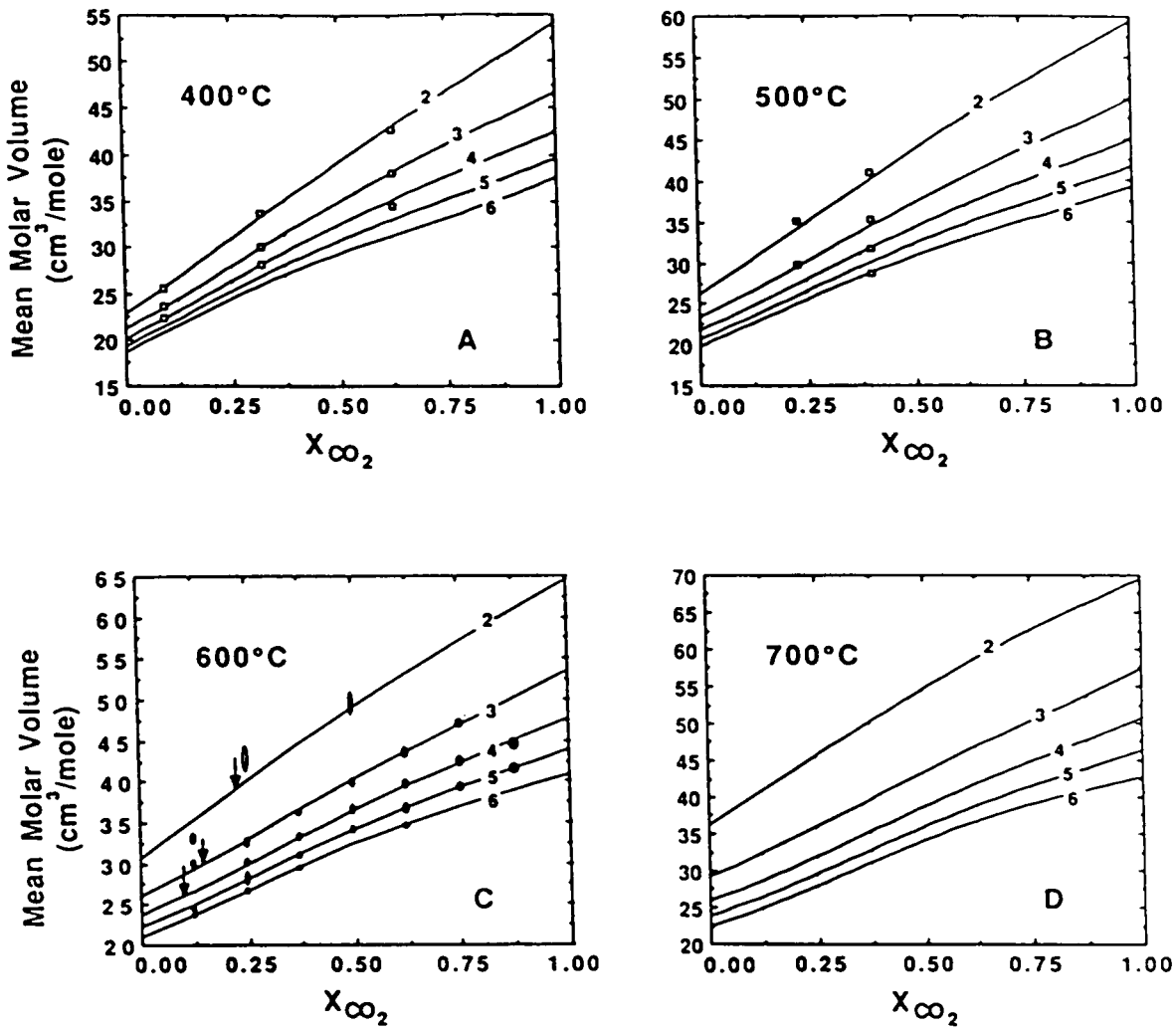

Figure 3.4 **Mean molar volumes of CO_2-H_2O mixtures.** Solid lines are MMVs predicted from Equation 3.20 from 2-6 kbar at 400°C (A), 500°C (B), 600°C (C) and 700°C (D). Open squares on Figures 3.4a and 3.4b are experimental data from Shmulovich et al. (1980). Filled ovals at 600°C (Fig. 3.4c) are synthetic fluid inclusion data. The size of each oval corresponds to our estimated error (2σ) in composition (horizontal axis) and volume (vertical axis). Opened ovals are MMVs calculated from inclusions that displayed CO_2 homogenization to the vapor (see text).

synthetic fluid inclusions (Appendix I) at 600°C are shown on Fig. 3.4c. The size of each oval corresponds to our best estimate of the error ($\pm 2\sigma$) in composition (horizontal axis) and volume (vertical axis) for each datum point and is the result of the error analysis described earlier.

Of the 107 MMVs reported in Appendix I, only those from samples for which CO_2 homogenization occurred to the liquid phase were used in the regression leading to Eq. 3.20. At 600°C (Fig. 3.4c) these data are represented by filled ovals, whereas, opened ovals correspond to samples for which CO_2 homogenization occurred in the vapor phase. Dashed arrows next to each opened oval indicate the isobar with which the datum point is associated. It is immediatly apparent that the open ovals (CO_2 homogenization to the vapor) lie significantly off the trend established by the filled ovals (CO_2 homogenization to the liquid). For reasons discussed previously, MMVs calculated from inclusions characterized by CO_2 homogenization to the vapor are significantly larger than the actual values and are included in Appendix I and Fig. 3.4c only for illustrative purposes.

Figure 3.5 is a histogram showing the percent deviation of all data used in the regression procedure to generate Eq. 3.20. Areas shaded with diagonal lines represent pure CO_2 data while the stippled region shows the distribution of the 92 CO_2-H_2O binary data points. Arrows indicating one- and two- standard deviations refer to the average 1σ and 2σ uncertainties in the raw data (Appendix I) and they *do not* represent standard deviations of values predicted by Eq. 3.20. They have been included here to show that the fit of the equation falls within most of the systematic variation in the data. It should be recalled that implicit in Eq. 3.20 is a theoretically perfect fit to the data for pure H_2O and this was achieved at some cost to the "goodness of fit" within the binary - particularly toward the H_2O-rich end. This is somewhat more apparent in Figs. 3.6a-d showing the percent deviation of each individual data point as a function of mole fraction CO_2. Each

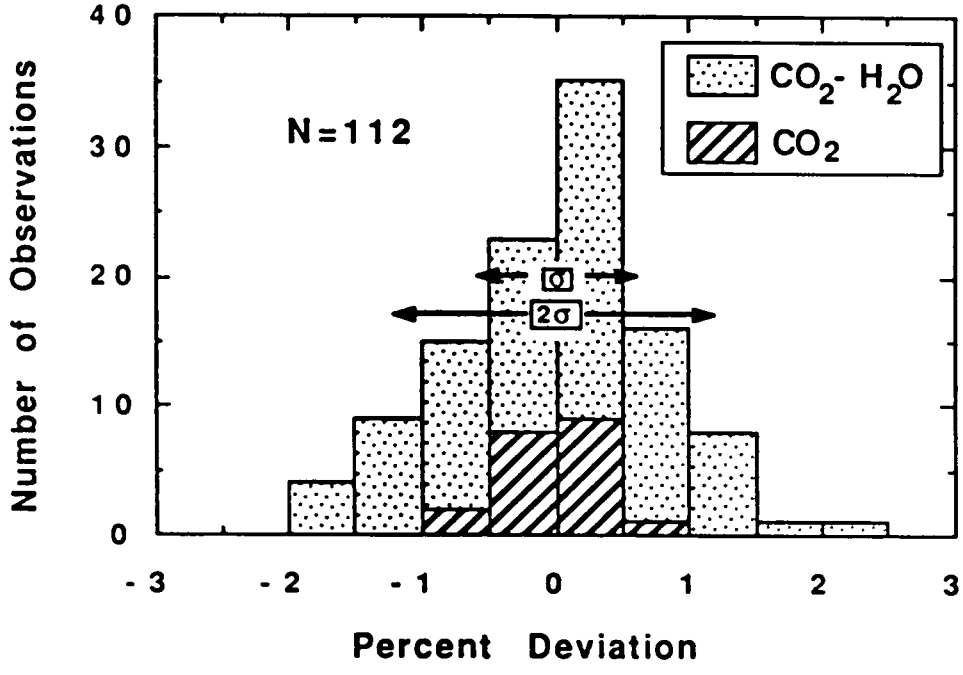

Figure 3.5 **Percent deviation of predicted values from volumetric data used to generate Equation 3.20.** Diagonally shaded regions correspond to volumetric data for pure CO_2 while stippled areas represent data for CO_2-H_2O mixtures. Arrows indicating one- and two-standard deviations refer to the average 1σ and 2σ uncertainties in the experimental data (Appendix 1). They *do not* represent standard deviations of values predicted by Equation 3.20.

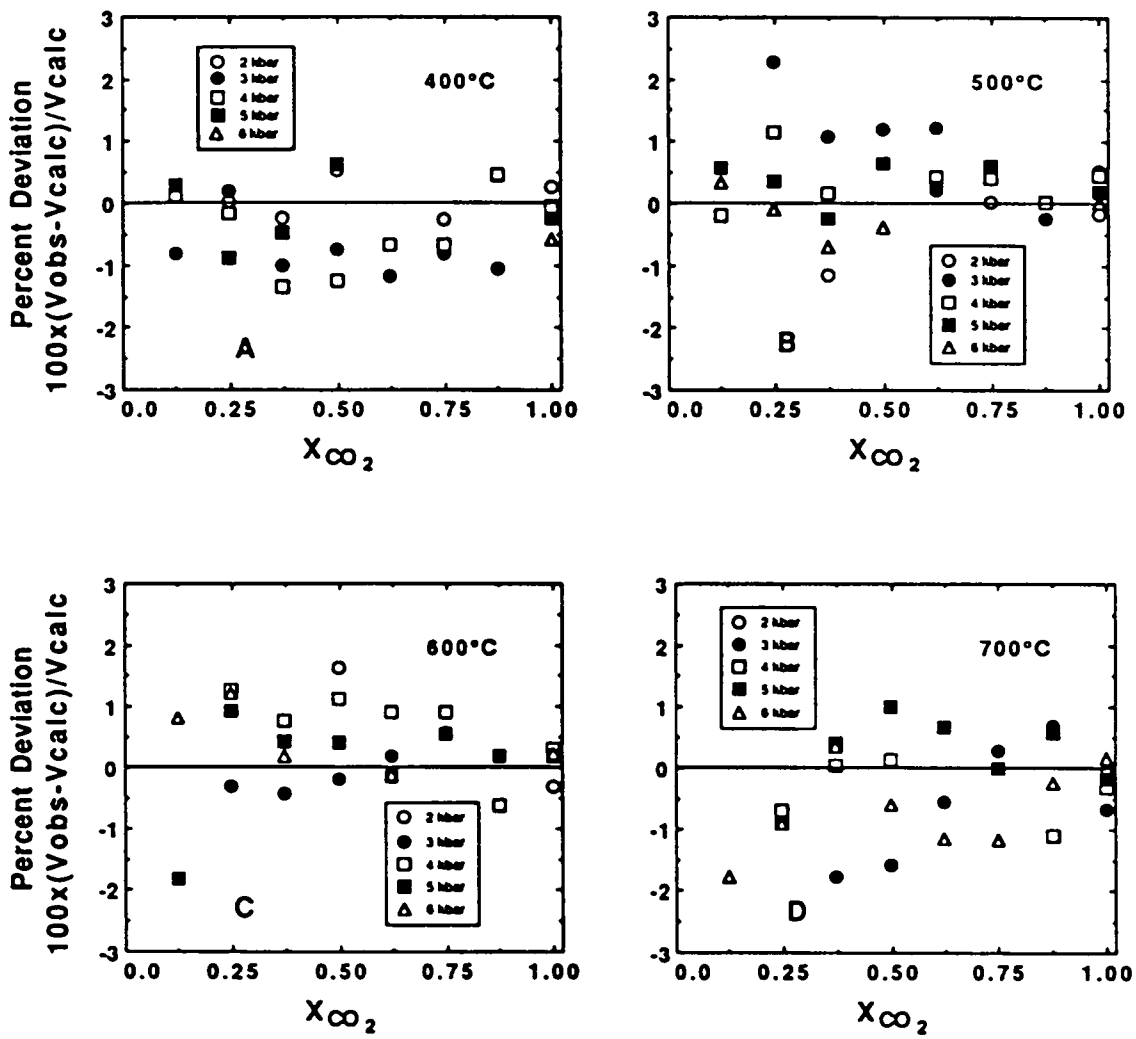

Figure 3.6 Percent deviations of individual datum at 400°C (A), 500°C (B), 600°C (C) and 700°C (D) from values predicted by Equation 3.20.

diagram shows a general trend of smaller deviations toward the CO_2 rich side culminating in the best fit corresponding to pure CO_2. Also evident from Figs. 3.6a-d is that there is no systematic trend in the deviation of the raw data from the predicted values (i.e. there appears to be no systematic displacement of given isobars or isotherms toward consistantly positive or negative values), rather, the residuals tend to be more-or-less randomly scattered about the origin suggesting that Eq. 3.20 provides a very reasonable approximation to the overall data set.

Comparison with Previous Volumetric Determinations for CO_2-H_2O

Of the various sets of experimental data on volumetric properties of CO_2-H_2O mixtures mentioned in the introduction, only the study of Shmulovich et al. (1980) has sufficient overlap with the present work to allow for comparison. MMVs calculated from Eq. 3.20 of the present study are compared with some of their data at 400° and 500°C (shown as open squares) in Figs. 3.4a&b, respectively. In general, very good agreement is found between the two data sets, although, at 500°C our data suggest slightly less positive excess volumes of mixing at 2 and 3 kbar than those given by Shmulovich et al.

Comparison with Volumetric Properties Predicted by Equations of State

In the absence of volumetric data for CO_2-H_2O mixtures at high pressures and temperatures, several equations of state have been developed to predict the fluid properties over the range of crustal conditions. The majority of these equations use volumetric data (or derivatives thereof) for the pure endmember components in conjunction with a variety of mixing rules to predict MMVs and thermodynamic properties of CO_2-H_2O mixtures.

Because of their immediate significance to fluid inclusion research, we have chosen to compare isochores predicted by the different equations rather than mean molar volumes. Figures 3.7a-d show comparisons for four different fluid compositions between isochores calculated using Eq. 3.20 (generated from the MMV data in Appendix I) and those predicted using the equations of state of Holloway (1981), Kerrick and Jacobs (1981), Bowers and Helgeson (1983) and Connolly and Bodnar (1983).

Pressures along isochores of constant composition calculated using Eq. 3.20 of the present study are predicted by the above equations of state to within ±300 to 400 bars on the average. For water-rich compositions at low pressures the available equations tend to predict higher pressures than the present study. For more CO_2-rich compositions (X_{CO2}~0.5 - 0.75), discrepancies of ~0.5 kbar occur at moderate to high pressures where these equations all tend to underestimate the positive excess volume of mixing resulting in predicted pressures that are lower than observed. The largest differences exibited between the various equations are found at high pressures, low temperatures and water-rich compositions (Figs. 3.7a&b). Here the individual pressure predictions span a range of nearly 800 bars with those calculated from Eq. 3.20 of the present study being consistently the highest values.

Excess Volumes of CO_2-H_2O Mixtures

The shapes of the V-X curves in Figs. 3.4a-d imply nearly ideal behavior of CO_2-H_2O mixtures at high pressures and temperatures as compared with the strong departures from ideality exhibited at low pressures (see Greenwood, 1969) and fluid unmixing at low temperatures (Todheide and Franck, 1963; Takenouchi and Kennedy, 1964). Although deviations from ideal mixing are small over the P-T-X range considered

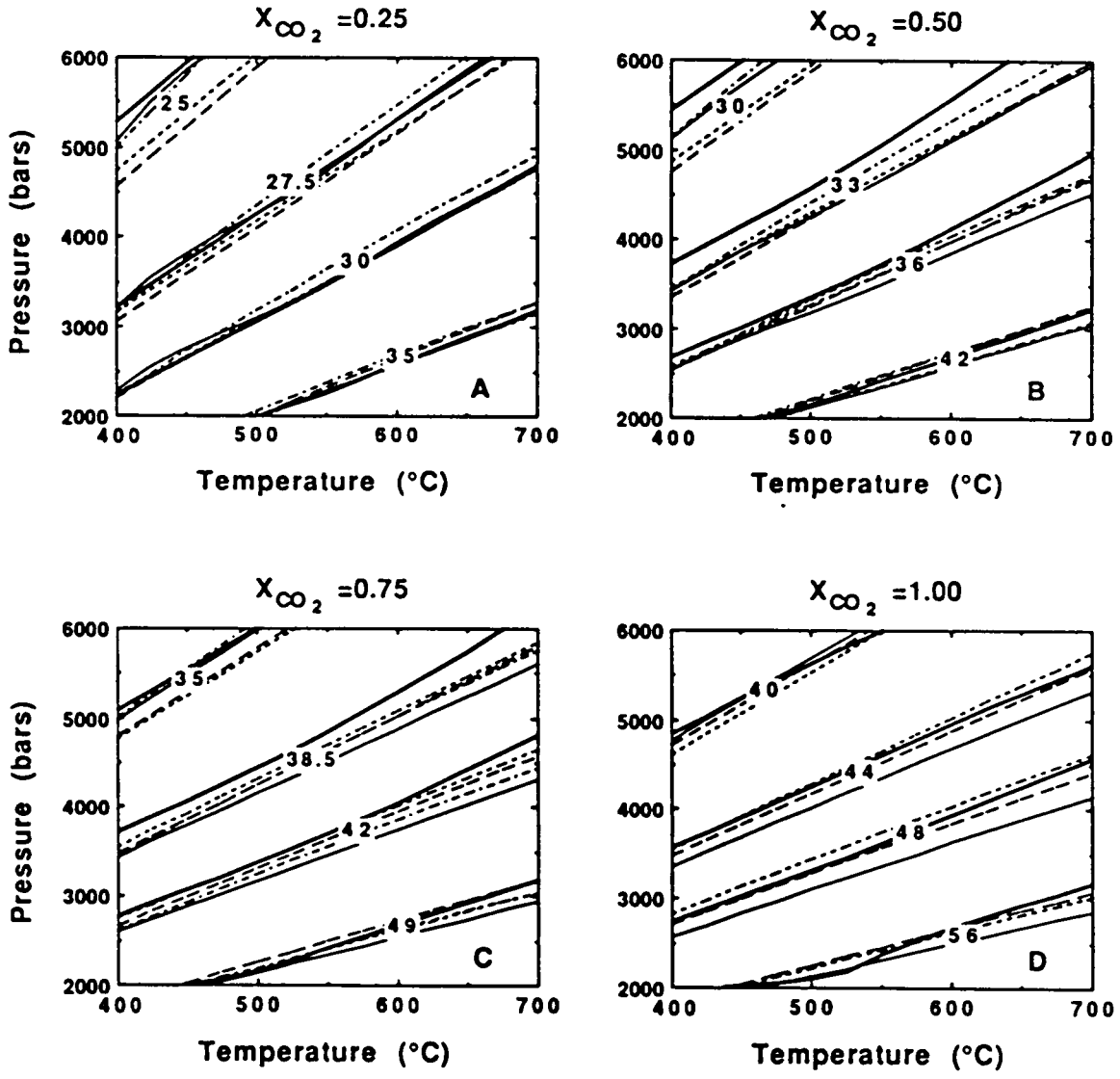

Figure 3.7 **Comparison of isochores calculated using Equation 3.20 (heavy solid line) with those predicted from the equations of state** of Holloway (1981; light solid line), Kerrick and Jacobs (1981; long-dashed line) Bowers and Helgeson (1983; dot-dashed line) and Connolly and Bodnar (1983; short-dashed line) for fluid compositions of 0.25 (A), 0.50 (B), 0.75 (C) and 1.00 (D) mole fraction CO_2. Numbers on curves are mean molar volumes (cm^3/mole).

in this study, the relative incompressibility of CO_2-H_2O mixtures at high pressure (high density) tends to magnify the effect of even subtle non-ideal behavior. Using fluid inclusion geobarometry as an example, from the relatively close spacing between isobars at high pressures shown in Figs. 3.4a-d it can be inferred that small errors in determining the bulk density of an inclusion will result in comparatively large errors in estimating trapping pressures.

The process of fitting an analytical expression to the present data set has led us to the conclusion that the MMVs of CO_2-H_2O mixtures are not quadratic functions of X_{CO2} over the P-T range of the present study. The quadratic dependence of these projections predicted by most equations of state is a simple consequence of the mixing rules used.

The curvature of the isobars in V-X_{CO2} space (Figs. 3.4a-d) is shown more clearly when the data are plotted as excess molar volumes (V^{EX}) (Figs. 3.8a-d). For most of the included P-T region, each V^{EX}-X_{CO2} curve is slightly asymetrical with the central portion concave down while that part of the curve corresponding to either one or both of the CO_2- or H_2O-rich regions is concave up. This fact was recognized by Shmulovich et al. (1980) who appropriately modelled the behavior of V^{EX} over a portion of P-T space using two-parameter Margules equations (cubic expressions in X_{CO2}). Considering the entire P-T range of the present study, and MMVs of CO_2-H_2O mixtures from synthetic inclusions together with those of the pure endmembers from Haar et al. (1984) and Shmonov and Shmulovich (1975), we found that only a fourth-order dependence could adequately describe the variation of V (V^{EX}) with fluid composition.

It should be stated that both the magnitude of V^{EX} and the shape of the V^{EX}-X_{CO2} curves shown in Figs. 3.8a-d and any quantities derived from them are highly dependent on the molar volumes of the pure endmembers - in this case CO_2 and H_2O. Differences in the volumetric data for either of these pure components could result in V^{EX}-X_{CO2}

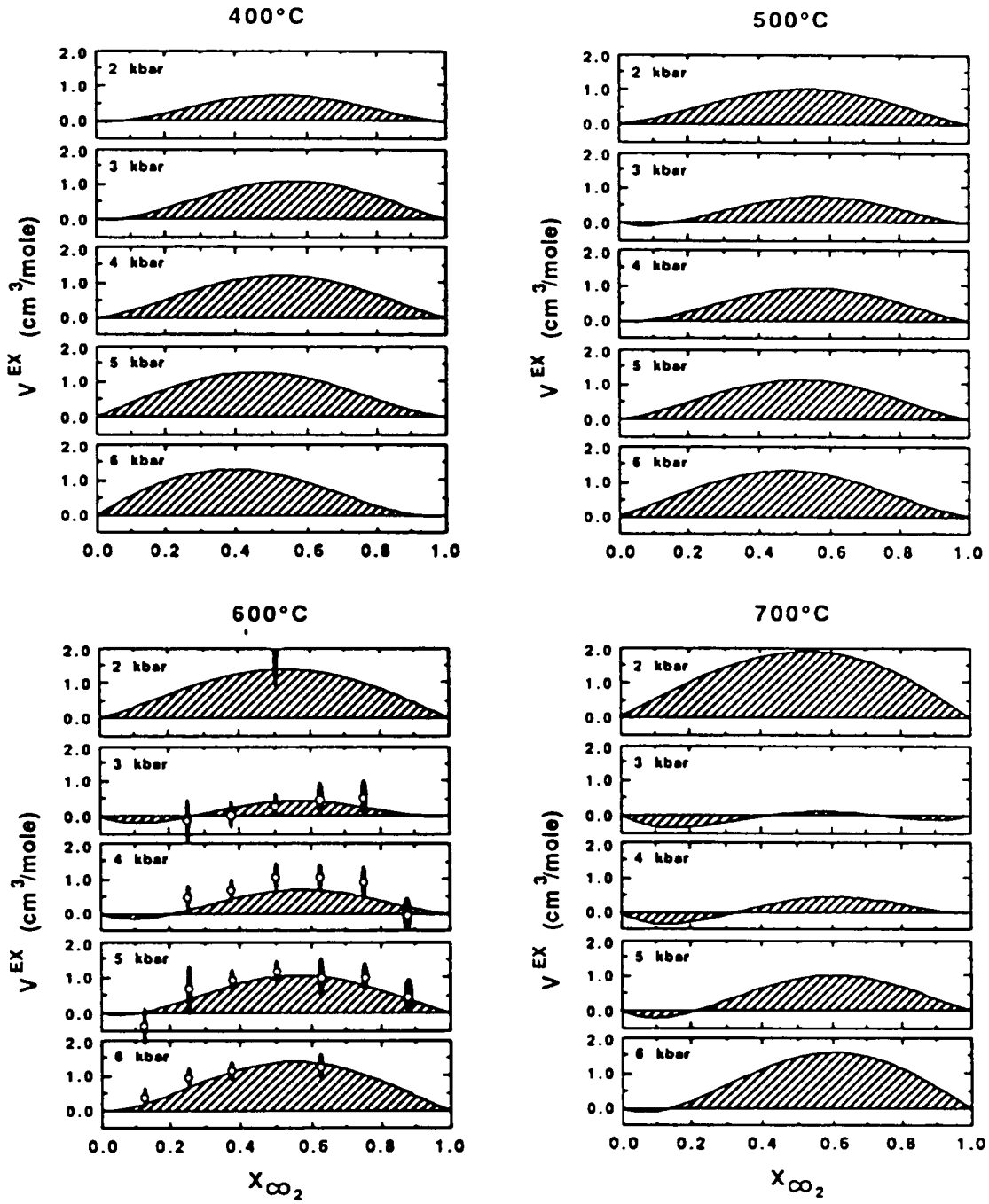

Figure 3.8 Excess molar volumes of CO_2-H_2O mixtures predicted using Equation 3.20 from 2-6 kbar at 400°C (A), 500°C (B), 600°C (C) and 700°C (D). Ovals at 600°C (Fig. 3.8c) represent synthetic fluid inclusion data. The size of each oval corresponds to our estimated error (2σ) in composition (horizontal axis) and V^{EX} (vertical axis). The 2 kbar isobars at 600°C and 700°C (Figs. 3.8c and d) and the 6 kbar isobar at 400°C (Fig. 3.8a) represent extrapolations beyond the range of data used to generate Equation 3.20.

curves that are considerably different than those shown. However, in this respect it should also be pointed out that the volumetric data for both pure H_2O and pure CO_2 are probably at least as accurate as the present data set for mixtures.

The 2 kbar isobars at 600° and 700°C shown in Figs. 3.8c&d would appear to represent notable exceptions to the above generalizations about the shapes of V^{EX}-X_{CO2} curves. However, as mentioned previously, these two curves are beyond the range of our data and therefore, represent extrapolations of our volume equation. The magnitude of V^{EX} and the shape of these two curves results from volumetric data generated from one of the above equations of state which was included in the regression leading to Eq. 3.20 to extend its region of applicability. Although this procedure appears to have resulted in predicted MMVs which are internally consistent in a general sense (e.g. see the 2 kbar isobar in Figs. 3.4a&b), the inconsistencies are readily apparent upon examination of V^{EX} (Figs. 3.8a-d). The 6 kbar isobar at 400°C shown in Fig. 3.8a also represents an extrapolation beyond the range of our data. In this case the predicted volumes are much more consistent with the rest of the data. Finally, it should be pointed out that at some pressure below 2 kbar larger positive excess volumes begin to develop as shown by the data of Greenwood (1969). His data indicate a positive deviation of ~20 % in the volume of mixing at 500°C, 500 bars for X_{CO2}=0.5. Thus, a minimum in excess volumes must occur somewhere between these two pressures.

Over the range of P-T conditions in the present study, CO_2-H_2O mixtures display very limited departures from ideality with maximum positive excess volumes of mixing (V^{EX}) of 1.6 cm^3/mole (4.4 %) at 6 kbars, 700°C and X_{CO2}=0.6 (Fig. 3.8d). At constant temperature, V^{EX} increases with increased pressure. Over all pressures and temperatures studied, V^{EX} has its maximum value between $0.4 \leq X_{CO2} \leq 0.6$; at high pressures, the peak shifts toward more CO_2-rich values as temperature increases, while at low pressures

no trend is apparent. Between 3 and 5 kbars, at constant pressure, V^{EX} decreases with increased temperature and becomes slightly negative for low CO_2 concentrations at 600° and 700°C. At 6 kbar, however, V^{EX} remains relatively constant at about 4% over the complete temperature range studied.

Partial Molar Volumes of CO_2 and H_2O

The partial molar volume (PMV) of a component in a mixture provides a measure of the relative contribution of that component to the total volume. Large changes in the PMV of a component over a small range of composition will result in significant departures from ideality for the mixture.

Partial molar volumes of CO_2 and H_2O in CO_2-H_2O mixtures were calculated using the slope-intercept method (Lewis and Randall, 1961). At constant pressure and temperature the partial molar volumes of the two components in the mixture are given by:

$$V_{H2O}=V_{CO2\text{-}H2O} - (\delta V_{CO2\text{-}H2O}/\delta X_{CO2})_{P,T} \times X_{CO2} \qquad (3.21)$$

$$V_{CO2}=V_{CO2\text{-}H2O} + (\delta V_{CO2\text{-}H2O}/\delta X_{CO2})_{P,T} \times X_{H2O} \qquad (3.22)$$

$$\{\delta V_{CO2\text{-}H2O}/\delta X_{CO2}\}_{P,T} = \Sigma_{ij}\,(j) \times X^{(j-1)} \times \{\Phi_{(i,j)}\} \qquad (3.23)$$

where V_{H2O} and V_{CO2} represent the partial molar volumes of H_2O and CO_2, respectively, $V_{CO2\text{-}H2O}$ is the mean molar volume of the mixture from Eq. 3.20a, $\{\delta V_{CO2\text{-}H2O}/\delta X_{CO2}\}_{P,T}$ is the partial derivative of MMV (Eq. 3.20a) at constant P and T, and $\Phi_{(i,j)}$ is from Eq. 3.20c. These two quantities are plotted against X_{CO2} in Figs.

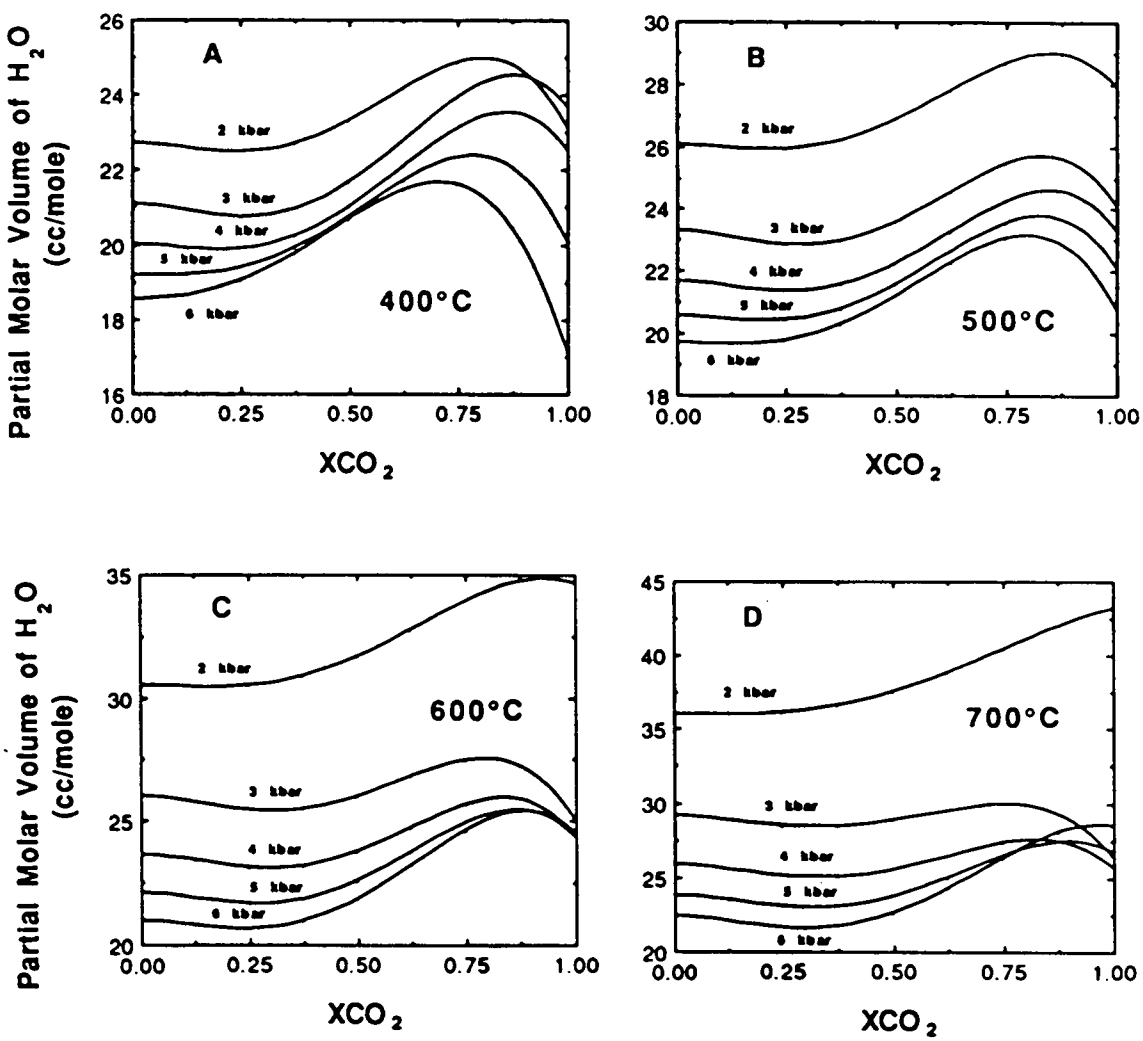

Figure 3.9 **Partial molar volumes of H_2O in CO_2-H_2O mixtures derived from Equation 3.20** from 2-6 kbar at 400°C (A), 500°C (B), 600°C (C) and 700°C (D). The 2 kbar isobars at 600°C and 700°C (Figs. 3.9c and d) and the 6 kbar isobar at 400°C (Fig. 3.9a) represent extrapolations beyond the range of data used to generate Equation 3.20.

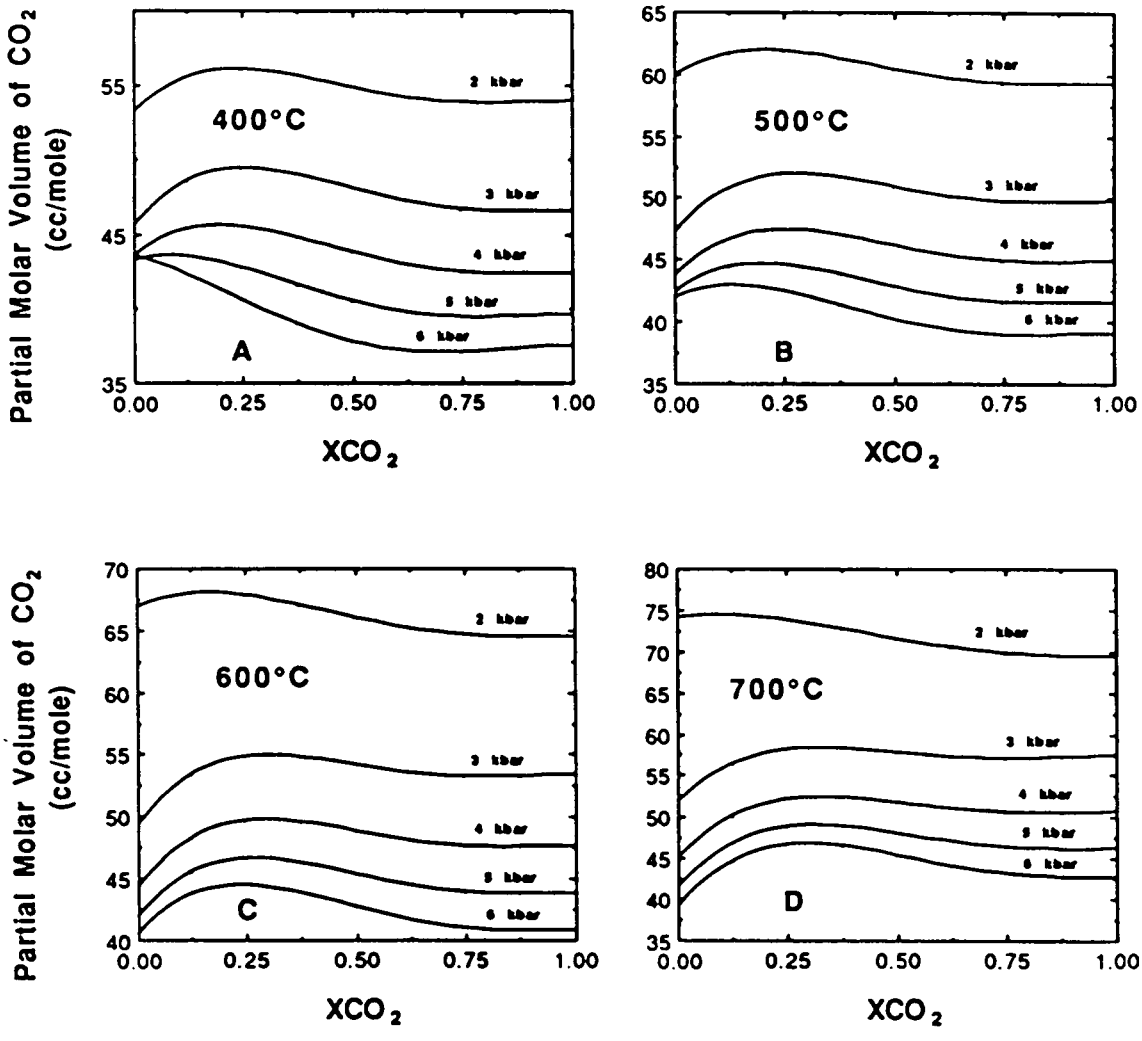

Figure 3.10 Partial molar volumes of CO_2 in CO_2-H_2O mixtures derived from Equation 3.20 from 2-6 kbar at 400°C (A), 500°C (B), 600°C (C) and 700°C (D). The 2 kbar isobars at 600°C and 700°C (Figs. 3.9c and d) and the 6 kbar isobar at 400°C (Fig. 3.9a) represent extrapolations beyond the range of data used to generate Equation 3.20.

3.9a-d (V_{H2O}) and 10a-d (V_{CO2}). The total variation in either V_{H2O} or V_{CO2} along any isobar shown is small relative to their absolute magnitudes. Compared with variations in PMVs of H_2O and NaCl in electrolyte solutions over similar P-T ranges (Bodnar, 1985), V_{H2O} and V_{CO2} in this binary system are almost independent of composition. This is consistent with the nearly ideal mixing of CO_2 and H_2O shown in Figs. 3.4a-d.

Isobars of PMVs at 2 kbars and 600° and 700°C and the 6 kbar isobar at 400°C shown in the corresponding diagrams of Figs. 3.9 & 3.10 as dashed curves, are outside the range of the data used to generate Eq. 3.20. Although our equation appears to predict reasonable MMVs along these isobars (Figs. 3.4a-d) the fact that they are extrapolations becomes apparent when calculating partial molar volumes. For example, the 2 kbar isobars of both V_{H2O} and V_{CO2} at 600° and 700°C (Figs. 3.9a-d and 3.10a-d, respectively) differ significantly in shape from the rest of the curves in each figure as does the 6 kbar isobar of V_{CO2} at 400°C (Fig. 3.10a).

DETERMINATION OF THE CO_2-H_2O SOLVUS

Empirical delineation of the solvus over a portion of PTX space in the CO_2-H_2O system was accomplished using measured total homogenization temperatures (Th (total)) of synthetic fluid inclusions formed in the one-phase field together with bulk compositions and MMVs determined as described above. Internal pressures at Th (total) were calculated for each inclusion using the equation of state for CO_2-H_2O of Connolly and Bodnar (1983). The pressure and temperature of total homogenization of each inclusion defines a point on the solvus unique to that particular bulk fluid composition and density, and thus, the array of many such points determined in this manner serves to delineate the boundary

between the one-phase and two-phase fields over a portion of PTX-space.

The above procedure for determining the solvus using synthetic fluid inclusion data can be illustrated using a schematic P-T projection of the CO_2-H_2O system at fixed composition of $X_{CO2} = 0.5$ (Fig. 3.11). Points A-D represent the formation conditions (P_F,T_F) of fluid inclusions in four different samples, all of which have the same bulk fluid composition ($X_{CO2} = 0.5$). Mean molar volumes of CO_2-H_2O fluids at each condition are calculated from Eq. 3.9 for $P_F \geq 2$ kbar, or using the equation of state of Connolly and Bodnar (1983) for inclusions synthesized at 1 kbar. The P-T trajectory of the isochore corresponding to each MMV and fluid composition (ρ_A-ρ_D) is then calculated using the equation of Connolly and Bodnar (1983)*. The intersection of the isochore with the total homogenization temperature of the inclusion (Th (total) = T_S) defines the pressure on the solvus (P_S) corresponding to that fluid composition and density. This technique is analogus to that employed by Knight and Bodnar (1989) in determining the critical pressures of H_2O-NaCl solutions.

Strictly speaking, P_S must be calculated using the MMV on the solvus (V_S). V_S, in turn, is derived from MMV at P_F and T_F (V_F) using T_S and P_S and the equations for V_Δ (Eq. 3.18) to correct for the volume change of the inclusion cavity between the two sets of P-T conditions. Thus, the quantities P_S and V_S were calculated iteratively using the equation of Connolly and Bodnar (1983) and the relation:

****

*The equation of Connolly and Bodnar was used because it is unique among the available equations of state for CO_2-H_2O mixtures in that it predicts reasonable MMVs at temperatures well below 400°C and thus, allows the extrapolation of isochores from formation conditions (P_F, T_F) down to P-T conditions on the solvus.

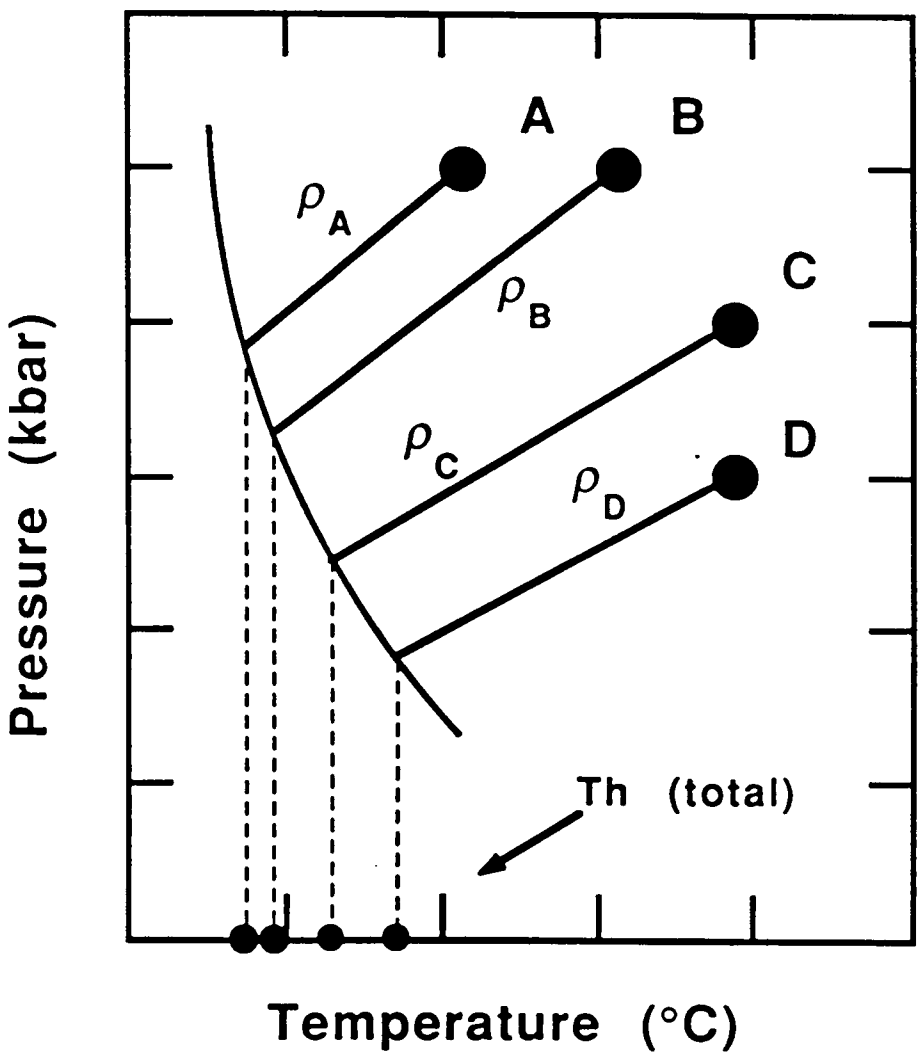

Figure 3.11 Schematic P-T projection of the CO_2-H_2O system at X_{CO2} = 0.5 illustrating the procedure for determining the solvus using synthetic fluid inclusions.

$$V_S = V_F \times (V_{\Delta (PS,TS)} / V_{\Delta (PF,TF)}) \qquad (3.24)$$

where P_S, V_S and T_S refer to conditions on the solvus, P_F, V_F and T_F refer to formation conditions and V_Δ is the volume change factor from Eq. 3.18. Acceptable values for P_S were achieved after two iterations. The complete array of individual P_S, T_S and X_{CO2} coordinates determined in this manner define the position of the solvus over a large portion of PTX-space.

Solvus coordinates determined from synthetic fluid inclusions in 83 samples grown over a wide range of P_F, T_F and X_{CO2} conditions are given in Appendix IV along with total homogenization temperatures (Th (total) = T_S) and corresponding mean molar volumes (V_S) and pressures (P_S) on the solvus. The mode of total homogenization is given as "l" to indicate total homogenization to the liquid phase or "v" signifying total homogenization to the vapor. The designations "c_l" and "c_v" imply total homogenization very near the critical point for that bulk composition but to the phase indicated by the subscript.

Total homogenization to the liquid (H_2O-rich phase) was observed for all but one inclusion containing 0.125 or 0.25 mole fraction CO_2. A few inclusions having bulk compositions of $X_{CO2} = 0.375$ displayed near-critical behavior at total homogenization (i.e. the meniscus separating the liquid and vapor phases had almost completely faded by Th (total); for a discussion of critical behavior in fluid inclusions see Sterner and Bodnar, 1984). Using measured Th (total)'s and calculated solvus pressures given in Appendix IV we can estimate the critical point for a mixture of 0.375 mole fraction CO_2 (actually $X_{CO2} = 0.3716 \pm 0.003$) to be at a temperature of 267° ± 2.5°C and at a pressure between 2440 and 2900 bars. The uncertainty in the pressure is difficult to estimate because the accuracy

of the Connolly and Bodnar equation of state at solvus conditions is unknown. Our estimate of the critical temperature for this composition is in good agreement with the value reported by Todheide and Franck (1963; T_C = 269°C for X_{CO2} = 0.375) but the critical pressure they report (P_C = 1500 bars) is 1000 to 1400 bars lower than our determination. On the other hand, the data of Takenouchi and Kennedy (1964) imply a much higher critical pressure for a fluid of composition 0.375 mole fraction CO_2 than our estimate of 2440 to 2900 bars.

Solvus coordinates in the CO_2-H_2O system determined using synthetic fluid inclusions as described above are shown as open circles in Figs. 3.12a-f for fluids containing 0.125, 0.25, 0.375, 0.50, 0.625 and 0.75 mole fraction CO_2, respectively. Also shown are the experimental determinations of Todheide and Franck (1963) and Takenouchi and Kennedy (1964) taken from their Figs. 3.2 and 3.8, respectively.

All inclusions with fluid compositions more CO_2-rich than XCO_2 = 0.375 displayed final homogenization to the vapor (CO_2-rich phase). The measurement of Th (total) to the vapor is subject to the same uncertainty as that described in the determination of Th (CO_2) in a previous section. As with the disappearance of the last bit of liquid CO_2 during homogenization of the CO_2 phases below 31.0°C, the final evaporation of the liquid coating the inclusion walls is difficult to detect with any degree of certainty. The result is that the apparent temperature of total homogenization to the vapor phase represents a minimum value for Th (total) and thus, a minimum value for T_S. In the delineation of the solvus for fluids of composition 0.125 and 0.25 mole fraction CO_2, average Th (total)'s of a few inclusions in each sample were used. This average value is reported in Appendix IV. In the case of total homogenization to the vapor, only the highest Th (total) measured in each sample was is reported in Appendix IV and it is these values that are plotted in Figs 3.12c-f. The average range in measured Th (total)'s for inclusions within the same

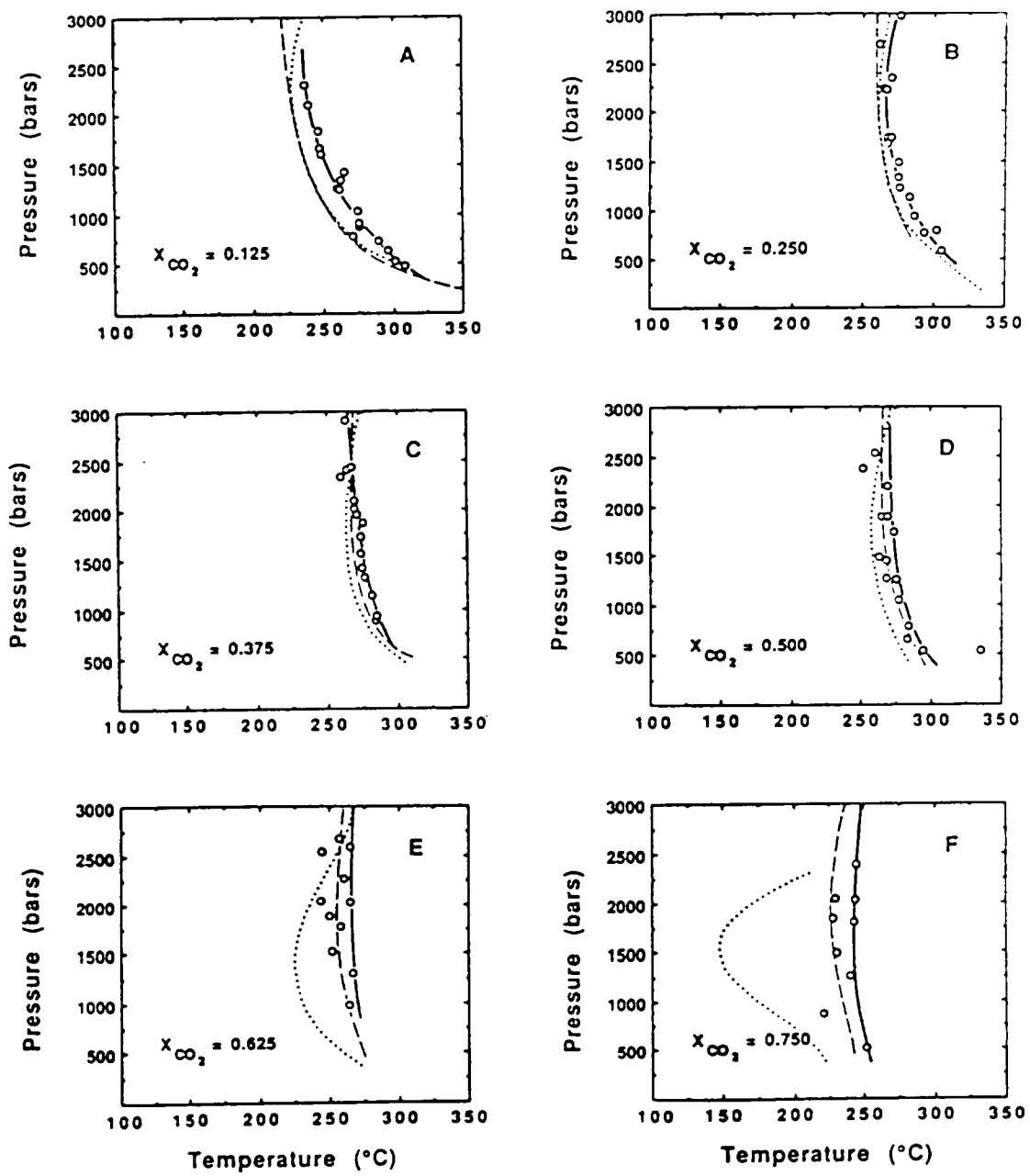

Figure 3.12 P-T projections of the solvus in the system CO_2-H_2O for compositions of 0.125 (A), 0.25 (B), 0.375 (C), 0.50 (D), 0.675 (E) and 0.75 (F). Open circles represent synthetic fluid inclusion data. Heavy solid lines indicate our estimated solvus position for each fluid composition (see text). Light solid and dashed curves represent the experimental determinations of Takenouchi and Kennedy (1964) and Todheide and Franck (1963), respectively.

sample was ~6°C for total homogenization to the liquid and ~25°C for total homogenization to the vapor. The solid curves drawn in Figs. 3.12a&b, therefore, represent solvus temperatures as a function of pressure for the indicated fluid compositions, whereas, the solid curves in Figs. 3.12c-f are understood to represent *minimum* temperatures at any given pressure.

Finally, the question arises of whether the inclusions used to determine the solvus have stretched or leaked during the measurement of Th (total). Those inclusions which displayed CO_2 homogenization to the liquid provided the opportunity to answer this question by re-measuring Th (CO_2) after the measurement of Th (total). This exercise was performed each time a Th (total) was measured and if the final Th (CO_2) was more than 0.2°C higher than the original determination (an infrequent occurance) the data were discarded. Inclusions in this study rarely showed any sign of stretching or partial decrepitation - either they decrepitated completely or they were unchanged by heating to Th (total). Inclusions that display CO_2 homogenization to the vapor were generally of considerably lower density compared with the others so it is even less likely that they would fail.

Phase relations between ~500 and ~3000 bars are in close agreement with the experimental determination of Todheide and Franck (1963). Somewhat higher temperatures (~15 - 20°C) are recorded for CO_2-poor (X_{CO2}=0.125) and CO_2-rich (X_{CO2}=0.75) compositions compared with their determination while considerably smaller (generally less than 5°C) discrepancies are found for intermediate compositions. Compared with the experimental determination of Takenouchi and Kennedy (1964) our study indicates considerably higher solvus temperatures for CO_2-rich compositions with maximum disagreement at about 1.5 kbars (eg. ~75°C for X_{CO2}=0.625, Fig. 3.12e; ~100°C for X_{CO2}=0.75, Fig. 3.12f). Figure 3.13 shows a P-X_{CO2} projection of the

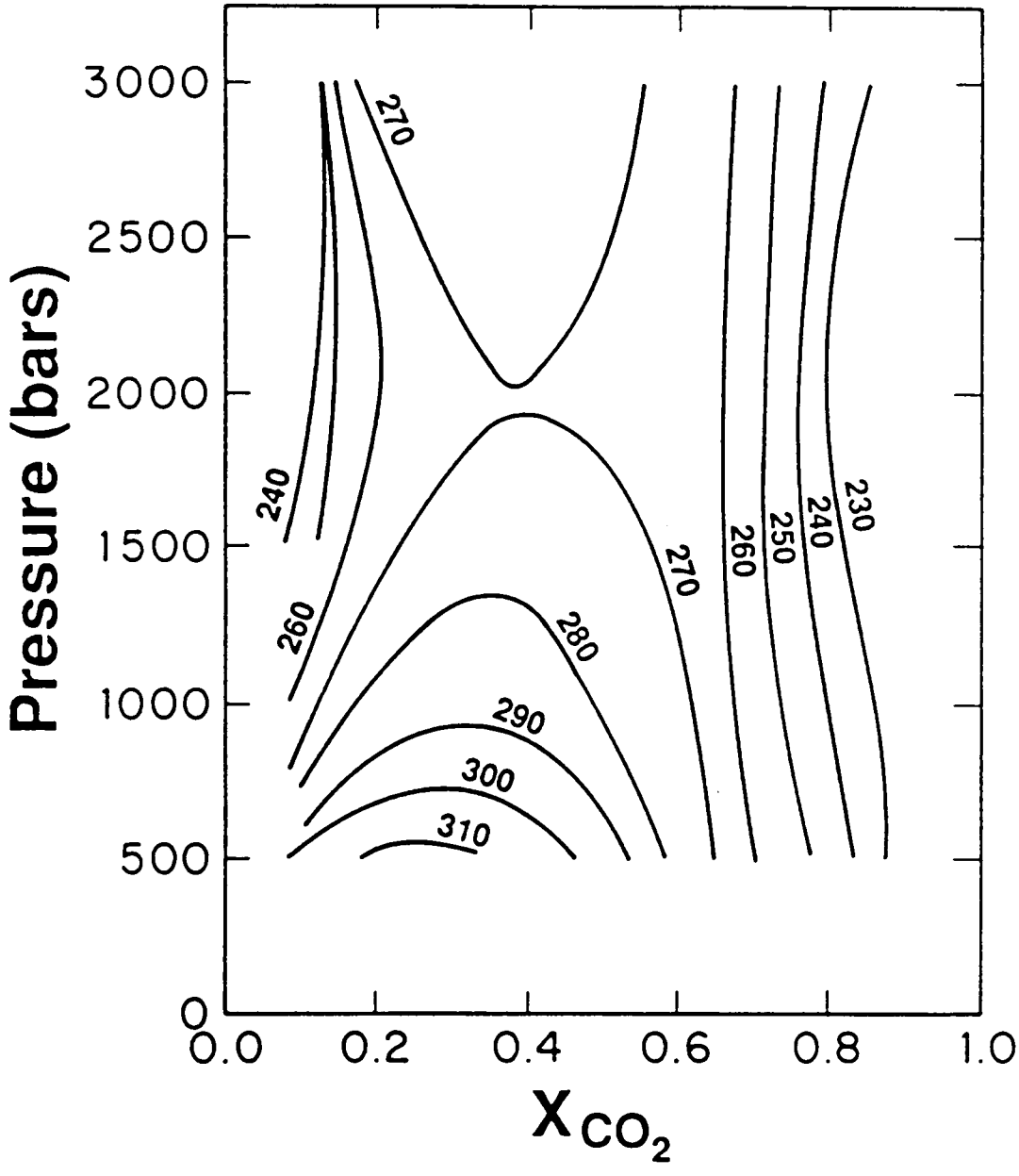

Figure 3.13 P-X projection of the solvus in the CO_2-H_2O system determined using synthetic fluid inclusions. Diagram was constructed by interpolation from solid curves in Figures 3.12a-f.

solvus in the CO_2-H_2O system constructed from the solid curves in Figs. 3.12a-f. According to our data, the thermal minimum on the CO_2-H_2O solvus occurs at ~2 kbars and X_{CO2}=0.37 and at a temperature of 269°C. This temperature is ~3-4°C higher than the above studies.

SUMMARY OF RESULTS

1) Deviations from ideal mixing of CO_2-H_2O mixtures are small (<2 cm^3/mole) and generally positive at high P and T.

2) Available equations of state predict pressures along isochores to within about ±500 bars.

3) Although the precision of the present determination is somewhat lower than generally achieved using more conventional approaches, the overall accuracy of our data (average σV_F = 1.16 %) may be reasonably close judging from intercomparisons between our data and that of Shmulovich et al. (1980) for CO_2-H_2O mixtures and Burnham et al. (1969) and Haar et al. (1984) for pure H_2O.

4) The solvus location in P-T-X space between ~500 and ~3000 bars is in close agreement with the experimental determination of Todheide and Frank (1963). Somewhat higher temperatures (~15 - 20°C) are recorded for CO_2-poor (X_{CO2}=0.125) and CO_2-rich (X_{CO2}=0.75) compositions compared with their determination while considerably smaller (generally less than 5°C) discrepancies are found for intermediate compositions.

5) Our solvus data for $X_{CO2} \geq 0.375$ actually represent minimum temperature estimates; they are slightly above those of Todheide and Frank (1963) and well above the determination of Takenouchi and Kennedy (1964) over much of this region. As we have discussed, it is possible that we have underestimated solvus temperatures in this region but it is unlikely that our reported temperatures are too high.

REFERENCES

Altunin V.V. and Gadetskii O.G. (1971) Equation of state and thermodynamic properties of liquid and gaseous carbon dioxide. *Thermal Engineering* **18**, 120-125.

Angus S., Armstrong B. and deReuck K.M. (1976) Carbon Dioxide: International Thermodynamic Tables of the Fluid State—3. Pergamon Press, Oxford, 385 pp.

Bodnar R.J. (1985) Pressure-Volume-Temperature-Composition (PVTX) Properties of the System H_2O-NaCl at Elevated Temperatures and Pressures. Unpublished Ph.D. thesis, The Pennsylvania State University.

Bodnar R.J. and Sterner S.M. (1985) Synthetic fluid inclusions in natural quartz. II. Application to PVT studies. *Geochim. Cosmochim. Acta* **49**, 1855-1859.

Bodnar R.J. and Sterner S.M. (1987) Synthetic fluid inclusions. In Hydrothermal Experimental Techniques (eds. G.C. Ulmer and H.L. Barnes), pp. 423-457. J. Wiley & Sons, New York.

Bodnar R.J., Burnham C.W. and Sterner S.M. (1985) Synthetic fluid inclusions in natural quartz. III. Determination of phase equilibrium properties in the system H_2O-NaCl to 100°C and 1500 bars. Geochim. Cosmochim. Acta 49, 1861-1873.

Boettcher A.L. and Kerrick D.M. (1971) Temperature calibration in cold-seal pressure vessels. In Research Techniques for High Pressure and High Temperature (ed. G.C. Ulmer). Springer-Verlag, New York, 367 pp.

Bottinga Y. and Richet P. (1981) High pressure and temperature equation of state and calculation of the thermodynamic properties of gaseous carbon dioxide. *Am. J. Sci.* **281**, 615-660.

Bowers T.S. and Helgeson H.C. (1983) Calculation of the thermodyanamic and geochemical consequences of nonideal mixing the system H_2O-CO_2-NaCl on phase relations in geologic systems: Equation of state for H_2O-CO_2-NaCl fluids at high pressures and temperatures. *Geochim. Cosmochim. Acta* **47**, 1247-1275.

Burnham C.W., Holloway J.R. and Davis N.F. (1969) The specific volume of water in the range 1000 to 8900 bars, 20° to 900°C. *Am. J. Sci.* **267-A**, 70-95.

Burruss R.C. (1981) Analysis of phase equilibria in C-O-H-S fluid inclusions. In Fluid Inclusions: Applications to Petrology (eds. L.S. Hollister and M.L. Crawford). Mineral. Assoc. Canada, Short Course Handbook **6**, 39-74.

Connolly, J.A.D. and Bodnar, R.J. 91983) A modified Redlich-Kwong equation of state for H_2O-CO_2 mixtures--Application to fluid inclusion studies (abs). *EOS* **64**, 350.

Dodds W.S., Stutzman L.F. and Sollami B.J. (1956) Carbon dioxide solubility in water. *Industrial and Engineering Chemistry* **1**, 92-95.

Franck E.U. and Tödheide K. (1959) Thermische Eigenschaften überkritischer Mischungen von Kohlendioxyd und Wasser bis zu 750°C and 2000 Atm. *Z. physik. Chem. Neue Folge*, Bd. **22**, 232-245.

Greenwood H.J. (1969) The compressibility of gaseous mixtures of carbon dioxide and water between 0 and 500 bars pressure and 450° and 850°C. *Am. J. Sci.* **267-A**, 191-208.

Haar L., Gallagher J.S. and Kell G.S. (1984) NBS/NRC Steam Tables: Thermodynamic and Transport Properties and Computer Programs for Vapor and Liquid States of Water in SI Units. Hemisphere Publishing Corporation, Washington, D.C., 320 pp.

Holloway J.R. (1981) Compositions and volumes of supercritical fluids in the earth's crust. In Fluid Inclusions: Applications to Petrology (eds. L.S. Hollister and M.L. Crawford). Mineral. Assoc. Canada, Short Course Handbook **6**, 13-38.

Hosieni K.R., Howald R.A. and Scanlon M.W. (1985) Thermodynamics of the lambda transition and the equation of state of quartz. *Am. Mineral.* **70**, 782-793.

Juza J., Kmonicek V. and Sifner O. (1965) Measurements of the specific volume of carbon dioxide in the range of 700 to 4000b and 50 to 475°C. *Physica* **31**, 1735-1744.

Keenan J.H., Keyes F.G., Hill P.G. and Moore, J.G. (1978) Steam Tables--Thermodynamic Properties of Water, including Vapor, Liquid, and Solid Phases. John Wiley and Sons, New York, 156 p.

Kennedy G.C. (1964) Pressure-volume-temperature relations in CO_2 at elevated temperatures and pressures. *Am. J. Sci.* **252**, 225-241.

Kerrick D.M. and Jacobs G.K. (1981) A modified Redlich-Kwong equation for H_2O, CO_2, and H_2O-CO_2 mixtures at elevated pressures and temperatures. *Am. J. Sci.* **281**, 735-767.

Khitarov N.I. and Malinin C.D. (1956) Experimental characteristics of a part of the system H_2O-CO_2. *Geochem. Internat.* **3**, 246-256.

Knight C.L. and Bodnar R.J. (1989) Synthetic fluid inclusions: IX. Critical PVTX properties of NaCl-H2O solutions. *Geochim. Cosmochim. Acta* **53**, 3-8.

Lemmlein G.G. and Klevtsov P.V. (1961) Relations among the principal thermodynamic parameters in a part of the system H_2O-NaCl. *Geochemistry* **1956**, 630-642.

Lowry H.H. and Erickson W.R. (1927) The densities of coexisting liquid and gaseous carbon dioxide and the solubility of water in liquid carbon dioxide. *J. Am. Chem. Soc.* **49**, 2729-2734.

Malinin S.D. (1959) The system water-carbon dioxide at high temperatures and pressures. *Geochem. Internat.* **3**, 292-306.

Malinin S.D. (1974) Thermodynamics of the H_2O-CO_2 system. *Geochem. Internat.* **10**, 1523-1549.

Parkinson W.J. and De Nevers N. (1969) Partial molal volume of carbon dioxide in water solutions. *I & EC Fundamentals* **8**, 709-713.

Roeder E. (1984) *Fluid Inclusions*. Mineralogical Society of America, Reviews in Mineralogy **12**, 644 p.

Shmonov V.M. and Shmulovich K.I. (1974) Molar volumes and the equation of state for CO_2 at 100-1000°C and 200-20,000 bar. *Dokl. AN SSSR* **217**, No. 4.

Shmulovich K.I., Shmonov V.M., Mazur V.A. and Kalinichev A.G. (1980) P-V-T and activity concentration relations in the H_2O-CO_2 system (homogeneous solutions). *Geochem. Internat.***12**, 1807-1824.

Song K.Y. and Kobayashi R. (1987) Water content of CO_2 in equilibrium with liquid water and/or hydrates. *SPE Formation Evaluation* **2**, 500-508.

Sterner S.M. and Bodnar R.J. (1984) Synthetic fluid inclusions in natural quartz. I. Compositional types synthesized and applications to experimental geochemistry. *Geochim. Cosmochim. Acta* **48**, 2659-2668.

Takenouchi S. and Kennedy G.C. (1961) The binary system H_2O-CO_2 at high temperatures and pressures. *Am. J. Sci.* **262**, 1055-1074.

Taylor, J.R. (1982) An Introduction to Error Analysis: The Study of Uncertainties in Physical Measurements. University Science Books, Mill Valley, California, 270 p.

Tödheide K. and Franck E.U. (1963) Das Zweiphaseugebiet und die kritische Kurve im System Kohlendioxid—Wasser bis zu Drucken von 3500 bar. *Z. physik. Chem. Neue Folge*, Bd. **37**, 387-401.

Werre R.W. Jr., Bodnar R.J., Bethke P.M. and Barton P.B. Jr. (1979) A novel gas-flow fluid inclusions heating/freezing stage. *Geol. Soc. Am. Abs. with prog.* **11**, 539.

Zakirov I.V. (1984) The P-V-T relations in the H_2O-CO_2 system at 300 and 400°C. *Geochem. Internat.* **21**, 13-20.

Zheleznyi B.V. (1969) The density of supercooled water. *Russian J. Phys. Chem.* **43**, 1311-1312.

APPENDIX I

Experimental conditions, microthermometric data and calculated mean molar volumes of synthetic fluid inclusions in the CO_2-H_2O binary system. T_F(°C) and P_F(bar) are the formation conditions, X_{CO2} is the mole fraction of CO_2, N is the number of inclusions measured and Th(CO_2) and σ_{Th} refer to the CO_2 homogenization temperature and associated uncertainty in this measurement, respectively. CO_2 homogenization to the liquid is indicated by "l" and homogenization to the vapor by "v". V_F is the mean molar volume at P and T, σV_F is the estimated error and "% Error" is the relative error.

T_F(°C)	P_F(bar)	X_{CO2}	N	Th(CO_2)	σ_{Th}	Mode	V_F	σV_F	% Error
400	1000	0.4964	5	30.4	0.46	v	70.223*	2.486	3.540
400	2000	0.7473	6	18.34	0.33	l	46.428	0.463	0.998
400	2000	0.4964	14	23.95	0.33	l	39.197	0.367	0.937
400	2000	0.3716	5	26.18	0.47	l	34.875	0.415	1.189
400	2000	0.2473	6	29.3	0.2	l	30.815	0.341	1.107
400	2000	0.1234	2	30	0.2	v	30.486*	0.581	1.907
400	3000	0.8736	6	-3.1	2.29	l	43.300	0.718	1.658
400	3000	0.7473	12	1.29	0.33	l	40.615	0.404	0.995
400	3000	0.6216	13	4.84	0.36	l	37.540	0.360	0.958
400	3000	0.4964	16	9.83	0.72	l	34.544	0.346	1.000
400	3000	0.3716	7	13.98	0.39	l	31.073	0.273	0.878
400	3000	0.2473	8	21.83	1.02	l	27.902	0.439	1.574
400	3000	0.1234	5	29.28	0.2	l	24.139	0.300	1.242
400	4000	0.8736	4	-17.9	0.6	l	40.161	0.448	1.115
400	4000	0.7473	5	-15.6	1.28	l	37.330	0.440	1.179
400	4000	0.6216	8	-10.16	1.36	l	34.827	0.409	1.174
400	4000	0.4964	13	-6.06	0.73	l	31.932	0.312	0.978
400	4000	0.3716	12	-0.48	0.29	l	28.979	0.249	0.861
400	4000	0.2473	7	10.38	0.73	l	26.196	0.498	1.901
400	4000	0.1234	4	24.5	0.4	l	23.084	0.260	1.127
400	5000	0.4964	3	-16.2	0.28	l	30.758	0.285	0.926
400	5000	0.3716	8	-12.51	0.69	l	27.842	0.262	0.943
400	5000	0.2473	18	-5.15	1.21	l	24.946	0.273	1.094
400	5000	0.1234	7	15.82	4.42	l	22.268	1.013	4.549
500	1000	0.7473	4	30.83	0.2	v	89.179*	2.876	3.226
500	1000	0.4964	4	30.27	0.2	v	72.053*	1.098	1.524
500	2000	0.7473	7	25.33	0.2	l	51.592	0.502	0.972
500	2000	0.6216	5	27.2	0.2	l	47.754	0.448	0.938
500	2000	0.3716	5	30	0.2	l	38.807	0.516	1.330
500	2000	0.2473	3	30.85	0.2	v	40.481*	1.942	4.798
500	2000	0.1234	2	27	0.2	v	34.355*	0.350	1.018

* calculated V_F is substantially in error because of CO_2 homogenization to the vapor (see text)

APPENDIX I Cont'd.

T_F(°C)	P_F(bar)	X_{CO2}	N	Th(CO_2)	σ_{Th}	Mode	V_F	σV_F	% Error
500	3000	0.8736	10	7.28	1.3	l	46.534	0.629	1.352
500	3000	0.7473	10	11.63	0.61	l	43.793	0.466	1.065
500	3000	0.6216	8	16.34	0.28	l	40.980	0.385	0.940
500	3000	0.4964	14	20.18	0.53	l	37.615	0.380	1.009
500	3000	0.3716	15	24.18	0.53	l	34.025	0.383	1.125
500	3000	0.2473	10	29.11	0.43	l	30.753	0.555	1.805
500	3000	0.1234	6	30.34	0.2	v	29.950*	0.718	2.399
500	4000	0.8736	10	-8.06	0.36	l	42.288	0.462	1.092
500	4000	0.7473	9	-2.61	0.64	l	39.863	0.417	1.045
500	4000	0.6216	13	2.64	0.31	l	37.183	0.352	0.946
500	4000	0.3716	10	13.64	0.51	l	31.097	0.289	0.928
500	4000	0.2473	10	22.61	0.47	l	28.149	0.290	1.029
500	4000	0.1234	4	30.07	0.2	l	24.584	0.396	1.612
500	5000	0.7473	3	-16.7	0.28	l	37.261	0.374	1.003
500	5000	0.6216	16	-11.1	1.03	l	34.787	0.381	1.096
500	5000	0.4964	14	-3.37	1.25	l	32.359	0.368	1.139
500	5000	0.3716	8	1.8	0.52	l	29.305	0.267	0.910
500	5000	0.2473	11	12.78	0.3	l	26.523	0.226	0.852
500	5000	0.1234	10	27.14	0.3	l	23.563	0.274	1.162
500	6000	0.4964	3	-19.6	0.2	l	30.525	0.282	0.923
500	6000	0.3716	10	-12.04	0.92	l	27.945	0.277	0.991
500	6000	0.2473	6	0.8	0.97	l	25.384	0.264	1.039
500	6000	0.1234	10	19.97	0.88	l	22.619	0.323	1.426
600	1000	0.4964	10	19.47	9.18	v	128.812*		8.833
600	2000	0.4964	9	30.73	0.21	l	49.561	1.312	2.646
600	2000	0.2473	5	30.63	0.25	v	42.696*	1.438	3.369
600	3000	0.7473	11	18.26	0.47	l	46.993	0.493	1.048
600	3000	0.6216	8	21.2	0.6	l	43.514	0.487	1.119
600	3000	0.4964	7	24.32	0.2	l	39.916	0.345	0.865
600	3000	0.3716	9	27.59	0.29	l	36.241	0.38	1.049
600	3000	0.2473	5	30.43	0.2	l	32.633	0.612	1.876
600	3000	0.1234	6	28.48	0.3	v	32.964*	0.542	1.645
600	4000	0.8736	4	0	1	l	44.573	0.537	1.205
600	4000	0.7473	10	6.82	0.65	l	42.498	0.447	1.051
600	4000	0.6216	8	11.51	0.44	l	39.621	0.378	0.954
600	4000	0.4964	11	16.72	0.64	l	36.641	0.378	1.031
600	4000	0.3716	9	21.63	0.46	l	33.266	0.328	0.987
600	4000	0.2473	8	27.8	0.28	l	30.086	0.323	1.073
600	4000	0.1234	5	30.3	0.2	v	30.179*	0.700	2.318
600	5000	0.8736	6	-12.58	1.13	l	41.549	0.498	1.198
600	5000	0.7473	4	-6.07	0.2	l	39.346	0.384	0.976
600	5000	0.6216	16	-1.35	2.19	l	36.587	0.584	1.595

* calculated V_F is substantially in error because of CO_2 homogenization to the vapor (see text)

APPENDIX I Cont'd.

T_F(°C)	P_F(bar)	X_{CO2}	N	Th(CO_2)	σ_{Th}	Mode	V_F	σV_F	% Error
600	5000	0.4964	17	6.01	0.55	l	34.052	0.321	0.942
600	5000	0.3716	15	12.84	0.7	l	31.090	0.312	1.005
600	5000	0.2473	16	21.96	1.66	l	28.131	0.667	2.371
600	5000	0.1234	7	29.45	0.39	l	24.383	0.512	2.101
600	6000	0.6216	5	-13.1	0.82	l	34.656	0.354	1.02
600	6000	0.3716	6	2.84	0.2	l	29.544	0.253	0.856
600	6000	0.2473	7	14.93	0.43	l	26.891	0.244	0.908
600	6000	0.1234	5	27.95	0.2	l	23.834	0.250	1.048
700	3000	0.8736	2	20.3	0.2	l	54.050	0.533	0.985
700	3000	0.7473	7	22.53	0.3	l	50.371	0.497	0.987
700	3000	0.6216	4	24.77	0.2	l	46.525	0.434	0.933
700	3000	0.4964	7	27.05	0.2	l	42.558	0.395	0.928
700	3000	0.3716	5	29.52	0.2	l	38.867	0.448	1.152
700	3000	0.2473	3	29.25	0.2	v	48.700*	0.545	1.118
700	3000	0.1234	3	27.25	0.2	v	34.885*	0.372	1.065
700	4000	0.8736	3	5.6	0.85	l	47.149	0.538	1.142
700	4000	0.4964	6	20.32	0.2	l	38.625	0.338	0.874
700	4000	0.3716	3	24.95	0.2	l	35.232	0.302	0.856
700	4000	0.2473	2	29.2	0.2	l	31.605	0.348	1.100
700	4000	0.1234	3	29.7	0.2	v	31.839*	0.530	1.666
700	5000	0.8736	7	-4.65	0.55	l	44.069	0.474	1.076
700	5000	0.7473	8	0.03	0.2	l	41.393	0.402	0.971
700	5000	0.6216	13	6.9	0.27	l	39.011	0.361	0.926
700	5000	0.4964	13	13.07	0.26	l	36.202	0.316	0.872
700	5000	0.3716	8	18.29	0.44	l	32.832	0.304	0.925
700	5000	0.2473	6	24.16	0.27	l	29.204	0.263	0.900
700	5000	0.1234	4	29.67	0.2	v	31.732*	0.518	1.633
700	6000	0.8736	4	-18.67	0.2	l	40.813	0.431	1.056
700	6000	0.7473	5	-12.98	0.44	l	38.481	0.391	1.015
700	6000	0.6216	4	-5.6	1.06	l	36.204	0.400	1.105
700	6000	0.4964	4	2.33	0.42	l	33.744	0.310	0.918
700	6000	0.3716	8	11.09	0.2	l	31.079	0.264	0.850
700	6000	0.2473	5	17.48	0.2	l	27.592	0.232	0.839
700	6000	0.1234	7	28.97	0.2	l	24.430	0.288	1.180

* calculated V_F is substantially in error because of CO_2 homogenization to the vapor (see text)

APPENDIX II

```
********** PROGRAM MOLVOL **********
*     THIS PROGRAM CALCULATES MMVs OF CO2-H2O MIXTURES                *
*     FROM THE FOLLOWING INPUT DATA FROM SYNTHETIC FLUID INCLUSIONS   *
*     PF=SYNTHESES PRESSURE IN BARS;  TF=SYNTHESES TEMPERATURE IN °C; *
*     XCO2;TH=TH(CO2);  MODE=MODE OF CO2 L/V HOMOGENIZATION,          *
*     1=TO THE LIQUID, 2=TO THE VAPOR                                 *
*     PROGRAM WRITTEN BY S. MICHAEL STERNER 10/9/88                   *
*******************************************************************************
      IMPLICIT DOUBLE PRECISION (A-Z)
      INTEGER MODE
      SAVE
   10 CONTINUE
      WRITE(9,*)'ENTER PF,TF,XCO2,TH,MODE'
      READ(9,*)PF,TF,XCO2,TH,MODE
      IF(TF.EQ.99.)GOTO 40
      MMVPT=0.0D0
C       MOLECULAR WEIGHTS
        MWH2O = 18.0152D0
        MWCO2 = 44.0098D0
        MWAGOX = 303.7556D0
        SAM=0.0D0
      WTFCO2=(XCO2*MWCO2)/((XCO2*MWCO2)+((1.0D0-XCO2)*MWH2O))
      WTFH2O=1.0D0-WTFCO2
C     ASSUME 1 GRAM TOTAL SOLUTION
      GCO2=WTFCO2
      GH2O=WTFH2O
C     CALCULATE GMCO2/100GMH2O IN AQUEOUS PHASE (CO2A)
      CO2A=7.2754D0-5.6634D-2*TH+7.8770D-4*TH**2-2.0370D-5*TH**3
C     CALCULATE GRAMS OF CO2 DISSOLVED IN AQUEOUS PHASE (GCO2A)
      GCO2A=GH2O*(CO2A/100.0D0)
C     CALCULATE CO2 DENSITY IN CO2 PHASE (RHOCO2) USING EQUATIONS
C     FROM LOWREY AND ERICKSON (1927)
      TMOD=31.0D0-TH
       IF(DABS(1.0D0-MODE).LT.0.010D0) THEN
         RHOCO2=0.4683D0+0.001442D0*TMOD+0.1318D0*TMOD**(1.0D0/3.0D0)
       ELSE
         RHOCO2=0.4683D0+0.001442D0*TMOD-0.1318D0*TMOD**(1.0D0/3.0D0)
       ENDIF
C     CALCULATE DENSITY OF AQUEOUS PHASE (RHOAQ)
      RHOAQ=1.0014D0+5.2777D-5*TH-1.0113D-5*TH**2+9.3537D-8*TH**3
C     CALCULATE VOLUME OF CO2 PHASE (VGAS)
      GCO2V=GCO2-GCO2A
      VGAS=GCO2V/RHOCO2
C     CALCULATE VOLUME OF AQUEOUS PHASE (VAQ)
      VAQ=(GH2O+GCO2A)/RHOAQ
C     CALCULATE BULK DENSITY (RHOBLK)
      RHOBLK=1.0D0/(VGAS+VAQ)
C     CALCULATE TOTAL VOLUME (V25) AND MMV (MMV25) AT ROOM TEMP
      V25=VGAS+VAQ
```

APPENDIX II Cont'd.

```
      MCO2=GCO2/MWCO2
      MH2O=GH2O/MWH2O
      TOTM=MH2O+MCO2
      SV25=V25/(GCO2+GH2O)
      MMV25=(V25)/TOTM
C     CALCULATE MMV AT P & T OF FORMATION BY CORRECTING FOR
C     EXPANSION AND CONTRACTION OF QUARTZ
      CALL QTZ(PF,TF,VCOREC)
      MMVPT=MMV25*VCOREC
      SVPT=SV25*VCOREC
      WRITE(9,1000)PF,TF,XCO2,TH,MODE,MMVPT,SVPT
 1000 FORMAT(1X,F5.0,1X,F4.0,1X,F6.4,1X,F6.2,1X,I1,1X,F6.2,1X,F7.4)
      GOTO 10
  40 CONTINUE
      STOP
      END
********** PROGRAM QTZ **********
*     THIS PROGRAM CORRECTS FLUID INCLUSION VOLUMES FOR THERMAL     *
*     EXPANSION AND COMPRESSIBILITY EXPERIENCED BY THE QUARTZ HOST  *
*     WHEN TAKEN FROM 20°C AND 1 BAR TO SOME FINAL P-T. THE         *
*     CORRECTED INCLUSION VOLUME IS VNEW = VOLD*VCOREC.             *
*     EQUATION OF STATE FOR QTZ FROM HOSIENI et al.(1985)           *
*********************************************************************
      SUBROUTINE QTZ(PBAR,TC,VCOREC)
      DOUBLE PRECISION ALPHA(7,5),BETA(5,5)
      IMPLICIT DOUBLE PRECISION (A-H,O-Z)
      T=273.15D0+TC
      P=PBAR/10
      TAB=846D0+0.265D0*P-0.11303229D-4*P*P-2.4632558D-9*P**3
      TMS=TAB-61D0
C     CALCULATE VOLUME OF ALPHA QUARTZ
      IF(T.LT.TMS) THEN
      DATA(ALPHA(1,J),J=1,5)/24.340296D0,3.238095D-4,7.855450D-7,
     A 1.018418D-9,5.083011D-13/
      DATA(ALPHA(2,J),J=1,5)/-1.218243D-4,-5.371956D-7,-1.357596D-9,
     A -1.73248D-12,-8.66629D-16/
      DATA(ALPHA(3,J),J=1,5)/1.170823D-7,5.474543D-10,1.376992D-12,
     A 1.886086D-15,9.986443D-19/
      DATA(ALPHA(4,J),J=1,5)/-7.99760D-11,-3.38035D-13,-8.22533D-16,
     A -1.14072D-18,-6.00664D-22/
      DATA(ALPHA(5,J),J=1,5)/3.031544D-14,1.203374D-16,2.743039D-19,
     A 3.586603D-22,1.754802D-25/
      DATA(ALPHA(6,J),J=1,5)/-5.78773D-18,-2.23346D-20,-4.71042D-23,
     A -5.49837D-26,-2.30557D-29/
      DATA(ALPHA(7,J),J=1,5)/4.329322D-22,1.658714D-24,3.241953D-27,
     A 3.236415D-30,1.010065D-33/
      SUM=-ALPHA(1,1)
      DO 20 J=1,5
       DO 20 I=1,7
```

```
        AAA=ALPHA(I,J)*((T-1000.D0)**(J-1))*(P**(I-1))
        SUM=AAA+SUM
   20 CONTINUE
        V=ALPHA(1,1)*(1D0+SUM)
       GO TO 50
       ELSE
C      CALCULATE VOLUME OF ALPHA QUARTZ BETWEEN A/B TRANSITION AND
C      60°C BELOW IT.
       DATA(BETA(1,J),J=1,5)/23.701266D0,-.1058728D-5,.854633D-8,
     A -.188601D-10,.1440728D-13/
       DATA(BETA(2,J),J=1,5)/-.1520712D-4,.2042034D-7,-.519449D-10,
     A .974922D-13,-0.714101D-16/
       DATA(BETA(3,J),J=1,5)/.2441776D-8,-0.806657D-11,.1837775D-13,
     A -.490703D-16,.492830D-19/
       DATA(BETA(4,J),J=1,5)/-.116290D-11,.3979281D-14,-.368804D-17,
     A .917195D-20,-.127623D-22/
       DATA(BETA(5,J),J=1,5)/.2140223D-15,-.80183D-18,.596339D-21,
     A -.701148D-24,.1175194D-26/
       IF(T.LT.TAB) THEN
       SUM=-BETA(1,1)
       DO 25 J=1,5
        DO 25 I=1,5
        AAA=BETA(I,J)*((T-1000.D0)**(J-1))*(P**(I-1))
        SUM=AAA+SUM
   25 CONTINUE
        VBETA=BETA(1,1)*(1D0+SUM)
       RLAM=0.265D0-2D0*0.11303229D-4*P-3D0*2.4632558D-9*P**2
       TH=TAB-T
       F=(.00351508*TH-.158514D-4*TH**2+.73366D
     A -7*TH**3-.116609D-9*TH**4)**0.5D0
       DELV=(RLAM/0.265D0)*F
       V=VBETA-DELV
       GO TO 50
       ELSE
C      CALCULATE VOLUME OF BETA QUARTZ
       SUM=-BETA(1,1)
       DO 30 J=1,5
        DO 30 I=1,5
        AAA=BETA(I,J)*((T-1000.D0)**(J-1))*(P**(I-1))
        SUM=AAA+SUM
   30 CONTINUE
        V=BETA(1,1)*(1D0+SUM)
   50 CONTINUE
       V20=22.65638
       VCOREC=V/V20
         ENDIF
         ENDIF
         RETURN
         END
```

APPENDIX III

Volumetric properties of CO_2-H_2O mixtures calculated using Eqn. 3.20. V_{H2O} is the molar volume of pure H_2O, V_R is the MMV of the mixture in excess of V_{H2O} at the same P and T, $V_{CO2\text{-}H2O}$ is the MMV of the mixture, V^{ID} is the ideal molar volume, V^{EX} is the excess volume of mixing and V_{H2O} and V_{CO2} are the partial molar volumes of H_2O and CO_2, respectively.

P (bar)	T (°C)	X_{CO2}	V_{H2O}	V_R	$V_{CO2\text{-}H2O}$	V^{ID}	V^{EX}	V_{H2O}	V_{CO2}
2000	400	0.0	22.73	0.00	22.73	22.73	0.00	22.73	53.19
2000	400	0.1	22.73	3.17	25.90	25.85	0.04	22.63	55.29
2000	400	0.2	22.73	6.49	29.22	28.98	0.24	22.50	56.07
2000	400	0.3	22.73	9.85	32.58	32.10	0.47	22.53	56.01
2000	400	0.4	22.73	13.16	35.89	35.23	0.66	22.81	55.51
2000	400	0.5	22.73	16.38	39.10	38.35	0.75	23.33	54.88
2000	400	0.6	22.73	19.47	42.20	41.48	0.72	24.00	54.32
2000	400	0.7	22.73	22.45	45.17	44.60	0.57	24.64	53.97
2000	400	0.8	22.73	25.35	48.08	47.73	0.35	24.97	53.86
2000	400	0.9	22.73	28.25	50.98	50.85	0.13	24.62	53.91
2000	400	1.0	22.73	31.25	53.98	53.98	0.00	23.12	53.98
3000	400	0.0	21.10	0.00	21.10	21.10	0.00	21.10	45.53
3000	400	0.1	21.10	2.60	23.70	23.65	0.05	20.97	48.22
3000	400	0.2	21.10	5.40	26.50	26.19	0.30	20.79	49.31
3000	400	0.3	21.10	8.26	29.36	28.74	0.62	20.79	49.36
3000	400	0.4	21.10	11.08	32.18	31.29	0.89	21.08	48.84
3000	400	0.5	21.10	13.79	34.89	33.84	1.05	21.70	48.09
3000	400	0.6	21.10	16.36	37.45	36.39	1.07	22.57	47.38
3000	400	0.7	21.10	18.76	39.86	38.94	0.92	23.52	46.86
3000	400	0.8	21.10	21.04	42.13	41.48	0.65	24.29	46.60
3000	400	0.9	21.10	23.25	44.34	44.03	0.31	24.50	46.55
3000	400	1.0	21.10	25.48	46.58	46.58	0.00	23.69	46.58
4000	400	0.0	20.01	0.00	20.01	20.01	0.00	20.01	43.51
4000	400	0.1	20.01	2.45	22.46	22.25	0.21	19.94	45.18
4000	400	0.2	20.01	5.01	25.02	24.49	0.53	19.87	45.62
4000	400	0.3	20.01	7.57	27.58	26.73	0.85	19.99	45.30
4000	400	0.4	20.01	10.05	30.06	28.97	1.09	20.38	44.59
4000	400	0.5	20.01	12.40	32.41	31.21	1.20	21.04	43.78
4000	400	0.6	20.01	14.59	34.61	33.45	1.16	21.89	43.08
4000	400	0.7	20.01	16.64	36.65	35.68	0.97	22.77	42.60
4000	400	0.8	20.01	18.57	38.59	37.92	0.67	23.41	42.38
4000	400	0.9	20.01	20.46	40.47	40.16	0.31	23.48	42.36
4000	400	1.0	20.01	22.39	42.40	42.40	0.00	22.54	42.40
5000	400	0.0	19.20	0.00	19.20	19.20	0.00	19.20	43.22
5000	400	0.1	19.20	2.43	21.63	21.24	0.39	19.19	43.57

APPENDIX III Cont'd.

P (bar)	T (°C)	X_{CO2}	V_{H2O}	V_R	$V_{CO2-H2O}$	V^{ID}	V^{EX}	V_{H2O}	V_{CO2}
5000	400	0.2	19.20	4.85	24.05	23.28	0.77	19.28	43.15
5000	400	0.3	19.20	7.18	26.39	25.32	1.06	19.56	42.31
5000	400	0.4	19.20	9.38	28.59	27.36	1.23	20.08	41.35
5000	400	0.5	19.20	11.43	30.64	29.40	1.24	20.79	40.49
5000	400	0.6	19.20	13.33	32.53	31.44	1.10	21.56	39.85
5000	400	0.7	19.20	15.11	34.31	33.48	0.83	22.19	39.51
5000	400	0.8	19.20	16.82	36.02	35.52	0.50	22.40	39.43
5000	400	0.9	19.20	18.54	37.75	37.56	0.19	21.84	39.51
5000	400	1.0	19.20	20.39	39.60	39.60	0.00	20.06	39.60
6000	400	0.0	18.56	0.00	18.56	18.56	0.00	18.56	43.58
6000	400	0.1	18.56	2.46	21.01	20.46	0.56	18.62	42.59
6000	400	0.2	18.56	4.78	23.34	22.35	0.99	18.85	41.27
6000	400	0.3	18.56	6.93	25.49	24.25	1.24	19.31	39.90
6000	400	0.4	18.56	8.90	27.45	26.14	1.31	19.96	38.69
6000	400	0.5	18.56	10.68	29.24	28.04	1.20	20.70	37.78
6000	400	0.6	18.56	12.33	30.89	29.94	0.95	21.36	37.24
6000	400	0.7	18.56	13.88	32.44	31.83	0.61	21.68	37.05
6000	400	0.8	18.56	15.43	33.99	33.73	0.26	21.35	37.15
6000	400	0.9	18.56	17.08	35.64	35.62	0.02	19.98	37.38
6000	400	1.0	18.56	18.96	37.52	37.52	0.00	17.10	37.52
2000	500	0.0	26.06	0.00	26.06	26.06	0.00	26.06	59.85
2000	500	0.1	26.06	3.47	29.54	29.39	0.15	25.99	61.48
2000	500	0.2	26.06	7.06	33.12	32.71	0.41	25.91	61.97
2000	500	0.3	26.06	10.66	36.72	36.03	0.69	26.00	61.74
2000	500	0.4	26.06	14.19	40.25	39.35	0.90	26.32	61.14
2000	500	0.5	26.06	17.61	43.67	42.68	1.00	26.90	60.45
2000	500	0.6	26.06	20.89	46.96	46.00	0.96	27.64	59.84
2000	500	0.7	26.06	24.05	50.12	49.32	0.80	28.39	59.43
2000	500	0.8	26.06	27.12	53.18	52.64	0.54	28.91	59.25
2000	500	0.9	26.06	30.15	56.21	55.97	0.25	28.89	59.25
2000	500	1.0	26.06	33.22	59.29	59.29	0.00	27.93	59.29
3000	500	0.0	23.31	0.00	23.31	23.31	0.00	23.31	47.20
3000	500	0.1	23.31	2.57	25.88	25.95	-0.08	23.16	50.32
3000	500	0.2	23.31	5.38	28.68	28.60	0.08	22.93	51.70
3000	500	0.3	23.31	8.28	31.59	31.25	0.34	22.86	51.95
3000	500	0.4	23.31	11.16	34.47	33.89	0.58	23.08	51.56
3000	500	0.5	23.31	13.95	37.26	36.54	0.73	23.61	50.91
3000	500	0.6	23.31	16.62	39.92	39.18	0.74	24.37	50.29
3000	500	0.7	23.31	19.14	42.45	41.83	0.62	25.16	49.86
3000	500	0.8	23.31	21.57	44.88	44.48	0.41	25.67	49.69
3000	500	0.9	23.31	23.98	47.29	47.12	0.16	25.50	49.71
3000	500	1.0	23.31	26.46	49.77	49.77	0.00	24.11	49.77

APPENDIX III Cont'd.

P (bar)	T (°C)	X_{CO2}	V_{H2O}	V_R	$V_{CO2-H2O}$	V^{ID}	V^{EX}	V_{H2O}	V_{CO2}
4000	500	0.0	21.69	0.00	21.69	21.69	0.00	21.69	43.74
4000	500	0.1	21.69	2.35	24.05	24.01	0.03	21.57	46.33
4000	500	0.2	21.69	4.90	26.59	26.33	0.26	21.40	47.36
4000	500	0.3	21.69	7.51	29.20	28.65	0.55	21.40	47.40
4000	500	0.4	21.69	10.07	31.77	30.97	0.79	21.69	46.88
4000	500	0.5	21.69	12.53	34.22	33.29	0.93	22.27	46.17
4000	500	0.6	21.69	14.85	36.54	35.61	0.93	23.08	45.51
4000	500	0.7	21.69	17.02	38.71	37.93	0.78	23.92	45.05
4000	500	0.8	21.69	19.09	40.78	40.25	0.53	24.52	44.85
4000	500	0.9	21.69	21.11	42.81	42.57	0.23	24.48	44.84
4000	500	1.0	21.69	23.20	44.89	44.89	0.00	23.32	44.89
5000	500	0.0	20.56	0.00	20.56	20.56	0.00	20.56	42.45
5000	500	0.1	20.56	2.29	22.86	22.67	0.19	20.48	44.23
5000	500	0.2	20.56	4.71	25.27	24.78	0.50	20.41	44.71
5000	500	0.3	20.56	7.12	27.69	26.88	0.80	20.53	44.38
5000	500	0.4	20.56	9.45	30.02	28.99	1.03	20.93	43.65
5000	500	0.5	20.56	11.65	32.22	31.09	1.13	21.60	42.83
5000	500	0.6	20.56	13.70	34.26	33.20	1.07	22.44	42.14
5000	500	0.7	20.56	15.60	36.17	35.30	0.86	23.26	41.70
5000	500	0.8	20.56	17.41	37.97	37.41	0.56	23.75	41.53
5000	500	0.9	20.56	19.19	39.75	39.51	0.24	23.53	41.56
5000	500	1.0	20.56	21.05	41.62	41.62	0.00	22.11	41.62
6000	500	0.0	19.70	0.00	19.70	19.70	0.00	19.70	41.99
6000	500	0.1	19.70	2.29	21.99	21.65	0.35	19.67	42.92
6000	500	0.2	19.70	4.61	24.32	23.59	0.73	19.70	42.79
6000	500	0.3	19.70	6.88	26.58	25.53	1.06	19.95	42.07
6000	500	0.4	19.70	9.02	28.72	27.47	1.26	20.47	41.11
6000	500	0.5	19.70	11.00	30.71	29.41	1.29	21.22	40.19
6000	500	0.6	19.70	12.82	32.52	31.35	1.17	22.09	39.48
6000	500	0.7	19.70	14.49	34.20	33.29	0.90	22.83	39.07
6000	500	0.8	19.70	16.09	35.79	35.23	0.56	23.15	38.95
6000	500	0.9	19.70	17.69	37.39	37.18	0.22	22.63	39.03
6000	500	1.0	19.70	19.41	39.12	39.12	0.00	20.77	39.12
2000	600	0.0	30.54	0.00	30.54	30.54	0.00	30.54	66.87
2000	600	0.1	30.54	3.70	34.23	33.93	0.30	30.49	67.91
2000	600	0.2	30.54	7.45	37.99	37.32	0.67	30.48	68.03
2000	600	0.3	30.54	11.18	41.72	40.72	1.00	30.64	67.58
2000	600	0.4	30.54	14.82	45.36	44.11	1.25	31.04	66.85
2000	600	0.5	30.54	18.34	48.87	47.50	1.37	31.69	66.05
2000	600	0.6	30.54	21.69	52.23	50.89	1.33	32.55	65.35
2000	600	0.7	30.54	24.90	55.44	54.29	1.15	33.48	64.84
2000	600	0.8	30.54	27.98	58.51	57.68	0.83	34.32	64.56

APPENDIX III Cont'd.

P (bar)	T (°C)	X_{CO2}	V_{H2O}	V_R	$V_{CO2-H2O}$	V^{ID}	V^{EX}	V_{H2O}	V_{CO2}
2000	600	0.9	30.54	30.97	61.50	61.07	0.43	34.81	64.47
2000	600	1.0	30.54	33.93	64.47	64.47	0.00	34.65	64.47
3000	600	0.0	26.01	0.00	26.01	26.01	0.00	26.01	49.30
3000	600	0.1	26.01	2.53	28.54	28.75	-0.21	25.84	52.86
3000	600	0.2	26.01	5.34	31.36	31.49	-0.13	25.56	54.53
3000	600	0.3	26.01	8.28	34.29	34.22	0.07	25.43	54.97
3000	600	0.4	26.01	11.22	37.23	36.96	0.27	25.58	54.71
3000	600	0.5	26.01	14.09	40.10	39.70	0.40	26.02	54.17
3000	600	0.6	26.01	16.84	42.85	42.43	0.42	26.67	53.64
3000	600	0.7	26.01	19.49	45.50	45.17	0.33	27.29	53.30
3000	600	0.8	26.01	22.06	48.08	47.91	0.17	27.55	53.21
3000	600	0.9	26.01	24.65	50.66	50.65	0.02	26.99	53.29
3000	600	1.0	26.01	27.37	53.38	53.38	0.00	25.03	53.38
4000	600	0.0	23.66	0.00	23.66	23.66	0.00	23.66	44.25
4000	600	0.1	23.66	2.26	25.92	26.06	-0.14	23.49	47.76
4000	600	0.2	23.66	4.79	28.45	28.46	-0.01	23.22	49.39
4000	600	0.3	23.66	7.45	31.11	30.86	0.24	23.10	49.78
4000	600	0.4	23.66	10.10	33.76	33.26	0.49	23.28	49.46
4000	600	0.5	23.66	12.66	36.32	35.66	0.66	23.80	48.84
4000	600	0.6	23.66	15.10	38.76	38.06	0.69	24.56	48.22
4000	600	0.7	23.66	17.40	41.06	40.47	0.59	25.36	47.78
4000	600	0.8	23.66	19.60	43.26	42.87	0.39	25.91	47.59
4000	600	0.9	23.66	21.77	45.43	45.27	0.16	25.76	47.61
4000	600	1.0	23.66	24.01	47.67	47.67	0.00	24.39	47.67
5000	600	0.0	22.12	0.00	22.12	22.12	0.00	22.12	41.87
5000	600	0.1	22.12	2.16	24.28	24.29	-0.01	21.96	45.08
5000	600	0.2	22.12	4.57	26.68	26.46	0.22	21.74	46.46
5000	600	0.3	22.12	7.06	29.18	28.63	0.54	21.69	46.64
5000	600	0.4	22.12	9.52	31.64	30.80	0.84	21.97	46.14
5000	600	0.5	22.12	11.87	33.99	32.97	1.02	22.61	45.37
5000	600	0.6	22.12	14.07	36.18	35.15	1.04	23.52	44.63
5000	600	0.7	22.12	16.10	38.21	37.32	0.90	24.52	44.09
5000	600	0.8	22.12	18.00	40.11	39.49	0.63	25.29	43.82
5000	600	0.9	22.12	19.83	41.95	41.66	0.29	25.41	43.79
5000	600	1.0	22.12	21.72	43.83	43.83	0.00	24.36	43.83
6000	600	0.0	20.99	0.00	20.99	20.99	0.00	20.99	40.53
6000	600	0.1	20.99	2.12	23.11	22.97	0.13	20.85	43.38
6000	600	0.2	20.99	4.45	25.43	24.96	0.47	20.68	44.45
6000	600	0.3	20.99	6.83	27.82	26.95	0.87	20.72	44.38
6000	600	0.4	20.99	9.15	30.13	28.93	1.20	21.11	43.67
6000	600	0.5	20.99	11.32	32.31	30.92	1.39	21.88	42.73
6000	600	0.6	20.99	13.31	34.29	32.91	1.39	22.96	41.85

APPENDIX III Cont'd.

P (bar)	T (°C)	X_{CO2}	V_{H2O}	V_R	$V_{CO2-H2O}$	V^{ID}	V^{EX}	V_{H2O}	V_{CO2}
6000	600	0.7	20.99	15.10	36.09	34.89	1.20	24.13	41.22
6000	600	0.8	20.99	16.74	37.73	36.88	0.85	25.09	40.89
6000	600	0.9	20.99	18.29	39.28	38.87	0.41	25.41	40.82
6000	600	1.0	20.99	19.87	40.85	40.85	0.00	24.57	40.85
2000	700	0.0	36.01	0.00	36.01	36.01	0.00	36.01	74.14
2000	700	0.1	36.01	3.84	39.85	39.35	0.50	36.00	74.47
2000	700	0.2	36.01	7.67	43.68	42.69	1.00	36.07	74.14
2000	700	0.3	36.01	11.43	47.45	46.02	1.42	36.32	73.41
2000	700	0.4	36.01	15.07	51.09	49.36	1.73	36.82	72.50
2000	700	0.5	36.01	18.56	54.57	52.70	1.87	37.59	71.56
2000	700	0.6	36.01	21.86	57.88	56.03	1.84	38.61	70.72
2000	700	0.7	36.01	24.98	60.99	59.37	1.62	39.81	70.07
2000	700	0.8	36.01	27.92	63.93	62.71	1.23	41.08	69.65
2000	700	0.9	36.01	30.71	66.72	66.05	0.67	42.27	69.43
2000	700	1.0	36.01	33.37	69.38	69.38	0.00	43.17	69.38
3000	700	0.0	29.15	0.00	29.15	29.15	0.00	29.15	51.80
3000	700	0.1	29.15	2.49	31.64	31.97	-0.33	28.96	55.78
3000	700	0.2	29.15	5.30	34.45	34.79	-0.34	28.63	57.73
3000	700	0.3	29.15	8.26	37.41	37.62	-0.20	28.43	58.36
3000	700	0.4	29.15	11.25	40.40	40.44	-0.04	28.51	58.24
3000	700	0.5	29.15	14.19	43.34	43.26	0.08	28.87	57.80
3000	700	0.6	29.15	17.03	46.18	46.08	0.10	29.41	57.37
3000	700	0.7	29.15	19.79	48.94	48.91	0.03	29.86	57.12
3000	700	0.8	29.15	22.51	51.66	51.73	-0.07	29.87	57.10
3000	700	0.9	29.15	25.27	54.42	54.55	-0.13	28.93	57.26
3000	700	1.0	29.15	28.22	57.37	57.37	0.00	26.41	57.37
4000	700	0.0	25.87	0.00	25.87	25.87	0.00	25.87	45.01
4000	700	0.1	25.87	2.16	28.04	28.35	-0.32	25.66	49.44
4000	700	0.2	25.87	4.69	30.56	30.83	-0.28	25.28	51.66
4000	700	0.3	25.87	7.39	33.26	33.32	-0.06	25.05	52.41
4000	700	0.4	25.87	10.12	35.99	35.80	0.19	25.13	52.29
4000	700	0.5	25.87	12.79	38.66	38.28	0.38	25.57	51.76
4000	700	0.6	25.87	15.35	41.22	40.76	0.46	26.28	51.18
4000	700	0.7	25.87	17.78	43.65	43.24	0.40	27.05	50.76
4000	700	0.8	25.87	20.11	45.98	45.73	0.25	27.55	50.59
4000	700	0.9	25.87	22.42	48.29	48.21	0.08	27.30	50.62
4000	700	1.0	25.87	24.82	50.69	50.69	0.00	25.70	50.69
5000	700	0.0	23.83	0.00	23.83	23.83	0.00	23.83	41.46
5000	700	0.1	23.83	2.03	25.86	26.07	-0.21	23.61	46.10
5000	700	0.2	23.83	4.42	28.26	28.31	-0.05	23.23	48.38
5000	700	0.3	23.83	7.00	30.83	30.54	0.29	23.01	49.07
5000	700	0.4	23.83	9.59	33.42	32.78	0.64	23.17	48.80

APPENDIX III Cont'd.

P (bar)	T (°C)	X_{CO2}	V_{H2O}	V_R	$V_{CO2-H2O}$	V^{ID}	V^{EX}	V_{H2O}	V_{CO2}
5000	700	0.5	23.83	12.09	35.92	35.02	0.90	23.78	48.07
5000	700	0.6	23.83	14.44	38.27	37.26	1.01	24.76	47.27
5000	700	0.7	23.83	16.59	40.43	39.50	0.93	25.94	46.64
5000	700	0.8	23.83	18.59	42.42	41.73	0.69	26.99	46.28
5000	700	0.9	23.83	20.48	44.31	43.97	0.34	27.46	46.19
5000	700	1.0	23.83	22.38	46.21	46.21	0.00	26.76	46.21
6000	700	0.0	22.39	0.00	22.39	22.39	0.00	22.39	39.20
6000	700	0.1	22.39	1.95	24.34	24.42	-0.08	22.16	43.96
6000	700	0.2	22.39	4.28	26.67	26.45	0.22	21.78	46.23
6000	700	0.3	22.39	6.78	29.17	28.48	0.68	21.61	46.80
6000	700	0.4	22.39	9.27	31.66	30.52	1.14	21.87	46.34
6000	700	0.5	22.39	11.64	34.03	32.55	1.48	22.66	45.39
6000	700	0.6	22.39	13.80	36.19	34.58	1.60	23.94	44.35
6000	700	0.7	22.39	15.71	38.10	36.61	1.49	25.54	43.49
6000	700	0.8	22.39	17.40	39.79	38.64	1.14	27.14	42.95
6000	700	0.9	22.39	18.90	41.29	40.68	0.61	28.32	42.73
6000	700	1.0	22.39	20.32	42.71	42.71	0.00	28.49	42.71

APPENDIX IV

Experimental conditions, microthermometric data and solvus coordinates determined from synthetic fluid inclusions in the CO_2-H_2O binary system. T_F(°C) and P_F(bar) are the formation conditions, X_{CO2} is the mole fraction of CO_2, and T_S is the temperature on the solvus and is equal to Th (total). Total homogenization to the liquid is indicated by "l" and homogenization to the vapor by "v". V_S is the mean molar volume on the solvus and P_S is the calculated solvus pressure. The designations "c_l" and "c_v" imply total homogenization very near the critical point for that bulk composition but to the phase indicated by the subscript.

XCO_2	P (bar)	T (°C)	T_S	Mode	V_S	P_S
0.1234	2000	400	271	l	26.593	785
0.1234	2000	500	301	l	30.16	525
0.1234	3000	400	265	l	24.294	1430
0.1234	3000	500	275	l	26.368	875
0.1234	3000	600	296	l	28.783	638
0.1234	3000	700	308	l	31.351	478
0.1234	4000	400	246	l	23.031	1840
0.1234	4000	500	259	l	24.525	1260
0.1234	4000	600	275	l	26.213	910
0.1234	4000	700	289	l	27.777	727
0.1234	5000	400	237	l	22.2	2300
0.1234	5000	500	247	l	23.345	1670
0.1234	5000	600	261	l	24.612	1250
0.1234	5000	700	274	l	25.72	1030
0.1234	6000	500	239	l	22.493	2100
0.1234	6000	600	248	l	23.48	1610
0.1234	6000	700	262	l	24.422	1340
0.2473	2000	400	283	l	30.709	1133
0.2473	2000	500	293	l	34.545	762
0.2473	2000	600	306	c_v	39.012	586
0.2473	3000	400	267	l	27.781	1680
0.2473	3000	500	276	l	29.852	1230
0.2473	3000	600	286	l	32.241	939
0.2473	3000	700	302	l	34.767	797
0.2473	4000	400	270	l	26.201	2340
0.2473	4000	500	270	l	27.682	1740
0.2473	4000	600	275	l	29.35	1330
0.2473	5000	400	276	l	25.163	2980

APPENDIX IV Cont'd.

XCO_2	P (bar)	T (°C)	T_{Solvus}	Mode	V_{Solvus}	P_{Solvus}
0.2473	5000	500	265	l	26.318	2230
0.2473	5000	600	267	l	27.591	1740
0.2473	5000	700	275	l	28.672	1490
0.2473	6000	500	261	l	25.337	2690
0.2473	6000	600	266	l	26.359	2220
0.3716	2000	500	284	v	38.905	889
0.3716	3000	400	275	v	31.306	1870
0.3716	3000	500	274	v	33.411	1416
0.3716	3000	600	281	v	35.819	1135
0.3716	3000	700	285	v	38.322	934
0.3716	4000	400	259	c_v	29.313	2340
0.3716	4000	500	271	v	30.866	1960
0.3716	4000	600	273	v	32.593	1559
0.3716	4000	700	276	v	34.119	1319
0.3716	5000	500	267	c_v	29.24	2440
0.3716	5000	600	269	c_v	30.629	2010
0.3716	5000	700	273	v	31.79	1730
0.3716	6000	500	263	c_l	28.048	2900
0.3716	6000	600	264	c_v	29.243	2410
0.3716	6000	700	269	v	30.357	2100
0.4964	1000	400	283	v	52.433	654
0.4964	1000	500	294	v	61.543	536
0.4964	1000	600	335	v	70.217	533
0.4964	2000	400	268	v	38.821	1267
0.4964	2000	600	284	v	47.745	788
0.4964	3000	400	265	v	34.688	1890
0.4964	3000	500	263	v	36.866	1480
0.4964	3000	600	275	v	39.332	1253
0.4964	3000	700	277	v	41.854	1052
0.4964	4000	400	252	v	32.254	2380
0.4964	4000	600	273	v	35.756	1730
0.4964	4000	700	268	v	37.337	1446
0.4964	5000	500	260	v	31.985	2530
0.4964	5000	600	269	v	33.54	2195
0.4964	5000	700	269	v	34.827	1890
0.6216	2000	500	264	v	47.161	993
0.6216	3000	400	250	v	37.841	1884
0.6216	3000	500	252	v	40.13	1524
0.6216	3000	600	266	v	42.686	1317
0.6216	4000	400	265	v	34.98	2590
0.6216	4000	500	244	v	36.753	2040
0.6216	4000	600	258	v	38.72	1777

APPENDIX IV Cont'd.

XCO_2	P (bar)	T (°C)	T_{Solvus}	Mode	V_{Solvus}	P_{Solvus}
0.6216	5000	500	245	v	34.493	2540
0.6216	5000	600	260	v	36.216	2268
0.6216	5000	700	265	v	37.635	2035
0.6216	6000	600	257	v	34.375	2680
0.7473	1000	500	252	v	72.896	518
0.7473	2000	500	221	v	50.959	875
0.7473	3000	400	228	v	40.758	1836
0.7473	3000	500	231	v	43.195	1493
0.7473	3000	600	240	v	45.869	1272
0.7473	4000	500	230	v	39.391	2040
0.7473	4000	600	243	v	41.492	1810
0.7473	5000	700	244	v	40.157	2030
0.7473	6000	700	245	v	38.092	2387

APPENDIX V

```
********** ERROR ANALYSIS **********************************************
*     CALCULATION OF CO2-H2O MMV'S AND ASSOCIATED ERROR ANALYSIS
************************************************************************
      IMPLICIT DOUBLE PRECISION (A-Z)
      PARAMETER (NVAR=10)
      DIMENSION HOMO(1,NVAR),A(35,NVAR)
      INTEGER ISTOP,MODE,TMODE,SAMPLE,I,J,K,L,M,N,NNN
      SAVE
      OPEN (UNIT=12, FILE='SMSTHAPPENDIX',STATUS='OLD')
      OPEN (UNIT=8, FILE='STDDEV',STATUS='NEW')
      WRITE(8,*)'  SAMPLE  PF   TF   XCO2 SXCO2    TH  N  STH M
     +THT TM   MMVPT   SVP   SVT   SVX   ERR % ERR'
      LNUM=0.
      SVPSUM=0.0D0
      SVTSUM=0.0D0
      SVXSUM=0.0D0
      ERRSUM=0.0D0
      PRCSUM=0.0D0
      SAM=0.
      NNN=0
      XBAR=0.
      DO 5 I=1,35
      DO 4 J=1,NVAR
      A(I,J)=0.
    4 CONTINUE
    5 CONTINUE
   10 CONTINUE
      K=1
   15 CONTINUE
      READ (12,1000) SAMPLE,PF,TF,XCO2,TH,MODE,THT,TMODE,GAGOX,ETH
 1000 FORMAT(I8,X,F5.0,X,F4.0,X,F6.4,X,F6.2,X,I1,X,F4.0,X,I1,
     +  X,F7.5,X,F5.1)
      IF(SAMPLE.EQ.1) GOTO105
      A(K,1)=SAMPLE
      A(K,2)=PF
      A(K,3)=TF
      A(K,4)=XCO2
      A(K,5)=TH
      A(K,6)=MODE
      A(K,7)=THT
      A(K,8)=TMODE
      A(K,9)=GAGOX
      A(K,10)=ETH
   66 CONTINUE
      K=K+1
      IF(A(K-1,1).EQ.0.AND.K.EQ.2) GO TO 65
      GOTO 80
C     FORMAT FOR SAMPLE NUMBER (A(K-1,1)) EQUALS ZERO
   65 WRITE(8,1010)NINT(A(K-1,1)),NINT(A(K-1,2)),
```

APPENDIX V Cont'd.

```
   +NINT(A(K-1,3)),A(K-1,4),SAM,
   +SAM,(K-2),SAM,NINT(A(K-1,6)),A(K-1,7),NINT(A(K-1,8)),
   +SAM,SAM,SAM,SAM,SAM,SAM
       WRITE(9,*)NINT(A(K-2,1))
 1010 FORMAT(X,I8,X,I4,X,I3,X,F6.4,X,F5.4,X,F6.2,X,I2,X,F4.2,
   +X,I1,X,F4.0,X,I1,X,F7.3,X,F5.3,X,F5.3,X,F5.3,X,F5.3,X,F5.3)
       GOTO10
C      CALCULATE AVERAGE (XBAR) AND STANDARD DEVIATION (SD)
C      FOR THCO2 OF EACH SAMPLE
  80   CONTINUE
       IF((A(K-1,1)-A(K-2,1)).EQ.0) GOTO15
       IF((A(K-1,1)-A(K-2,1)).NE.0.AND.K.NE.2) GOTO50
       IF((A(K-1,1)-A(K-2,1)).NE.0.AND.K.EQ.2) GOTO15
        GO TO 10
  50 CONTINUE
       SUM=0.
       ASUM=0.
       DO 35,M=1,(K-2)
       SUM=SUM+A(M,10)
       NNN=NNN+1
  35 CONTINUE
       XBAR=SUM/(K-2)
       DO 40 N=1,(K-2)
       ASUM=ASUM+(A(N,10)-XBAR)**2
  40 CONTINUE
       ASUM=ASUM/(K-3)
       SD=DSQRT(ASUM)
       CALL MOLVOL(NINT(A(K-2,1)),A(K-2,2),A(K-2,3),A(K-2,4),SXCO2,
   +A(K-2,9),XBAR,SD,NINT(A(K-2,6)),MMVPT,SVP,SVT,SVX,ERR,
   +EPF,ETF,SAGOX,SYLD,SIGH2O,METH)
       PERC=(ERR/MMVPT)*100
C      FORMAT OUTPUT LAST DATA POINT IS (K-2),ORDER OF OUTPUT IS;
C
SAMPLE,PF,TF,XCO2,SXCO2,XBAR,N,SD,MODE,THT,TMODE,MMVPT,SVP,SVT,SVX,ERR
       WRITE(8,1020)NINT(A(K-2,1)),NINT(A(K-2,2)),
   +NINT(A(K-2,3)),A(K-2,4),SXCO2,
   +XBAR,N,SD,NINT(A(K-2,6)),A(K-2,7),NINT(A(K-2,8)),
   +MMVPT,SVP,SVT,SVX,ERR,PERC
       WRITE(9,*)NINT(A(K-2,1))
 1020 FORMAT(X,I8,X,I4,X,I3,X,F6.4,X,F5.4,X,F6.2,X,I2,X,F4.2,
   +X,I1,X,F4.0,X,I1,X,F7.3,X,F5.3,X,F5.3,X,F5.3,X,F5.3,X,F5.3)
C      COMPUTE AVERAGE ERROR FOR INCLUSIONS WITH THCO2 TO LIQUID
       IF(NINT(A(K-2,1)).GT.0.AND.NINT(A(K-2,6)).EQ.1) THEN
       LNUM=LNUM+1
       SVPSUM=SVPSUM+SVP
       SVTSUM=SVTSUM+SVT
       SVXSUM=SVXSUM+SVX
       ERRSUM=ERRSUM+ERR
       PRCSUM=PRCSUM+PERC
```

```
      END IF
C     RESET VARIABLES TO ZERO
      XBAR=0.
      SD=0.
      DO 100 LL=1,NVAR
      HOMO(1,LL)=A(K-1,LL)
  100 CONTINUE
      DO 51 II=1,35
      DO 41 JJ=1,NVAR
      A(II,JJ)=0.
   41 CONTINUE
   51 CONTINUE
      DO 101 MM=1,NVAR
      A(1,MM)=HOMO(1,MM)
      K=1
  101 CONTINUE
      GOTO 66
  105 CONTINUE
      SVPAVE=SVPSUM/LNUM
      SVTAVE=SVTSUM/LNUM
      SVXAVE=SVXSUM/LNUM
      ERRAVE=ERRSUM/LNUM
      PRCAVE=PRCSUM/LNUM
C     FORMAT FOR INITIAL ERROR ESTIMATES
      WRITE(8,1030)NNN,SVPAVE,SVTAVE,SVXAVE,ERRAVE,PRCAVE,
     +EPF,ETF,SAGOX,(SYLD*100.D0),SIGH2O,METH
 1030 FORMAT(/'TOTAL NUMBER OF INCLUSIONS MEASURED = ',I3/
     +'AVERAGE SVP OF INCLUSIONS THAT HOMOGENIZE TO LIQUID CO2 = '
     +,F5.3,'%'/
     +'AVERAGE SVT OF INCLUSIONS THAT HOMOGENIZE TO LIQUID CO2 = '
     +,F5.3,'%'/
     +'AVERAGE SVX OF INCLUSIONS THAT HOMOGENIZE TO LIQUID CO2 = '
     +,F5.3,'%'/
     +'AVERAGE ERR OF INCLUSIONS THAT HOMOGENIZE TO LIQUID CO2 = '
     +,F5.3,'%'/
     +'AVERAGE ERROR % OF INCLUSIONS THAT HOMOGENIZE TO LIQUID CO2 = '
     +,F5.3,'%'/
     +'ERROR IN EXPERIMENTAL PRESSURE (SPF) = ',F4.3,
     +' * FORMATION PRESSURE'/
     +'ERROR IN EXPERIMENTAL TEMPERATURE (STF) = ',F4.3,
     +' * FORMATION TEMPERATURE'/
     +'ERROR IN MASS OF SILVER OXALATE (SAGOX) = ',F6.5,' GRAMS'/
     +'ERROR IN YIELD OF SILVER OXALATE (SYLD) = 0',F5.4,' PERCENT'/
     +'ERROR IN MASS OF WATER (SIGH2O) = ',F6.5,' GRAMS'/
     +'MINIMUM ERROR IN THCO2 (STH) = ',F3.2,' DEGREES')
      CLOSE (UNIT=8)
         CLOSE (UNIT=12)
      STOP
         END
```

APPENDIX V Cont'd.

```
C     ********** SUBROUTINE MOLVOL **********
C     FROM "CO2-H2O VOLUMES III, 8/1/89"
C     CO2 WT % FIXED
C     SOLY OF CO2 EQU FIXED
C     VCOREC EQ FOR QTZ FIXED
      SUBROUTINE MOLVOL(SAMPLE,PF,TF,XCO2,SXCO2,GAGOX,TH,
     +STH,MODE,MMVPT,SVP,SVT,SVX,ERR,
     +EPF,ETF,SAGOX,SYLD,SIGH2O,METH)
      IMPLICIT DOUBLE PRECISION (A-Z)
      INTEGER ISTOP,MODE,RECLEN,SAMPLE
      SAVE
      MMVPT=0.0D0
C      MOLECULAR WEIGHTS
       MWH2O = 18.0152D0
       MWCO2 = 44.0098D0
       MWAGOX = 303.7556D0
       SAM=0.0D0
     WTFCO2=(XCO2*MWCO2)/((XCO2*MWCO2)+((1.0D0-XCO2)*MWH2O))
      WTFH2O=1.0D0-WTFCO2
C     ASSUME 1 GRAM TOTAL SOLUTION
      GCO2=WTFCO2
      GH2O=WTFH2O
C     CALCULATE GMCO2/100GMH2O IN AQUEOUS PHASE (CO2A) USING
C     EQUATION GENERATED BY REGRESSION OF DATA FROM DODDS et al.(1956)
      CO2A=7.2754D0-5.6634D-2*TH+7.8770D-4*TH**2-2.0370D-5*TH**3
C     CALCULATE GRAMS OF CO2 DISSOLVED IN AQUEOUS PHASE (GCO2A)
      GCO2A=GH2O*(CO2A/100.0D0)
C     CALCULATE CO2 DENSITY IN CO2 PHASE (RHOCO2) USING EQUATIONS
C     FROM LOWREY AND ERICKSON (1927)
      TMOD=31.0D0-TH
       IF(DABS(1.0D0-MODE).LT.0.010D0) THEN
        RHOCO2=0.4683D0+0.001442D0*TMOD+0.1318D0*TMOD**(1.0D0/3.0D0)
       ELSE
        RHOCO2=0.4683D0+0.001442D0*TMOD-0.1318D0*TMOD**(1.0D0/3.0D0)
       ENDIF
C     CALCULATE DENSITY OF AQUEOUS PHASE (RHOAQ) USING EQUATION GENERATED
C     FROM REGRESSION OF DATA FROM PARKINSON AND DE NEVERS (1969) ABOVE
C     0°C AND VALUES BELOW 0°C EXTRAPOLATED FROM PURE WATER DATA OF
C     ZHELEZNYI(1969)
      RHOAQ=1.0014D0+5.2777D-5*TH-1.0113D-5*TH**2+9.3537D-8*TH**3
C     CALCULATE VOLUME OF CO2 PHASE (VGAS)
      GCO2V=GCO2-GCO2A
      VGAS=GCO2V/RHOCO2
C     CALCULATE VOLUME OF AQUEOUS PHASE (VAQ)
      VAQ=(GH2O+GCO2A)/RHOAQ
C     CALCULATE BULK DENSITY (RHOBLK)
      RHOBLK=1.0D0/(VGAS+VAQ)
C     CALCULATE TOTAL VOLUME AT ROOM TEMP
      (V25)
```

APPENDIX V Cont'd.

```
      V25=VGAS+VAQ
C     CALCULATE MEAN MOLAR VOLUME OF INC AT ROOM TEMP. (MMV25)
      MCO2=GCO2/MWCO2
      MH2O=GH2O/MWH2O
      TOTM=MH2O+MCO2
      SV25=V25/(GCO2+GH2O)
      MMV25=(V25)/TOTM
C     CALCULATE MMV AT P & T OF FORMATION BY CORRECTING FOR
C     EXPANSION AND CONTRACTION OF QUARTZ
      CALL QTZ(PF,TF,VCOREC)
      MMVPT=MMV25*VCOREC
      SVPT=SV25*VCOREC
      ERR=0.0D0
      CALL ERROR(SAMPLE,PF,TF,XCO2,SXCO2,GAGOX,TH,STH,
     +MODE,SVP,SVT,SVX,ERR,
     +EPF,ETF,SAGOX,SYLD,SIGH2O,METH)
      GO TO 40
   35 CONTINUE
       SAM=0.0D0
   40 CONTINUE
   45 CONTINUE
    RETURN
      END

C     ********** PROGRAM QTZ **********
C     THIS PROGRAM CORRECTS FLUID INCLUSION VOLUMES FOR THERMAL
C     EXPANSION AND COMPRESSIBILITY EXPERIENCED BY THE QUARTZ HOST
C     WHEN TAKEN FROM 20°C AND 1 BAR TO SOME FINAL P-T. THE
C     CORRECTED INCLUSION VOLUME IS VNEW = VOLD*VCOREC.
C
C     EQUATION OF STATE FOR QTZ FROM HOSIENI et al.(1985)
C
      SUBROUTINE QTZ(PBAR,TC,VCOREC)
      DOUBLE PRECISION ALPHA(7,5),BETA(5,5)
      IMPLICIT DOUBLE PRECISION (A-H,O-Z)
      T=273.15D0+TC
      P=PBAR/10
      TAB=846D0+0.265D0*P-0.11303229D-4*P*P-2.4632558D-9*P**3
      TMS=TAB-61D0
C     CALCULATE VOLUME OF ALPHA QUARTZ
      IF(T.LT.TMS) THEN
      DATA(ALPHA(1,J),J=1,5)/24.340296D0,3.238095D-4,7.855450D-7,
     A 1.018418D-9,5.083011D-13/
      DATA(ALPHA(2,J),J=1,5)/-1.218243D-4,-5.371956D-7,-1.357596D-9,
     A -1.73248D-12,-8.66629D-16/
      DATA(ALPHA(3,J),J=1,5)/1.170823D-7,5.474543D-10,1.376992D-12,
     A 1.886086D-15,9.986443D-19/
      DATA(ALPHA(4,J),J=1,5)/-7.99760D-11,-3.38035D-13,-8.22533D-16,
     A -1.14072D-18,-6.00664D-22/
```

```
      DATA(ALPHA(5,J),J=1,5)/3.031544D-14,1.203374D-16,2.743039D-19,
     A 3.586603D-22,1.754802D-25/
      DATA(ALPHA(6,J),J=1,5)/-5.78773D-18,-2.23346D-20,-4.71042D-23,
     A -5.49837D-26,-2.30557D-29/
      DATA(ALPHA(7,J),J=1,5)/4.329322D-22,1.658714D-24,3.241953D-27,
     A 3.236415D-30,1.010065D-33/
      SUM=-ALPHA(1,1)
      DO 20 J=1,5
       DO 20 I=1,7
       AAA=ALPHA(I,J)*((T-1000.D0)**(J-1))*(P**(I-1))
       SUM=AAA+SUM
   20 CONTINUE

       V=ALPHA(1,1)*(1D0+SUM)
   21 FORMAT(F8.5)
      GO TO 50
      ELSE
C     CALCULATE VOLUME OF ALPHA QUARTZ BETWEEN A/B TRANSITION AND
C     60°C BELOW IT.
      DATA(BETA(1,J),J=1,5)/23.701266D0,-.1058728D-5,.854633D-8,
     A -.188601D-10,.1440728D-13/
      DATA(BETA(2,J),J=1,5)/-.1520712D-4,.2042034D-7,-.519449D-10,
     A .974922D-13,-0.714101D-16/
      DATA(BETA(3,J),J=1,5)/.2441776D-8,-0.806657D-11,.1837775D-13,
     A -.490703D-16,.492830D-19/
      DATA(BETA(4,J),J=1,5)/-.116290D-11,.3979281D-14,-.368804D-17,
     A .917195D-20,-.127623D-22/
      DATA(BETA(5,J),J=1,5)/.2140223D-15,-.80183D-18,.596339D-21,
     A -.701148D-24,.1175194D-26/
      IF(T.LT.TAB) THEN
      SUM=-BETA(1,1)
      DO 25 J=1,5
       DO 25 I=1,5
       AAA=BETA(I,J)*((T-1000.D0)**(J-1))*(P**(I-1))
       SUM=AAA+SUM
   25 CONTINUE

       VBETA=BETA(1,1)*(1D0+SUM)
      RLAM=0.265D0-2D0*0.11303229D-4*P-3D0*2.4632558D-9*P**2
      TH=TAB-T
      F=(.00351508*TH-.158514D-4*TH**2+.73366D
     A -7*TH**3-.116609D-9*TH**4)**0.5D0
      DELV=(RLAM/0.265D0)*F
      V=VBETA-DELV
   26 FORMAT(F8.5,2X,F8.5,2X,F8.5)
      GO TO 50
      ELSE
C     CALCULATE VOLUME OF BETA QUARTZ
      SUM=-BETA(1,1)
```

```
      DO 30 J=1,5
       DO 30 I=1,5
       AAA=BETA(I,J)*((T-1000.D0)**(J-1))*(P**(I-1))
       SUM=AAA+SUM
 30 CONTINUE

       V=BETA(1,1)*(1D0+SUM)
 31 FORMAT(F8.5)
 50 CONTINUE
      V20=22.65638
      VCOREC=V/V20
        ENDIF
        ENDIF
        RETURN
        END

C     ********** SUBROUTINE ERROR **********
C     THIS SUBROUTINE CALCULATES THE ERROR ASSOCIATED WITH EACH
C     VOLUME (MMVPT) CALCULATED FOR CO2-H2O MIXTURES USING STANDARD
C     FORMULATIONS FOR THE PROPOGATION OF RANDOM INDEPENDENT ERRORS.
C
C
      SUBROUTINE ERROR(SAMPLE,PF,TF,XCO2,SXCO2,GAGOX,TH,STH,
     +MODE,SVP,SVT,SVX,ERR,
     +EPF,ETF,SAGOX,SYLD,SIGH2O,METH)
      IMPLICIT DOUBLE PRECISION (A-Z)
      INTEGER ISTOP,MODE,RECLEN,SAMPLE
              DATA MWH2O,MWCO2,MWAGOX/18.0152D0,44.0098D0,303.7556D0/
C
C     CALCULATE ERRORS ASSOCIATED WITH INPUT VARIABLES
C     "GQ" EQUALS THE NUMBER OF STANDARD DEVIATIONS OF
C     ERROR ASSOCIATED WITH EACH INPUT VARIABLE
              GQ=2.0D0
C      ERROR IN 'PF' IS SPF
              EPF=0.0025D0*GQ
              SPF=PF*EPF
C      ERROR IN 'TF' IS STF
              ETF=0.0025D0*GQ
              STF=TF*ETF
              YLD=.9847091
C      ERROR IN 'TH' IS STH
              METH=0.1D0
      IF(STH.LE.0.1D0)STH=METH
              STH=STH*GQ
C      TABULATE INDIVIDUAL ERRORS
              SAGOX=.00003*GQ
              SYLD=.003652*GQ
              SIGH2O=.00003*GQ
**************************************************
```

APPENDIX V Cont'd.

```
C                SPF=0.0D0
C                STF=0.0D0
C                STH=0.0D0
C                SAGOX=0.0D0
C                SYLD=0.0D0
C                SIGH2O=0.0D0
*****************************************************
C       CALCULATE ERROR IN XCO2 IS SXCO2
C        CALCULATE INITIAL MASS OF H2O FROM XCO2 AND INITIAL MASS
C        OF SILVER OXALATE (AGOX)
                 IMOCO2=(GAGOX/MWAGOX)*2.0D0*YLD
                 IGCO2=IMOCO2*MWCO2
                 IGH2O=(IMOCO2/XCO2-IMOCO2)*MWH2O
                 MOH2O=IGH2O/MWH2O
C       PROPOGATE ERRORS
C                IMOCO2=GAGOX/MWAGOX*2.*YLD
                 SG1=(DSQRT((SAGOX/GAGOX)**2+(SYLD/YLD)**2))*IMOCO2
                 SIGCO2=SG1*MWCO2
                 SG2=SIGH2O/MWH2O
                 SXCO2=DSQRT( (SG1/IMOCO2)**2+((DSQRT((SG1)**2
     +  + (SG2)**2))/(MOH2O+IMOCO2))**2 ) * XCO2
C       CALCULATE ERROR IN WEIGHT FRACTION CO2 AND WATER
         WTFCO2=(XCO2*MWCO2)/((XCO2*MWCO2)+((1.0D0-XCO2)*MWH2O))
         WTFH2O=1.0D0-WTFCO2
C       ASSUME 1 GRAM TOTAL SOLUTION
                 GCO2=WTFCO2
                 GH2O=WTFH2O
                 SGH2O=(GH2O/IGH2O)*SIGH2O
                 SGCO2=(GCO2/IGCO2)*SIGCO2
C       CALCULATE GMCO2/100GMH2O IN AQUEOUS PHASE (CO2A)
        CO2A=7.2754D0-5.6634D-2*TH+7.8770D-4*TH**2-2.0370D-5*TH**3
                 DCO2A=-5.6634D-2+2.*7.8770D-4*TH-3.*2.0370D-5*TH**2
                 SCO2A=DABS(DCO2A)*STH
C       CALCULATE GRAMS OF CO2 DISSOLVED IN AQUEOUS PHASE (GCO2A)
         GCO2A=GH2O*(CO2A/100.0D0)
         SGCO2A=DSQRT( (SGH2O/GH2O)**2 + (SCO2A/CO2A)**2 )/100.*GCO2A
C       CALCULATE CO2 DENSITY IN CO2 PHASE (RHOCO2)
        TMOD=31.0D0-TH
         IF(DABS(1.0D0-MODE).LT.0.010D0) THEN
         RHOCO2=0.4683D0+0.001442D0*TMOD+0.1318D0*TMOD**(1.0D0/3.0D0)
         DRHOCO=0.001442D0+0.1318D0/3.0D0*TMOD**(-2.0D0/3.0D0)
         SRHOCO=DABS(DRHOCO)*STH
                   ELSE
         RHOCO2=0.4683D0+0.001442D0*TMOD-0.1318D0*TMOD**(1.0D0/3.0D0)
         DRHOCO=0.001442D0-0.1318D0/3.0D0*TMOD**(-2.0D0/3.0D0)
         SRHOCO=DABS(DRHOCO)*STH
                   ENDIF
C       CALCULATE DENSITY OF AQUEOUS PHASE (RHOAQ)
```

APPENDIX V Cont'd.

```
      RHOAQ=1.0014D0+5.2777D-5*TH-1.0113D-5*TH**2+9.3537D-8*TH**3
      DRHOAQ=5.2777D-5-1.0113D-5*2.0D0*TH+9.3537D-8*3.0D0*TH**2
            SRHOAQ=DABS(DRHOAQ)*STH
C     CALCULATE VOLUME OF CO2 PHASE (VGAS)
            GCO2V=GCO2-GCO2A
            SGCO2V=DSQRT((SGCO2)**2+(SGCO2A)**2)
            VGAS=GCO2V/RHOCO2
            SVGAS=DSQRT((SGCO2V/GCO2V)**2+(SRHOCO/RHOCO2)**2)
C     CALCULATE VOLUME OF AQUEOUS PHASE (VAQ)
            VAQ=(GH2O+GCO2A)/RHOAQ
            SVAQ=DSQRT( ((DSQRT((SGH2O)**2+(SGCO2A)**2))
     +  /(GH2O+GCO2A))**2
     +  + (SRHOAQ/RHOAQ)**2)*VAQ
C     CALCULATE BULK DENSITY (RHOBLK)
            RHOBLK=1.0D0/(VGAS+VAQ)
            SRHOBL=(DSQRT((SVGAS)**2+(SVAQ)**2))/(VGAS+VAQ)**2
C     CALCULATE TOTAL VOLUME AT ROOM TEMP
      (V25)
            V25=VGAS+VAQ
            SIGV25=DSQRT((SVGAS)**2+(SVAQ)**2)
C     CALCULATE MEAN MOLAR VOLUME OF INC AT ROOM TEMP. (MMV25)
            MCO2=GCO2/MWCO2
            SMCO2=SGCO2/MWCO2
            MH2O=GH2O/MWH2O
            SMH2O=SGH2O/MWH2O
            TOTM=MH2O+MCO2
            STOTM=DSQRT((SMH2O)**2+(SMCO2)**2)
            SV25=V25/(GCO2+GH2O)
            QQQ=((SGCO2)**2+(SGH2O)**2)/(GCO2+GH2O)**2
            SSV25=DSQRT((SIGV25/V25)**2 + QQQ)*SV25
            MMV25=(V25)/TOTM
            SMMV25=DSQRT((SIGV25/V25)**2+(STOTM/TOTM)**2)*MMV25
C     CALCULATE MMV AT P & T OF FORMATION BY CORRECTING FOR
C     EXPANSION AND CONTRACTION OF QUARTZ
      CALL QTZ(PF,TF,VCOREC)
      MMVPT=MMV25*VCOREC
      SMMVPT=SMMV25*VCOREC
      SVPT=SV25*VCOREC
      SSVPT=SSV25*VCOREC
      TK=TF+273.15
      SVX=SMMVPT
      CALL VLDR(PF,TK,XCO2,STF,SPF,SVT,SVP)
      ERR=DSQRT((SVP)**2+(SVT)**2+(SVX)**2)
        RETURN
        END

C     ********** PROGRAM VOLUME DERIVATIVES **********
C     THIS PROGRAM CALCULATES ERRORS IN EXPERIMENTALLY DETERMINED
VOLUMES
```

```
C     OF H2O-CO2 MIXTURES THAT RESULT FROM ERRORS IN EXPERIMENTAL
C     TEMPERATURE (VOLUME ERROR = SVT) AND PRESSURE (VOLUME ERROR = SVP)
C     USING SUBROUTINE "PRESS" AND SUBROUTINE "OLUME"
C     X=MOLE FRACTION CO2; V,SVT,SVP=CC/MOLE; T=°K; P=BARS;
C     ST=ERROR IN T IN °; SP=ERROR IN P IN BARS
C
      SUBROUTINE VLDR(P,TK,X,ST,SP,SVT,SVP)
      IMPLICIT DOUBLE PRECISION (A-Z)
      TST=TK+ST
      PSP=P+SP
      CALL OLUME(P,TK,X,V)
      CALL OLUME(P,TST,X,VST)
      CALL OLUME(PSP,TK,X,VSP)
      SVT=DABS(V-VST)
      SVP=DABS(V-VSP)
        RETURN
        END

C     ********** PROGRAM VOLUME **********
C     THIS PROGRAM CALCULATES MOLAR VOLUMES OF H2O-CO2 MIXTURES
C     ITTERATIVELY FROM H2O-CO2 EQUATION OF STATE IN SUBROUTINE
C     "PRESS" X=MOLE FRACTION CO2, V=CC/MOLE, T=°K, P=BARS
C
      SUBROUTINE OLUME(P,TK,X,V)
      IMPLICIT DOUBLE PRECISION (A-Z)
      V=120
      PP=-10000
      INCREM=10
      I=0
  221 V=V-INCREM
      I=I+1
      IF (I.GE.100)THEN
      WRITE(9,*) 'EXCEEDED MAX IT AT',V,INCREM,XCO2,TF,PEQ
      GO TO 220
      END IF
      CALL PRESS(X,TK,V,PEQ)
      DIF = P-PEQ
      LS=PP-PEQ
      IF(LS.GE.0.0D0)THEN
       V=V+INCREM
       GO TO 222
       END IF
      D=DABS(DIF)
C     WRITE(9,*) 'I,P,PEQ,TF,X',I,P,PEQ,TF,X
      IF(D.LE.0.01D0)GO TO 220
      IF(DIF)222,220,219
  219 PP=PEQ
      GO TO 221
  222  V=V+INCREM
```

APPENDIX V Cont'd.

```
      INCREM=INCREM/10
      GO TO 221
  220 CONTINUE
        RETURN
        END

C     ********** PROGRAM PRESS **********
C     THIS PROGRAM CALCULATES PRESSURES FROM H2O-CO2 EQUATION OF
C     STATE OF KERRICK AND JACOBS (1981)
C     X=MOLE FRACTION CO2, V=CC/MOLE, T=°K, P=BARS
C
      SUBROUTINE PRESS(X,TK,V,P)
      IMPLICIT DOUBLE PRECISION (A-Z)
      R=83.1441D0
      T=TK
      BH2O=29
      BCO2=58
      CH2O=(290.78D0-(0.30276D0*T)+(1.4774D-4*T*T))*10**6.0D0
      DH2O=(-8374+(19.437*T)-(8.148D-3*T*T))*10**6.0D0
      EH2O=(76600-(133.9*T)+(0.1071*T*T))*10**6.0D0
      CCO2=(28.31+(0.10721*T)-(8.81D-6*T*T))*10**6.0D0
      DCO2=(9380-(8.53*T)+(1.189D-3*T*T))*10**6.0D0
      ECO2=(-368654+(715.9*T)+(0.1534*T*T))*10**6.0D0

      ACO2=CCO2+(DCO2/V)+(ECO2/(V**2.0D0))
      AH2O=CH2O+(DH2O/V)+(EH2O/(V**2.0D0))
      G=(ACO2*AH2O)**0.5D0
      B=BH2O*(1.0D0-X)+BCO2*X
      A=AH2O*(1.0D0-X)**2.0D0+ACO2*(X)**2.0D0+2.0D0*(1-X)*X*G

      Y=B/(4*V)
      P=(R*T*(1+Y+Y**2.0D0-Y**3.0D0)/(V*(1-Y)**3.0D0))
     A -A/(T**0.5D0*V*(V+B))
C     WRITE(9,*)X,TK,V,P
C
        RETURN
        END
```

APPENDIX VI

This table contains the actual measured CO_2 homogenization temperatures used in computing mean molar volumes of CO_2-H_2O mixtures in Chapter 3. (v) and (l) signify homogenization to the vapor or liquid phases, respectively.

Sample Number = 1128820, 1000 bars, 400°C, XCO2 = .4964
Average Th(CO2) = 30.40 (v), Th(Total) = 283. (v)
Measured Th(CO2);
30.60 30.60 30.20 30.20

Sample Number = 1128815, 1000 bars, 500°C, XCO2 = .7473
Average Th(CO2) = 30.83 (v), Th(Total) = 252. (v)
Measured Th(CO2);
30.90 30.80 30.80

Sample Number = 1128819, 1000 bars, 500°C, XCO2 = .4964
Average Th(CO2) = 30.27 (v), Th(Total) = 294. (v)
Measured Th(CO2);
30.30 30.30 30.20

Sample Number = 1128818, 1000 bars, 600°C, XCO2 = .4964
Average Th(CO2) = 19.47 (v), Th(Total) = 335. (v)
Measured Th(CO2);
23.40 23.20 21.70 22.80 16.70 9.60
19.90 21.90 16.00

Sample Number = 1128809, 2000 bars, 400°C, XCO2 = .7473
Average Th(CO2) = 18.34 (l), Th(Total) = 0. (l)
Measured Th(CO2);
18.30 18.50 18.50 18.10 18.30

Sample Number = 1128805, 2000 bars, 400°C, XCO2 = .4964
Average Th(CO2) = 23.95 (l), Th(Total) = 268. (v)
Measured Th(CO2);
24.10 24.10 24.10 23.90 23.90 23.90
23.50 24.00 24.00 24.10 23.80 23.90
24.00

Sample Number = 5158914, 2000 bars, 400°C, XCO2 = .3716
Average Th(CO2) = 26.18 (l), Th(Total) = 0. (v)
Measured Th(CO2);
26.20 26.00 26.50 26.00

APPENDIX VI Cont'd.

Sample Number = 7038901, 2000 bars, 400°C, XCO2 = .2473
Average Th(CO2) = 29.30 (l), Th(Total) = 283. (l)
Measured Th(CO2);
29.20 29.20 29.40 29.30 29.40

Sample Number = 5158922, 2000 bars, 400°C, XCO2 = .1234
Average Th(CO2) = 30.00 (v), Th(Total) = 271. (l)
Measured Th(CO2);
30.00

Sample Number = 1128810, 2000 bars, 500°C, XCO2 = .7473
Average Th(CO2) = 25.33 (l), Th(Total) = 221. (v)
Measured Th(CO2);
25.30 25.30 25.40 25.40 25.30 25.30

Sample Number = 5158906, 2000 bars, 500°C, XCO2 = .6216
Average Th(CO2) = 27.20 (l), Th(Total) = 264. (v)
Measured Th(CO2);
27.20 27.20 27.20 27.20

Sample Number = 5158904, 2000 bars, 500°C, XCO2 = .3716
Average Th(CO2) = 30.00 (l), Th(Total) = 284. (v)
Measured Th(CO2);
30.00 30.00 30.00 30.00

Sample Number = 1128802, 2000 bars, 500°C, XCO2 = .2473
Average Th(CO2) = 30.85 (v), Th(Total) = 293. (l)
Measured Th(CO2);
30.90 30.80

Sample Number = 5158902, 2000 bars, 500°C, XCO2 = .1234
Average Th(CO2) = 27.00 (v), Th(Total) = 301. (l)
Measured Th(CO2);
27.00

Sample Number = 1128807, 2000 bars, 600°C, XCO2 = .4964
Average Th(CO2) = 30.73 (l), Th(Total) = 284. (v)
Measured Th(CO2);
30.70 30.70 30.60 30.60 30.70 30.90
30.80 30.80

Sample Number = 1128803, 2000 bars, 600°C, XCO2 = .2473
Average Th(CO2) = 30.63 (v), Th(Total) = 306. (v)
Measured Th(CO2);
30.50 30.60 30.60 30.80

APPENDIX VI Cont'd.

Sample Number = 5158816, 3000 bars, 400°C, XCO2 = .8736
Average Th(CO2) = -3.10 (l), Th(Total) = 0. (l)
Measured Th(CO2);
-1.80 -3.40 -3.40 -2.20 -4.70

Sample Number = 12168709, 3000 bars, 400°C, XCO2 = .7473
Average Th(CO2) = 1.29 (l), Th(Total) = 228. (v)
Measured Th(CO2);
1.20 1.20 1.20 1.20 1.00 1.30
1.30 1.60 1.30 1.40 1.50

Sample Number = 5158812, 3000 bars, 400°C, XCO2 = .6216
Average Th(CO2) = 4.84 (l), Th(Total) = 250. (v)
Measured Th(CO2);
4.80 4.90 5.00 5.00 5.00 5.10
4.50 4.60 4.70 4.80 4.90 4.80

Sample Number = 12168701, 3000 bars, 400°C, XCO2 = .4964
Average Th(CO2) = 9.83 (l), Th(Total) = 265. (v)
Measured Th(CO2);
10.30 9.90 9.10 9.60 9.50 10.30
10.30 10.10 9.40 9.60 9.70 10.00
10.10 9.80 9.80

Sample Number = 5158808, 3000 bars, 400°C, XCO2 = .3716
Average Th(CO2) = 13.98 (l), Th(Total) = 275. (v)
Measured Th(CO2);
13.90 13.80 13.80 14.00 14.10 14.30

Sample Number = 12168705, 3000 bars, 400°C, XCO2 = .2473
Average Th(CO2) = 21.83 (l), Th(Total) = 267. (l)
Measured Th(CO2);
21.50 22.30 21.30 21.40 21.50 22.50
22.30

Sample Number = 5158804, 3000 bars, 400°C, XCO2 = .1234
Average Th(CO2) = 29.28 (l), Th(Total) = 265. (l)
Measured Th(CO2);
29.20 29.30 29.40 29.20

Sample Number = 5158815, 3000 bars, 500°C, XCO2 = .8736
Average Th(CO2) = 7.28 (l), Th(Total) = 0. (l)
Measured Th(CO2);
7.20 7.20 7.30 7.10 6.40 6.30
8.00 7.90 8.10

Sample Number = 12168710, 3000 bars, 500°C, XCO2 = .7473
Average Th(CO2) = 11.63 (l), Th(Total) = 231. (v)
Measured Th(CO2);

11.50	11.60	12.30	11.50	11.50	11.90
11.30	11.40	11.70			

Sample Number = 5158811, 3000 bars, 500°C, XCO2 = .6216
Average Th(CO2) = 16.34 (l), Th(Total) = 252. (v)
Measured Th(CO2);

16.30	16.20	16.40	16.40	16.60	16.20
16.30					

Sample Number = 12168702, 3000 bars, 500°C, XCO2 = .4964
Average Th(CO2) = 20.18 (l), Th(Total) = 263. (v)
Measured Th(CO2);

20.70	20.80	20.10	20.00	20.00	20.20
20.00	20.10	20.10	20.00	20.00	20.10
20.20					

Sample Number = 5158807, 3000 bars, 500°C, XCO2 = .3716
Average Th(CO2) = 24.18 (l), Th(Total) = 274. (v)
Measured Th(CO2);

24.00	24.00	24.10	24.20	24.10	23.70
24.50	24.60	24.50	24.50	23.90	24.00
24.20	24.20				

Sample Number = 12168706, 3000 bars, 500°C, XCO2 = .2473
Average Th(CO2) = 29.11 (l), Th(Total) = 276. (l)
Measured Th(CO2);

29.00	29.30	29.20	29.20	29.30	29.10
29.20	28.60	29.10			

Sample Number = 5158803, 3000 bars, 500°C, XCO2 = .1234
Average Th(CO2) = 30.34 (v), Th(Total) = 275. (l)
Measured Th(CO2);

30.40	30.40	30.20	30.30	30.40

Sample Number = 12168711, 3000 bars, 600°C, XCO2 = .7473
Average Th(CO2) = 18.26 (l), Th(Total) = 240. (v)
Measured Th(CO2);

18.20	18.30	18.30	18.50	18.50	18.60
18.20	18.10	17.80	18.10		

Sample Number = 7038902, 3000 bars, 600°C, XCO2 = .6216
Average Th(CO2) = 21.20 (l), Th(Total) = 266. (v)
Measured Th(CO2);
21.30 21.70 21.20 21.00 21.00 20.80
21.40

Sample Number = 7038903, 3000 bars, 600°C, XCO2 = .4964
Average Th(CO2) = 24.32 (l), Th(Total) = 275. (v)
Measured Th(CO2);
24.30 24.30 24.20 24.30 24.30 24.50

Sample Number = 5158806, 3000 bars, 600°C, XCO2 = .3716
Average Th(CO2) = 27.59 (l), Th(Total) = 281. (v)
Measured Th(CO2);
27.80 27.50 27.80 27.50 27.50 27.60
27.40 27.60

Sample Number = 12168707, 3000 bars, 600°C, XCO2 = .2473
Average Th(CO2) = 30.43 (l), Th(Total) = 286. (l)
Measured Th(CO2);
30.40 30.40 30.50 30.40

Sample Number = 1158802, 3000 bars, 600°C, XCO2 = .1234
Average Th(CO2) = 28.48 (v), Th(Total) = 296. (v)
Measured Th(CO2);
28.40 28.50 28.70 28.50 28.30

Sample Number = 2118918, 3000 bars, 700°C, XCO2 = .8736
Average Th(CO2) = 20.30 (l), Th(Total) = 0. (l)
Measured Th(CO2);
20.30

Sample Number = 7038904, 3000 bars, 700°C, XCO2 = .7473
Average Th(CO2) = 22.53 (l), Th(Total) = 0. (l)
Measured Th(CO2);
22.50 22.80 22.60 22.50 22.40 22.40

Sample Number = 2118916, 3000 bars, 700°C, XCO2 = .6216
Average Th(CO2) = 24.77 (l), Th(Total) = 0. (l)
Measured Th(CO2);
24.80 24.80 24.70

Sample Number = 5178915, 3000 bars, 700°C, XCO2 = .4964
Average Th(CO2) = 27.05 (l), Th(Total) = 277. (v)
Measured Th(CO2);
27.00 27.00 27.10 27.10 27.00 27.10

APPENDIX VI Cont'd.

Sample Number = 5178914, 3000 bars, 700°C, XCO2 = .3716
Average Th(CO2) = 29.52 (l), Th(Total) = 285. (v)
Measured Th(CO2);
29.50 29.50 29.60 29.50

Sample Number = 2118913, 3000 bars, 700°C, XCO2 = .2473
Average Th(CO2) = 29.25 (v), Th(Total) = 302. (v)
Measured Th(CO2);
29.20 29.30

Sample Number = 5178912, 3000 bars, 700°C, XCO2 = .1234
Average Th(CO2) = 27.25 (v), Th(Total) = 308. (l)
Measured Th(CO2);
27.20 27.30

Sample Number = 8308812, 4000 bars, 400°C, XCO2 = .8736
Average Th(CO2) = -17.90 (l), Th(Total) = 0. (l)
Measured Th(CO2);
-18.20 -17.60 -17.90

Sample Number = 9078812, 4000 bars, 400°C, XCO2 = .7473
Average Th(CO2) = -15.60 (l), Th(Total) = 0. (l)
Measured Th(CO2);
-14.70 -15.70 -15.80 -16.20

Sample Number = 8308809, 4000 bars, 400°C, XCO2 = .6216
Average Th(CO2) = -10.16 (l), Th(Total) = 265. (v)
Measured Th(CO2);
-10.70 -10.70 -10.60 -10.80 -9.40 -9.50
-9.40

Sample Number = 9078808, 4000 bars, 400°C, XCO2 = .4964
Average Th(CO2) = -6.06 (l), Th(Total) = 252. (v)
Measured Th(CO2);
-6.00 -5.70 -5.80 -5.70 -5.50 -6.50
-6.60 -6.50 -5.80 -6.10 -6.20 -6.30

Sample Number = 8308806, 4000 bars, 400°C, XCO2 = .3716
Average Th(CO2) = -.48 (l), Th(Total) = 259. (v)
Measured Th(CO2);
-.50 -.40 -.30 -.40 -.30 -.60
-.40 -.70 -.40 -.70 -.60

APPENDIX VI Cont'd.

Sample Number = 9078804, 4000 bars, 400°C, XCO2 = .2473
Average Th(CO2) = 10.38 (l), Th(Total) = 270. (l)
Measured Th(CO2);
10.10 10.60 11.00 10.00 10.30 10.30

Sample Number = 8308803, 4000 bars, 400°C, XCO2 = .1234
Average Th(CO2) = 24.50 (l), Th(Total) = 246. (l)
Measured Th(CO2);
24.70 24.30 24.50

Sample Number = 8308811, 4000 bars, 500°C, XCO2 = .8736
Average Th(CO2) = -8.06 (l), Th(Total) = 0. (l)
Measured Th(CO2);
-8.30 -8.20 -8.30 -8.00 -7.90 -8.00
-8.10 -7.90 -7.80

Sample Number = 9078811, 4000 bars, 500°C, XCO2 = .7473
Average Th(CO2) = -2.61 (l), Th(Total) = 230. (v)
Measured Th(CO2);
-3.00 -3.10 -2.20 -2.30 -2.40 -2.60
-2.70 -2.60

Sample Number = 8308808, 4000 bars, 500°C, XCO2 = .6216
Average Th(CO2) = 2.64 (l), Th(Total) = 244. (v)
Measured Th(CO2);
2.50 2.60 2.60 2.60 2.70 2.80
2.90 2.60 2.60 2.90 2.40 2.50

Sample Number = 8308805, 4000 bars, 500°C, XCO2 = .3716
Average Th(CO2) = 13.64 (l), Th(Total) = 271. (v)
Measured Th(CO2);
13.60 13.70 13.60 13.80 13.80 13.00
13.70 13.80 13.80

Sample Number = 9078803, 4000 bars, 500°C, XCO2 = .2473
Average Th(CO2) = 22.61 (l), Th(Total) = 270. (l)
Measured Th(CO2);
22.70 22.40 22.40 22.50 22.40 22.50
23.10 22.70 22.80

Sample Number = 8308802, 4000 bars, 500°C, XCO2 = .1234
Average Th(CO2) = 30.07 (l), Th(Total) = 259. (l)
Measured Th(CO2);
30.10 30.00 30.10

Sample Number = 8308810, 4000 bars, 600°C, XCO2 = .8736
Average Th(CO2) = .00 (l), Th(Total) = 0. (l)
Measured Th(CO2);
-.50 .00 .50

Sample Number = 9078810, 4000 bars, 600°C, XCO2 = .7473
Average Th(CO2) = 6.82 (l), Th(Total) = 243. (v)
Measured Th(CO2);
7.00 7.00 6.70 6.00 6.80 7.00
6.90 7.00 7.00

Sample Number = 8308807, 4000 bars, 600°C, XCO2 = .6216
Average Th(CO2) = 11.51 (l), Th(Total) = 258. (v)
Measured Th(CO2);
11.20 11.20 11.60 11.70 11.70 11.60
11.60

Sample Number = 9078806, 4000 bars, 600°C, XCO2 = .4964
Average Th(CO2) = 16.72 (l), Th(Total) = 273. (v)
Measured Th(CO2);
17.00 16.90 17.00 17.30 16.50 16.40
16.50 16.60 16.70 16.30

Sample Number = 8308804, 4000 bars, 600°C, XCO2 = .3716
Average Th(CO2) = 21.63 (l), Th(Total) = 273. (v)
Measured Th(CO2);
21.30 21.80 21.40 21.60 21.80 21.80
21.90 21.40

Sample Number = 9078802, 4000 bars, 600°C, XCO2 = .2473
Average Th(CO2) = 27.80 (l), Th(Total) = 275. (l)
Measured Th(CO2);
27.80 27.80 27.70 27.70 27.70 28.10
27.80

Sample Number = 8308801, 4000 bars, 600°C, XCO2 = .1234
Average Th(CO2) = 30.30 (v), Th(Total) = 275. (l)
Measured Th(CO2);
30.20 30.40 30.30 30.30

Sample Number = 2118908, 4000 bars, 700°C, XCO2 = .8736
Average Th(CO2) = 5.60 (l), Th(Total) = 0. (l)
Measured Th(CO2);
5.90 5.30

APPENDIX VI Cont'd.

Sample Number = 2118905, 4000 bars, 700°C, XCO2 = .4964
Average Th(CO2) = 20.32 (l), Th(Total) = 268. (v)
Measured Th(CO2);
20.40 20.30 20.30 20.30 20.30

Sample Number = 2118904, 4000 bars, 700°C, XCO2 = .3716
Average Th(CO2) = 24.95 (l), Th(Total) = 276. (v)
Measured Th(CO2);
24.90 25.00

Sample Number = 7038905, 4000 bars, 700°C, XCO2 = .2473
Average Th(CO2) = 29.20 (l), Th(Total) = 0. (l)
Measured Th(CO2);
29.20

Sample Number = 2118902, 4000 bars, 700°C, XCO2 = .1234
Average Th(CO2) = 29.70 (v), Th(Total) = 289. (l)
Measured Th(CO2);
29.70 29.70

Sample Number = 10138808, 5000 bars, 400°C, XCO2 = .4964
Average Th(CO2) = -16.20 (l), Th(Total) = 0. (l)
Measured Th(CO2);
-16.30 -16.10

Sample Number = 7038906, 5000 bars, 400°C, XCO2 = .3716
Average Th(CO2) = -12.51 (l), Th(Total) = 0. (l)
Measured Th(CO2);
-12.80 -12.20 -12.50 -12.40 -12.50 -12.10
-13.10

Sample Number = 10138804, 5000 bars, 400°C, XCO2 = .2473
Average Th(CO2) = -5.15 (l), Th(Total) = 276. (l)
Measured Th(CO2);
-5.00 -4.90 -4.80 -5.50 -5.40 -4.60
-4.40 -5.00 -5.00 -6.10 -4.40 -6.90
-5.00 -5.00 -5.10 -5.20 -5.30

Sample Number = 10028804, 5000 bars, 400°C, XCO2 = .1234
Average Th(CO2) = 15.82 (l), Th(Total) = 237. (l)
Measured Th(CO2);
14.40 12.20 17.40 15.70 18.10 17.10

Sample Number = 10138811, 5000 bars, 500°C, XCO2 = .7473
Average Th(CO2) = -16.70 (l), Th(Total) = 0. (l)
Measured Th(CO2);
-16.60 -16.80

Sample Number = 10028811, 5000 bars, 500°C, XCO2 = .6216
Average Th(CO2) = -11.10 (l), Th(Total) = 245. (v)
Measured Th(CO2);
-11.70 -11.60 -11.30 -11.70 -11.50 -11.50
-11.50 -10.50 -10.40 -10.20 -10.60 -10.80
-11.40 -10.80 -11.00

Sample Number = 10138807, 5000 bars, 500°C, XCO2 = .4964
Average Th(CO2) = -3.37 (l), Th(Total) = 260. (v)
Measured Th(CO2);
-3.70 -3.50 -4.80 -3.30 -3.60 -3.40
-2.40 -2.40 -3.20 -3.20 -3.20 -4.00
-3.10

Sample Number = 10028807, 5000 bars, 500°C, XCO2 = .3716
Average Th(CO2) = 1.80 (l), Th(Total) = 267. (v)
Measured Th(CO2);
1.50 2.20 1.90 1.80 2.00 1.70
1.50

Sample Number = 10138803, 5000 bars, 500°C, XCO2 = .2473
Average Th(CO2) = 12.78 (l), Th(Total) = 265. (l)
Measured Th(CO2);
12.90 12.90 12.90 12.80 12.60 12.60
12.60 13.00 12.70 12.80

Sample Number = 10028803, 5000 bars, 500°C, XCO2 = .1234
Average Th(CO2) = 27.14 (l), Th(Total) = 247. (l)
Measured Th(CO2);
27.00 27.00 27.00 27.30 27.10 27.10
27.30 27.40 27.10

Sample Number = 10028814, 5000 bars, 600°C, XCO2 = .8736
Average Th(CO2) = -12.58 (l), Th(Total) = 0. (l)
Measured Th(CO2);
-11.70 -12.50 -12.90 -12.60 -13.20

Sample Number = 10138810, 5000 bars, 600°C, XCO2 = .7473
Average Th(CO2) = -6.07 (l), Th(Total) = 0. (l)
Measured Th(CO2);
-6.10 -6.10 -6.00

Sample Number = 10028810, 5000 bars, 600°C, XCO2 = .6216
Average Th(CO2) = -1.35 (l), Th(Total) = 260. (v)
Measured Th(CO2);

-.70	-.70	-.80	-3.40	-.20	-.70
-1.20	-3.40	-2.60	-2.40	-1.40	.00
-.60	-.70	-1.40			

Sample Number = 10138806, 5000 bars, 600°C, XCO2 = .4964
Average Th(CO2) = 6.01 (l), Th(Total) = 269. (v)
Measured Th(CO2);

5.70	5.60	6.00	5.80	6.00	6.00
6.50	6.30	6.00	6.00	6.00	6.60
5.80	5.70	6.10	6.10		

Sample Number = 10028806, 5000 bars, 600°C, XCO2 = .3716
Average Th(CO2) = 12.84 (l), Th(Total) = 269. (v)
Measured Th(CO2);

12.70	12.90	12.70	12.70	13.00	13.10
12.70	12.20	12.50	13.00	13.60	12.60
12.80	13.30				

Sample Number = 10138802, 5000 bars, 600°C, XCO2 = .2473
Average Th(CO2) = 21.96 (l), Th(Total) = 267. (l)
Measured Th(CO2);

22.00	22.50	22.10	22.20	22.30	22.20
22.30	22.10	22.10	19.20	21.10	22.20
22.40	22.40	22.30			

Sample Number = 10028802, 5000 bars, 600°C, XCO2 = .1234
Average Th(CO2) = 29.45 (l), Th(Total) = 261. (l)
Measured Th(CO2);

29.50	29.20	29.20	29.60	29.60	29.60

Sample Number = 1108908, 5000 bars, 700°C, XCO2 = .8736
Average Th(CO2) = -4.65 (l), Th(Total) = 0. (l)
Measured Th(CO2);

-4.70	-4.40	-4.30	-4.60	-5.00	-4.90

Sample Number = 1108907, 5000 bars, 700°C, XCO2 = .7473
Average Th(CO2) = .03 (l), Th(Total) = 244. (v)
Measured Th(CO2);

.00	.00	.00	.00	.00	.20
.00					

APPENDIX VI Cont'd.

Sample Number = 1108906, 5000 bars, 700°C, XCO2 = .6216
Average Th(CO2) = 6.90 (l), Th(Total) = 265. (v)
Measured Th(CO2);

7.00	7.20	6.80	6.80	7.00	6.90
6.80	6.90	6.70	6.90	7.00	6.80

Sample Number = 1108905, 5000 bars, 700°C, XCO2 = .4964
Average Th(CO2) = 13.07 (l), Th(Total) = 269. (v)
Measured Th(CO2);

13.00	13.00	12.90	13.20	12.90	13.20
13.20	13.00	13.30	13.00	13.10	13.00

Sample Number = 1108904, 5000 bars, 700°C, XCO2 = .3716
Average Th(CO2) = 18.29 (l), Th(Total) = 273. (v)
Measured Th(CO2);

18.30	18.00	18.70	18.20	18.40	18.20
18.20					

Sample Number = 12168802, 5000 bars, 700°C, XCO2 = .2473
Average Th(CO2) = 24.16 (l), Th(Total) = 275. (l)
Measured Th(CO2);

24.40	24.10	24.10	24.10	24.10

Sample Number = 1108902, 5000 bars, 700°C, XCO2 = .1234
Average Th(CO2) = 29.67 (v), Th(Total) = 274. (l)
Measured Th(CO2);

29.60	29.70	29.70

Sample Number = 5178905, 6000 bars, 500°C, XCO2 = .4964
Average Th(CO2) = -19.60 (l), Th(Total) = 0. (l)
Measured Th(CO2);

-19.60	-19.60

Sample Number = 5178904, 6000 bars, 500°C, XCO2 = .3716
Average Th(CO2) = -12.04 (l), Th(Total) = 263. (l)
Measured Th(CO2);

-12.00	-11.40	-11.30	-12.00	-12.40	-12.20
-12.00	-12.40	-12.70			

Sample Number = 5178903, 6000 bars, 500°C, XCO2 = .2473
Average Th(CO2) = .80 (l), Th(Total) = 261. (l)
Measured Th(CO2);

1.10	1.20	.00	.70	1.00

Sample Number = 5178902, 6000 bars, 500°C, XCO2 = .1234
Average Th(CO2) = 19.97 (l), Th(Total) = 239. (l)
Measured Th(CO2);
20.10 19.90 20.70 19.10 19.80 19.80
19.80 20.30 20.20

Sample Number = 5288906, 6000 bars, 600°C, XCO2 = .6216
Average Th(CO2) = -13.10 (l), Th(Total) = 257. (v)
Measured Th(CO2);
-12.80 -12.70 -13.50 -13.40

Sample Number = 5288904, 6000 bars, 600°C, XCO2 = .3716
Average Th(CO2) = 2.84 (l), Th(Total) = 264. (v)
Measured Th(CO2);
2.90 2.90 2.80 2.80 2.80

Sample Number = 5288903, 6000 bars, 600°C, XCO2 = .2473
Average Th(CO2) = 14.93 (l), Th(Total) = 266. (l)
Measured Th(CO2);
14.80 14.80 14.80 15.10 15.30 14.80

Sample Number = 5178924, 6000 bars, 600°C, XCO2 = .1234
Average Th(CO2) = 27.95 (l), Th(Total) = 248. (l)
Measured Th(CO2);
28.00 28.00 27.90 27.90

Sample Number = 2118928, 6000 bars, 700°C, XCO2 = .8736
Average Th(CO2) = -18.67 (l), Th(Total) = 0. (l)
Measured Th(CO2);
-18.70 -18.70 -18.60

Sample Number = 2118927, 6000 bars, 700°C, XCO2 = .7473
Average Th(CO2) = -12.98 (l), Th(Total) = 245. (v)
Measured Th(CO2);
-12.90 -13.10 -13.20 -12.70

Sample Number = 5178922, 6000 bars, 700°C, XCO2 = .6216
Average Th(CO2) = -5.60 (l), Th(Total) = 0. (l)
Measured Th(CO2);
-5.80 -5.00 -6.00

Sample Number = 2118925, 6000 bars, 700°C, XCO2 = .4964
Average Th(CO2) = 2.33 (l), Th(Total) = 0. (l)
Measured Th(CO2);
2.50 2.40 2.10

APPENDIX VI Cont'd.

Sample Number = 5178921, 6000 bars, 700°C, XCO2 = .3716
Average Th(CO2) = 11.09 (l), Th(Total) = 269. (v)
Measured Th(CO2);

11.10	11.10	11.00	11.20	11.20	11.00
11.00					

Sample Number = 2248901, 6000 bars, 700°C, XCO2 = .2473
Average Th(CO2) = 17.48 (l), Th(Total) = 0. (l)
Measured Th(CO2);

17.40	17.50	17.50	17.50

Sample Number = 2118922, 6000 bars, 700°C, XCO2 = .1234
Average Th(CO2) = 28.97 (l), Th(Total) = 262. (l)
Measured Th(CO2);

29.00	28.90	29.00	29.00	28.90	29.00

The vita has been removed from the scanned document